Characterization of Evoked Potentials During Deep Brain Stimulation in the Thalamus

by

Alexander Rafael Kent

Department of Biomedical Engineering
Duke University

Date:_____

Approved:

_____
Warren M. Grill, Supervisor

_____
Nicole Calakos

_____
Craig S. Henriquez

_____
Marc A. Sommer

_____
Patrick D. Wolf

Dissertation submitted in partial fulfillment of
the requirements for the degree of Doctor
of Philosophy in the Department of
Biomedical Engineering in the Graduate School
of Duke University

2013

ABSTRACT

Characterization of Evoked Potentials During Deep Brain Stimulation in the Thalamus

by

Alexander Rafael Kent

Department of Biomedical Engineering
Duke University

Date:_____
Approved:

_____
Warren M. Grill, Supervisor

_____
Nicole Calakos

_____
Craig S. Henriquez

_____
Marc A. Sommer

_____
Patrick D. Wolf

An abstract of a dissertation submitted in partial
fulfillment of the requirements for the degree
of Doctor of Philosophy in the Department of
Biomedical Engineering in the Graduate School of
Duke University

2013

Abstract

Deep brain stimulation (DBS) is an established surgical therapy for movement disorders. The mechanisms of action of DBS remain unclear, and selection of stimulation parameters is a clinical challenge and can result in sub-optimal outcomes. Closed-loop DBS systems would use a feedback control signal for automatic adjustment of DBS parameters and improved therapeutic effectiveness. We hypothesized that evoked compound action potentials (ECAPs), generated by activated neurons in the vicinity of the stimulating electrode, would reveal the type and spatial extent of neural activation, as well as provide signatures of clinical effectiveness. The objective of this dissertation was to record and characterize the ECAP during DBS to determine its suitability as a feedback signal in closed-loop systems. The ECAP was investigated using computer simulation and *in vivo* experiments, including the first preclinical and clinical ECAP recordings made from the same DBS electrode implanted for stimulation.

First, we developed DBS-ECAP recording instrumentation to reduce the stimulus artifact and enable high fidelity measurements of the ECAP at short latency. *In vitro* and *in vivo* validation experiments demonstrated the capability of the instrumentation to suppress the stimulus artifact, increase amplifier gain, and reduce distortion of short latency ECAP signals.

Second, we characterized ECAPs measured during thalamic DBS across stimulation parameters in anesthetized cats, and determined the neural origin of the ECAP using pharmacological interventions and a computer-based biophysical model of a thalamic network. This model simulated the ECAP response generated by a population of thalamic neurons, calculated ECAPs similar to experimental recordings, and indicated the relative contribution from different types of neural elements to the composite ECAP. Signal energy of the ECAP increased with DBS amplitude or pulse width, reflecting an increased extent of activation. Shorter latency, primary ECAP phases were generated by direct excitation of neural elements, whereas longer latency, secondary phases were generated by post-synaptic activation.

Third, intraoperative studies were conducted in human subjects with thalamic DBS for tremor, and the ECAP and tremor responses were measured across stimulation parameters. ECAP recording was technically challenging due to the presence of a wide range of stimulus artifact magnitudes across subjects, and an electrical circuit equivalent model and finite element method model both suggested that glial encapsulation around the DBS electrode increased the artifact size. Nevertheless, high fidelity ECAPs were recorded from acutely and chronically implanted DBS electrodes, and the energy of ECAP phases was correlated with changes in tremor.

Fourth, we used a computational model to understand how electrode design parameters influenced neural recording. Reducing the diameter or length of recording

contacts increased the magnitude of single-unit responses, led to greater spatial sensitivity, and changed the relative contribution from local cells or passing axons. The effect of diameter or contact length varied across phases of population ECAPs, but ECAP signal energy increased with greater contact spacing, due to changes in the spatial sensitivity of the contacts. In addition, the signal increased with glial encapsulation in the peri-electrode space, decreased with local edema, and was unaffected by the physical presence of the highly conductive recording contacts.

It is feasible to record ECAP signals during DBS, and the correlation between ECAP characteristics and tremor suggests that this signal could be used in closed-loop DBS. This was demonstrated by implementation in simulation of a closed-loop system, in which a proportional-integral-derivative (PID) controller automatically adjusted DBS parameters to obtain a target ECAP energy value, and modified parameters in response to disturbances. The ECAP also provided insight into neural activation during DBS, with the dominant contribution to clinical ECAPs derived from excited cerebellothalamic fibers, suggesting that activation of these fibers is critical for DBS therapy.

Dedication

This dissertation is dedicated to my parents, Peter Kent and Pilar Moyano, and to Meghan Petrie.

Contents

List of Tables

List of Figures

List of Abbreviations

AMPA - α-amino-3-hydroxyl-5-methyl-4-isoxazoleproprionic acid;

AN anterior nucleus;

ANOVA analysis of variance;

APV - DL-2-amino-5-phosphonovaleric acid;

CE counter electrode;

CER cerebellum;

C_{DL} double-layer capacitance;

CNQX 6-cyano-7-nitroquinoxaline-2,3-dione;

CSD current source density;

CTX cortex;

C_V volume capacitance;

DBS deep brain stimulation;

DPS distortion per sample;

ECAP evoked compound action potential;

ECoG electrocorticogram;

EEG electroencephalogram;

EMG electromyogram;

ENG electroneurogram;

EPSP excitatory post-synaptic potential;

ET essential tremor;

ETI electrode-tissue interface;

FDA food and drug administration;

FEM finite element model;

FFT fast Fourier transform;

FXTAS fragile X-associated tremor/ataxia syndrome;

GABA γ-aminobutyric acid;

PLSD protected least significant difference;

GPi globus pallidus interna;

HC hippocampus;

IC internal capsule;

IPG implantable pulse generator;

IPI interpulse interval;

IPSP inhibitory post-synaptic potential;

LFP local field potential;

LGN lateral geniculate nucleus;

MPTP 1-methyl-4-phenyl-1,2,3,6-tetrahydropyridine;

NMDA N-methyl-D-aspartate;

PD Parkinson's disease;

PES peri-electrode space;

PID proportional-integral-derivative;

P-P peak-to-peak;

PPD peripeduncular nucleus;

PPT pedunculopontine nucleus;

PSD power spectral density;

PW pulse width;

RE reference electrode;

R_F Faradaic resistance

RMS root mean square;

RN reticular nucleus;

RT Rubin-Terman model;

R_V volume resistance;

SD standard deviation;

SE standard error;

SEP somatosensory evoked potential;

SNr substantia nigra pars reticulata;

STN subthalamic nucleus;

TC thalamocortical relay;

TIN thalamic interneuron;

TTX tetrodotoxin;

UPDRS unified Parkinson's disease rating scale;

VA ventral anterior nucleus;

Vc ventral caudal nucleus;

V_{CLIN} clinical voltage;

Vim ventral intermediate nucleus;

V_{REC} recorded voltage;

V_M transmembrane potential

VL ventral lateral nucleus;

VPL ventral posterolateral nucleus;

VPM ventral posteromedial nucleus;

VTA volume of tissue activated;

Z-N Ziegler-Nichols tuning method;

Acknowledgements

Completing my dissertation was an incredibly enriching experience, and I am so grateful to all those who contributed to this project.

First, I would like to acknowledge the support and encouragement of my memorable Ph.D. advisor and mentor, Dr. Warren Grill. I feel very lucky to have worked with such a knowledgeable and accomplished person. He quickly set me along a productive research path by conceptualizing exciting research projects, providing an open door to discuss my work, giving insights when I encountered difficulties, and lending words of encouragement. He is a great teacher, both inside and outside the classroom, who pushed me to reach my full potential and helped to set me off on the next stage of my career.

Next, I would like to thank the other members of my committee, Drs. Nicole Calakos, Craig Henriquez, Marc Sommer, and Patrick Wolf, for their timely and valuable feedback.

I am deeply appreciative of the contributions from my labmates in the Neural Prosthetics Laboratory. Everyone in the lab has provided a fun, friendly, and intellectually-challenging environment. Brandon Swan made substantial contributions to the clinical study discussed in Chapter 4, including helping in the development of the protocol, working with Institutional Review Boards, recruiting patients, conducting the research, and analyzing the results. David Brocker also assisted in conducting several

clinical experiments and in analyzing results. Gilda Mills, our dedicated and versatile lab manager, helped with animal care and surgical assistance in the preclinical experiments described in Chapters 2 & 3, and also handled a multitude of other administrative and financial aspects of my research. Drs. Amorn Wongsarnpigoon and Merrill Birdno were wonderful role models, and discussions with them helped to guide my research and career. Merrill also provided me with the computational model used in Chapters 3-5 and Appendix A, and assisted me with its use. Finally, I would like to thank the undergraduate research assistants who worked with me, including Patrick Ye, Siddhartha Kosaraju, and Victor Kuo, who laid the groundwork for many aspects of this work.

As well, I would like to thank our collaborators at Duke University Hospital, including Dr. Dennis Turner and Dr. Nandan Lad, and at Emory University Hospital, including Dr. Robert Gross and Dr. Otis Smart. Dr. Turner also provided helpful insights during initial protocol development for both the preclinical and clinical studies discussed in Chapters 2-4.

I am forever appreciative of the support and encouragement of my family and friends. My parents, Peter Kent and Pilar Moyano, instilled in me their strong work ethic, love of learning, and persistence, which helped me endure and overcome the difficulties of graduate school. They also provided a great deal of encouragement and

advice. My fiancée, Meghan Petrie, has given me her unwavering love and support, making many sacrifices along the way, and was vital to my success in graduate school.

Financial support was provided by a National Institutes of Health Fellowship F31 NS070460 and grant R01 NS079312, a Duke University Department of Biomedical Engineering Robert Plonsey Fellowship, and a Medtronic Foundation Fellowship. Computational facilities were provided through the Duke University Shared Cluster Resource.

1. Introduction: Recording neural activity to understand the mechanisms of deep brain stimulation and develop closed-loop control systems

Deep brain stimulation (DBS) is an established surgical therapy for movement disorders (Benabid et al., 1991, Limousin et al., 1995, Gross and Lozano, 2000, Krauss et al., 2004), and is being investigated as a therapy for other neurological disorders. DBS is FDA-approved for treatment of the symptoms of Parkinson's disease (PD), which include tremor, rigidity, bradykinesia, and postural instability, essential tremor (ET), and dystonia. Patients may chose to undergo surgery to receive a DBS system if they suffer long-term complications from pharmacological treatments, such as dyskinesias, on-off fluctuations, or a loss of effectiveness with levodopa therapy for PD (Chou, 2007), or if they have treatment-resistant ET (Lyons and Pahwa, 2004). An electrode is implanted into a targeted region of the brain and connected via a subcutaneous wire to an implanted pulse generator (IPG), which delivers electrical stimulation through the electrode. The DBS electrode is typically implanted in the subthalamic nucleus (STN) or globus pallidus internus (GPi) for PD, GPi for dystonia, and the ventral intermediate (Vim) nucleus of the thalamus for ET. DBS is also a promising therapy for treatment of epilepsy (Hodaie et al., 2002), obsessive-compulsive disorder (Nuttin et al., 2003), pain (Kumar et al., 1997, Owen et al., 2006), and depression (Mayberg et al., 2005).

The origins of DBS (Hariz et al., 2010) date back to the 1950s, at which time intraoperative electrical stimulation was used to explore brain targets prior to lesioning

(Gildenberg, 2005). Subsequently, chronic subcortical stimulation was tested for treatment of psychosis (Delgado et al., 1952), then chronic pain (Hosobuchi et al., 1973, Mazars, 1975), epilepsy (Cooper et al., 1980, Upton et al., 1985), and finally movement disorders (Bechtereva et al., 1975, Cooper et al., 1980, 1982). The modern form of DBS, as a first-hand alternative procedure to lesioning, was introduced by Benabid and colleagues, who in 1987 demonstrated the efficacy of chronic DBS in the thalamus for patients with tremor (Benabid et al., 1987), and in 1993 used STN-DBS for PD (Pollak et al., 1993). The FDA approved Medtronic's DBS system for tremor in 1997, for PD in 2002, and for dystonia in 2003, and its long-term therapeutic effectiveness was demonstrated (Pahwa et al., 2006, Blomstedt et al., 2007, Hariz et al., 2008). DBS systems have now been implanted in over 100,000 patients worldwide.

Despite the clinical efficacy of DBS for movement disorders, there remains a lack of understanding of its mechanisms of action (Grill and McIntyre, 2001, McIntyre et al., 2004b), which limits the full development and optimization of this treatment. A better understanding of DBS could enhance the clinical implementation of this therapy in at least four ways. First, by understanding which neural elements are activated by stimulation and contribute to symptom reduction or side effects, the tuning of stimulation parameters could be optimized. Recording neural activity from the brain could provide insight into neural activation and therefore guide the rational selection of stimulation parameters. Second, an improved understanding of DBS would enable the

design of new technologies, such as novel stimulation waveforms and electrode shapes, which selectively activate the neural elements that generate clinical benefit. Third, understanding of mechanisms could enable identification of alternative brain targets for treatment of movement disorders, such as the pedunculopontine (PPT) nucleus, peripeduncular (PPD) nucleus (Mazzone et al., 2005, Zrinzo et al., 2007), or zona incerta (Kitagawa et al., 2005, Plaha et al., 2006) for PD. These alternative brain targets may provide greater benefit or be more surgically accessible than the current targets. Finally, a better understanding of DBS mechanisms could accelerate the application of DBS to other neurological disorders beyond movement disorders.

The purpose of the work described in this dissertation was to record and analyze evoked compound action potentials (ECAPs) during DBS. Such signals may have utility for programming stimulation parameters and provide insight to understand better the mechanisms of action of DBS. The approach was to record ECAPs in preclinical and clinical studies across stimulation parameters, use pharmacological manipulation and computational modeling to identify the neural origin of the recorded signal, and correlate the characteristics of the ECAP with the symptom response. This first chapter includes a summary of current approaches to parameter selection, a discussion of methodologies used to understand the mechanisms of DBS or to investigate rational selection of stimulation parameters, and an outline of the approaches used in this dissertation.

1.1 DBS parameter selection: current methods and limitations

Following implantation of the DBS system, stimulation parameters are selected to meet the following three goals: 1) maximize symptom suppression, 2) minimize side effects, and 3) maximize the battery life of the IPG (Volkmann et al., 2002). Stimulation parameters include DBS amplitude, pulse duration, frequency, and contact polarity, and these are adjusted by an external programmer that communicates with the IPG via telemetry. There are over 25,000 available combinations of parameters in a typical IPG, but few data describing the relationships between these parameters and clinical outcomes (Kuncel and Grill, 2004). Consequently, the selection of stimulation parameters is an *ad hoc* process that requires a great deal of clinical expertise and often deprives patients of the optimal benefits of DBS.

Guidelines have been suggested to assist programmers in selecting DBS parameters (Volkmann et al., 2002, Kuncel and Grill, 2004, Volkmann et al., 2006). The current-distance relationship states that neural activation thresholds increase with distance from the electrode (Ranck, 1975), and governs selection of DBS amplitude. Appropriate selection of DBS amplitude will activate a sufficient volume of the targeted brain region to generate a clinical response while minimizing spread to adjacent regions that can cause side effects, with a typical therapeutic range of 1-3.5 V (Volkmann et al., 2002). Pulse width is selected on the basis of the current-duration relationship, in which longer pulse widths reduce activation thresholds (Ranck, 1975). The typical therapeutic

range is 60-210 μs/phase, and exceeding 210 μs/phase results in thresholds that are close to rheobase and reduces the size of the therapeutic window (Volkmann et al., 2002). Moreover, using a shorter pulse width is preferable to minimize charge delivery at threshold and thereby reduce the likelihood of electrode and tissue damage (Merrill et al., 2005). Medtronic IPGs deliver charge-balanced, biphasic pulses, which minimizes the risk of electrode and tissue damage that could result from accumulation of charge at the electrode-tissue interface (Kuncel and Grill, 2004). These biphasic pulses use a low-amplitude, long-duration recharge phase so as to avoid affecting the neural excitation that was generated by the primary phase. For selection of DBS frequency, maximum clinical benefit is obtained between 130-185 Hz for PD (Limousin et al., 1995, Moro et al., 2002, Timmermann et al., 2004, Fogelson et al., 2005) and at frequencies greater than 90 Hz for ET (Benabid et al., 1991, Grill et al., 2004, Ushe et al., 2004, Kuncel et al., 2007), whereas symptoms may be exacerbated at frequencies less than 50 Hz (Birdno and Grill, 2008). Generally, the DBS frequency is set to 130 Hz, and increased only if the patient has an unsatisfactory response and further increases in DBS amplitude or pulse width generate side effects (Volkmann et al., 2002). Finally, the contact(s) that are selected for stimulation generally have the best efficacy, largest therapeutic window, and lowest threshold for clinical benefit, which maximizes battery life (Volkmann et al., 2002, Volkmann et al., 2006). Monopolar stimulation is preferred due to lower thresholds (Pollak et al., 1998), but bipolar configurations are used to reduce current spread when

side effects are observed at relatively low DBS amplitudes (Volkmann et al., 2002, Kuncel and Grill, 2004). Finally, additional contacts are used for stimulation when a broader current distribution is required to generate a sufficient volume of activated tissue for therapeutic benefit.

Power consumption is proportional to the product of DBS pulse width, frequency, and the square of the applied voltage. To extend battery life, these DBS parameters should be minimized, although not at the expense of therapeutic benefit. Importantly, older IPG models, such as Medtronic's Itrel II and Soletra, used a voltage doubler and tripler circuit above 3.6 V and 7.3 V, and exceeding these voltages led to a significant reduction in the battery life (Volkmann et al., 2002, Kuncel and Grill, 2004).

Despite these general guidelines, the selection of stimulation parameters remains an empirical process that requires significant clinical expertise. DBS settings are programmed both after surgery and at follow-up visits (Ondo and Bronte-Stewart, 2005), and it can take at least 3-6 months to obtain the best therapeutic outcomes (Bronstein et al., 2011) due to the transient micro-lesion effect (Volkmann et al., 2006), as well as concomitant adjustments of medications. During the first 6 months following implantation, patients require an average of almost 6 parameters adjustment sessions, and an additional 5 sessions during the subsequent 18 months (Ondo and Bronte-Stewart, 2005). Further, each programming session takes substantial time, with the initial programming session typically taking 1-2 hours, and subsequent sessions 30-60 minutes.

Since over 40% of programmers are physicians, the need for repeated programming is both inconvenient and costly.

Furthermore, the current approach to parameter selection can deprive patients of the optimal benefits of stimulation. If symptom suppression is not satisfactory, simply increasing amplitude, pulse width, or frequency can produce delayed exacerbation of symptoms or side effects, and cause more rapid battery depletion (Moro et al., 2002, Kuncel et al., 2006, Volkmann et al., 2006, Kuncel et al., 2007). Conversely, measuring the steady state symptom response across a range of parameters is not feasible because symptoms do not respond immediately or uniformly to DBS. While the response time is only on the order of seconds for tremor (Beuter and Titcombe, 2003), it is on the order of minutes for bradykinesia and hours for gait and postural instability in PD (Temperli et al., 2003). Moreover, it is unclear how to program parameters when there are no overt responses to DBS, such as in epilepsy. Consequently, there is sub-optimal management of motor symptoms in movement disorders, with decreased symptom fluctuations in the DBS *on* state of only approximately 60% in PD (Witjas et al., 2007). Further, if not programmed correctly, side effects can result, including paresthesias (Pahwa et al., 2006), dyskinesias (Hamani et al., 2005), hemiballism (Limousin et al., 1995, Limousin et al., 1996), stimulation-induced muscle contractions (Ashby et al., 1999), and cognitive and behavioral adverse effects (Romito and Albanese, 2010, Bronstein et al., 2011). The therapeutic outcome of DBS can be improved with expert reprogramming in many

patients (37%) complaining of sub-optimal results (Okun et al., 2005) and a majority of patients (55%) with long-term stable responses (Moro et al., 2006). Although patients are aware of the need for periodic readjustment of parameters, one study found that a majority (70%) was frustrated with the decreasing effectiveness of DBS prior to readjustment and anxious that full clinical benefit would not be restored (Perozzo et al., 2001).

1.2 Patient-specific models of DBS may guide parameter selection

Computational modeling software (Cicerone) was developed to help guide DBS parameter selection, and thereby reduce the clinical burden of the current programming approach and optimize outcomes for patients. Cicerone estimates the volume of tissue activated (VTA) during DBS across stimulation parameters in a patient-specific manner, and identifies parameters that best localize activation to the targeted brain region (Frankemolle et al., 2010). This software package integrates patients' MRI and CT images, microelectrode recording data, and a three-dimensional brain atlas to build a model representing the DBS electrode within the brain. It then calculates the VTA using the finite element method and biophysical cable models of neural elements (Butson and McIntyre, 2005, Chaturvedi et al., 2010). The Cicerone-identified parameters were as effective in reducing PD symptoms as those identified by a clinician and reduced power consumption by over 50%. Further, the model parameters may have reduced cognitive and cognitive-motor side effects that were present with the clinically-identified

parameters. This patient-specific modeling platform could be used to suggest an initial parameter set that is modified by the clinician as necessary, and could thereby maximize clinical outcomes and minimize the amount of time required for parameter selection. However, it is unclear if this system could be used to update parameter settings after changes in either the disease state or the response to DBS over time.

1.3 Recorded neural activity: improving the understanding of the mechanisms of DBS and potential use as a feedback control signal

Neural recordings from the brain have been used to study pathological activity in movement disorders with and without DBS, and are being explored as feedback control signals for DBS implantation and parameter selection. These include single-unit recordings, local field potentials (LFPs), evoked compound action potentials (ECAPs), and neurochemical recordings. One potential use of these measurements is to understand which neural elements are activated during effective DBS or result in side effects. Second, these recordings could provide a feedback signal to assist in localizing the DBS electrode relative to brain structures during implantation surgery. Finally, these feedback signals may reflect the clinical state and help guide DBS programming, preferably without requiring additional hardware or changes to neurosurgery. These signals could be used in a closed-loop DBS system that provides automatic adjustment of stimulation parameters as the disease progresses (Krack et al., 2003, Deuschl et al., 2006, Hariz et al., 2008, Weaver et al., 2012) or the response to stimulation changes over

time (Blomstedt et al., 2007, Priori et al., 2012, Rosa et al., 2012). The benefits of such a system include an elimination of the need for repeated programming sessions (Priori et al., 2012), improvement in clinical outcomes due to frequent parameter adjustments (Moro et al., 2006, Yu and Neimat, 2008, Bronstein et al., 2011), and identification of parameters that extend battery life (Priori et al., 2012).

1.3.1 The theoretical basis of recording extracellular fields

Interpretation of neural signals requires an understanding of their origin and of the effect of recording conditions on the measured waveforms. The extracellular fields measured from the brain are generated by neuronal transmembrane currents, and the recorded waveform is determined by the relative position of the electrode with respect to neuronal geometry. Neural excitation is associated with action potential propagation along the axon or dendrites, with an outward passive current at the leading edge, followed by inward Na^+ current, and subsequently by outward K^+ current at the trailing edge (Plonsey and Barr, 2007). This generates an extracellular current loop, in which current flows into the cell at the site of the action potential (*sink*), travels along the core of the cell, and exits at various, adjacent regions (*sources*) to return to the sink (Humphrey and Schmidt, 1991).

Current source density (CSD) analysis can be used to understand better the contribution to recorded field potentials of transmembrane currents generated by a neuronal population (Mitzdorf, 1985). Extracellular potentials (Φ) are generated by the

sum of contributions from current sources and sinks, and are governed by the Poisson equation:

$$\nabla \cdot (\sigma \nabla \Phi) = I_V \qquad \text{(Equation 1.1)}$$

where σ is the conductivity of the extracellular medium and I_V is the CSD (Plonsey and Barr, 2007). The sources can be represented using monopole or dipole approximations, for which the solution to Equation 1.1 is given by the following:

$$\Phi = \frac{1}{4\pi\sigma} \sum_{j=1}^{N} \frac{I_j}{r_j} \qquad \text{(monopole source)} \qquad \text{(Equation 1.2)}$$

$$\Phi = \frac{1}{4\pi\sigma} \sum_{j=1}^{N} \frac{I_j d_j \cos_j \theta}{r_j^{\,2}} \qquad \text{(dipole source)} \qquad \text{(Equation 1.3)}$$

where I_j is the current from the source j, and r_j is the distance from source j to the recording site (Plonsey and Barr, 2007). For the dipole source, d_j is the distance separating the dipole sources and θ is the polar angle of the recording site relative to the vector formed by the dipole sources. Therefore, the recorded waveform shape is determined both by distance to the cell and by the location relative to neural morphology, varying with positioning near currents sources or sinks in the dendrites, axon, or soma (Holt and Koch, 1999).

CSD analysis suggests that spatial alignment of neurons and temporal synchrony of their firing leads to higher amplitude extracellular potentials (Buzsaki et al., 2012, Lempka and McIntyre, 2013). In structures that have cytoarchitecturally regular structures, such as cortical pyramidal neurons whose apical dendrites lie in parallel,

superposition of activity is maximized and field potentials are strongest. Temporal synchrony is more likely to occur for relatively slow-acting events such as synaptic activity, so LFPs are generally thought to arise from dendritic synaptic currents. Moreover, it is thought that excitatory post-synaptic potentials (EPSPs) generate field potentials with amplitudes that are an order of magnitude greater than those of inhibitory post-synaptic potentials (IPSPs), due to the more shallow changes in transmembrane potential associated with the latter (Mitzdorf, 1985). Action potentials generate strong currents, but generally lead to smaller field potentials due to temporal dispersion, unless there is synchronous action potential generation in many neurons (Buzsaki et al., 2012).

The recorded field potentials are also modulated by properties of the volume conductor and electrode. First, the recording electrode captures the spatial average of biopotentials that are present across the uninsulated contact surface (Plonsey, 1965). Second, low-pass filtering by dendrites and by the capacitive and inductive properties of the extracellular medium (Bedard et al., 2004, 2006, Buzsaki et al., 2012) results in an inverse relationship between the magnitude of power in recorded field potentials and temporal frequency. Additionally, this relationship is a consequence of there being a longer time window for neuronal contributions to lower frequency field potentials. Third, the measured waveform is high-pass filtered by the electrode-tissue interface (Wise and Angell, 1975). Nevertheless, a computational modeling study demonstrated

that the interface impedance and the capacitive properties of the brain tissue had a negligible effect on LFPs recorded from a DBS electrode, although the former can have a more significant effect when recording with high impedance microelectrodes (Lempka and McIntyre, 2013).

Experimental and theoretical studies have investigated the spatial limit of detection for different neural signals. Several studies have demonstrated that single-unit activity can be detected up to 100-200 μm from a neuron (Henze et al., 2000, Moffitt and McIntyre, 2005). Similarly, neuronal contributions to stimulus evoked field potentials in the 3-100 Hz band were up to 250 um from the electrode (Katzner et al., 2009). It remains unclear whether LFPs extend only a few hundred micrometers (Liu and Newsome, 2006, Katzner et al., 2009, Xing et al., 2009) or several millimeters from the source (Kreiman et al., 2006, Kajikawa and Schroeder, 2011, Lempka and McIntyre, 2013), and the spatial reach appears to depend on the neuron morphology, synapse distribution, and correlation in synaptic activity (Linden et al., 2011).

1.3.2 Single-unit activity

Pathological motor symptoms associated with PD and ET are accompanied by changes in neuronal activity that can be observed at the single-unit level. In addition to firing rate, functional brain processes are mediated by firing patterns (Bevan et al., 2002, Terman et al., 2002) and oscillations (Gatev et al., 2006, Uhlhaas and Singer, 2006, Wilke et al., 2006). Pathological increases in bursting and lower frequency oscillations in the

basal ganglia and thalamus (Bergman et al., 1994, Nini et al., 1995, Vitek et al., 1999, Deuschl et al., 2001, Levy et al., 2002, Tang et al., 2005, Hammond et al., 2007) may lead to inferior information processing (Rosin et al., 2011) and the manifestation of motor symptoms in movement disorders (Bergman et al., 1998, Wichmann et al., 1999, Magnin et al., 2000, Deuschl et al., 2001, Amirnovin et al., 2004). Specifically, increased tonic and phasic activity in the basal ganglia increases inhibition of thalamocortical neurons and results in akinesia and rigidity in PD (Bergman et al., 1994, Bergman et al., 1998). Moreover, thalamic cell bursting activity was correlated with EMG measurements during periods of tremor in ET and PD patients, and therefore, may drive generation of tremor (Lenz et al., 1988, Hua et al., 1998, Magnin et al., 2000).

Single-unit recordings have helped to elucidate changes in network activity generated by DBS, and consequently, improved our understanding of the mechanisms of action of this therapy. The effect of single stimulation pulses on neural activity varies based on the region stimulated, with short duration (25 ms) neural inhibition in GPi and substantia nigra pars reticulata (SNr), no apparent effect in STN, and neural excitation in the Vim thalamus (Dostrovsky and Lozano, 2002). However, high-frequency stimulation in these target nuclei was consistently found to produce inhibition in recorded cell bodies (Dostrovsky et al., 2000, Welter et al., 2004, Meissner et al., 2005). Cellular inhibition was proposed to occur through activation of inhibitory afferent inputs (McIntyre et al., 2004b), depression of excitatory afferent input terminals (Anderson et

al., 2006), and/or depolarization blockade (Beurrier et al., 2001, Bikson et al., 2001). This result suggested that DBS generates therapeutic benefit through a lesion-like inhibitory effect. Conversely, other investigators demonstrated that axons were activated by high-frequency stimulation (Hashimoto et al., 2003, Hershey et al., 2003, Zhao et al., 2004), and that this activity was propagated to downstream nuclei (Jech et al., 2001, Anderson et al., 2003, Hashimoto et al., 2003, Windels et al., 2003, Degos et al., 2005, Phillips et al., 2006). These seemingly contradictory results were resolved by modeling studies that suggested the occurrence of both cell body inhibition and axonal activation (Grill and McIntyre, 2001, McIntyre et al., 2004b).

Based on the strong dependence of clinical effectiveness on regularized, high frequency stimulation trains (Birdno et al., 2007, Birdno and Grill, 2008), an informational lesion hypothesis was suggested to underlie the clinical response to DBS (Grill et al., 2004, Kuncel et al., 2007). This theory suggests that DBS overrides pathological firing and replaces it with non-physiological but less pathological regularized firing, which gets propagated to downstream nuclei. High-frequency stimulation led to a reduction in the number of neurons with oscillatory behavior (Meissner et al., 2005), a decrease in the coefficient of variation of the cellular firing rate (Grill et al., 2004), and a disruption of intrinsic bursting in the basal ganglia and thalamus (Anderson et al., 2003, Degos et al., 2005, Birdno et al., 2007). The pathologically intrinsic patterns of activity were replaced by neuronal firing that was

regularized and time-locked to the stimulus pulse train (Hashimoto et al., 2003, Bar-Gad et al., 2004, Dorval et al., 2008, Xu et al., 2008, McConnell et al., 2012). Although high-frequency stimulation can also drive somatic bursting (Welter et al., 2004) with interspike intervals phase-locked to the stimulation frequency or its subharmonics (Garcia et al., 2003, Garcia et al., 2005), this may not reach downstream nuclei due to collision block with antidromic action potentials generated in the axon (Johnson et al., 2008).

Single-unit recordings have been used successfully as a feedback control signal in closed-loop DBS. Rosin and colleagues recorded neuronal activity in the primary motor cortex (M1) of MPTP-treated primates, and delivered GPi stimulation pulses with 80 ms latency following each neural spike (Rosin et al., 2011). In comparison to continuous, open-loop stimulation, closed-loop DBS more effectively alleviated parkinsonian motor symptoms. Further, closed-loop stimulation disrupted tremor-related oscillatory activity in the GPi and M1 to a greater extent than continuous stimulation. While stimulating and recording from the same brain region would reduce surgical complexity in clinical translation, it was found that using GPi recordings as a feedback for GPi-DBS worsened motor symptoms, although adjustment of the post-spike stimulation delay may have improved the outcome.

Although initial results are encouraging, there exist several potential shortfalls to the use of single-unit recordings in closed-loop DBS systems. First, the long-term

stability of microelectrode recordings may be inadequate for human use (Williams et al., 1999). Second, chronic microelectrode recording would require implantation of additional hardware during neurosurgery, thereby increasing surgical complexity. Third, chronic implantation of microelectrodes is not currently FDA-approved for patients with movement disorders, although microelectrode recordings are a routine part of the DBS electrode implant procedure to identify the targeted brain region. Conversely, macroelectrodes, such as contacts on the DBS electrode, are generally not suitable for recording activity from individual neurons. However, even it were technically feasible to record multi-unit spiking activity from macroelectrodes (Winestone et al., 2012), measuring the activity of cell bodies within the implanted nucleus may not be indicative of network activity during DBS (Grill and McIntyre, 2001, McIntyre et al., 2004b) or provide a suitable feedback signal (Rosin et al., 2011).

1.3.3 Local field potentials

LFPs also provide insight into brain processes under normal and pathological conditions, and have been investigated as a feedback control signal for DBS. The LFP reflects synchronous oscillatory activity from a large population of neurons (Brown and Williams, 2005), and may provide a surrogate marker of oscillatory activity at the single-unit level (Creutzfeldt et al., 1966, Frost, 1968). Indeed, single-unit recordings were phase-locked with LFP oscillations, although not all neurons with oscillatory activity were coherent with the LFP (Kuhn et al., 2005, Weinberger et al., 2006). The magnitude

of the LFP reflects the number of oscillatory neurons and the degree of their synchronization (Kuhn et al., 2005, Weinberger et al., 2006, Linden et al., 2011). It is thought that these oscillations are pathologically elevated in PD and other neurological disorders (Llinas et al., 1999), and that high-frequency DBS disrupts these oscillations (Brown et al., 2004, Meissner et al., 2005, Silberstein et al., 2005a, Wingeier et al., 2006, Rosa et al., 2011) and restores more physiological firing patterns (Silberstein et al., 2005b).

LFP analysis is generally separated into distinct frequency bands that provide insight into brain function under physiological and pathological conditions, and the effect of DBS on these brain rhythms. Neural synchronization at low frequencies (approximately 4-10 Hz and including the theta band) recorded from the STN or GPi may be associated with dystonia (Liu et al., 2002, Silberstein et al., 2003) and tremor in PD (Brown et al., 2001, Brown, 2003), and thalamic oscillations may be related to tremor in ET and PD (Kane et al., 2009, Pedrosa et al., 2012). Further, basal ganglia activity in this band was elevated in PD during dyskinesias (Foffani et al., 2005, Alonso-Frech et al., 2006, Rodriguez-Oroz et al., 2011). It has been hypothesized that low frequency basal ganglia activity holds the cortex in a low frequency, anti-kinetic state in PD and generates the muscle contractions that result in tremor (Brown, 2003). However, tremor-related oscillations were not always observed or the most prominent feature within these LFPs (Brown and Williams, 2005). Furthermore, low-frequency oscillations

increased after administration of levodopa (Silberstein et al., 2003, Priori et al., 2004) or DBS (Giannicola et al., 2012a), and the extent of increase was correlated to clinical improvement, which contradicts the hypothesis that these oscillations are an anti-kinetic phenomenon. One group found that very low-frequency (1-2 Hz) oscillations increased in the STN after DBS was applied for a period sufficient to generate clinical improvement, and that this was persistent for several minutes after DBS was turned *off* (Priori et al., 2006, Rossi et al., 2008). However, rather than resulting from changes to network activity, this may have been caused by a reduction in the impedance of the electrode-tissue interface after stimulation, and a corresponding increase in the contribution of blood pressure-related tissue pulsation to the measured signal (Priori et al., 2006, Rosa et al., 2010).

The most commonly studied LFPs are in the beta band (13-35 Hz) due to their seemingly close reflection of the PD motor state, including dyskinesias (Silberstein et al., 2005a), bradykinesia, and rigidity (Kuhn et al., 2006, Ray et al., 2008, Kuhn et al., 2009, Pogosyan et al., 2010). Beta oscillations appear to reflect an anti-kinetic state, as beta power decreased in the STN and GPi during movement preparation and execution (Cassidy et al., 2002, Levy et al., 2002, Priori et al., 2002, Kuhn et al., 2004, Williams et al., 2005). In patients with PD, beta synchronization in the STN was elevated (Bronte-Stewart et al., 2009), particularly the low beta band (13-20 Hz) in the absence of dopamine (Priori et al., 2004, Marceglia et al., 2007), and which may have been driven by

the cortex (Marsden et al., 2001, Levy et al., 2002, Williams et al., 2002). Short intervals of STN-DBS reduced beta activity immediately after stimulation (Brown et al., 2004, Wingeier et al., 2006, Bronte-Stewart et al., 2009), similar to the effect of dopaminergic therapy (Brown et al., 2001, Silberstein et al., 2003, Priori et al., 2004, Alonso-Frech et al., 2006, Ray et al., 2008, Kuhn et al., 2009). However, prolonged delivery of DBS sufficient to generate clinical improvement that was sustained for several minutes after DBS was turned *off* did not produce significant changes in beta after DBS (Foffani et al., 2006). Additionally, STN beta oscillations were not well correlated to tremor scores (Kuhn et al., 2006, Weinberger et al., 2009), although 8-27 Hz LFP oscillations in the Vim thalamus were coherent with oscillatory muscle contractions in subjects with tremor (Marsden et al., 2000). Other disadvantages of using the beta band as the only marker of the PD motor state include the fact that these oscillations were not easily detectable in all PD patients (Giannicola et al., 2010), and were expressed differently across genders despite similar clinical manifestations of the disease (Marceglia et al., 2006). Alternatively, the ratio of low frequency power to beta band power may be a more useful indicator of pathological STN activity in PD (Giannicola et al., 2012b).

Two other LFP bands that have been investigated are gamma (60-80 Hz) and very high frequencies (around 250-350 Hz) (Priori et al., 2012). Gamma synchronization within the STN-GPi-cortical structural loop was observed in PD after dopaminergic treatment (Brown et al., 2001, Cassidy et al., 2002, Williams et al., 2002). Activity in this

band appears to be pro-kinetic, increasing before and during voluntary movement (Cassidy et al., 2002), and increasing gamma activity was correlated with greater PD symptom reduction following dopaminergic treatment (Kuhn et al., 2006). There is a reciprocal relationship between beta and gamma frequencies (Cassidy et al., 2002), and in untreated PD the beta activity may suppress gamma activity in the basal ganglia and contribute to the manifestation of bradykinesia (Brown and Marsden, 1998, Brown, 2003). Lastly, very high frequency LFP activity can be recorded from the STN in persons with and without PD (Danish et al., 2007), and increases in amplitude during voluntary movement (Foffani et al., 2003) and following administration of levodopa (Foffani et al., 2003, Lopez-Azcarate et al., 2010). It has been proposed that very high frequency oscillations are required for functional brain processes within the basal ganglia, and that high frequency stimulation could serve as a sub-harmonic drive of this activity (Foffani et al., 2003).

LFPs can be recorded from the DBS electrode, and their long-term stability was investigated. In the acute stage after DBS implantation, the peri-electrode space is filled with extracellular fluid (Yousif et al., 2008b), and in the chronic stage 6-8 weeks post-implantation this gets replaced with a glial scar (Griffith and Humphrey, 2006, Nielsen et al., 2007, Sun et al., 2008). The corresponding transition at the electrode-tissue interface led to reductions in the amplitude of the low frequency LFP band over the first 30 days (Yousif et al., 2008b, Rosa et al., 2010), although this was stabilized by 7 years

(Giannicola et al., 2012b). Conversely, beta band LFPs recorded at 30 days and 7 years after implant were similar to those recorded in the acute stage, and had comparable responses to DBS (Rosa et al., 2010, Rosa et al., 2011, Giannicola et al., 2012b).

There exist potential applications in functional neurosurgery and closed-loop DBS systems for LFP signal recordings. During DBS electrode implantation in the STN, the contact pair with the greatest beta activity was typically well-positioned within the STN, and this pair was independently chosen for chronic stimulation (Chen et al., 2006, Miyagi et al., 2009, Holdefer et al., 2010, Yoshida et al., 2010). Further, the therapeutic stimulation voltage was correlated with the distance between the contact used for stimulation and the depth of peak beta activity (Yoshida et al., 2010), and improvements in clinical symptoms with STN-DBS were inversely related to beta power in the *off* condition (Ray et al., 2008). A commercial, implantable interface was developed that enables simultaneous stimulation and recording of LFPs (Rouse et al., 2011) to explore the feasibility of a closed-loop DBS system for PD (Stanslaski et al., 2009) and epilepsy (Stanslaski et al., 2012). One LFP-based closed-loop approach entails triggering stimulation to changes to LFP bands, which were significantly different under tremulous and non-tremulous conditions and could be differentiated from movement-related changes (Burgess et al., 2010). This triggered stimulation system could conserve battery life compared to continuous stimulation. The feasibility of LFP-based closed-loop systems was demonstrated in computational models using an adaptive minimum

variance controller (Santaniello et al., 2011) or variations of the proportional-integral-derivative (PID) controller (Guo and Rubin, 2011, Gorzelic et al., 2013).

There are at least two underlying limitations to LFP-based closed-loop systems that still need to be addressed. First, a direct causality between LFP activity and clinical symptoms must be identified (Brown and Williams, 2005). These pathological oscillations may not provide a bidirectional relationship with clinical symptoms if they are instead an epiphenomenon reflective of the movement disorder (Priori et al., 2012). However, recent work demonstrated linear and non-linear causal relationships between tremor and both theta and broadband (>2 Hz) LFPs in the STN and Vim (Smirnov et al., 2008, Tass et al., 2010). Second, it is possible that LFPs recorded from the DBS electrode may not have a local origin, but instead result from volume conduction (Wennberg and Lozano, 2003, Brown and Williams, 2005, Linden et al., 2011). Although the use of differential recording can minimize the amplitude of non-local sources (Brown and Williams, 2005), the local nature of the LFP signal must be verified by establishing relationships between LFPs and local neuronal activity (Buzsaki et al., 2012).

1.3.4 Evoked compound action potentials

Measurement of ECAPs during electrical stimulation was used to probe neural circuitry and has been proposed as an intraoperative method to localize the DBS electrode. This response is generated by the synchronous activation of a population of neurons near the recording electrode, resulting in the generation of transmembrane

currents in activated neurons that create recordable voltages. ECAP recordings have been used to investigate connections within the Papez circuit and to explore the feasibility of modulating activity in the hippocampus (HC) with delivery of DBS in the anterior nucleus (AN) of the thalamus for the treatment of epilepsy (Stypulkowski et al., 2011). Using reciprocal stimulation and recording in the HC and AN thalamus, it was found that the characteristics of the ECAPs were dependent on the location of the stimulating electrode as well as the DBS amplitude and frequency. In another application, cortico-STN pathways were probed through measurement of EEG-based ECAPs from the frontocentral cortex during STN stimulation (Rosa et al., 2012). Studies have shown that these cortical responses were not simply DBS-related epiphenomena, but instead reflected changes in cortical excitability (Pierantozzi et al., 1999, Airaksinen et al., 2011, Devergnas and Wichmann, 2011).

Somatosensory evoked potentials (SEPs) were recorded during stimulation of the median, tibial, or digital nerves and may provide clinical utility (Valls-Sole et al., 2008). It is thought that SEPs recorded from DBS electrodes in the Vim were generated by EPSPs in the ventral caudal (Vc) nucleus of the thalamus (Hanajima et al., 2004), and that those recorded from the STN resulted either from volume conduction from non-local sources (Hanajima et al., 2004, Valls-Sole et al., 2008), muscle afferent inputs, or thalamo-STN projections (Pesenti et al., 2003). SEPs could be recorded during intraoperative DBS electrode implantation within the thalamus to enable determination of the electrode

position relative to the sensory pathway, where the response would be maximal (Valls-Sole et al., 2008). The electrode could also be localized with respect to the horizontal position about the posterior commissure, at which there is a polarity phase reversal of the SEP response (Hanajima et al., 2004).

1.3.5 Neurochemical recordings

Another neural signal demonstrating potential for use in closed-loop DBS systems is derived from neurochemical recordings. The wireless instantaneous neurotransmitter concentration sensor system allows for electrochemical dopamine and glutamate measurement using amperometry and fast-scan cyclic voltammetry (Lee et al., 2009). A probe was designed with interleaved stimulation and glutamate recording electrodes near the electrode tip for implantation into the STN, and dopamine recording electrodes located more dorsally on the electrode shaft for implantation in the striatum. In addition to providing guidance on DBS placement within the STN, which receives glutamatergic inputs from the cortex and PPT, neurochemical feedback from the STN and striatum could provide guidance for parameter adjustment to maintain optimal neurotransmitter levels. The basis for this feedback system is the dopamine release hypothesis, which asserts that the clinical benefit of STN-DBS is derived from activation of surviving nigrostriatal dopaminergic neurons, generating striatal dopamine release and reversing motor deficits. However, this theory has not yet been fully validated, and

the proposed neurotransmitter recording methodology and electrode design have not been approved for clinical use.

1.4 A non-neuronal feedback signal: application of symptomatic surface tremor recordings in closed-loop DBS

The use of surface EMG or accelerometry recordings also shows promise as a biophysical feedback signal for closed-loop systems (Shukla et al., 2012). Low frequency EMG activity was used to reliably predict the onset of tremor prior to its visual manifestation (Graupe et al., 2010, Basu et al., 2011). A 20 s stimulation train was triggered by the presence of EMG activity, resulting in a mean tremor-free period of 20 s after DBS was turned *off* (Graupe et al., 2010). This technique could potentially result in stimulation being *off* for almost half the time compared to continuous stimulation, which would extend battery life considerably. The disadvantage of this approach is that the patient would need to continuously wear a surface EMG electrode or accelerometer, or additional hardware would need to be surgically implanted to obtain these measurements.

1.5 Investigating ECAPs as a feedback control signal for selection of stimulation settings

While ECAPs have been recorded previously from the DBS electrode, they have not been explored as a feedback control signal for programming stimulation parameters in DBS systems. Nevertheless, they have been used for this purpose in cochlear implants, where ECAPs were recorded from non-stimulating contacts on the electrode

(Brown and Abbas, 1990, Miller et al., 2008). Taking a similar recording approach with the four-contact DBS lead, the measured signal would be a spatial average of the potentials generated by individual neurons near the electrode. It was therefore expected that the ECAP generated during DBS could provide a population view of the number and type of activated neural elements.

1.5.1 Use of ECAPs in cochlear implants

Cochlear implants are a treatment option for persons with sensorineural hearing loss, in which cochlear hair cells die due to congenital or environmental factors (Ramsden, 2002, Rauschecker and Shannon, 2002, Zeng, 2004, Middlebrooks et al., 2005). A multi-contact electrode is inserted into the cochlea and rests along the cochlear nerve, applying stimulation in a tonotopic fashion according to the sounds recorded by an external microphone. Cochlear implants have demonstrated excellent clinical effectiveness (Bond et al., 2009), and recent work has focused on using recorded ECAPs to assist in programming stimulation parameters.

The ECAP signal represents the summation of potentials generated by synchronous activation of nerve fibers within the cochlear nerve (Briaire and Frijns, 2005), and can have amplitudes as large as 1.5 mV and latencies as short as 0.2-0.4 ms (Jeon et al., 2010). Computational models suggested that the ECAP magnitude increases with the number and size of single fiber action potentials (SFAPs), and to a lesser extent the synchrony of SFAPs, whereas the duration of the ECAP is determined by the

duration and synchrony of the SFAPs (Rubinstein, 2004, Briaire and Frijns, 2005). The amplitude can, to a first approximation, be assumed proportional to the number of activated nerve fibers, and the recorded waveform is weighted towards the closest fibers (Miller et al., 2008). Further, the ECAP magnitude was greatest when the recording contact was closest to the stimulation contact, although this also generated a large stimulus artifact that could overlap the ECAP and make signal analysis more difficult (Miller et al., 2008). Finally, the ECAP amplitude and the slope of the ECAP growth function (ECAP magnitude versus stimulation amplitude) are believed to depend on the size of the surviving neural population (Hall, 1990) and the position of the electrode relative to the nerve (Miller et al., 1998).

The ECAP signal characteristics vary with the applied stimulation waveform shape, polarity, amplitude, and frequency. Charge-balanced, biphasic waveforms produced higher ECAP thresholds than monophasic waveforms (Miller et al., 2001b). This indicated that a high-amplitude recharge phase can affect activation of nerve fibers (van den Honert and Mortimer, 1979), and when possible should be distributed into several shorter duration pulses or delayed after the primary stimulation phase. The stimulation polarity also had an effect on the amplitude and latency of the ECAP response, although the direction of this effect varied with the species tested (Miller et al., 1998). The effect of polarity may have resulted from the orientation of nerve fibers relative to the electrode and/or neural degeneration of peripheral processes (Macherey et

al., 2008, van Wieringen et al., 2008). Increasing stimulation amplitude initially generated increases in ECAP magnitude before eventually reversing (Miller et al., 1998, Matsuoka et al., 2001, Westen et al., 2011), possibly due to changes in the site of excitation of a sub-population of nerve fibers (Briaire and Frijns, 2005). Finally, increasing stimulation frequency reduced ECAP amplitudes, beginning at frequencies as low as 250 Hz, resulting from neural refractoriness or adaptation (Miller et al., 2008).

The use of ECAPs has been successfully translated to the clinic for programming of stimulation parameters in cochlear implants. Neural response telemetry and neural response imaging, developed by Cochlear Ltd. and Advanced Bionics Corp., respectively, allow for easy acquisition of the ECAP signal in human patients. While statistically significant correlations were demonstrated between ECAP threshold and perceptional measures, such as the thresholds for an audible response, most comfortable level, and maximum comfortable level, these correlations were not strong (Miller et al., 2008, Jeon et al., 2010). Therefore, their use has been limited to locating general stimulation level contours, and must still be supplemented by perceptional data measures to identify parameters that generate robust therapeutic results (Briaire and Frijns, 2005, Jeon et al., 2010). Further, the quality of the ECAP recording and the size of the stimulus artifact varied substantially across subjects (Miller et al., 2008). These issues have limited the development of a closed-loop system that uses ECAPs alone as the feedback control signal. Nevertheless, for infants or persons with physical or

developmental impairments where behavioral feedback is not available, the ECAP may provide the only reliable method to ensure that the stimulation level is perceptible (Hughes et al., 2000, Miller et al., 2008). Other clinical applications of the ECAP include testing the integrity of the implant (Rubinstein, 2004), identifying redundant or interacting electrodes (Boex et al., 2003), and comparing the effectiveness of novel stimulation paradigms (Miller et al., 2008). The ECAP can also be used to identify changes in neural responses (Miller et al., 2008), measure cell survival (Hall, 1990), and better understand cochlear neurophysiology, such as the refractory period (Miller et al., 2001a). The former would be critical in providing continuing clinical benefit as the disease progressed over time.

1.5.2 Application of ECAPs in DBS

Full development of a closed-loop DBS system has not yet been accomplished, and the ECAP shows potential for use as a feedback control signal. Due to temporal synchronization of activity generated by each DBS pulse, we hypothesized that a robust ECAP response could be recorded near the electrode. Further, we hypothesized the presence of ECAP signatures of clinical effectiveness that would indicate sufficient activation of the appropriate types of neural elements necessary for therapeutic benefit. Recording ECAPs from non-stimulating contacts on the DBS electrode eliminates requirements for additional hardware or changes to the neurosurgical approach.

Therefore, the ECAP may provide a suitable feedback control signal for DBS parameter selection and in closed-loop DBS systems.

1.6 Dissertation objectives and organization

The data presented above suggest that neural activity recorded during DBS can be used to guide the selection of DBS settings, reducing the clinical burden of parameter selection and optimizing patient outcomes. The successful clinical implementation of ECAP recording in cochlear implants led us to posit that ECAPs could provide insight into neural activation during DBS and thereby assist in selection of stimulation amplitude, pulse width, frequency, and contact configuration. The purpose of this work was to explore the feasibility of ECAP recording and the suitability of this signal for parameter selection. The approach was to develop instrumentation to suppress the stimulus artifact and enable high-fidelity ECAP recording, understand the neural contribution to the ECAP through coupled preclinical experiments and computational models, establish correlations between signal characteristics and motor symptom responses in clinical experiments, and investigate the effect of the DBS electrode and recording conditions on the measured response. This work focused on ECAP recording during Vim-DBS for treatment of movement disorders, although this could be subsequently extended to other brain targets and neurological disorders. Results from these studies provide insight both into the potential use of ECAPs in DBS programming as well as the mechanisms of action of DBS.

The chapters of this dissertation are organized and formatted as publishable manuscripts, with each chapter addressing one of the following main objectives.

1.6.1 Recording evoked potentials during deep brain stimulation: development and validation of instrumentation to suppress the stimulus artifact

In **Chapter 2**, we discuss the development and validation of instrumentation used to record ECAPs during DBS. Our approach was to record ECAP signals using instrumentation designed to suppress the stimulus artifact. In a conventional amplifier system, the artifact can generate amplifier saturation at high gains and distort the ECAP signal. To prevent amplifier saturation, our recording instrumentation made use of a series of amplifier stages and several additional circuit elements. The performance of this instrumentation was assessed through *in vitro* experiments, in which mock ECAP signals were recorded in the presence of a stimulus artifact to characterize the input-output fidelity of the recording instrumentation. We also assessed whether ECAPs could be recorded *in vivo* during thalamic DBS in the cat without contamination by the artifact. Finally, we used an electrical circuit equivalent model to understand better the sources of the artifact and its reduction by the instrumentation circuit elements. The results presented in this chapter were published (Kent and Grill, 2012).

1.6.2 Neural origin of evoked potentials during deep brain stimulation

The objectives of the experiments in **Chapter 3** were to measure *in vivo* ECAP signals during thalamic DBS in the cat and to determine the neural origin of the signals

using pharmacological interventions and a computational model. We assessed how ECAP characteristics were dependent on stimulation parameters (amplitude, pulse width, frequency, and contact configuration), electrode position, and the presence of pharmacological blockers. In addition, we used a computational model of thalamic DBS to calculate an ECAP response, and compared this to the experimentally recorded signal. The model allowed us to investigate the contribution to the ECAP of different neural elements, including pre-synaptic axons, local cells, and passing axons, activated directly by stimulation or through post-synaptic mechanisms. This study demonstrated the insight provided by the ECAP signal into the type and extent of neural activation during DBS. The results presented in this chapter were published (Kent and Grill, 2013).

1.6.3 Measurement of evoked potentials during thalamic deep brain stimulation

The purpose of the experiments in **Chapter 4** was to assess the feasibility of recording ECAPs in the clinical setting, identify the origin of the ECAP and any stimulus artifact, and correlate the ECAP characteristics with the efficacy of DBS treatment. We quantified both the ECAP response and tremor symptoms in human subjects with movement disorders as a function of the amplitude, frequency, and polarity of thalamic DBS. These experiments could not be accomplished with the clinically implanted pulse generator, and we used an intraoperative setting that allowed for direct connection of our recording instrumentation to the DBS brain lead during electrode implantation or IPG replacement surgeries. Additionally, we used computational models, including a

modified version of the thalamic DBS model from **Chapter 3**, to investigate the types of elements contributing to the ECAP and the role of local impedance on the size of the stimulus artifact. The results of this study allowed us to identify ECAP signatures of clinical effectiveness, evaluate the suitability of using ECAPs as a feedback signal for DBS programming, and understand better the mechanisms of action of DBS.

1.6.4 Analysis of electrode characteristics for neural recording during deep brain stimulation

In **Chapter 5**, we determined how single-unit evoked responses, as well as population ECAP and LFP signals, were affected by the presence and geometry of the DBS electrode, as well as changes in the composition of the peri-electrode space. First, the model from **Chapter 4** was modified to determine how the signals were modulated by the high conductivity of the recording contacts. Second, we modified the model to analyze how the geometry of the electrode affected the recorded potentials. This allowed us to identify specifications for electrode designs with superior recording capabilities. Finally, we analyzed how signal characteristics would be expected to change under acute and chronic recording conditions by adjusting conductivity in the peri-electrode space. The results from this modeling study informed recording conditions and electrode design for improved neural recording fidelity.

1.6.5 Closed-loop deep brain stimulation based on evoked compound action potentials: a simulation analysis

In **Appendix A**, we implemented in the computational model from **Chapter 3** an ECAP-based closed-loop DBS system. We used a PID controller and its variants to adjust automatically DBS amplitude and/or pulse width and thereby maintain ECAP signal energy near a target value. The fraction of thalamocortical soma transmembrane potential power in the burst-driver band (4.8-6.8 Hz) served as a proxy for tremor magnitude (Birdno et al., 2012), and was used to select the target ECAP value. After steady-state was reached, disturbances were introduced that affected the bursting characteristics of thalamocortical neurons and the DBS-generated potentials via glial encapsulation, to investigate the response of this closed-loop system compared to continuous, open-loop DBS. This study enabled evaluation of the feasibility of an ECAP-based closed-loop DBS system.

1.6.6 Comparison of local field potential and tremor spectrograms

In **Appendix B**, we compared theta and beta band LFPs recorded clinically from the DBS brain lead with the onset and amplitude of tremor. Based on literature, we hypothesized that an increase in theta band power or suppression of beta band power would be concurrent with tremor. LFPs and tremor were measured in the absence of stimulation using the same instrumentation and intraoperative clinical setup from **Chapter 4**, and with subjects holding their arm in different positions to evoke tremor

with various amplitudes and durations. We studied frequency-time spectrograms for temporal association analysis.

1.6.7 Investigating a harmaline tremor model in anesthetized cats

In **Appendix C**, we attempted to generate tremor in anesthetized cats via harmaline administration, for potential use in a preclinical study investigating the correlation between ECAP characteristics and motor symptoms during DBS. In literature, harmaline tremor was typically generated in awake or decerebrated animals. We tested different anesthesia regimens, harmaline formulations and dosages, and body positions for the manifestation of tremor.

2. Recording evoked potentials during deep brain stimulation: development and validation of instrumentation to suppress the stimulus artifact

This chapter has been previously published and is used with permission (Kent and Grill, 2012).

2.1 Introduction

Deep brain stimulation (DBS) is a surgical therapy to treat medically refractory movement disorders, such as essential tremor (ET) (Benabid et al., 1991, Pahwa et al., 2006) and Parkinson's disease (PD) (Benabid et al., 1994), as well as other neurological disorders including epilepsy (Hodaie et al., 2002). The DBS electrode is implanted in the ventral intermediate (Vim) nucleus of the thalamus for tremor and the subthalamic nucleus (STN) or internal segment of the globus pallidus (GPi) for PD. An implantable pulse generator (IPG) is connected to the electrode via a subcutaneous wire and delivers high frequency stimulation to the targeted brain region. Following implantation, the parameters of stimulation, including voltage, frequency, and pulse width are selected to produce symptom suppression (Kuncel and Grill, 2004).

Current approaches to the selection of stimulation parameters are a significant clinical burden and improper programming may deprive patients of the optimal benefits of DBS. There are over 25,000 available combinations of stimulation voltage, frequency, and pulse width in a typical IPG (Medtronic Soletra 7426), but few data describing the relationships between stimulation parameters and clinical outcomes (Kuncel and Grill,

2004). Further, because symptoms do not respond immediately or uniformly to DBS (Temperli et al., 2003), it is not feasible to measure the steady-state symptom response to a wide range of stimulation parameters, as required to identify the most effective settings. The time course of response to DBS is on the order of seconds for tremor (Beuter and Titcombe, 2003), but minutes for bradykinesia (Temperli et al., 2003), making programming more challenging for the latter. Moreover, it is unclear how to select parameters when there are no immediate or overt responses to stimulation, such as for epilepsy. Consequently, there are typically a large number of parameter adjustments necessary at follow-up visits, making programming time-consuming and costly (Ondo and Bronte-Stewart, 2005), and many patients spend appreciable time with sub-optimal DBS treatment (Okun et al., 2005, Moro et al., 2006).

Measuring neural activity during DBS may provide a means for rational selection of stimulation parameters. One strategy records ongoing EEG-like brain rhythms known as local field potentials (LFPs), which are μV-level signals reflecting synchronized neural activity (Marceglia et al., 2007). For example, elevated theta oscillations (4-7 Hz) are observed within the thalamus of ET subjects at the characteristic frequency of pathological tremor (Kane et al., 2009), and elevated beta frequency power (13-35 Hz) is present within the STN and GPi of PD subjects (Brown and Williams, 2005). LFPs are modulated following treatment with DBS, suggesting that clinical efficacy is dependent on the disruption of pathological synchronization (Rossi et al., 2008, Bronte-Stewart et

al., 2009). However, a direct causal link between LFP activity measured during DBS and the corresponding motor symptoms has not yet been identified (Brown and Williams, 2005).

We propose to record electrically evoked compound action potentials (ECAPs) during DBS, providing insight into the activity of neurons directly affected by stimulation. Each DBS pulse activates an ensemble of neurons near the electrode. Transmembrane currents generated during activation of individual neural elements create voltages that can be recorded from non-stimulating contacts on the DBS electrode. The characteristics of the ECAP are expected to depend on the type and spatial extent of neural element activation during DBS. The ECAP could thus provide signatures of clinical effectiveness that correspond to sufficient activation of the appropriate type(s) of neural elements (Kuncel et al., 2007), and could be used to tune stimulation parameters during DBS programming sessions. An analogous ECAP recording strategy has been used during cochlear nerve stimulation as a feedback signal for programming cochlear implants (Miller et al., 2008, Jeon et al., 2010). The ECAP could also be used as a feedback control signal in closed-loop DBS systems that provide automated, periodic tuning of stimulation parameters to respond to patient needs.

The purpose of this study was to develop and evaluate instrumentation to record ECAPs during DBS. Recording the ECAP is challenging due to the large stimulus artifact that can cause amplifier saturation and mask the ECAP signal (McGill et al., 1982, Rossi

et al., 2007). Available techniques to remove the stimulus artifact are inadequate for ECAP recording during DBS. Several techniques rely on signal processing strategies, including curve fitting (Wagenaar and Potter, 2002), template subtraction (Hashimoto et al., 2002), polarity averaging (Brown and Abbas, 1990), and masker-probe paradigms (Miller et al., 2000). Although several of these strategies have been used with some success in cochlear nerve ECAP recordings (Miller et al., 1999, Miller et al., 2000, Alvarez et al., 2007), they are performed after the amplification stage and thus limit the gain that can be used without amplifier saturation. Hardware methods are also used to reduce the artifact, including signal filtering for DBS LFP recordings (Rossi et al., 2007), but this requires separation of the artifact and physiological signal in the frequency domain. Alternatively, sample-and-hold amplifiers (Babb et al., 1978) have enabled artifact-free recording from stimulating electrodes within 2 ms after the stimulation pulse (Jimbo et al., 2003, Blum et al., 2007), though have exhibited inconsistent performance (Grumet et al., 2000).

We sought to develop instrumentation that could reduce the artifact during the amplification stage and thereby enable high gain recording of ECAPs. The performance of this instrumentation was assessed through *in vitro* experiments, in which mock ECAPs were recorded in the presence of a stimulus artifact to characterize the input-output fidelity of the system. The instrumentation was then used to demonstrate that ECAPs could be recorded *in vivo* from the thalamus of the cat, with signal characteristics

dependent on stimulation parameters. Finally, an electrical circuit equivalent model was developed to determine both the sources of the stimulus artifact recorded during the *in vitro* and *in vivo* experiments and the mechanisms of artifact reduction by the instrumentation. Preliminary results of this study were presented in a conference paper (Kent and Grill, 2011).

2.2 Methods

The design objective for the instrumentation was to make high fidelity ECAP recordings in the presence of a stimulus artifact. We used differential recordings from non-stimulating contacts on the DBS electrode to eliminate the need for additional recording electrodes and ensure that the recording contacts were near the neurons activated by stimulation. We sought to limit the artifact magnitude such that sufficient amplifier gain could be used without saturation, and to limit the artifact duration to avoid distorting short latency ECAPs. The instrumentation combined battery-powered biopotential amplifiers in a serial configuration with diode clamps, amplifier blanking, and a relay at the stimulator. *In vitro* and *in vivo* experiments were conducted to characterize the ability to limit the size of the stimulus artifact, enable higher gains without amplifier saturation, and record ECAPs with high fidelity.

2.2.1 In vitro experimental setup

We used an *in vitro* setup to reproduce the experimental conditions of the DBS electrode within the brain (Fig. 2.1A) (Rossi et al., 2007). A DBS electrode was immersed

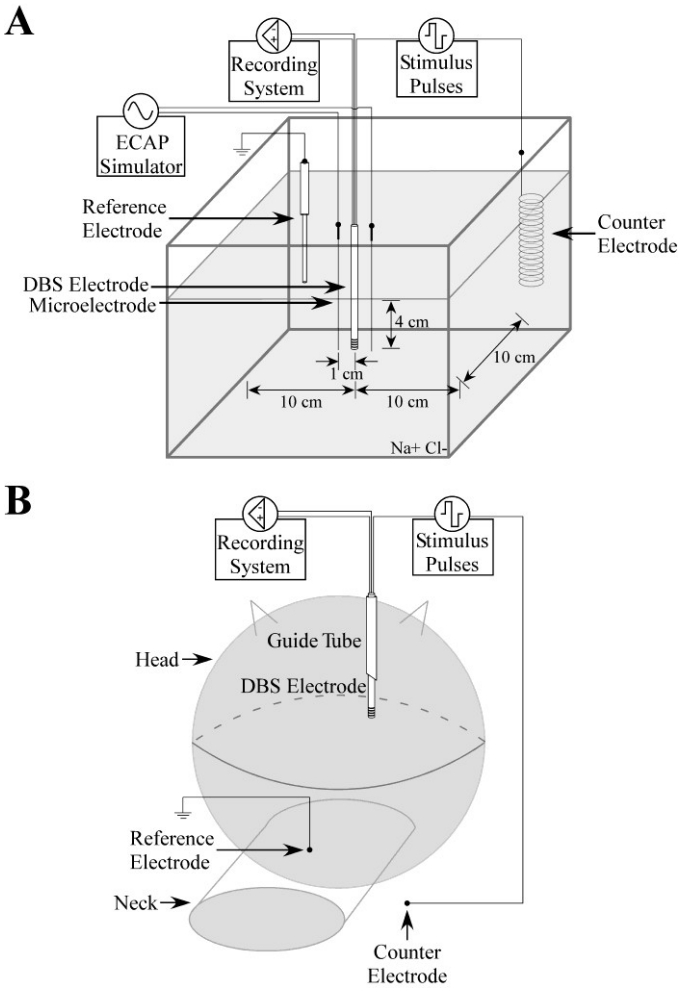

Figure 2.1: Schematic of the experimental setups used to record ECAPs during DBS. A: For *in vitro* testing, the DBS electrode, tungsten microelectrodes, Ag/AgCl recording circuit reference electrode, and counter electrode were immersed in a saline bath. The microelectrodes were positioned on either side of the DBS electrode to deliver the mock ECAP (mECAP). B: For *in vivo* testing, the mini DBS electrode was implanted through a guide tube into the ventrolateral (VL) nucleus of the thalamus in an anesthetized cat. We used a stainless steel retractor placed in the ipsilateral chest muscle as the counter electrode, and a Ag/AgCl electrode placed on the back of the neck as the recording circuit reference.

in a saline bath (137 mM NaCl) and was used to deliver monopolar or bipolar

stimulation, with two of the non-stimulating contacts connected to the recording system.

Two DBS electrodes were tested: a clinical DBS electrode (Model 3387, Medtronic) and a custom mini DBS electrode (NuMed). The clinical DBS electrode had a lead body diameter of 1.27 mm, and four contacts of 1.5 mm height separated by 1.5 mm spacing. The mini DBS electrode, which was also used in the subsequent *in vivo* experiment, had a lead body diameter of 0.625 mm, and four contacts of 0.5 mm height separated by 0.5 mm spacing. Each DBS pulse triggered generation of a mock ECAP (mECAP), synthesized by a waveform generator (Model 33120A, Agilent) as a single cycle of sinusoidal current and delivered by a pair of tungsten microelectrodes near the DBS electrode. Given that the bulk of the power in the physiological ECAP frequency spectrum is in the 100 Hz to 4 kHz band, we used a 4 kHz mECAP sinusoid (0.25 ms duration), which would be most challenging to record with high fidelity due to the short signal duration. A helical stainless steel wire was used as the counter electrode for monopolar stimulation configurations, and a Ag/AgCl electrode (Model RE-5B, BASi) was used as the recording circuit reference. A custom program written in LabView (National Instruments) controlled delivery of DBS pulses, trigger pulses for the mECAP, timing of digital outputs to operate components in the recording instrumentation, and sampling of the signal (80 kHz sampling rate).

2.2.2 Testing artifact reduction and recording fidelity

Using the *in vitro* setup, we recorded the mECAP signal in the presence of a stimulus artifact across various stimulation parameters, DBS contact configurations, and

recording system configurations. Charge-balanced, biphasic DBS was applied with clinically relevant stimulation parameters of 1-3 V amplitude, 50-500 μs/phase pulse width (symmetric and asymmetric pulses), 100 Hz frequency, and cathodic-phase first polarity. Three different contact configurations were used for stimulation and recording, with contacts designated 0-1-2-3 in the ventral-to-dorsal direction: monopolar stimulation with either symmetrical recording contacts *(monopolar symmetric*: 1+ stimulation, 0+/2- recording) or asymmetrical recording contacts (*monopolar asymmetric*: 0+ stimulation, 1+/2- recording), as well as bipolar stimulation (*bipolar*: 1+/2- stimulation, 0+/3- recording). The parameters for the mECAP were 0.1-2 ms latency and 0.1-0.5 mA peak-to-peak (P-P) input amplitude, which generated recorded amplitudes of 0.18-0.88 mV_{P-P} in the monopolar symmetric configuration. We recorded these signals both with and without the circuit components used to suppress the artifact, as well as with a single commercial biopotential amplifier (SR560, Stanford Research Systems). The extent of artifact reduction between recording systems was quantified by the change in amplifier gain that could be achieved without amplifier saturation and by distortion of the mECAP signal.

The signals recorded across these stimulation and recording conditions were analyzed to quantify mECAP distortion. For each trial, we collected a raw data set consisting of stimulus artifact and mECAP measurements for 10 s. Due to the small magnitude of the mECAPs, stimulus-triggered averaging was applied 64 times to

improve the signal-to-noise ratio. The distortion of the recorded mECAP sinusoid was measured against an ideal sinusoidal voltage with the same duration and latency (accounting for phase shift), and with the ideal sinusoid magnitude fit using a least-squares approach. The sampling frequency of the ideal sinusoid was matched to that of the recorded sinusoid so that point-wise analysis could be performed. The magnitudes of both the ideal and recorded sinusoids were then normalized to the amplitude of the ideal sinusoid to avoid bias against larger magnitude mECAPs. Finally, distortion was measured as the root-mean square error between the magnitude-normalized recorded and ideal sinusoids. This value was divided by the number of samples in the sine wave to get an average distortion per sample (DPS) value.

2.2.3 In vivo experimental setup and ECAP recording

We investigated the feasibility of recording *in vivo* ECAPs during thalamic DBS in an adult cat (Fig. 2.1B). Animal care and experimental procedures were reviewed and approved by the Institutional Animal Care and Use Committee of Duke University. The animal was initially anesthetized with ketamine HCl (35 mg/kg i.m.) and maintained with alpha chloralose (65 mg/kg i.v. supplemented at 15 mg/kg as needed). Artificial respiration maintained end tidal CO_2 at 3-4%, core temperature was maintained at 38°C with heating pads, arterial blood pressure was monitored with a catheter in the carotid artery, and fluids were continuously administered (10-15 ml/kg/hr).

The ventrolateral (VL) nucleus of the thalamus was targeted for implantation of the mini DBS electrode. The VL thalamus is the feline homologue of the Vim thalamus in primates (Berman and Jones, 1982). The anesthetized cat lay prone with the head fixed in a stereotactic frame. Following a craniotomy, the VL thalamus was located using stereotactic technique (Snider and Niemer, 1961, Berman and Jones) in conjunction with single-unit microelectrode recordings. Neurons in the dorsal region of the VL thalamus exhibited increased activity in response to passive movement of the contralateral hind limb (Berman and Jones, 1982). Once the location of the VL thalamus was identified, a guide tube was inserted vertically into the brain using a micromanipulator, and the mini DBS electrode was inserted through the guide tube into the VL thalamus. To confirm that the electrode was correctly placed in the VL thalamus, we recorded evoked responses from two contacts on the DBS electrode (0+/2-) during electrical stimulation of the contralateral sciatic nerve (biphasic pulses of 1 mA amplitude, 7 Hz frequency, and 50 μs/phase pulse width).

The ECAP generated *in vivo* by DBS was measured across a range of clinically relevant stimulation parameters. Charge-balanced, biphasic DBS was applied at 1-3 V amplitude, 10 or 100 Hz frequency, 50 or 100 μs/phase pulse width, and both cathodic- and anodic-phase first polarities. The two contact configurations tested were monopolar symmetric (1+ stimulation, 0+/2- recording) and monopolar asymmetric (3+ stimulation, 2+/1- recording). A stainless steel retractor placed in the ipsilateral chest muscle acted as

the counter electrode and a Ag/AgCl electrode (Model EL504, Biopac Systems) placed on the back of the neck was used as the reference electrode. To evaluate the performance of the instrumentation *in vivo*, we recorded ECAPs both with and without the circuit components used to suppress the artifact, and with the conventional amplifier. The animal was killed by intravenous injection of Euthasol (Virbac), and postmortem recordings were made at several time points to confirm the biological origin of the antemortem ECAPs. During all trials, ECAPs were recorded for 10 s, with trials separated by 10 s, and stimulus-triggered averaging was applied 64 times.

2.2.4 Histology

Following completion of ECAP recording, the anatomical location of the mini DBS electrode was determined. The electrode was removed and the animal was immediately perfused transcardially with saline followed by 10% formalin. The hemisphere of the brain containing the electrode path was excised and post-fixed in 10% formalin for 24 hours at 4°C. Subsequently, the tissue sample was placed in 30% sucrose at 4°C until it sank, cryoprotected with optimal cutting temperature compound (Tissue-Tek, Sakura), and frozen at -80°C (McConnell et al., 2009). The sample was cryosectioned into 50 μm coronal sections and mounted on glass slides. The sections were defatted and Nissl stained with 0.1% cresyl violet. Finally, the electrode track and nuclei of interest were identified at 2.5x magnification, such that the location of the electrode could be registered to a stereotactic atlas of the cat brain (Snider and Niemer, 1961).

2.2.5 Computational model of the stimulus artifact

An electrical circuit equivalent model was developed, using PSpice (Cadence OrCAD Capture CIS v16.3) and Comsol Script v1.2 (COMSOL) finite element modeling software, to study the sources of the stimulus artifact and mechanisms of artifact reduction by the recording instrumentation. The model included circuit representations of the DBS contact interface, saline or neural tissue medium, DBS voltage source, and components of the recording instrumentation (Fig. 2.2). The monopolar symmetric configuration was modeled in the electrical circuit equivalent simulations, with biphasic DBS delivered between contact 1 and a return electrode, and contacts 0 and 2 serving as inputs to the recording amplifier. The AC-coupled amplifier had a 100 MΩ, 25 pF parallel input impedance in series with a 0.1 μF capacitor at each input. The electrode-tissue interface (ETI) at each DBS contact was represented as a parallel capacitance and resistance with values derived from literature (Wei and Grill, 2009), assuming biphasic DBS pulses of 1 mA amplitude.

The DBS contacts and return electrode were electrically interconnected by impedance representations of the saline or neural tissue medium. To calculate the bulk resistance of the medium, a three-dimensional model of the DBS electrode within a spherical volume conductor was developed in Comsol Script. The volume of the spherical conductor matched the approximate volume of the saline bath or cat skull, 3,502 or 524 cm^3, respectively. The saline and neural tissue volume conductors were

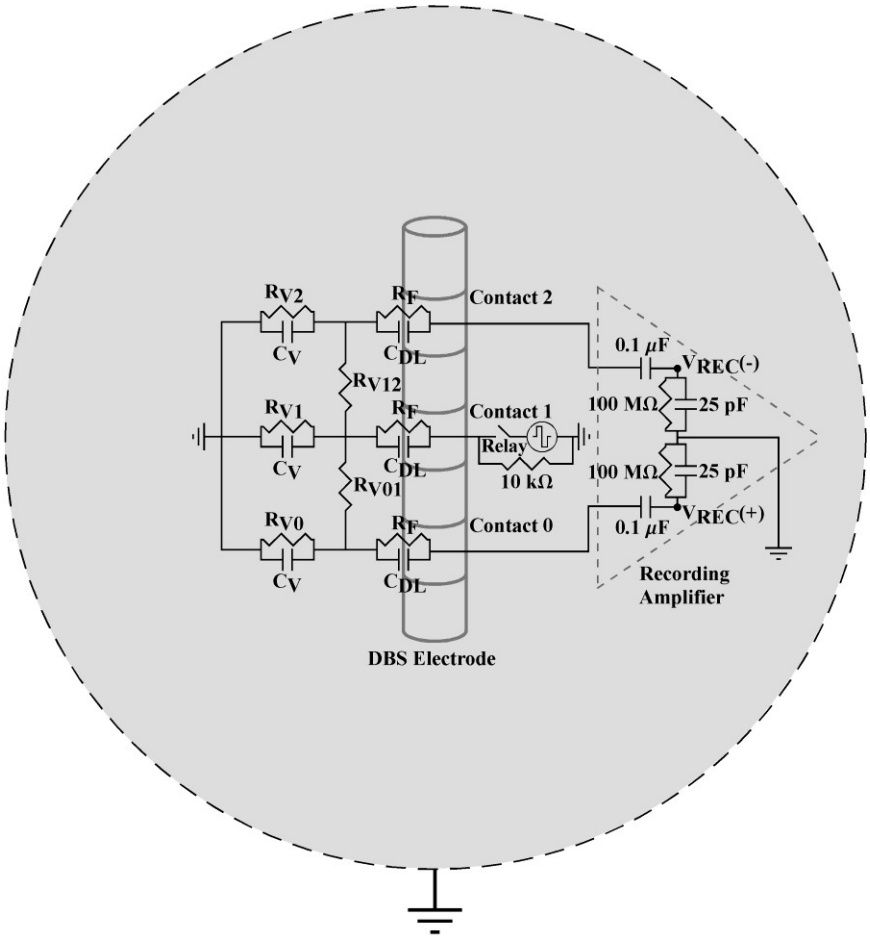

Figure 2.2: Electrical circuit equivalent model used to calculate the stimulus artifact generated by DBS applied between contact 1 and a spherical return electrode, with differential recordings made from contacts 0 and 2 (monopolar symmetric configuration).The electrode-tissue interface was composed of a parallel double-layer capacitance (C_{DL}) and charge transfer Faradaic resistance (R_F). The volume conductor included both the resistance between contacts (R_{V01} and R_{V12}) and the resistance between each contact and the return electrode (R_{V0}, R_{V1}, and R_{V2}). The capacitance of the volume conductor (C_V) was parallel to the resistance between contacts and the return electrode. The input impedance of the recording amplifier was represented in the model, and the model output was the recorded differential voltage (V_{REC}) across the amplifier impedance.

assumed to be homogenous, represented with conductivities (σ_v) of 2 S/m (Geddes and Baker, 1967) and 0.3 S/m (Ranck, 1963), respectively. The clinical or mini DBS electrode

was represented in the model with the appropriate geometrical dimensions, with contact 1 placed at the center of the volume conductor, and the conductivities of the DBS contacts and insulated shaft were 5×10^{6} S/m and 1×10^{-13} S/m, respectively (Yousif et al., 2008a). A 1 V boundary condition was specified at one contact surface and the exterior boundary of the volume conductor was grounded. Comsol Script created a variable resolution mesh and solved the Poisson equation using the conjugate gradients method. The resistance was calculated using Ohm's law ($R = 1\ V / I_{norm}$), where I_{norm} was determined by integrating the normal current density over the contact surface. The resistance between two DBS contacts was calculated in a similar fashion, with the two contacts of interest set to ±0.5 V and the normal current density integrated across the contact surface.

The permittivity of the medium was incorporated into the circuit model by placing capacitors between the DBS contacts and return electrode, parallel to the volume conductor resistance (Butson and McIntyre, 2005). Saline and neural tissue permittivity values were estimated from previous studies, having dielectric constants (K) of 75 (for 137 mM NaCl at DC) (Wang and Anderko, 2001) and 1×10^{4} - 1×10^{6} (at frequencies below 1 kHz) (Schwan and Kay, 1957, Foster and Schwan, 1989), respectively. The permittivity (ε) was calculated as:

$$\varepsilon = K\varepsilon_0 \qquad \text{(Equation 2.1)}$$

where ε_0 is the permittivity of free space (8.85×10^{-12} F/m). Subsequently, the bulk capacitance was calculated by assuming that the geometry of the DBS contact within the volume conductor was one of two concentric spherical conducting shells. The capacitance of this spherical capacitor was then calculated as:

$$C_V = 4\pi\varepsilon \frac{r_a r_b}{r_b - r_a} \qquad \text{(Equation 2.2)}$$

where r_a and r_b are the radii of the DBS contact and volume conductor, respectively (Young and Freedman, 2004). The radius used for the DBS contact was set such that the surface area of the spherical contact and actual cylindrical contact were matched, and the radius of the volume conductor was identical to that used in the Comsol Script model.

The circuit model was used to solve for the stimulus artifact voltage, measured across the amplifier inputs, resulting from DBS pulses of 3 V amplitude, 100 Hz frequency, 50 μs/phase pulse width, and cathodic-phase first polarity. Three models were constructed, in accord with the experimental studies: (i) an *in vitro* model, with the clinical DBS electrode in the saline bath, (ii) an *in vivo* model, with the mini DBS electrode in neural tissue, and (iii) a postmortem *in vivo* model, with the mini DBS electrode in dead neural tissue. For the postmortem *in vivo* model, the dielectric constant K was reduced from the antemortem model by 2.7% (Schmid et al., 2003), and the conductivity σ_v was reduced by 28% (Surowiec et al., 1986).

2.3 Results

We developed an instrumentation system to record ECAPs during DBS, evaluated the performance of the system through *in vitro* and *in vivo* experiments, and conducted analysis of an electrical circuit equivalent model to analyze the source of the stimulus artifacts and their reduction by the elements of the instrumentation.

2.3.1 Instrumentation design

The DBS-ECAP instrumentation used three stages of series amplification and several circuit components to limit the stimulus artifact and enable high fidelity recording of short latency, small amplitude ECAP signals (Fig. 2.3(i)). Differential recordings were made from two non-stimulating contacts on the DBS electrode to reduce common-mode noise, and served as inputs to a battery-powered preamplifier (A_1, SR560), which provided gain and high input impedance. Two additional amplifier stages (A_2 and A_3, SR560) were placed in series to increase gain further and to filter the signal with a 10 Hz to 10 kHz pass-band. Anti-parallel diode clamps (1N4154, Fairchild Semiconductor) were placed at the inputs of A_2 and A_3 to ground the line if the input voltage exceeded approximately ±0.7 V, thereby selectively clipping the stimulus artifact and enabling increased gain without saturation. To achieve further increases in gain, the signal paths in amplifiers A_2 and A_3 were internally grounded through an opto-isolated CMOS multiplexer (74HC4053), blanking the output for the duration of each stimulus pulse and the subsequent 60 μs. The rapid turn-off time of this CMOS switch (10 μs)

ensured that short latency ECAP responses could still be recorded. In addition, a low-resistance, rapid-response PhotoMOS relay (AQV212(A), Panasonic) was used to disconnect the stimulating electrodes between DBS pulses. This limited capacitive discharge from the ETI through the stimulator after each pulse, and thereby reduced the duration of the stimulus artifact (McGill et al., 1982). A 10 kΩ parallel resistor was placed across the stimulating electrodes to allow accumulated charge on the stimulating contacts to discharge between pulses. Further, this resistor enabled near-critical damping of the signal recovery from artifact to baseline. The digital pulse controlling the closing of the stimulator relay was turned off 40 μs before the end of the DBS pulse to account for the intrinsic delay of the relay. The digital pulses controlling the amplifier blanking and closing of the stimulator relay were turned on 2 ms before each DBS pulse to account for turn on delays, and to discharge any charge remaining on the stimulating electrodes.

Several strategies were implemented to reduce the risk of inadvertent electrical injury to the subject. The front end of each amplifier stage was AC-coupled to prevent exposure to DC voltages. Further, anti-series, current-limiting diodes (1N5285, Central Semiconductor) were placed between the DBS leads and each input to the preamplifier to limit current to less than 0.3 mA in the event of an instrumentation malfunction. Finally, DBS generated by the LabView controller was applied through an optically-isolated stimulator (bp isolator, FHC) (Birdno et al., 2008, Dorval et al., 2010).

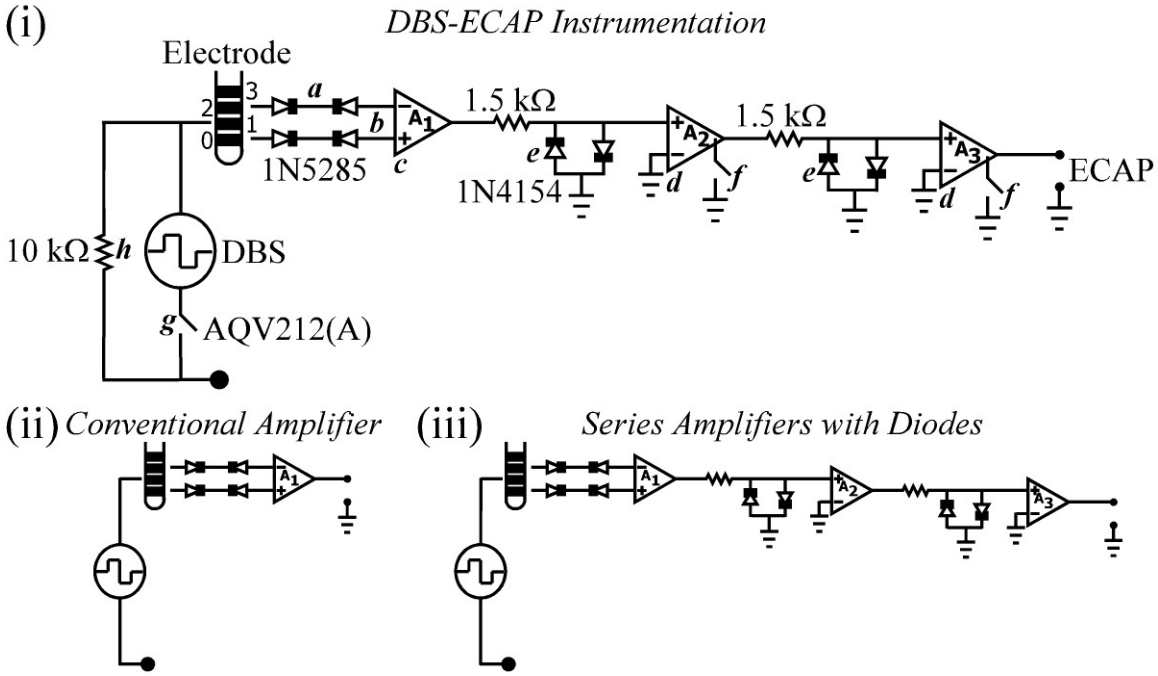

Figure 2.3: Diagram of ECAP recording instrumentation. (i) DBS-ECAP instrumentation used for stimulus artifact reduction and ECAP recording during DBS. (a) Anti-series, current-limiting diodes (1N5285) were connected to the DBS lead prior to the amplification stages. (b) Differential recordings were made from two DBS contacts, and (c) served as inputs to the preamplifier (A_1). (d) Two additional series amplifier stages (A_2 and A_3) further increased the gain and filtered the signal with a 10 Hz to 10 kHz pass-band. (e) Anti-parallel diodes (1N4154) were placed at the inputs of A_2 and A_3. (f) During each stimulus pulse, an opto-isolated CMOS multiplexer (74HC4053) internally grounded the signal path in amplifiers A_2 and A_3. (g) A PhotoMOS relay (AQV212(A)) disconnected the stimulating electrodes in between DBS pulses. (h) The parallel resistance enabled any accumulated charge on the stimulating electrodes to discharge between pulses, and enabled near-critical damping of the signal recovery from artifact to baseline. Diagrams of the (ii) conventional amplifier, and (iii) series amplifiers with (anti-parallel) diodes are also provided. Two additional setups that were tested include the series amplifiers without diodes and the series amplifiers with diodes and stimulator relay (not shown).

2.3.2 In vitro evaluation of the DBS-ECAP instrumentation

In vitro experiments were conducted to characterize the capability of the DBS-ECAP instrumentation to reduce the stimulus artifact and record mECAPs with high fidelity. Compared to a conventional amplifier (Fig. 2.3(ii)), the series amplifiers with diodes (Fig. 2.3(iii)) reduced the magnitude of the stimulus artifact (Fig. 2.4A) and enabled an increase in gain by a factor of 25 (Table 2.1). Conversely, the series amplifiers

Table 2.1: Maximum gain (G) possible without saturation for the different recording system configurations and contact configurations tested *in vitro*. DBS was applied with 3 V amplitude, 100 Hz frequency, 50 μs pulse width, and cathodic-phase first polarity. The gain is also provided at each amplifier stage for recording system configurations with multiple stages.

Recording System	Monopolar Symmetric	Monopolar Asymmetric	Bipolar
Conventional Amplifier	**100**	**20**	**10**
Series Amplifiers with Diodes	**2,500** G_1=100,G_2=5,G_3=5	**500** G_1=20,G_2=5,G_3=5	**250** G_1=10,G_2=5,G_3=5
DBS-ECAP Instrumentation	**100,000** G_1=100,G_2=200,G_3=5	**40,000** G_1=20,G_2=200,G_3=10	**50,000** G_1=10,G_2=500,G_3=10

without diodes saturated at the equivalent gain (Fig. 2.4B). Even with the use of the series amplifiers with diodes, there remained a relatively large amplitude, long duration stimulus artifact with a triphasic waveform shape (Fig. 2.4C). The use of the series amplifiers with diodes and stimulator relay reduced the magnitude and duration of the third phase of the artifact by limiting capacitive discharge through the stimulator after each pulse. Subsequent addition of amplifier blanking, completing the DBS-ECAP

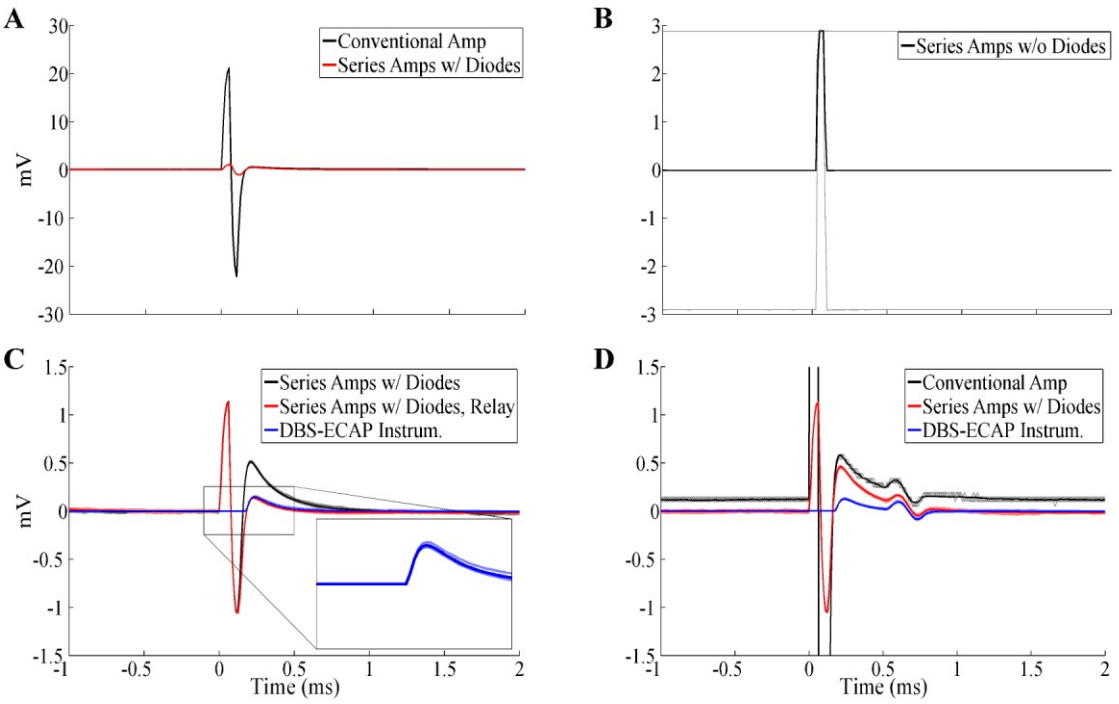

Figure 2.4: *In vitro* stimulus artifact waveforms measured with the different recording system configurations. DBS was applied at time 0 with 3 V amplitude, 100 Hz frequency, 50 μs pulse width, and cathodic-phase first polarity using the monopolar symmetric configuration. The stimulus-triggered average waveform (bold traces) and single trials (light traces) are shown. A: Comparison of artifacts recorded with the conventional amplifier (black trace) and series amplifiers with diodes (red trace). B: Using the series amplifiers without diodes, the amplifiers saturated at the equivalent gain used for the series amplifiers with diodes. This resulted in clipping of the signal at the positive and negative voltage supply rails, and distortion of the stimulus artifact waveform due to the nonlinearity of the amplifier output. Some single trial traces are obscured by overlapping traces. C: Comparison of artifacts recorded with the series amplifiers with diodes (black trace) series amplifiers with diodes and stimulator relay (red trace), and DBS-ECAP instrumentation (blue trace). The inset shows a zoomed view of the stimulus artifact waveform for the DBS-ECAP instrumentation. D: Comparison of artifacts and mECAPs recorded with the conventional amplifier (black trace), series amplifiers with diodes (red trace), and DBS-ECAP instrumentation (blue trace). Each DBS pulse triggered a 4 kHz sinusoidal mECAP with 0.18 mV_{P-P} amplitude (0.1 mA_{P-P} input amplitude) and 0.5 ms latency.

instrumentation, suppressed the first two phases of the artifact (corresponding to the two phases of the DBS pulse). Compared to the conventional amplifier, use of the DBS-

ECAP instrumentation enabled an increase in gain by a factor of 1,000-5,000, depending on the contact configuration (Table 2.1). However, the maximum gain used with the DBS-ECAP instrumentation during mECAP recording was limited to that of the series amplifiers with diodes (Table 2.1) to avoid diode clipping of the mECAP and to enable comparison of these two recording system configurations at equal gain.

The recording fidelity of the DBS-ECAP instrumentation was examined through analysis of the distortion of mECAP signals generated by applying a single cycle of a sinusoidal current between two microelectrodes (Fig. 2.4D). The higher gains enabled by the series amplifiers with diodes provided higher fidelity recording compared to the conventional amplifier. Further, the DBS-ECAP instrumentation limited the magnitude and duration of the third phase of the artifact, thereby reducing the temporal overlap of the artifact with short latency mECAPs and further increasing fidelity. Additional distortion analysis across DBS and mECAP parameters, contact configurations, and recording system configurations is provided in the Appendix. Use of the mini DBS electrode during *in vitro* testing generated similar stimulus artifact and mECAP waveforms to those recorded with the clinical DBS electrode (data not shown).

2.3.3 In vivo ECAP recording

The mini DBS electrode (Fig. 2.5A) was implanted in the VL nucleus of the cat thalamus for *in vivo* ECAP recording. The VL thalamus was identified by recording single thalamic neurons that exhibited increased activity during passive contralateral

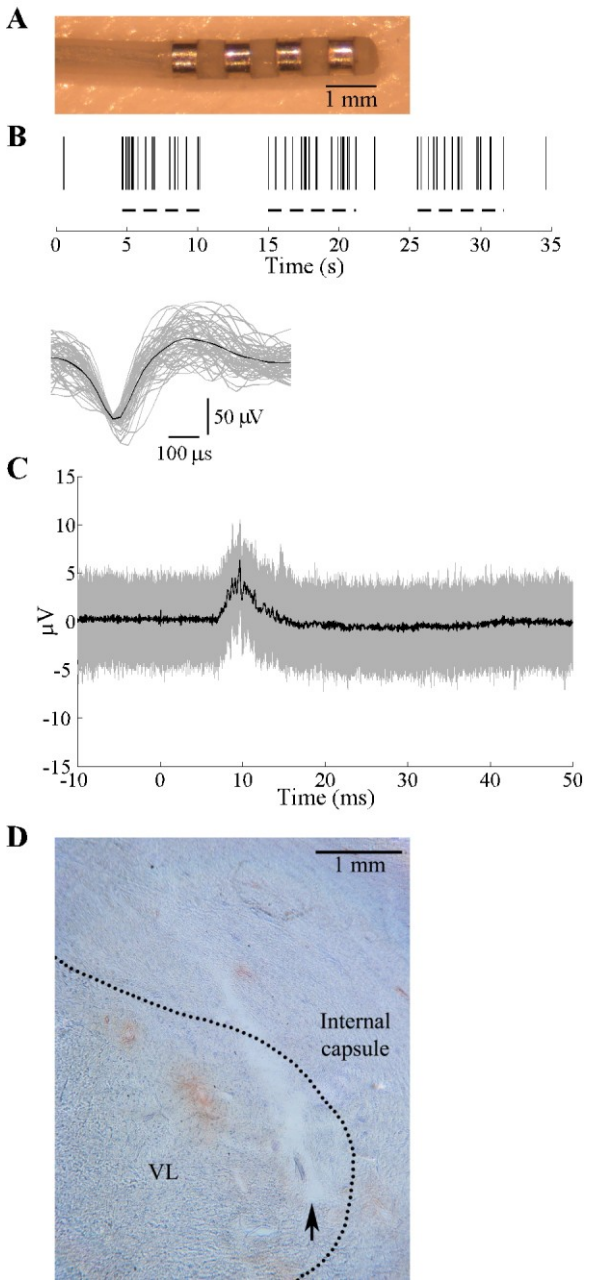

Figure 2.5: The DBS electrode was implanted in the VL thalamus in an anesthetized cat. A: A mini DBS electrode was used for *in vivo* ECAP recording during thalamic DBS. B: The location of the VL thalamus was identified by recording the activity of single thalamic neurons with a microelectrode during stereotactic surgery. *Top*: Raster plot of spiking in a neuron showing increased activity during passive contralateral hind limb movement (dashed lines). *Bottom*: Waveforms of 61 discriminated spike waveforms recorded from the neuron (gray traces) and average

waveform across all spikes (black trace). C: Accurate implantation into the VL thalamus was verified by recording the evoked response from the DBS electrode during contralateral sciatic nerve stimulation, applied at time 0. The stimulus-triggered average (black trace) and single trials (gray traces) are shown. D: Postmortem histology confirmed the location of the DBS electrode within the VL thalamus, with the nuclear boundary indicated by the dashed line. The arrow indicates the location of the ventral tip of the electrode.

hind limb movement (Fig. 2.5B). Accurate implantation of the DBS electrode into the VL thalamus was confirmed subsequently by recording evoked responses from the DBS electrode during electrical stimulation of the contralateral sciatic nerve (Fig. 2.5C). Postmortem histology confirmed the position of the implanted electrode in the VL thalamus (Fig. 2.5D).

The *in vivo* ECAP response was recorded using the different recording system configurations to examine the relative performance of the DBS-ECAP instrumentation (Fig. 2.6). Comparing responses to cathodic- and anodic-phase first stimulation enables one to distinguish the physiological ECAP signal, which is similar for symmetric, biphasic pulses (McIntyre and Grill, 2000), from the stimulus artifact, which is inverted for opposite polarities. The stimulus artifact recorded with the conventional amplifier was reduced in magnitude with the use of the series amplifiers with diodes, enabling higher gains (Figs. 2.6A,B), but the long duration of the artifact distorted the physiological ECAP. In contrast, the DBS-ECAP instrumentation suppressed the stimulus artifact and enabled high fidelity recording of ECAPs (Fig. 2.6C).

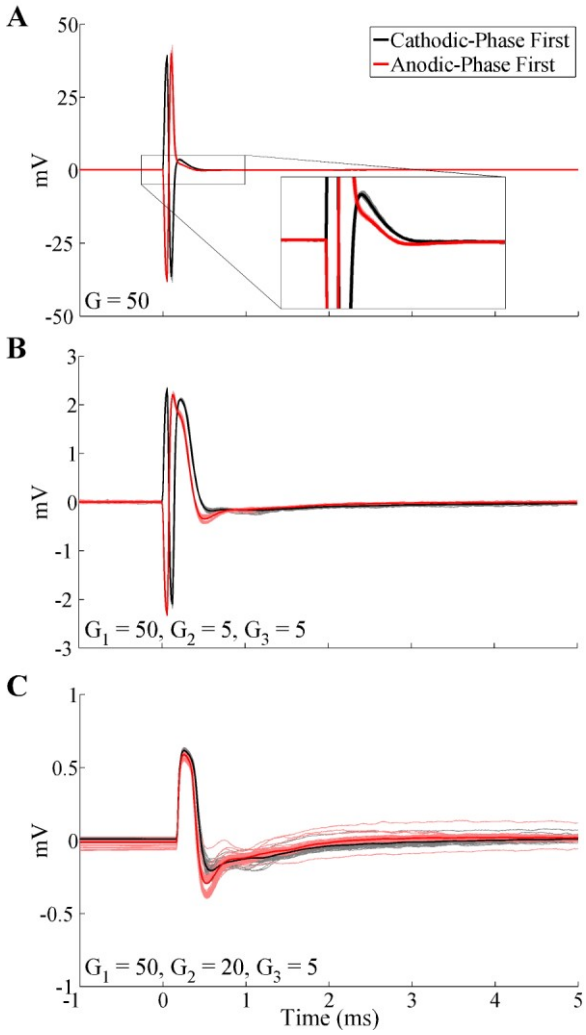

Figure 2.6: The stimulus artifact and ECAP during *in vivo* recording using the monopolar symmetric configuration with the conventional amplifier (A), series amplifiers with diodes (B), and DBS-ECAP instrumentation (C). The gains (G) used at the amplification stages of each recording system configuration are shown at the lower left of each graph. DBS was applied with 3 V amplitude, 100 Hz frequency, and 50 μs pulse width, with both cathodic-phase first (black traces) and anodic-phase first (red traces) polarities. The stimulus-triggered average waveform (bold traces) and single trials (light traces) are shown.

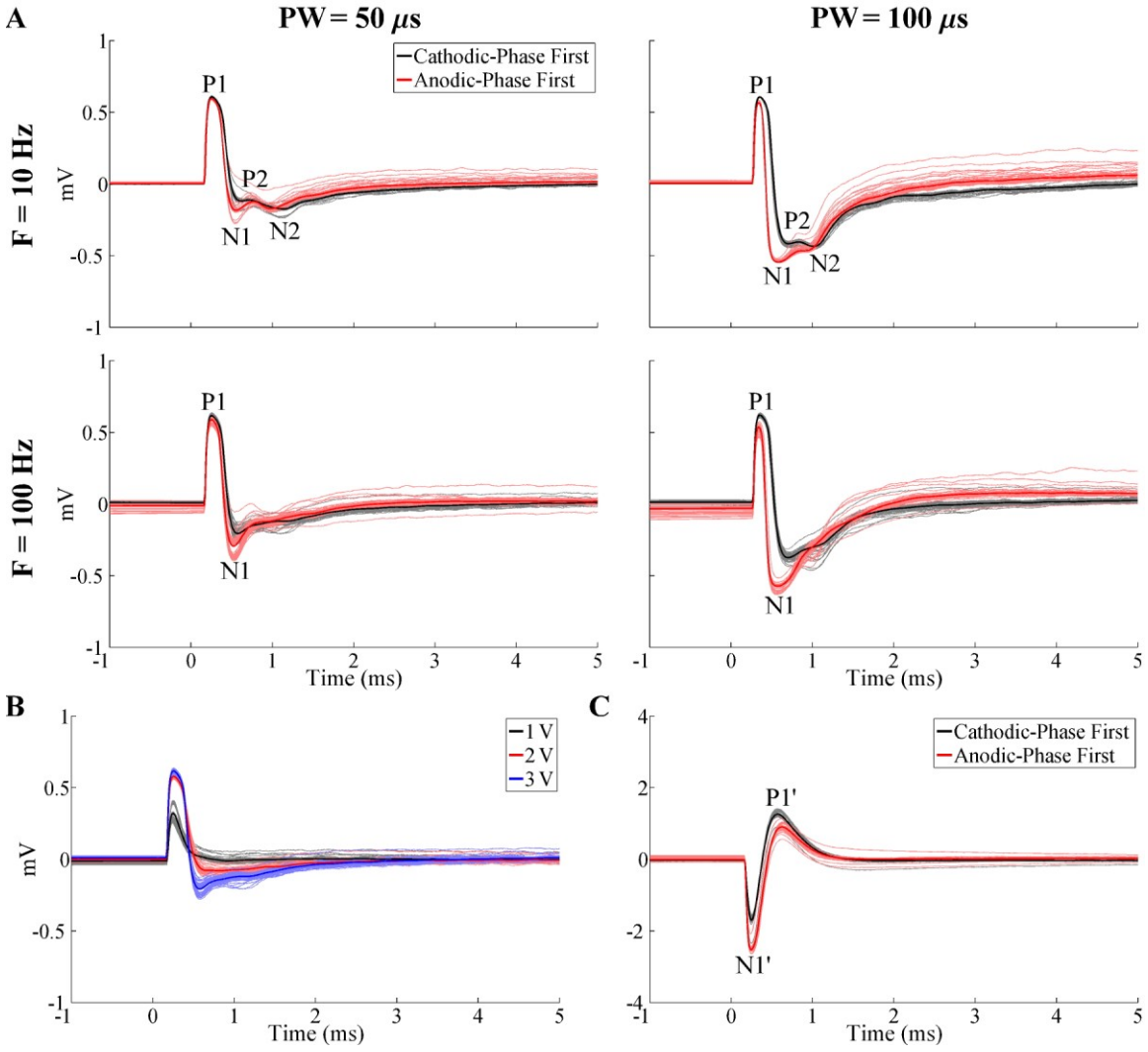

Figure 2.7: Effect of stimulation parameters on the *in vivo* ECAP response recorded with the DBS-ECAP instrumentation. A: ECAPs recorded using the monopolar symmetric configuration across DBS pulse widths (PW) and frequencies (F) at a 3 V amplitude. The results for cathodic-phase first (black traces) and anodic-phase first (red traces) polarities are shown. B: ECAPs recorded using the monopolar symmetric configuration across DBS amplitudes at 100 Hz frequency and 50 μs pulse width, and with cathodic-phase first polarity. C: ECAPs recorded using the monopolar asymmetric configuration with 3 V amplitude, 100 Hz frequency, and 50 μs pulse width. The results for cathodic- and anodic-phase first polarities are shown. For all figures, the stimulus-triggered average waveform (bold traces) and single trials (light traces) are shown. The amplifier gains used for the monopolar symmetric and asymmetric configurations were 5,000 and 2,500, respectively.

We examined how the ECAP characteristics were dependent on stimulation parameters (Fig. 2.7). In the monopolar symmetric configuration, ECAPs had an early positive (P1) phase followed by a later negative (N1) phase (Fig. 2.7A). The magnitude and duration of these phases generally increased with DBS pulse width and amplitude (Figs. 2.7A,B), and the N1 phase was absent with low amplitude (1 V) DBS. Secondary positive (P2) and negative (N2) phases were observed at 10 Hz DBS (Fig. 2.7A). While these secondary phases were also present at the beginning of the stimulus train during 100 Hz DBS, their amplitudes progressively decayed during the stimulus train, and were not present in the average waveform. ECAPs recorded using the monopolar asymmetric configuration exhibited an early negative (N1') phase and later positive (P1') phase (Fig. 2.7C).

We measured the ECAP at multiple time points following euthanasia to confirm that the ECAP was a biological signal. While phases P1 and N1 were both still evident at 1 min following euthanasia (Fig. 2.8A), the latter was lost at 3 min (Fig. 2.8B). Postmortem recording at 5 min resulted only in a stimulus artifact, with inverted waveforms for opposite stimulation polarities, rather than a physiological ECAP response (Fig. 2.8C).

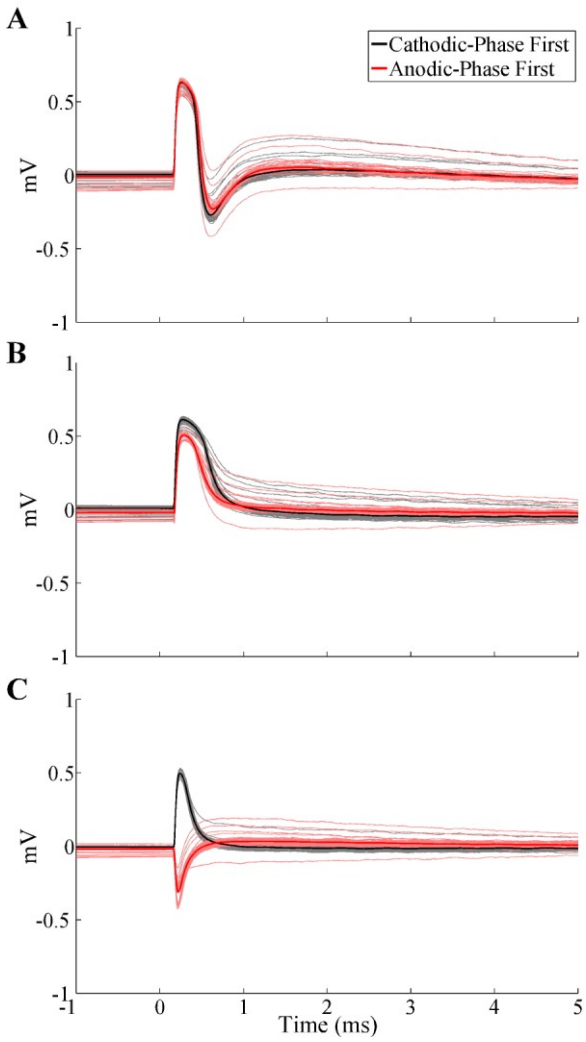

Figure 2.8: Postmortem *in vivo* ECAPs at 1 min (A), 3 min (B), and 5 min (C) after euthanasia recorded with the DBS-ECAP instrumentation using the monopolar symmetric configuration. DBS was applied with 3 V amplitude, 100 Hz frequency, 50 μs pulse width, and both cathodic-phase first (black traces) and anodic-phase first (red traces) polarities. The stimulus-triggered average waveform (bold traces) and single trials (light traces) are shown.

2.3.4 Computational analysis of stimulus artifact sources and components for artifact reduction

An electrical circuit equivalent model was used to analyze the sources of the stimulus artifact recorded *in vitro* and *in vivo*, and to understand better the mechanism of

artifact rejection by the stimulator relay of the DBS-ECAP instrumentation. The parameter values used in the circuit models are provided in Table 2.2. The stimulus artifact was calculated as the differential voltage across the recording amplifier inputs, with and without use of the AQV212(A) stimulator relay, which had a 0.83 Ω on resistance and operational timing matching that used experimentally.

Table 2.2: Electrical circuit equivalent model parameters used for *in vitro* and *in vivo* models. The *in vivo* model used two sets of parameters to calculate the stimulus artifact in antemortem and postmortem recordings. The volume capacitance values shown for the *in vivo* models were calculated for dielectric constants of 3×10^5 and 2.92×10^5 for antemortem and postmortem, respectively. The resistance values of the volume conductor were calculated for conductivities of 0.3 and 0.216 S/m, respectively.

Parameter	*In Vitro*	*In Vivo* (Ante.)	*In Vivo* (Post.)
Interface double-layer capacitance (C_{DL}, μF)	2.22	1.56	1.56
Interface Faradaic resistance (R_F, kΩ)	0.96	1.50	1.50
Volume resistance between contacts 0 & 1 (R_{V01}, Ω)	200.11	3208.69	4469.48
contacts 1 & 2 (R_{V12}, Ω)	199.80	3270.33	4546.37
contact 0 & return (R_{V0}, Ω)	127.26	2141.15	2980.29
contact 1 & return (R_{V1}, Ω)	126.90	2184.88	3044.96
contact 2 & return (R_{V2}, Ω)	128.34	2183.59	3071.81
Volume capacitance between contacts & return (C_V, nF)	5.80E-3	9.38	9.13

The artifact calculated with the *in vitro* model (Fig. 2.9A) had a waveform shape similar to that recorded experimentally with the clinical DBS electrode in the saline bath using the conventional amplifier (Fig. 2.9B). The peak-to-peak magnitude of the model and experimental artifacts were approximately 16 mV and 49 mV, respectively, and this difference likely resulted from errors associated with model assumptions. Addition of

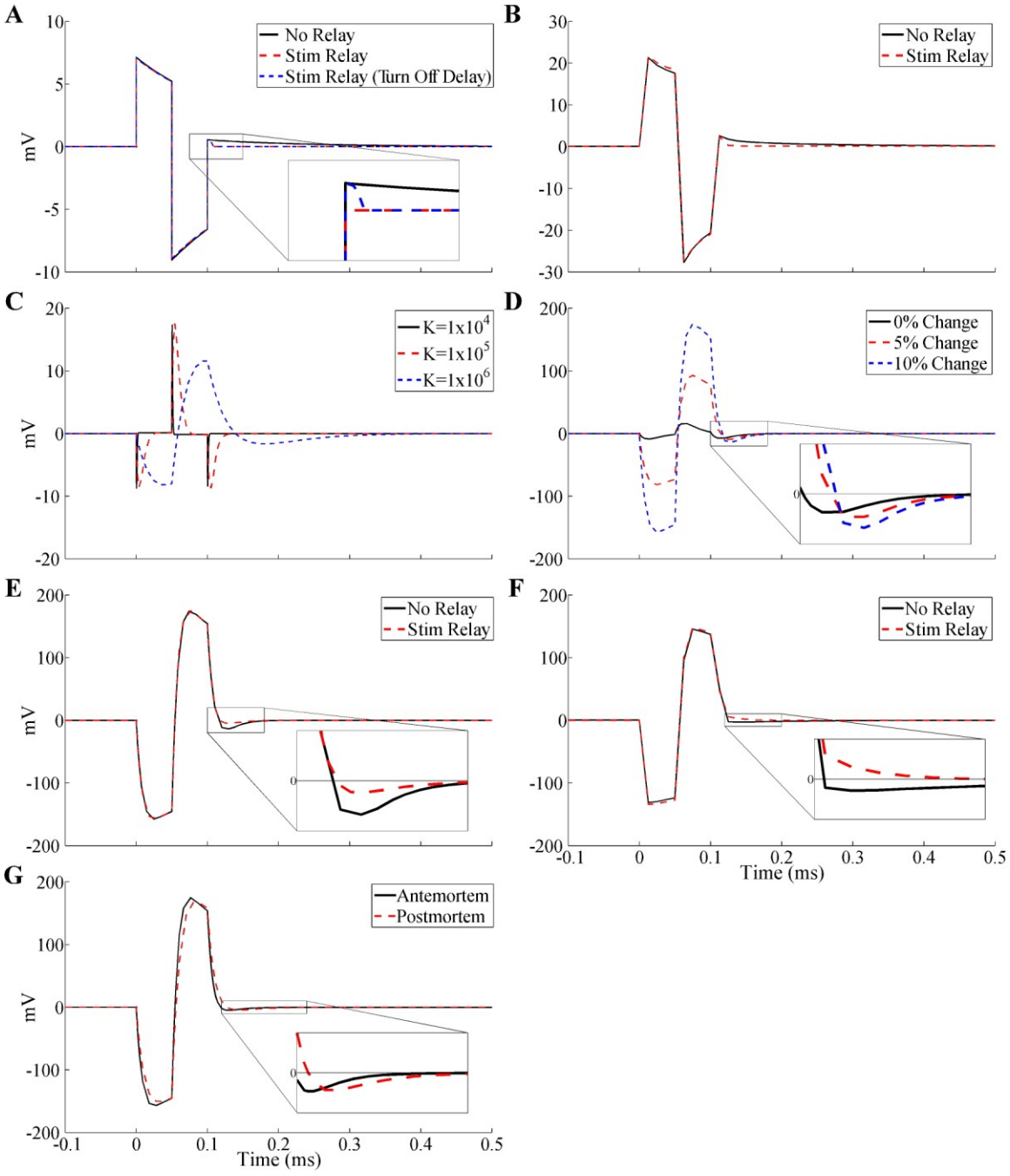

Figure 2.9: Stimulus artifact waveforms calculated with the *in vitro* and *in vivo* electrical circuit equivalent models and comparison to experimentally recorded artifacts using the monopolar symmetric configuration. DBS was applied with 3 V amplitude, 100 Hz frequency, 50 μs pulse width, and cathodic-phase first polarity. A: *In vitro* circuit model artifacts calculated without the stimulator relay (black trace),

and with the relay either turned off immediately after the pulse (red trace) or with a 25 μs turn off delay (blue trace). B: Stimulus-triggered average artifact waveforms from the *in vitro* experiment recorded with a conventional amplifier without signal filtering, with the stimulator relay absent (black trace) and present (red trace). C: Sensitivity analysis of *in vivo* circuit model artifact to dielectric constant (K) values between 1×10^4 and 1×10^6. A dielectric constant of 3×10^5 was used for subsequent circuit model analysis. D: Sensitivity analysis of *in vivo* circuit model artifact to changes in the bulk tissue resistance. The resistance was decreased between contacts 0 and 1, and increased between contacts 1 and 2, by the indicated value. A 10% bulk conductivity change was used for subsequent circuit model analysis. E: *In vivo* circuit model artifacts calculated with and without the stimulator relay. F: Stimulus-triggered average artifact waveforms from a postmortem *in vivo* cat experiment. Recordings were made with a conventional amplifier without signal filtering, both with and without the stimulator relay. G: Comparison of circuit model artifact waveforms calculated using parameter values from the original, antemortem (black trace) and postmortem (red trace) models. The stimulator relay was used for these data.

the stimulator relay in the *in vitro* experiment reduced, but did not eliminate, the third phase of the artifact observed with the conventional amplifier (Fig. 2.9B). Conversely, results from the circuit model indicated that turning the stimulator relay off immediately after the DBS pulse prevented capacitive discharging from the ETI and eliminated the third artifact phase (Fig. 2.9A). However, when a short (25 μs) turn off delay was added to the stimulator relay after the end of the DBS pulse, the model reproduced the reduced-magnitude third artifact phase seen experimentally. Although the digital pulse controlling the stimulator relay was turned off 40 μs before the end of the DBS pulse to account for this turn off delay in the *in vitro* experiment, the typical measured delay for the AQV212(A) relay is longer than 40 μs, and may have contributed to this observed post-stimulus delay time. The 25 μs turn off delay was used for subsequent model trials with the stimulator relay.

We next conducted sensitivity analysis to determine how the stimulus artifact calculated with the *in vivo* circuit model depended on the dielectric constant and conductivity of the tissue. The stimulus artifact was calculated for dielectric constant values of neural tissue from 1×10^4 to 1×10^6 (Fig. 2.9C). The variations in tissue capacitance led to substantial changes in the waveform shape of the artifact, since higher capacitances resulted in longer time constants for charging and discharging of the tissue. Using a dielectric constant value of 3×10^5 resulted in an artifact (Fig. 2.9D, black trace) that best matched the experimental waveform shape (Fig. 2.9F). We next investigated the effect of inhomogeneity of tissue conductivity by decreasing the tissue resistance between contacts 0 and 1 by 5 to 10%, and increasing that between contacts 1 and 2 by the same percentage (Fig. 2.9D). A greater degree of inhomogeneity increased the magnitude of the stimulus artifact, due to the larger differential voltage generated at the two recording contacts. A change in tissue resistance values of 10% produced a model artifact waveform with a magnitude similar to that observed experimentally, and was used for subsequent artifact calculations. The presence of tissue inhomogeneities likely generated the larger stimulus artifact magnitudes *in vivo* compared to *in vitro*.

Discharging of the tissue capacitance following DBS pulses led to an increased duration of the third phase of the artifact *in vivo*. This phenomenon was observed experimentally (Fig. 2.9F), and was qualitatively reproduced with the circuit model (Fig. 2.9E). The stimulator relay did decrease capacitive discharging from the ETI and thereby

reduce the magnitude of the third phase, but it did not prevent discharging of the tissue capacitance. The increase in artifact duration resulting from discharging of medium capacitance was only observed *in vivo*, since the permittivity of tissue is several orders of magnitude greater than that of saline.

The model was also used to investigate the increase in stimulus artifact amplitude in postmortem *in vivo* recordings (Fig. 2.8). Decreases in tissue conductivity and permittivity, expected after euthanasia (Surowiec et al., 1986, Schmid et al., 2003), increased the duration of the third artifact phase in the model (Fig. 2.9G). Further, local changes in brain conductivity that increased the extent of tissue inhomogeneity increased both the magnitude and duration of the artifact (Fig. 2.9D). These changes may explain the larger artifacts observed 5 minutes after euthanasia.

2.4 Discussion

We designed and evaluated the performance of instrumentation for high fidelity recording of ECAPs from the DBS electrode during stimulation. By reducing the magnitude and duration of the stimulus artifact, the DBS-ECAP instrumentation enabled recording of small amplitude, short latency mECAPs *in vitro*. The ability of the instrumentation to record physiological ECAPs was confirmed during *in vivo* DBS in the cat thalamus. The characteristics of the *in vivo* ECAP were dependent on stimulation parameters and may provide insight into the type and spatial extent of neural element

activation during stimulation. Thus, the ECAP signal may be a suitable feedback control signal for tuning DBS parameters and in closed-loop DBS systems.

2.4.1 Design and evaluation of instrumentation

Several hardware-based strategies were used to limit the stimulus artifact. We employed multiple amplifier stages with anti-parallel diode clamps at the inputs to clip selectively the stimulus artifact and provide overvoltage protection. The magnitude of the artifact was reduced further by amplifier blanking, in which the signal paths in the second and third amplifier stages were grounded during each DBS pulse. To reduce the duration of the third phase of the artifact, and minimize the extent of temporal overlap with the ECAP, we used a stimulator relay to reduce capacitive discharge of the ETI immediately after each DBS pulse (McGill et al., 1982). This relay disconnected the low impedance path available through the constant-voltage stimulator, thereby limiting the discharging current through the high impedance 10 kΩ parallel resistance. Accumulated charge was able to discharge between pulses through this parallel resistance and during the 2 ms pre-stimulus period in which the relay was closed. The parallel resistance also enabled near-critical damping of the signal recovery from artifact to baseline. Replacing the resistor with a potentiometer could enable rapid selection of a parallel resistance that achieved full critical damping of the system.

Other techniques used to suppress the stimulus artifact in neural recordings were not optimal for this application. Signal processing techniques such as curve fitting,

template subtraction, polarity averaging, and masker-probe paradigms are applied after the signal has been amplified and require lower gains to avoid saturation. Further, the performance of the template subtraction and polarity averaging techniques suffers from the assumptions that the artifact shape is constant between stimulus pulses (Wagenaar and Potter, 2002) and that the artifact perfectly follows the stimulus pulse in polarity (Bahmer et al., 2010), respectively. Signal filtering was not feasible due to overlapping frequency spectra of the ECAP signal and stimulus artifact. Alternatively, sample-and-hold amplifiers have not demonstrated the capacity to make artifact-free recordings of sub-ms latency neural activity, as required to capture physiological ECAPs, and have yielded inconsistent results.

Our novel DBS-ECAP instrumentation reduced the artifact magnitude and enabled a total *in vitro* gain of 40,000-100,000 without saturation during 3 V DBS, depending on the contact configuration. These gains far surpassed the conventional amplifier by a factor of 1,000-5,000. Further, the reductions in artifact duration and use of high gains facilitated low distortion recording of physiologically-realistic mECAPs at latencies as short as 0.5 ms and amplitudes as small as 0.11-0.30 mV_{P-P} (Appendix). This was the case for all contact configurations when using clinically-relevant DBS parameters of 3 V amplitude, 100 Hz frequency, and 50 μs pulse width. Conversely, the conventional amplifier recorded mECAPs with relatively high distortion. Long, asymmetric DBS pulses precluded low distortion recording of ECAPs with the DBS-

ECAP instrumentation except at latencies of at least 1 ms. Since physiological ECAPs have latencies in the sub-ms range, it may not be feasible to use long, asymmetric pulses, such as those generated by the present clinical device (Miocinovic et al., 2009), during ECAP recording.

The 4 kHz mECAP frequency used for *in vitro* validation was selected to examine the limits of instrumentation performance in recording physiological ECAPs. The bulk of the power of the *in vivo* ECAPs was in the 100 Hz to 4 kHz band. The DPS values were consistently lower for 1 kHz mECAPs compared to 4 kHz mECAPs when recorded with the DBS-ECAP instrumentation because any distortion influenced a shorter proportion of the longer 1 kHz signal, and the reported distortion values can be considered an upper bound.

We expect that the high recording fidelity of the DBS-ECAP instrumentation observed at 100 Hz DBS will translate across the entire range of clinical DBS frequencies. Increasing the DBS frequency from 100 to 180 Hz decreases the interpulse interval from 10 to 5.56 ms, but after accounting for the 2 ms pre-stimulus amplifier blanking period, this would still provide a recording window of 3.56 ms from the start of the stimulus pulse at 180 Hz DBS. Since the physiological ECAP signal returned to baseline by approximately 3 ms post-stimulus (Fig. 2.7), we do not anticipate increases in distortion, generated by temporal overlap of the ECAP signal with the subsequent amplifier

blanking period, as the DBS frequency is increased to the high end of the clinical range. This was validated through *in vitro* testing of mECAPs at 180 Hz (data not shown).

The contact configurations used for stimulation and ECAP recording influenced the fidelity of the recording (Appendix). The stimulus artifact magnitude was larger when the voltages generated during stimulation were not symmetrical at the recording contacts (i.e., the monopolar asymmetric and bipolar configurations). This required reductions in amplifier gain (Table 2.1) and made it more challenging to record short latency mECAPs. Moreover, the recorded mECAP magnitude increased with the distance between recording contacts (maximal in the bipolar configuration), since the contacts measured a larger differential-mode signal. Collectively, this suggests that high fidelity recording is most challenging in the monopolar asymmetric configuration, due to the short distance between recording contacts and their non-symmetrical positioning about the stimulating contact. This was confirmed through the distortion analysis of mECAP recordings made *in vitro* across contact configurations.

The artifact waveforms calculated with the electrical circuit equivalent model were similar in magnitude and shape to the *in vitro* and *in vivo* artifacts, and provided insight into the origin of the artifact (Fig. 2.9). In the *in vitro* experiment, the only source of the third artifact phase was capacitive discharging from the ETI, which was limited with the use of the stimulator relay. However, the turn off delay of the relay, which was approximately 25 μs after the end of the DBS pulse, allowed some discharging.

Consequently, the size of the third phase was reduced but not eliminated. This suggests that using a stimulator relay with a shorter turn off delay may improve the performance of this system. The model indicated that there were two sources of the third artifact phase observed *in vivo*: capacitive discharging after each DBS pulse of (1) the tissue capacitance, and (2) the ETI. Previous computational (Butson and McIntyre, 2005, Tracey and Williams, 2011) and experimental (Lempka et al., 2010) studies have also demonstrated that the tissue capacitance is charged during the DBS pulse (influencing the DBS waveform shape). The stimulator relay cannot suppress the artifact resulting from discharging of the tissue capacitance, and thus the third phase is larger *in vivo* than *in vitro*. We investigated a means to rapidly discharge the tissue capacitance by shorting the amplifier inputs with a PhotoMOS relay for 100 μs immediately after each pulse. However, this technique did not reduce the third phase of the *in vivo* artifact, and electrical equivalent circuit modeling indicated that the lack of effect was caused by negligible current flow through the relay due to its internal impedance (data not shown). Finally, the peak-to-peak magnitude of the artifact recorded with the conventional amplifier was greater *in vivo* than *in vitro*, and results from the circuit model suggest that this may have been caused by inhomogeneities in the neural tissue, which were not present in the saline bath.

2.4.2 Insight provided by the physiological ECAP

The results from our *in vivo* experiment confirmed that physiological ECAPs could be recorded during thalamic DBS. The DBS-ECAP instrumentation enabled high gain recordings of ECAPs, uncontaminated by the stimulus artifact, during DBS of the VL thalamus. This could be performed using both the monopolar symmetric and asymmetric configurations (Fig. 2.7), of which the latter was revealed by *in vitro* analysis to be the most challenging configuration for high fidelity recording. The similarity of ECAP waveform shapes recorded during cathodic- and anodic-phase first polarity stimulation corroborated the neural origin of the signal, and the elimination of the ECAP response at 5 min after euthanasia (Fig. 2.8) further verified the biological origin of the recorded signal. The increase in stimulus artifact magnitude observed after euthanasia could have been caused by decreases in bulk tissue conductivity and permittivity (Surowiec et al., 1986, Schmid et al., 2003) and/or local changes in brain conductivity that increased the extent of tissue inhomogeneity. Electrical circuit equivalent modeling indicated that these changes increased the magnitude and duration of the third phase of the artifact.

Measuring the ECAP across DBS parameters provided insight into the activation patterns during DBS. The magnitude and duration of the ECAP phases increased with DBS amplitude and pulse width, as a result of activation of additional neural elements having higher stimulation thresholds (Ranck, 1975). ECAPs generated with the

monopolar symmetric configuration had an early positive (P1) phase and later (N1) negative phase. To interpret this finding, we used results from the modeled cochlear ECAP response, in which a large negative phase, flanked on each side by small positive phases, corresponded to action potential propagation near the recording contact (Briaire and Frijns, 2005). We propose that P1 was generated by early dorsal activity (near the negative recording contact) whereas N1 corresponded to later ventral activity (near the positive contact). Furthermore, we observed secondary positive (P2) and negative (N2) phases during low frequency DBS, and at the beginning of the pulse train during high frequency DBS. This suggests that the P2 and N2 phases corresponded to post-synaptic activity, and the loss of these phases at high stimulation frequencies corresponded to a reduction in post-synaptic activity (Anderson et al., 2006). Recording the ECAP with the monopolar asymmetric configuration revealed an early negative (N1') phase and later positive (P1') phase. These two phases likely corresponded to dorsal-to-ventral propagation of action potentials, initiated in cells near the stimulating contact, and propagating first past the positive recording contact (N1') and subsequently past the negative contact (P1').

These findings suggest that the ECAP may provide signatures of clinical effectiveness and be a suitable feedback signal in closed-loop DBS systems. For example, the ECAP magnitude could indicate when there is sufficient neural activation for clinical efficacy. As DBS amplitude is increased from 1 to 3 V, the *in vivo* ECAP increased in

magnitude (Fig. 2.7B), and tremor decreases over this same range (Kuncel et al., 2007). We therefore expect a correlation between ECAP magnitude and tremor that could be used to set the DBS amplitude in a closed-loop system. An analogous correlation has been established for cochlear implants between the cochlear nerve ECAP magnitude and perceptional hearing levels (Jeon et al., 2010).

2.4.3 Study limitations

The electrical circuit equivalent model provided insight into the sources of the stimulus artifact; however, there are several limitations that should be noted. First, calculations of medium resistance and capacitance assumed a spherical volume conductor surrounding the DBS electrode, with the return electrode at the volume conductor boundary. Further, the medium capacitance calculations assumed that the DBS contacts were spherical. In the *in vitro* and *in vivo* experiments, the return electrode did not bound the DBS electrode, but rather was located at a single, distant position (Fig. 2.1). This model assumption may have resulted in underestimation of the medium resistance and overestimation of the medium capacitance between DBS contacts and the return electrode. Further, neither the saline tank nor the DBS contacts were actually spherical, but these assumptions likely had a negligible effect on model results due to the large difference in size between DBS contacts and the volume conductor, which would be expected to mitigate the effects of these geometric approximations.

The second limitation was an assumption in the circuit model that the mini DBS electrode had the same ETI properties as the clinical DBS electrode, for which the impedance values were measured (Wei and Grill, 2009). However, when the interface resistance and capacitance values were modified to account for the smaller surface area of the mini DBS electrode, the effect on the artifact waveform was negligible (data not shown). Third, this model did not include capacitive coupling between stimulating and recording leads (McGill et al., 1982, Grumet, 1999), which was reasonable considering this would generate a common-mode stimulus artifact and be rejected at the differential preamplifier stage. The fourth limitation was that we did not account for the frequency-dependence of tissue permittivity (Bossetti et al., 2008) in calculating bulk volume capacitance, and it remains unclear which permittivity value best represents brain tissue (Butson and McIntyre, 2005). However, under conditions of voltage-controlled stimulation in a homogenous medium, using a frequency-independent permittivity can closely approximate the solution of a fully dispersive model (Grant and Lowery, 2010). Fifth, the medium capacitance between two DBS contacts was not included in the circuit model.

The final major limitation of the circuit model was that changes in neural tissue properties measured after euthanasia in literature were made in porcine (Schmid et al., 2003) and bovine (Surowiec et al., 1986) brains, rather than the cat. Further, the change in permittivity was measured at high frequencies (900 MHz), outside of the bandwidth of

the DBS pulse (Schmid et al., 2003). Similarly, the change in conductivity was measured at a relatively high frequency (100 kHz) (Surowiec et al., 1986). Therefore the tissue properties used in the postmortem *in vivo* circuit model were only approximations for impedance changes in the cat brain during DBS.

A limitation of the experimental methods used in this study was that a clinical DBS electrode was used for most of the *in vitro* testing, whereas a mini DBS electrode was used in the *in vivo* experiments. We chose to evaluate the *in vitro* performance of the DBS-ECAP instrumentation with the clinical DBS electrode since the ECAP recording technique is intended for clinical translation. Conversely, the mini DBS electrode was more appropriate for the size of the cat brain. Nevertheless, the stimulus artifact and mECAP waveforms recorded with the clinical DBS electrode were very similar to those recorded with the mini DBS electrode during *in vitro* testing.

2.5 Appendix

Distortion values were calculated as the error between the recorded and ideal mECAPs, and decreased as DBS pulse width was reduced or mECAP latency increased (Fig. 2.10A). With 3 V DBS in the monopolar symmetric configuration, the DBS-ECAP instrumentation recorded small magnitude (0.18 mV_{P-P}) mECAPs with relatively low DPS values in the range of 0.17 to 0.26 at latencies of only 0.5 ms after DBS pulses of 50 or 100 μs duration, or latencies of 1 ms after long, asymmetric DBS pulses with 50 μs first phase and 500 μs second phase (Fig. 2.10A, filled bars). In cases where a very short

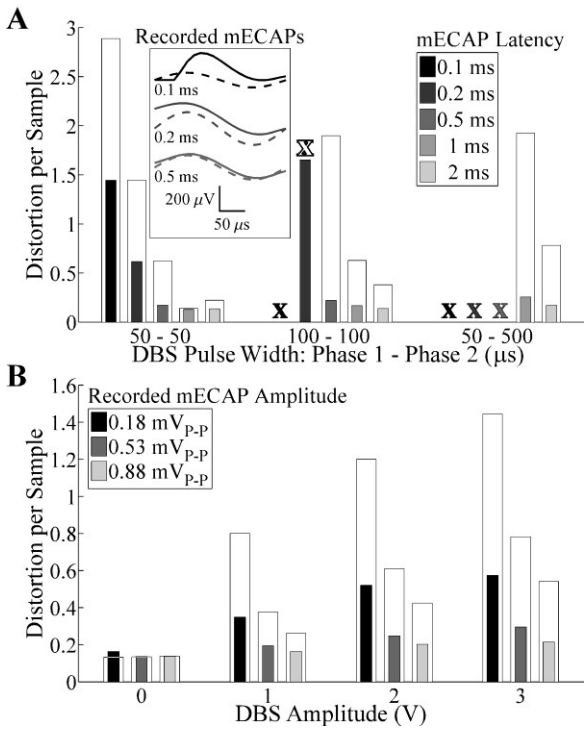

Figure 2.10: Distortion per sample of the mECAP across DBS and mECAP stimulation parameters, measured *in vitro* with the monopolar symmetric configuration. A: Effect of DBS pulse width and mECAP latency on distortion. DBS parameters were 3 V amplitude, 100 Hz frequency, and cathodic-phase first polarity, and sinusoidal mECAP parameters were 0.18 mV_{P-P} amplitude (0.1 mA_{P-P} input amplitude) and 4 kHz frequency. The narrow, filled bars show distortion values for the DBS-ECAP instrumentation, whereas the wider, open bars show the distortion for the series amplifiers with diodes. For some trials, the mECAP was masked and these are marked by a white X when masked with series amplifiers with diodes, and a filled X when masked with both instrumentation systems. The inset shows mECAPs recorded with the DBS-ECAP instrumentation (solid trace) and ideal mECAP sinusoid (dashed trace) for a DBS pulse width of 50 μs and the denoted mECAP latency. B: Effect of DBS and mECAP amplitudes on distortion. DBS parameters were 100 Hz frequency, 50 μs pulse width, and cathodic-phase first polarity, and the sinusoidal mECAP parameters were 0.2 ms latency and 4 kHz frequency. Data presentation is otherwise identical to that in (A).

latency mECAP was coupled with a relatively long DBS pulse width, the mECAP was masked by amplifier blanking. Using the series amplifiers with diodes, the mECAP was

more distorted (Fig. 2.10A, open bars) and masked by the artifact in some trials, while using the conventional amplifier resulted in a minimum DPS value of 1.26 across all combinations of DBS pulse widths and mECAP latencies tested.

Distortion decreased as DBS amplitude was reduced or mECAP amplitude was increased (Fig. 2.10B). Short latency mECAPs overlapped with the stimulus artifact, and larger mECAP amplitudes or smaller DBS amplitudes increased the relative magnitude of the mECAP signal over the artifact. Applying 50 μs DBS pulses with the monopolar symmetric configuration, the DBS-ECAP instrumentation recorded short latency (0.2 ms) mECAPs with relatively low DPS values under 0.35 at mECAPs amplitudes of only 0.18 mV_{P-P} for 0 or 1 V DBS, and amplitudes of 0.53 mV_{P-P} for 2 or 3 V DBS (Fig. 2.10B, filled bars). Using the series amplifiers with diodes, distortion was larger (Fig. 2.10B, open bars). The conventional amplifier could record mECAPs with DPS values under 0.5 at a DBS amplitude of 1 V, only with a large mECAP amplitude of 0.88 mV_{P-P}.

Compared to the monopolar symmetric configuration, the minimum mECAP latencies and amplitudes necessary for low distortion recording were generally equivalent for the bipolar configuration and greater for the monopolar asymmetric configuration with the DBS-ECAP instrumentation. This disparity across contact configurations was generated by differences in the magnitude of the stimulus artifacts and of the recorded mECAPs for a given input amplitude. For example, a mECAP with 0.1 mA_{P-P} input amplitude corresponded to a recorded amplitude of 0.18, 0.11, and 0.30

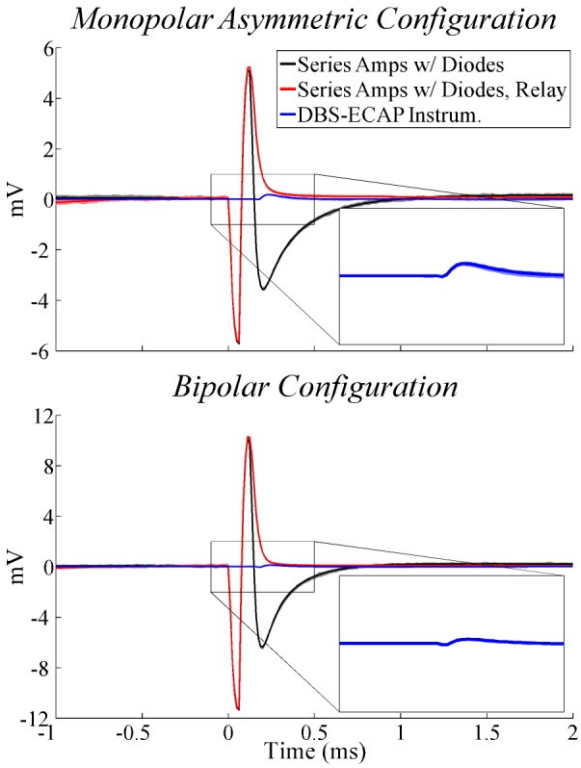

Figure 2.11: *In vitro* stimulus artifact waveforms measured with the monopolar asymmetric and bipolar contact configurations, using the series amplifiers with diodes (black traces), series amplifiers with diodes and stimulator relay (red traces), and DBS-ECAP instrumentation (blue traces). DBS was applied with 3 V amplitude, 100 Hz frequency, 50 μs pulse width, and cathodic-phase first polarity. The stimulus-triggered average waveform (bold traces) and single trials (light traces) are shown. The insets show a zoomed view of the stimulus artifact waveforms for the DBS-ECAP instrumentation.

$mV_{P\text{-}P}$ for the monopolar symmetric, monopolar asymmetric, and bipolar configurations, respectively. Further, the artifact magnitude increased from monopolar symmetric to asymmetric configurations, and from monopolar asymmetric to bipolar configurations (Figs. 2.4C, 2.11), which decreased the amplifier gain possible without saturation (Table 2.1). Moreover, the relative magnitude of the stimulus artifact and mECAP has a critical

influence on the recording fidelity (Fig. 2.10B), and likely also contributed to the differences in distortion observed between contact configurations.

3. Neural origin of evoked potentials during thalamic deep brain stimulation

This chapter has been previously published and is used with permission (Kent and Grill, 2013).

3.1 Introduction

Deep brain stimulation (DBS) is a clinically effective treatment for movement disorders, including Parkinson's disease (PD) (Benabid et al., 1994) and essential tremor (ET) (Benabid et al., 1991, Pahwa et al., 2006), and is being investigated for other neurological disorders such as epilepsy (Hodaie et al., 2002). Present DBS systems operate in an open-loop fashion, in which patients receive invariant stimulation 24 hr/day indefinitely, and a physician closes the loop through periodic re-tuning of stimulation parameters (Kuncel and Grill, 2004). The selection of stimulation parameters can be time-consuming and costly (Ondo and Bronte-Stewart, 2005), may not result in optimal settings for the patient (Okun et al., 2005, Moro et al., 2006), and presents a significant clinical burden. The efficacy of therapy can be improved by more frequent parameter adjustment (Moro et al., 2006, Frankemolle et al., 2010, Lee et al., 2010), potentially compensating for progression of the disease state (Krack et al., 2003, Deuschl et al., 2006, Weaver et al., 2012). We are exploring evoked potentials as a feedback signal for closed-loop control of DBS parameters, and the objective of this work was to characterize evoked potentials during stimulation.

Closed-loop DBS systems would automatically and periodically adjust stimulation parameters to optimize symptom relief and reduce the time required for programming. One potential closed-loop feedback signal is the local field potential (LFP) recorded from the DBS electrode and reflecting synchronized network activity (Marceglia et al., 2007, Santaniello et al., 2011) that is correlated to motor symptoms in PD (Smirnov et al., 2008, Tass et al., 2010) and ET (Kane et al., 2009). Beta band (13-35 Hz) activity in PD (Brown and Williams, 2005) and theta band (4-7 Hz) activity in ET (Kane et al., 2009) are disrupted by DBS (Ray et al., 2008, Bronte-Stewart et al., 2009, Rosa et al., 2011, Santaniello et al., 2011, Eusebio et al., 2012), suggesting that LFP recordings might be used to identify clinically effective stimulation parameters (Yoshida et al., 2010). Additionally, a closed-loop DBS system used single-unit activity from primary motor cortex (M1) as a trigger for each stimulus pulse in the globus pallidus interna (GPi), and demonstrated greater symptom reduction than continuous, open-loop stimulation (Rosin et al., 2011).

We are investigating evoked compound action potentials (ECAPs) as a potential feedback control signal for closed-loop DBS. The ECAP is generated by the transmembrane currents of activated neurons near the electrode following each stimulation pulse, and therefore provides insight into the activity of neural elements that are affected by stimulation. We previously demonstrated that ECAPs can be recorded from the DBS electrode during thalamic stimulation (**Chapter 2**). Similarly, clinical

recordings of ECAPs made from the cochlea served as a feedback signal in the selection of stimulation parameters in cochlear implants (Miller et al., 2008, Jeon et al., 2010), and closed-loop cochlear systems have been designed (Mc Laughlin et al., 2012).

In this work we quantified the effects of changes in stimulation parameters on the characteristics of the ECAPs recorded during thalamic DBS in cats. Characteristic changes in the ECAP across stimulation parameters could potentially provide insight into the type and extent of neural activation during DBS. We combined administration of pharmacological agents to block specific neural elements and a computational model of thalamic DBS (Birdno et al., 2012) to determine the contribution of different neural elements to the ECAP.

3.2 Methods

We combined experimental measurements and computational modeling to quantify changes in the ECAP across DBS parameters and to identify the neural origin of the ECAP.

3.2.1 In vivo ECAP recording

We recorded the ECAPs generated during thalamic DBS in 17 male, domestic short-haired cats (Table 3.1), initially anesthetized with ketamine HCl (35 mg/kg i.m.) and maintained with alpha chloralose (65 mg/kg i.v. supplemented at 15 mg/kg as needed). A ventilator maintained end tidal CO_2 at 3-4%, body temperature was maintained at 38°C with heating pads, arterial blood pressure was monitored with a

catheter, and fluids were administered continuously (10-15 ml/kg/h). The Institutional Animal Care and Use Committee of Duke University reviewed and approved all animal care and experimental procedures. The methods were reported previously in detail (**Chapter 2**), and are reviewed briefly here.

Table 3.1: Summary of *in vivo* experiments, including DBS electrode location as identified from histology, stimulation and recording contacts for the three contact configurations, and the pharmacological agents tested in order of administration. The asterisk (*) indicates that the DBS electrode location was not confirmed with histology, but was consistent with evoked responses recorded during sciatic nerve stimulation. VPL: ventral posterolateral nucleus, VL: ventral lateral nucleus, VA: ventral anterior nucleus, LGN: lateral geniculate nucleus.

		Stimulation (Recording)			
Cat	**Electrode Location**	***Mono. Symm.***	***Mono. Asymm.***	***Bipolar***	**Pharmacological Agent(s) (Volume Injected in μL)**
A	VPL-VL	1 (0+/2-)	0 (1+/2-)	--	--
B	VA	1 (0+/2-)	2 (1+/0-)	--	--
C	VPL-VL	1 (0+/2-)	3 (2+/1-)	--	--
D	VPL-VL	1 (0+/2-)	0 (1+/2-)	--	--
E	VPL-VL	1 (0+/2-)	0 (1+/2-)	--	--
F	VPL-VL	2 (1+/3-)	0 (1+/2-)	0+/2- (1+/3-)	--
G	LGN	1 (0+/2-)	0 (1+/2-)	0+/2- (1+/3-)	TTX (10)
H	VPL-VL	2 (1+/3-)	1 (2+/3-)	0+/2- (1+/3-)	Saline (5), CNQX/APV (5)
I	VPL-VL	1 (0+/2-)	0 (1+/2-)	0+/2- (1+/3-)	Saline (5), CNQX/APV (5)
J	VPL-VL*	2 (1+/3-)	0 (1+/2-)	0+/2- (1+/3-)	Isoflurane, Saline (5), CNQX/APV (10)
K	VPL-VL	2 (1+/3-)	3 (2+/1-)	1+/3- (0+/2-)	Isoflurane, 2% Lidocaine (20)
L	VPL-VL	2 (1+/3-)	1 (2+/3-)	0+/2- (1+/3-)	Isoflurane, 2% Lidocaine (20)
M	VPL-VL*	2 (1+/3-)	3 (2+/1-)	0+/2- (1+/3-)	Muscimol (20)
N	Dorsal thalamus	1 (0+/2-)	0 (1+/2-)	0+/2- (1+/3-)	Muscimol (10)
O	VPL-VL	1 (0+/2-)	1 (2+/3-)	0+/2- (1+/3-)	5% Lidocaine (20), CNQX/APV (20)
P	VPL-VL	1 (0+/2-)	3 (2+/1-)	1+/3- (0+/2-)	10% Lidocaine (20), CNQX/APV (10)
Q	VPL-VL	1 (0+/2-)	2 (1+/0-)	1+/3- (0+/2-)	10% Lidocaine (20), CNQX/APV (20)

With the cat prone and the head fixed in a stereotactic frame, a craniotomy was performed and thalamic nuclei were located using stereotactic technique and single-unit microelectrode recordings. The target implantation site was the ventrolateral (VL) nucleus of the thalamus, which is a cerebellar receiving area (Jimenez Castellanos, 1949, Berkley, 1983, Steriade et al., 1997) and appears to represent the feline homologue of the human ventral intermediate (Vim) nucleus of the thalamus (Steriade et al., 1997). The medial and lateral ventral posterior (VPM and VPL) nuclei form the ventrobasal complex (referred to as the ventrolateral complex by some authors (Butler and Hodos, 2005)) and function as the principal somatosensory relay nuclei (Jimenez Castellanos, 1949, Steriade et al., 1997). The VL thalamus also receives somatosensory input, including Group I muscle afferents (Boivie, 1971, Jones and Burton, 1974, Craig and Burton, 1985, Hirai and Jones, 1988), and the border region between the VPL and VL in the cat receives converging somatosensory and cerebellar afferents (Berkley, 1983). We attempted to identify the location of the VPL-VL thalamic complex through single-unit recording of neurons responding to passive movement of the contralateral hind limb (Mallart, 1968, Berkley, 1983). A guide tube was then inserted into the brain using a micromanipulator, and a mini DBS electrode (Numed) implanted through the guide tube into the VPL-VL thalamus (Fig. 3.1A). The mini DBS electrode had a lead body diameter of 0.625 mm, and four contacts of 0.5 mm height separated by 0.5 mm. Accurate implantation was confirmed by recording with the DBS electrode responses

evoked by electrical stimulation of the contralateral sciatic nerve. At the conclusion of each experiment, the anatomical location of the electrode with reference to a stereotactic atlas of the cat brain (Snider and Niemer, 1961) was determined from Nissl stained sections of formalin-fixed brain samples (McConnell et al., 2009). For all experiments, we verified that the ECAP was indeed a biological response by recording the neural activity at several time points following euthanasia and confirming that the ECAP was eventually abolished.

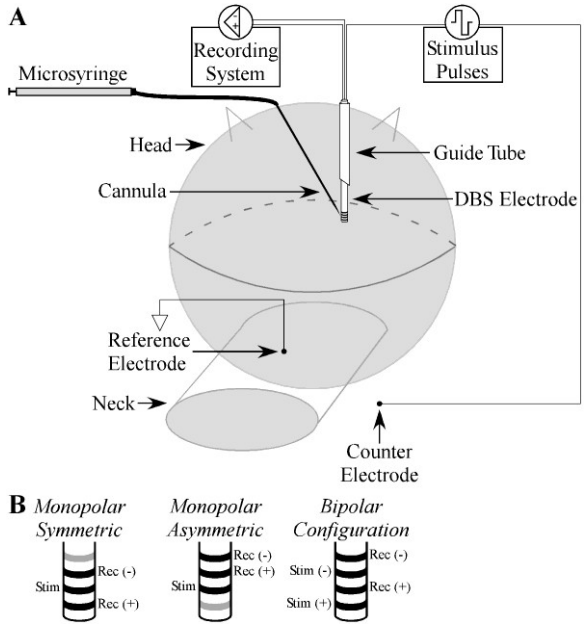

Figure 3.1: Experimental setup used to record ECAPs *in vivo* during DBS. A: The mini DBS electrode was inserted through a guide tube and implanted in the VPL-VL thalamic complex, and was used to deliver stimulation and record the resulting ECAP. Pharmacological agents were administered through a needle cannula, with injection speed and volume controlled using a microsyringe. Modified from (Kent and Grill, 2012). B: Example DBS contact connections used for stimulation and recording across the three contact configurations tested. The contacts that were not used are colored grey.

DBS was symmetric biphasic pulses with zero inter-phase delay. Voltage-controlled stimulation was used for clinical relevance, and parameters ranged from 1-3 V amplitude, 10 or 100 Hz frequency, 50 or 100 μs/phase pulse width, and both cathodic- and anodic-phase first polarities. Impedances measured between each contact and the counter electrode were approximately 1 kΩ, resulting in a maximum charge of 0.3 μC/phase and maximum charge density of 30 μC/cm^2. Differential ECAP recordings were made from two non-stimulating contacts and a Ag/AgCl reference electrode (Model EL504, Biopac Systems) placed on the neck using our previously developed DBS-ECAP instrumentation (**Chapter 2**). This DBS-ECAP hardware was used to suppress the stimulus artifact, which could otherwise mask or distort experimental ECAP signals. It uses three stages of amplification, an amplifier blanking technique, and other circuit components to reduce selectively the amplitude and duration of the artifact. Three different contact configurations were used for stimulation and differential recording: monopolar stimulation between a contact on the DBS electrode and a stainless steel retractor in the ipsilateral chest with either symmetrical recording contacts (*monopolar symmetric*) or asymmetrical recording contacts (*monopolar asymmetric*), as well as *bipolar* stimulation in which stimulation and recording contacts were interleaved (Fig. 3.1B). ECAP recording trials were 10 s in duration and were separated by 10 s. A LabView program controlled the DBS output, digital pulses to operate the DBS-ECAP instrumentation, and sampling (80 kHz) of the ECAP.

We conducted pharmacological interventions to block specific neural elements and determine the corresponding effect on the ECAP (Table 3.1). Most pharmacological agents were administered using local microinjection through a 22G needle cannula, which was connected to a 250 μL microsyringe (Model 1725, Hamilton) via saline-filled tubing (Fig. 3.1A). The agent was loaded at the cannula end of the injection system, and the cannula was implanted using a second micromanipulator at a distance of less than 1 mm anterior or posterior to the stimulation contact. Within one minute of cannula implantation, we injected 5-20 μL of the agent at approximately 5 μL/min. Following administration and again after washout, ECAPs were recorded across a range of stimulation parameters using the monopolar symmetric contact configuration. Some animals received multiple pharmacological treatments, with successive administration after recovery from the prior treatment.

Agents were chosen to inhibit synaptic transmission or neural excitation. First, we blocked post-synaptic excitation by administering CNQX (2.54 mM, Sigma-Aldrich) and APV (2.15 mM, Sigma-Aldrich), which are glutamate AMPA and NMDA receptor antagonists, respectively. Second, the $GABA_A$ receptor agonist muscimol (8.8 mM, Sigma-Aldrich) was injected to inhibit post-synaptic cells. Third, we administered sodium channel antagonists tetrodotoxin (TTX, 100 μM, EMD Chemicals) or 2-10% lidocaine HCl (0.07-0.35 M, Sigma-Aldrich) for non-selective inhibition of neural excitation. To limit dilution of lidocaine HCl by the saline present in the tubing of the

microinjection system, 5 μL mineral oil was loaded into the system to serve as a border between the saline and lidocaine (Noudoost and Moore, 2011). Fourth, 2% isoflurane anesthesia was administered through the ventilator, which selectively inhibited pre-synaptic inputs in the rodent thalamus (Joksovic et al., 2009, Ying et al., 2009) and brainstem (Wu et al., 2004). As well, a saline control was injected to test whether the fluid flow generated by microinjection changed ECAP characteristics (Rathnasingham et al., 2004, Rohatgi et al., 2009). Due to the relatively long half-life of TTX (Boehnke and Rasmusson, 2001) and CNQX/APV (Long et al., 1990), we did not wait for signal recovery from washout of these agents, and these were the final agents tested in an experiment.

3.2.2 Computational model of the ECAP

We used a three-stage computational model of thalamic DBS to calculate the ECAP and determine the neural elements that contributed to the compound response (Fig. 3.2). The first stage was a finite element method (FEM) model used to calculate the voltages generated in the modeled tissue during DBS. The results of the FEM were coupled to the second stage, multi-compartment cable models of a population of thalamocortical (TC) neurons and their pre-synaptic inputs, to calculate the transmembrane potentials and currents in the neural elements during DBS. In the third stage of the model, we used the reciprocity theorem to calculate the ECAP generated by the transmembrane currents of the neural elements.

A FEM model was constructed in COMSOL Script 1.2 (COMSOL) to calculate the voltages generated by a three-dimensional representation of the mini DBS electrode within a prism representation of the cat VL thalamus (Fig. 3.2A) (Birdno et al., 2012). The dimensions of the thalamic nucleus were similar to the original model, except that the perpendicular distance between prism bases along the superior-inferior axis was reduced from 10 mm to 2.8 mm, which more closely matched the anatomy of the cat (Jimenez Castellanos, 1949). DBS contacts 0 to 2 were located within the VL thalamus, where contacts were labeled 0-1-2-3 in a ventral-to-dorsal direction. The electrode and VL thalamus laid within a cylindrical representation of surrounding brain tissue, oriented parallel to the electrode with a diameter 64 times that of the electrode and centered at the electrode tip. This modeled tissue volume was sufficiently large because doubling the diameter changed the potentials by only 4.2±2.4% (mean ± SD). The tissue was homogenous and isotropic with a resistivity of 300 Ω-cm (Moffitt and McIntyre, 2005), and the resistivities of the DBS electrode contacts and insulating material were 20×10^{-6} Ω-cm and 1×10^{15} Ω-cm, respectively (Yousif et al., 2008a). The boundary of the active DBS stimulation contact(s) was set to ±1 V and the outer boundary of the cylindrical representation of the tissue was grounded. All other internal boundaries were set to a condition of continuity of normal current density. COMSOL Script created a variable resolution mesh with approximately 350,000 tetrahedral elements, which was a sufficient mesh density as doubling the number of elements changed the potentials by

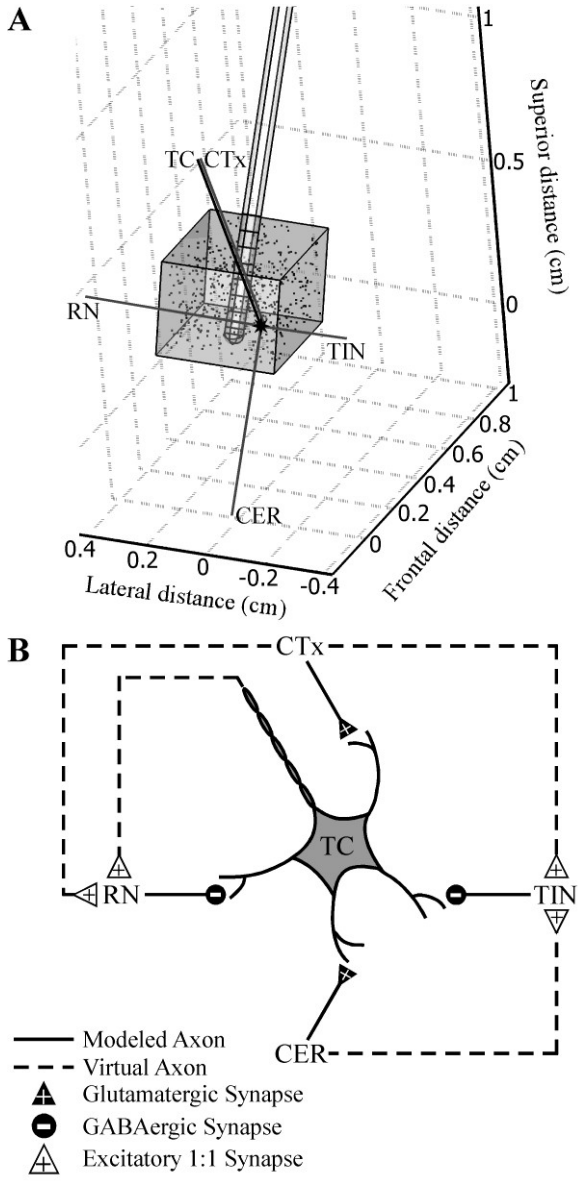

Figure 3.2: Computational model of a population of thalamic neurons used to calculate ECAPs during thalamic DBS. A: The FEM model geometry included a mini DBS electrode implanted in a prism representation of the cat VL thalamus, all encompassed in a cylindrical representation of surrounding brain tissue (not shown). The VL thalamus contained 500 thalamocortical (TC) neurons, with cell locations indicated by the dots, and pre-synaptic inputs from the cortex (CTx), cerebellum (CER), reticular nucleus (RN), and thalamic interneurons (TIN). The anatomical positions of the elements are shown for one neural unit, including the cell body, dendritic tree, and axon of the TC cell (black shapes) and the axons of the pre-synaptic

inputs (grey lines). B: The synaptic connections made between neural elements in the model included glutamatergic and GABAergic synapses from pre-synaptic elements to the TC neuron. Additionally, there were excitatory 1:1 synapses between the neural elements, implemented using virtual axons. Modified from (Birdno et al., 2012).

only 0.2±0.1%. Voltages were calculated by solving the Poisson equation at the mesh nodes using the conjugate gradient method. Since the bulk conductivity was linear, potentials generated at different stimulation amplitudes were scaled versions of the original solution.

In the second stage, the FEM solution was coupled to validated multi-compartment cable models (McIntyre et al., 2004a, Birdno et al., 2012) implemented in NEURON 7.1 (Hines and Carnevale, 2001) (Fig. 3.2). The model of a population of thalamic neurons included 500 TC neurons, with cell body locations randomly distributed within the VL thalamus, and their pre-synaptic inputs, including excitatory glutamatergic inputs from the cortex (CTx) and cerebellum (CER), and inhibitory GABAergic inputs from the reticular nucleus (RN) and local thalamic interneurons (TIN) (Birdno et al., 2012). The TC neurons had a multi-compartment soma, initial segment, and branching dendritic tree (McIntyre et al., 2004a), and the myelinated axons of the TC neurons and pre-synaptic inputs were represented with a double-cable model (McIntyre et al., 2002). Additionally, there were reliable 1:1 synapses (one input spike corresponded to one time-delayed output spike) from TC and CTx to RN, and from CTx and CER to TIN, implemented with virtual terminating axons. The synaptic time delays representing conduction of the action potentials down the virtual axons were reduced to

0.225 ms for connections to TIN and 0.3 ms for connections to RN, from the values in the original model, to match better the latency of experimentally-recorded post-synaptic potentials (Ando et al., 1995). Neural elements that intersected with the electrode were removed from analysis. Further, we removed the intrinsic activity applied to CTx and CER inputs and the TC somatic noise present in the original model.

The voltages calculated with the FEM were interpolated at the locations of the neural elements, scaled according to the DBS amplitude, and applied to elements using the *extracellular* mechanism in NEURON. The time-dependent DBS waveform was symmetric and biphasic with specified pulse width and frequency, and both cathodic- and anodic-phase first polarities were applied. The transmembrane potential and current at model compartments were calculated by backward Euler implicit integration. Neural activation was detected using a -20 mV threshold at the initial segment of the TC neuron or the proximal end of pre-synaptic inputs. The simulation time was 1.5 s, with a pre-stimulation period of 0.5 s, and a 25 μs time step.

The final stage of the model was the calculation of ECAPs using the reciprocity theorem. The theorem of reciprocity states that the voltage at a particular point in space resulting from a unit current source at the electrode contact translates to the voltage that would be imposed on the contact by a unit current at the particular point (Helmholtz, 1853). Applying this theorem, the FEM model was solved with a unit current source placed at the boundary of one of the recording contacts, and subsequently repeated for

the other recording contact. The potentials generated by the current source were interpolated at the compartment locations of the neural elements. By the reciprocity theorem, the scale factors were used to calculate the voltage impressed on the contact by transmembrane currents calculated from the NEURON simulation at each time step (Moffitt and McIntyre, 2005). The voltages generated by these currents at each recording contact were summed across every compartment of all neural elements, and the time-dependent ECAP calculated as the differential voltage between the two recording contacts. We accounted for the true cell density (65 cells/mm^2 in 50 μm sections (Hirai et al., 1989)) by scaling the ECAP magnitude by a factor of 102. As well, we filtered the model-generated signals with two cascaded first-order 10 Hz - 10 kHz bandpass filters to replicate the filtering performed experimentally.

We used template subtraction to remove the stimulus artifact, generated by passive charging and discharging of the membrane capacitance of neural elements (Briaire and Frijns, 2005), from the model-generated ECAP. The artifact template was calculated using a sub-threshold stimulation train (0.01 V), with pulse width, frequency, and polarity identical to those used in the trial of interest. This template was scaled according to the amplitude of DBS in the trial of interest and subtracted from the signal (Fig. 3.3).

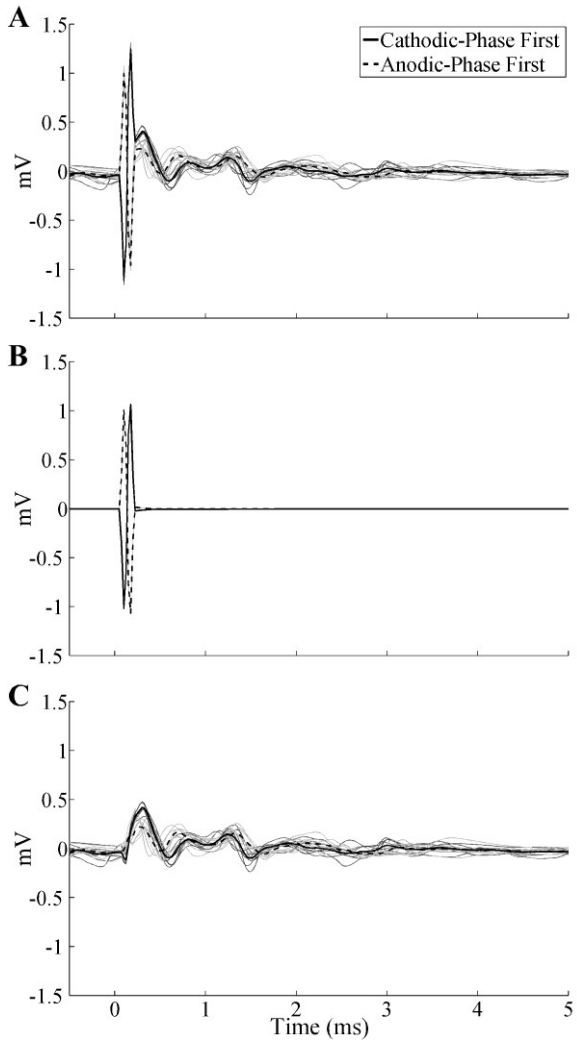

Figure 3.3: Template subtraction method used to remove the stimulus artifact from the model ECAP. Responses were calculated using a monopolar symmetric contact configuration with 100 Hz frequency and 50 μs/phase pulse width. The stimulus-triggered average ECAP (bold lines) are shown for cathodic- and anodic-phase first DBS polarities. The single trials (light traces) are also shown for the two polarities in dark and light grey, respectively. A: The signal calculated at 3 V included a stimulus artifact followed by the ECAP. B: A template of the stimulus artifact was calculated at a sub-threshold amplitude of 0.01 V, and scaled (300x) to create the artifact at 3 V. C: Subtracting the artifact template from the original signal produced an artifact-free ECAP.

Model ECAPs were calculated using stimulation parameters, contact configurations, and pharmacological conditions matching those tested experimentally. We modeled the effects of TTX and lidocaine by blocking sodium channels. The effects of CNQX/APV were represented by blocking excitatory glutamatergic receptors on TC cells and 1:1 synaptic receptors on TINs. Muscimol was modeled by increasing the concentration of GABA to which $GABA_A$ receptors were exposed by 20% of the maximum concentration present in the untreated case for the entire simulation. This was based on the 15-20% of $GABA_A$ receptors bound by muscimol in cat motor thalamic nuclei (Kultas-Ilinsky et al., 1988). We also calculated the ECAP after selective inhibition of pre-synaptic inputs, which was the presumed effect of isoflurane. For the bipolar contact configuration, we investigated the effect on the ECAP of a ventral or dorsal shift of the electrode along its axis, such that contact 0 or 2 was outside the VL thalamus, respectively. We also modeled the ECAP generated in the internal capsule (IC), which is adjacent and lateral to the VPL-VL thalamus, by replacing the neural elements with a population of 500 passing axons with 2 μm diameter lying parallel to the DBS electrode.

3.2.3 Data analysis

Stimulus-triggered averaging (64 responses for experimental signals and 8 responses for computational signals) was applied to the ECAPs to improve the signal-to-noise ratio. We quantified ECAP characteristics by calculating the signal energy of the experimental and computational ECAPs. First, any offset present in the stimulus-

triggered averaged ECAP signal was calculated as the mean of the final 1 ms of signal and subtracted. Second, the integral of the square of the signal was calculated for different ECAP phases.

Experimental and computational ECAPs were compared both qualitatively, through analysis of waveform shape, and quantitatively through calculation of correlation coefficients for ECAP signal energy values across stimulation parameters. Subsequently, neural element activation in the model was analyzed as the percentage of neural elements (TC neurons and pre-synaptic inputs from CTx, CER, TIN, and RN) that fired an action potential following a stimulus pulse within a given 0.1 ms bin, and analyzed over the same time interval used for calculation of the stimulus-triggered average ECAP.

Differences in experimental ECAP characteristics across stimulation parameters were identified with the non-parametric Wilcoxon signed-rank test following a Bonferroni correction (α=0.002), using Statview 5 (SAS Institute).

3.3 Results

The characteristics of ECAPs during thalamic DBS were consistent across experiments but varied systematically with stimulation parameters. Pharmacological interventions resulted in clear changes in ECAP waveforms and provided insight into the neural origin of the different ECAP phases. The model-generated ECAPs were similar to the experimental waveforms across stimulation conditions and following

pharmacological interventions, and provided additional insight into the type and extent of neural element activation constituting the ECAP signal.

3.3.1 Experimental and computational ECAPs

The mini DBS electrode was implanted in the VPL-VL thalamic complex accurately in 14 of 17 experiments (Table 3.1), and quantitative analysis of ECAP characteristics was performed using results from experiments with accurate electrode implantation.

The characteristics of ECAPs recorded with the monopolar symmetric configuration were dependent on the electrode position and DBS parameters (Figs. 3.4A-E, top row). Characterization of ECAPs with the monopolar asymmetric and bipolar contact configurations is presented in the Appendix. ECAPs exhibited primary positive (P1) and negative (N1) phases with latencies of approximately 0.25 and 0.75 ms, respectively, and secondary phases of either short latency (P2 at 1 ms and N2 at 1.5 ms) and short duration (less than 1 ms), or long latency (P2 at 3 ms) and long duration (on the order of 10 ms), as shown in cat Q (Figs. 3.4A-D) or cat I (Fig. 3.4E), respectively. The secondary phase latency was always greater than 0.7 ms. ECAPs had short latency secondary phases in 8 experiments, long latency secondary phases in 3 experiments, and both types were present in 3 experiments (in which case the additional phases were labeled in succession as P3, N3, etc.). When the short latency secondary response was

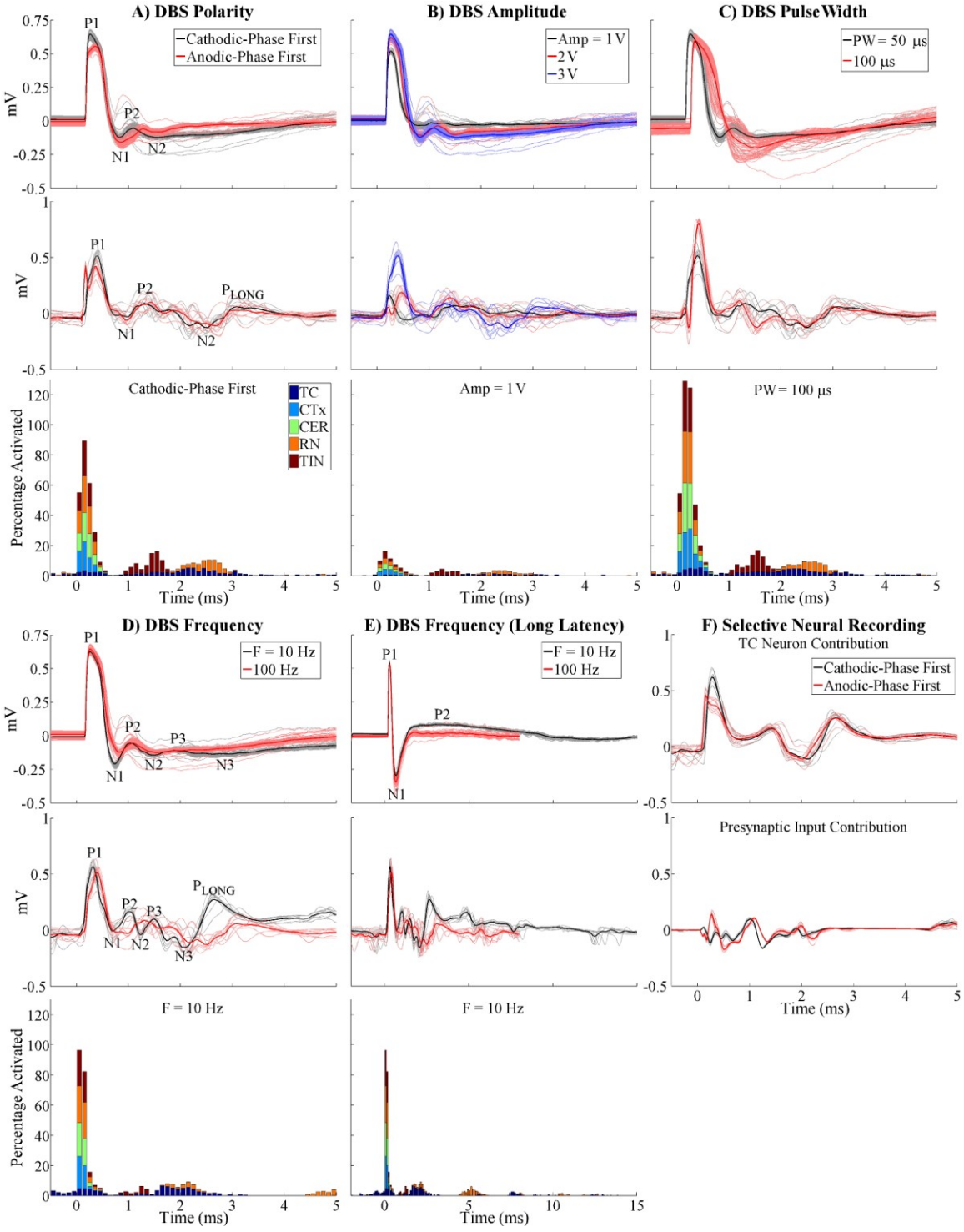

Figure 3.4: ECAPs recorded with the monopolar symmetric contact configuration. A-E: Comparison of ECAPs recorded experimentally (top row) with

those calculated using the computational model (middle row), and percentage of model elements activated in 0.1 bins following DBS pulses (bottom row). The latter was calculated for each element type individually and is shown in a stacked bar format, in which activation of a specific type of neural element (0-100%) is given by the height of the corresponding segment within the bar. The "standard" DBS parameter set was 3 V amplitude, 100 Hz frequency (F), 50 μs/phase pulse width (PW), and cathodic-phase first polarity, and one parameter (polarity, amplitude, PW, or F) was varied between subplots. The stimulus-triggered average ECAP (bold lines) and single trials (light traces) are shown, and ECAP phases are labeled. The experimental recordings were from cat Q (A-D) or cat I (E). The ECAP signal appears cutoff at 100 Hz DBS in (E) because the interpulse interval (corresponding to the ECAP recording window) was 10 ms. F: Model ECAP contributions individually from TC neurons or pre-synaptic inputs with 3 V, 10 Hz, 50 μs/phase, and both cathodic- and anodic-phase first polarities.

present, the electrode was generally implanted centrally within the VPL-VL thalamus or at the lateral border, while when the long latency secondary response was present the electrode was typically located at the dorsolateral border. ECAPs were similar for cathodic- and anodic-phase first polarities (Fig. 3.4A). Moreover, the magnitude and duration of the phases generally increased with DBS amplitude (Fig. 3.4B) and pulse width (Fig. 3.4C). The latency of primary phases also increased with longer pulse widths, and N1 masked the secondary phases at 100 μs pulse width for cat Q (Fig. 3.4C). The P1 phase had a lower DBS amplitude threshold than the other phases in 5 of 14 cats, N1 had the lowest threshold in 1 cat, and P1 and N1 had the same threshold in the remaining cats. Further, we never observed the presence of secondary phases without N1 also being present. Reducing DBS frequency from 100 Hz to 10 Hz led to increases in the magnitude of secondary phases, and in some experiments, also generated additional P3 and N3 phases (Figs. 3.4D,E).

The signal energy of ECAPs was quantified across experiments for the entire ECAP signal and separately for the primary and secondary phases (Fig. 3.5A). The ECAP energy (Fig. 3.5B) increased with higher DBS amplitudes ($P<0.0001$) and pulse widths ($P<0.002$). There was also a small effect of frequency, and ECAP energy was greater at 10 Hz than 100 Hz for amplitudes of 2 or 3 V and a pulse width of 100 μs ($P<0.002$). Similar trends were observed between the signal energy of primary phases and DBS amplitude ($P<0.001$) and pulse width ($P<0.002$), except that no frequency effect was observed (Fig. 3.5C). Lastly, the signal energy of secondary phases (Fig. 3.5D) increased with DBS amplitude ($P<0.002$) and pulse width ($P<0.002$) only at 10 Hz, and was generally greater at 10 Hz than 100 Hz across tested amplitudes and pulse widths ($P<0.002$). This difference between DBS frequencies was not simply a reflection of cropping of the secondary phases by the shorter interpulse interval (IPI) at 100 Hz compared to 10 Hz DBS. The ECAP returned to baseline prior to the end of the IPI at 100 Hz in 10 out of 14 experiments. In the other 4 experiments (cats J, L, P, and Q), the final ECAP value at the end of the IPI was only 4.9%±0.7% (mean ± SE, range: 0.3-23.7%) of the peak ECAP magnitude across stimulation parameters, and removing these experiments from the statistical analysis did not change the statistical significance between 10 and 100 Hz DBS as identified in Fig. 3.5D. The variance observed in signal energy measurements across experiments was generated both by variance between

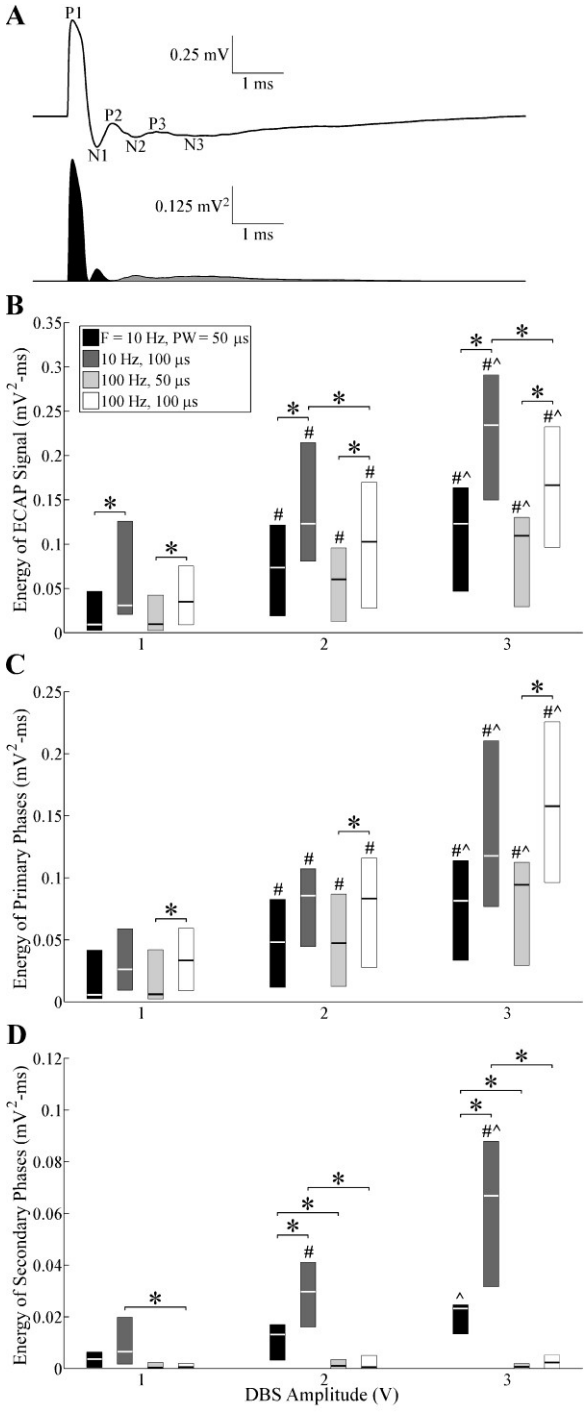

Figure 3.5: Quantification of ECAP characteristics across experiments with the monopolar symmetric contact configuration. A: The ECAP signal was squared, and signal energy was calculated by integrating across the entire ECAP signal and separately for the primary phases (dark fill) and secondary phases (grey fill). The

signal energy values across experiments for the (B) entire ECAP signal, (C) primary phases, and (D) secondary phases. The boxes have lines at the lower quartile, median, and upper quartile values. Statistical differences between parameters were identified using the Wilcoxon signed-rank test with Bonferroni correction: # significantly greater than 1 V DBS, ∧ significant greater than 2 V DBS, * significant difference between indicated bars (P<0.002). Polarity was treated as a replicate.

different response classes (i.e., short latency, long latency, or both short and long latency secondary phases) and by variance within each class.

We used a computational model of thalamic DBS to calculate the ECAP and the corresponding neural element activation. The model-generated ECAP calculated for three cell populations with different random distributions of TC locations within the VL thalamus had qualitatively similar waveform characteristics, and we used one population for all subsequent analysis.

The model ECAP waveform characteristics closely matched those of the experimentally recorded waveforms in phase polarity, magnitude, and latency across DBS parameters. For the monopolar symmetric configuration with 100 Hz DBS, model responses had the expected primary phases P1 and N1 followed by secondary phases, which included both shorter latency P2 and N2 phases and a longer latency positive phase (P_{LONG}) akin to the secondary phase in cat I (Figs. 3.4A-E, middle row). Greater DBS amplitudes and pulse widths typically led to increases in the magnitude and/or duration of ECAP phases. The latency of the P1 phase also increased with a longer pulse width. Moreover, model ECAPs were similar for opposite stimulation polarities. Finally, when DBS frequency was reduced from 100 to 10 Hz, the model response exhibited

additional secondary phases, P3 and N3, and increases in the magnitude of existing secondary phases, as observed experimentally. There were strong correlations between the signal energies of the model-generated and experimental ECAPs (Fig. 3.6). Both the computational and experimental ECAP signal energies had low values for secondary phases at 100 Hz DBS, and data were log-transformed to allow for a linear regression (Fig. 3.6C).

We used the model to deconstruct the ECAP signal and determine the neural elements contributing to the ECAP components. Monopolar stimulation generated direct activation of all model elements, but predominately pre-synaptic elements, within approximately 0.6 ms of pulse onset, which corresponded in time with the primary P1 and N1 phases (Figs. 3.4A-E, bottom row). Subsequently, TC neurons and inputs from RN and TIN were post-synaptically activated in the 0.9-3.1 ms window, aligning with both the short and long latency secondary phases. The RN inputs were then reactivated via the TC-to-RN excitatory synapse in the 4.4-6.3 ms window, and contributed to the long latency secondary phase (P_{LONG}) (Fig. 3.4E). Transmembrane potential recordings from individual neural elements measured during DBS are provided in the Appendix. We selectively recorded the potentials generated by either individual activation of the TC neurons or the pre-synaptic inputs to determine their corresponding ECAP contributions, and found that the former was primarily responsible for the P1, P3-N3, and P_{LONG} phases, whereas the latter generated the N1 and P2-N2 phases and

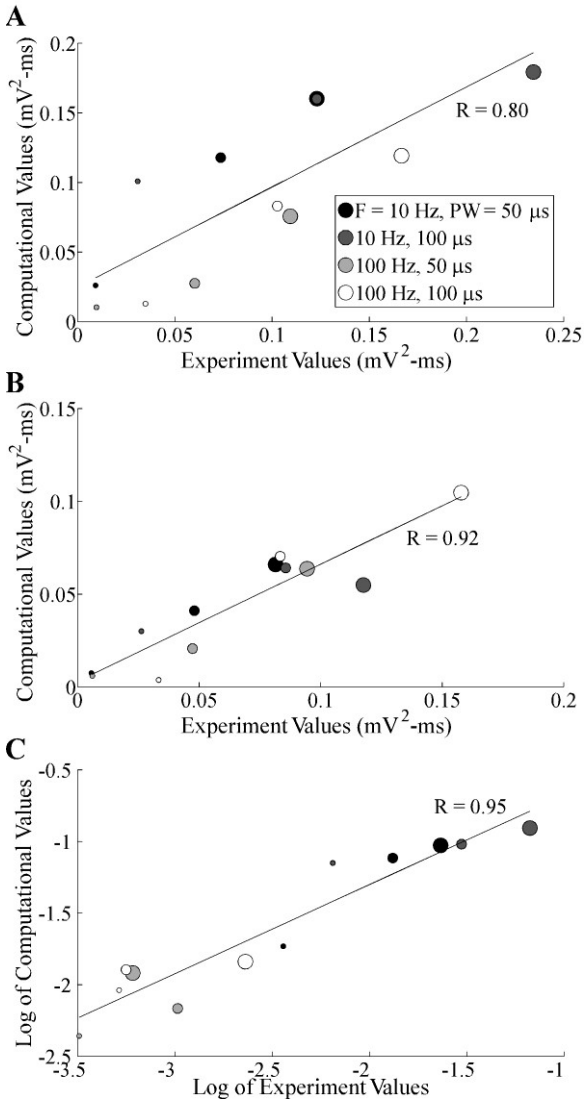

Figure 3.6: Correlation between values of ECAP signal energy from the computational model and *in vivo* experiments, measured with the monopolar symmetric configuration, for the entire ECAP signal (A), primary phases (B), and secondary phases (C). Each data point corresponds to computational and median experimental signal energy values for a single set of stimulation parameters. The size of the data point is proportional to the DBS amplitude (1 to 3 V), and color indicates the corresponding DBS pulse width and frequency. Polarity was treated as a replicate. The correlation coefficients for the linear trend lines (black lines) are provided (P<0.002).

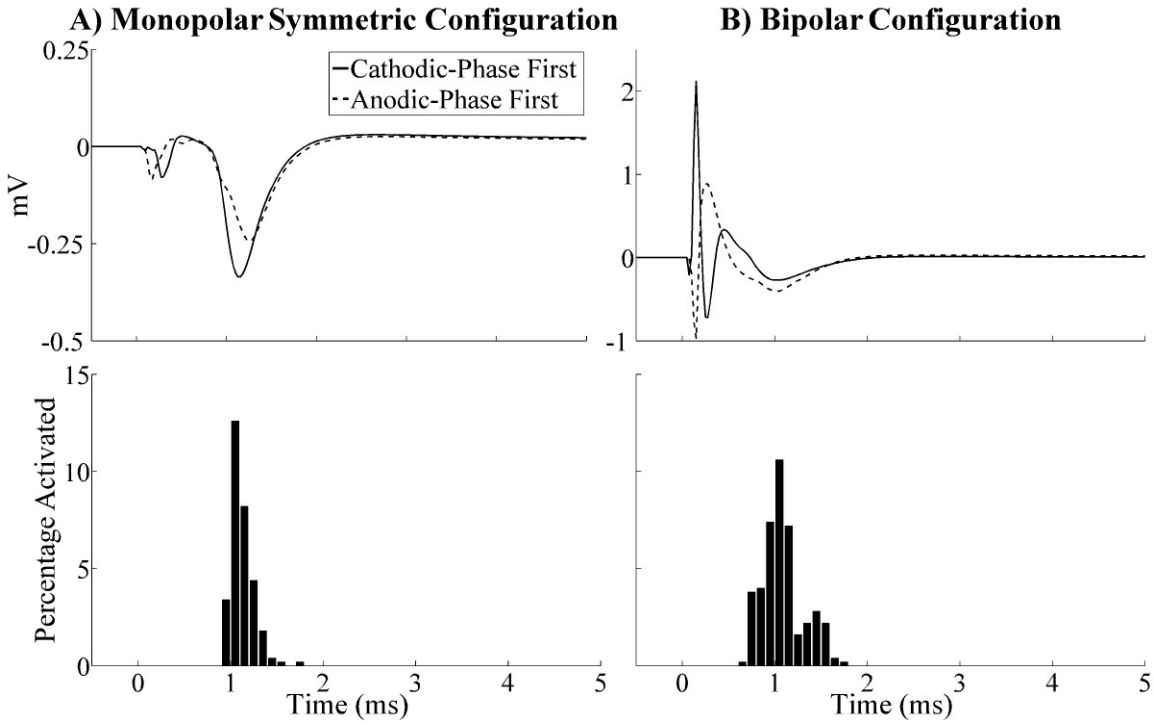

Figure 3.7: Model ECAPs calculated from a population of parallel axons using the monopolar symmetric (A) or bipolar (B) contact configurations. The DBS parameters were 3 V, 10 Hz, 50 μs/phase, and both cathodic- and anodic-phase first polarities. The stimulus-triggered average ECAP is shown and overlapping the single trials (top row), and the percentage activation of the parallel axons in 0.1 ms bins following DBS pulses for cathodic-phase first polarity is also provided (bottom row). There was a small residual artifact for the bipolar configuration after template subtraction, observed as inverted peaks for opposite stimulation polarities.

contributed to the P$_{LONG}$ phase (Fig. 3.4F). Increasing DBS amplitude or pulse width generated a greater extent of direct neural excitation, which paralleled an increase in magnitude and/or duration of primary ECAP phases. In some cases, this also led to a corresponding increase in post-synaptic activation and larger secondary ECAP phases. Decreasing DBS frequency from 100 Hz to 10 Hz reduced the extent of RN and TIN post-synaptic activity, and increased the synchronization of TC post-synaptic activity (i.e.,

less temporal dispersion of activation times). The latter may have been responsible for generation of P3-N3 and increase in magnitude and duration of P_{LONG}. Lastly, stimulation of a population of parallel axons, representing a lateral shift toward the IC that was characteristic of electrode placement in some experiments, generated neural activation in the range of 0.9-1.8 ms and a corresponding negative ECAP phase with this same latency (Fig. 3.7A).

3.3.2 Pharmacological interventions

We quantified the effect on ECAP characteristics of pharmacological agents to determine the neural origin of the ECAP. Saline microinjection generated negligible changes in 2 of 3 cats tested (Fig. 3.8A), and a moderate increase in N1 in cat J, which may have still been recovering from isoflurane administration. Microinjection of CNQX/APV led to a large reduction in the magnitude and duration of both short and long latency secondary phases in 4 of 6 cats (Fig. 3.8A). CNQX/APV also caused a decrease (3 cats) or increase (1 cat) in the magnitude of N1, and P1 was reduced in 2 of these cats. Administration of muscimol shifted secondary phases towards longer latencies and generated a shorter latency negative signal feature (N_{MUSC}) following N1 in both cats tested (Fig. 3.8B). A similar but less pronounced negative signal feature was also observed after administration of CNQX/APV in cat I (Fig. 3.8A) and lidocaine in cat K, but was not reproduced in any other experiment. ECAP signal recovery from the effects of muscimol was observed after a 1 hr washout in 1 of 2 cats tested (Fig. 3.8B).

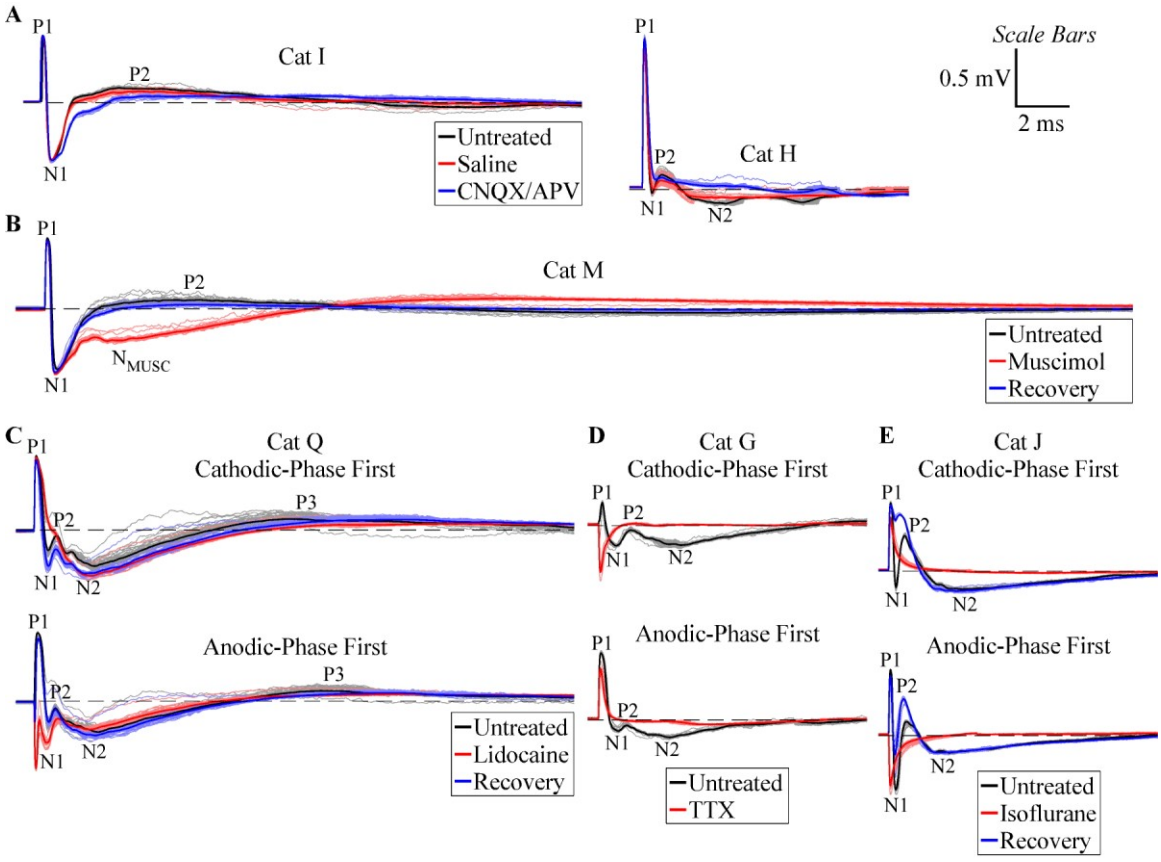

Figure 3.8: Effect of pharmacological interventions on the ECAPs measured with the monopolar symmetric contact configuration from different experiments (see Table 3.1). DBS was applied with 3 V, 10 Hz, 50 or 100 μs/phase, and with cathodic-phase first polarity unless otherwise denoted. The stimulus-triggered average ECAP (bold lines) and single trials (light traces) are shown. The dashed line indicates 0 mV. The ECAP phases are labeled on the untreated traces. A: Signal recorded before treatment and 5 min after administration of 5 μL of saline or 5 μL CNQX/APV. B: Signal recorded before treatment, 5 min after administration of 20 μL of muscimol, and following recovery after a 1 hr washout period. A negative phase (N_{MUSC}) was generated after muscimol administration that was not observed in the untreated condition. C: Signal recorded before treatment, 5 min after administration of 20 μL of 10% lidocaine, and following recovery after a 2 hr washout period. D: Signal recorded before treatment and 20 min after administration of 10 μL TTX. E: Signal recorded before treatment, 10 min after administration of isoflurane anesthesia, and following recovery after a 1 hr washout period. The ECAP signal was abolished with administration of TTX and isoflurane, and reduced with lidocaine, and the resulting signals contained residual stimulus artifact observed as inverted peaks for opposite stimulation polarities.

Administration of 5-10% lidocaine reduced the ECAP magnitude, with recovery of the signal observed after at least 30 min in 2 of 3 cats (Fig. 3.8C). Conversely, 2% lidocaine led to relatively small and inconsistent changes in ECAP characteristics in 2 of 2 cats. Microinjection of TTX completely eliminated the ECAP in the one cat tested (Fig. 3.8D). Administering isoflurane anesthesia also completely abolished the signal (Fig. 3.8E) in 2 of 3 cats, whereas only P1 was eliminated in the other cat. The ECAP recovered in 2 of 3 cats following cessation of isoflurane administration and a washout period of at least 30 min.

The model was also used to simulate the effects of the pharmacological interventions performed experimentally. Administration of CNQX/APV was modeled by blocking excitatory receptors on TC and TIN, which eliminated post-synaptic activation of these elements relative to the untreated case (Figs. 3.9A,B). Further, CNQX/APV resulted in reduced direct activation of TC neurons, due to the decrease in excitatory input, hyperpolarization of TC somata, and an increased stimulation threshold (Fig. 3.9B). These changes were manifested as a reduction in secondary ECAP phases, while primary phases were relatively unaffected. The residual secondary phase activity was generated by post-synaptic activation of RN inputs, and was eliminated by inhibiting all model synapses (Fig. 3.9C). Administration of muscimol was modeled as an increase in the concentration of GABA at GABAergic receptors on TC neurons, and led to hyperpolarization of TC somata (Fig. 3.9D). As a result, direct activation of TC

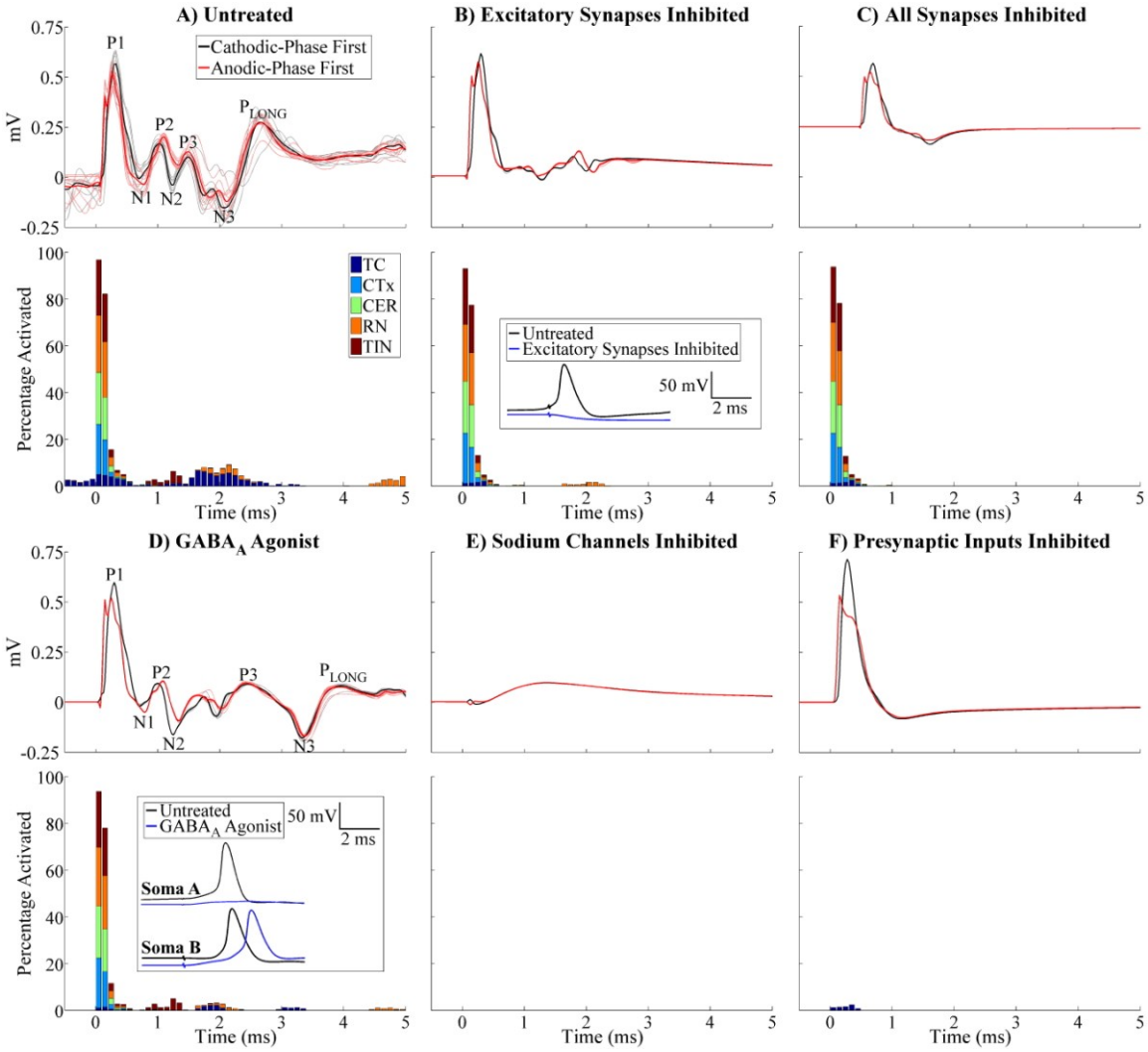

Figure 3.9: Simulation of effects of pharmacological agents on the model-generated ECAP. The ECAP (top row), and percentage of neural elements activated in 0.1 bins following the DBS pulse (bottom row) are shown for the untreated case (A), and after inhibition of excitatory receptors on TC and TIN (B), inhibition of all synapses (C), addition of a GABA$_A$ agonist (D), inhibition of sodium channels (E), and inhibition of pre-synaptic inputs (F). The monopolar symmetric contact configuration was used, with DBS applied using 3 V, 10 Hz, 50 μs/phase, and both cathodic- and anodic-phase first polarities. Percentage activation is shown for cathodic-phase first polarity. The insets in (B) and (D) show the transmembrane potential recordings from TC somata following a DBS pulse applied at t=2 ms for the untreated case and after pharmacological intervention. The cell hyperpolarization generated by inhibition of excitatory synapses blocked direct activation of the TC cell. Similarly, cell hyperpolarization generated by the presence of the GABA$_A$ agonist led to inhibition

of post-synaptic activity in Soma A, and delayed generation of an action potential in Soma B.

neurons was reduced, and post-synaptic activation was either inhibited in some cells or delayed in others. The effect on the ECAP was evident in secondary phases P3, N3, and PLONG as a shift towards longer latencies, which matched the changes observed experimentally. Blocking sodium channels abolished all neural activation and the corresponding ECAP (Fig. 3.9E), as observed with experimental administration of TTX and to a lesser extent with lidocaine. Selectively inhibiting pre-synaptic inputs, presumed to be the mechanism of action of isoflurane (Wu et al., 2004, Joksovic et al., 2009, Ying et al., 2009), abolished all ECAP phases except P1 (Fig. 3.9F), which differed from the experimental effect, where the ECAP was completely eliminated in a majority of experiments.

3.4 Discussion

This study characterized the evoked potentials generated by DBS, quantified their dependence on stimulation parameters, and determined the neural elements contributing to the different phases of the ECAP. For the monopolar symmetric configuration, the primary phases corresponded to direct neural activation and secondary phases to post-synaptic activation. The ECAP phases increased in magnitude and/or duration with DBS amplitude and pulse width, suggesting a greater extent of neural activation, and were modulated by DBS frequency due to changes in post-synaptic activity. If these systematic changes in ECAP characteristics observed across

stimulation parameters are correlated with changes in symptoms, the ECAP may be suitable as a feedback control signal for closed-loop DBS systems. Further, these ECAP signatures of clinical efficacy could inform design of electrodes and stimulation methods for selective stimulation of the neural elements mediating the symptom relieving effects of DBS. Finally, the electrode position dependent character of the ECAP may provide a signal useful for electrode targeting during implantation or contact selection during programming of stimulation parameters.

3.4.1 Neural origin of ECAP phases

We combined experimental pharmacology with model-based deconstruction to identify the neural elements that generated the different components of the ECAP. The primary P1 and N1 phases recorded with the monopolar symmetric configuration occurred at latencies of <1 ms and were generated by direct neural excitation. This was evident from the direct activation of model elements within 0.6 ms, and by the lack of any consistent effect on these phases of pharmacological agents targeting synaptic transmission. More specifically, the model indicated that P1 was generated by TC neuron activation and N1 by pre-synaptic axon activation. Local circuit currents generated by action potential propagation in the TC neuron would be expected to generate a triphasic waveform with a dominant negative phase at an external recording contact (Gold et al., 2006). Since the TC axon projects past the dorsal, negative recording contact, this would be recorded predominately as a positive voltage, and therefore result

in the P1 phase. Likewise, pre-synaptic inputs, including CER and CTx inputs, project past both the positive and negative recording contacts, respectively, and would result in contributions to ECAP phases of both polarities, including the N1 phase.

The secondary phases of the ECAP recorded with the monopolar symmetric configuration occurred at latencies >0.7 ms and were generated by post-synaptic activation. This conclusion was supported by several results, including the post-synaptic activation of model elements in the 0.9 – 6.3 ms window, the effects of DBS frequency on secondary phases, the reduction in magnitude with application of glutamate receptor antagonists CNQX/APV, and the invariable association between the presence of N1 generated by pre-synaptic inputs and the secondary phases in experimental recordings. The model indicated that the short latency secondary phases were generated by post-synaptic activation of TC, RN, and TIN elements, whereas long latency phases apparently resulted from late post-synaptic activation of TC neurons and from the re-excitation of RN by these TC neurons in the 4.4-6.3 ms window. These long latency phases were observed in 6 of 14 experiments, and in these experiments the electrode was implanted near the dorsal and/or lateral VPL-VL thalamic border, potentially near local RN cells receiving input from TC neurons or near passing axons within the IC. Therefore, post-synaptic activation of RN local cells, which were not explicitly represented in the model, may have also contributed to the longer latency secondary phase. On the other hand, IC axons were directly activated at a latency of 0.9-1.8 ms, and

were therefore unlikely to be the source of these phases with latencies >3 ms. An additional source of the long latency secondary phases could have been activation derived from reciprocal thalamocortical-corticothalamic connections (Hersch and White, 1981, Briggs and Usrey, 2007), which also were not represented in the model. The average time required for action potential propagation in the reciprocal pathway from the lateral geniculate (LGN) nucleus of the thalamus to the primary visual cortex and back to the LGN in non-human primates was 9.3 ms (Briggs and Usrey, 2007), which was within the latency range observed for long latency secondary ECAP phases measured in this study.

3.4.2 Identification of neural elements through pharmacological interventions.

Specific pharmacological interventions enabled identification of the neural elements contributing to the different phases of the ECAP. First, the predominate effect of CNQX/APV was a reduction in post-synaptic activity and corresponding secondary ECAP phases, but there were also changes to the primary ECAP phases recorded experimentally and associated with direct neural excitation. The latter may have resulted from a reduced direct excitability of TC neurons due to a decrease in the relative strength of excitatory inputs, although the model suggested this would have a negligible effect on primary phases. Alternatively, the effect of CNQX/APV on experimentally recorded primary phases could have been generated by antagonism of the thalamic triad in the VL thalamus. In this thalamic triad, a CER afferent makes

synaptic connections to both a post-synaptic TC dendrite and a pre-synaptic input from a local interneuron, and the latter establishes synaptic contact with the same TC dendrite (Sato et al., 1996). There is evidence for AMPA and NMDA receptors on the pre-synaptic terminal of local interneurons in a similar triad arrangement within the LGN of cats (Sherman, 2004). Therefore, antagonism of the triad arrangement in the VL thalamus by CNQX/APV could have decreased the direct excitability of TIN inputs and reduced the amplitude of primary phases, particularly the N1 phase. Because the thalamic triad was not explicitly represented in the model, an effect of CNQX/APV on primary ECAP phases would not have been observed.

Second, hyperpolarization of TC neurons by muscimol reduced their propensity for direct activation and inhibited or delayed post-synaptic activation, with the latter shifting the secondary ECAP phases towards longer latencies. A novel negative phase feature was also revealed following injection of muscimol, and in some experiments after delivery of CNQX/APV and lidocaine. This could have been otherwise masked by other secondary ECAP phases, and may have corresponded to the early latency P2-N2 phases generated by post-synaptic activation of TIN (Fig. 3.9D).

Third, inhibiting neural activation with lidocaine or TTX generally led to a reduction or abolition of all ECAP phases, respectively. Whereas Levy and colleagues found that 2% lidocaine was sufficient to reduce neural activity at least 0.78 mm from the injection site (Levy et al., 2001), we observed ECAP reduction only with higher

concentrations of 5-10%, more closely matching results from (Boehnke and Rasmusson, 2001). The smaller effect of lidocaine relative to TTX may be explained by the use-dependent effects in neurons of the former (Strichartz, 1973, Courtney, 1975, Khodorov et al., 1976, Balser et al., 1996) but not the latter (Ulbricht and Wagner, 1975, Cohen et al., 1981), or from the larger effective spread of TTX compared to lidocaine (Boehnke and Rasmusson, 2001).

Fourth, we found that isoflurane abolished the ECAP, suggesting non-selective inhibition of both pre- and post-synaptic elements. Whereas some studies identified selective inhibition of pre-synaptic afferents by isoflurane (Wu et al., 2004, Joksovic et al., 2009, Ying et al., 2009), another study found an increase in GABAergic inhibition and depression of glutamate release (Detsch et al., 2002), which would be expected to decrease the excitatory drive of post-synaptic TC neurons. In fact, the selective elimination of P1 in one experiment following administration of isoflurane is indicative of selective TC inhibition, although this was not a consistent result across experiments.

There was a residual stimulus artifact in the recordings after neuronal inhibition following administration of TTX, isoflurane, or lidocaine. Similar results were observed in **Chapter 3** at 5 minutes following euthanasia, and it was hypothesized that the artifact size increased in the post-mortem condition due to the generation of tissue inhomogeneities and/or decreases in tissue conductivity and permittivity. Similarly, it is possible that microinjection generated local changes in conductivity near the electrode

and thereby increased the size of the artifact. Alternatively, a latent artifact may have been present in the untreated condition and distorted the short latency ECAP phases.

3.4.3 Effect of DBS parameters on the ECAP

Changes in ECAP characteristics across DBS parameters measured experimentally and calculated with the computational model were in strong agreement, and provided insight into the effect of stimulation parameters on neural activation.

Delivery of stimulus pulses with opposite polarities generated similar neural responses. This suggested that a polarity averaging technique (Brown and Abbas, 1990) could reduce the stimulus artifact with minimal error. The small effect of polarity on the neural response was expected for symmetric, biphasic pulses delivered with monopolar and bipolar contact configurations (McIntyre and Grill, 2000). In contrast, applying opposite stimulation polarities with the asymmetric waveforms used in clinical DBS systems can generate differential effects on neural activation (McIntyre and Grill, 2000, Wang et al., 2012) and clinical outcomes (Yousif et al., 2012).

Increasing DBS amplitude and pulse width led to an increase in ECAP amplitude and signal energy, reflecting a greater extent of direct neural activation, which could in turn generate additional post-synaptic activation. Compared to the model, the experimental waveforms exhibited smaller changes in ECAP magnitude across DBS amplitudes (Fig. 3.4B). This may have resulted from a neural stun or microlesion effect of nearby elements following experimental electrode implantation, which could reduce

differences in the volume of tissue activated across stimulation amplitudes. This was confirmed in the computational model by removing neural elements that passed within 200 μm of the DBS electrode, after which we observed smaller relative increases in ECAP magnitude with greater DBS amplitudes (data not shown). Using a longer pulse width increased the latency of primary ECAP phases, which could have been caused by activation of higher threshold neural elements (Kuncel and Grill, 2004) near the end of the longer pulse. These elements would make longer latency contributions to the recorded ECAP and shift the time at which the phases were observed.

Decreasing the frequency from 100 Hz to 10 Hz resulted in an increase in the number and magnitude of secondary phases. This could arise from neurotransmitter depletion and less reliable synaptic transmission at high frequencies (Wang and Kaczmarek, 1998, Urbano et al., 2002, Wesseling and Lo, 2002, Zucker and Regehr, 2002, Anderson et al., 2006). However, neurotransmitter depletion was not represented in the model, and on the contrary, the model exhibited greater post-synaptic activation of RN and TIN at 100 Hz. Alternatively, the model indicated that there was increased synchronization of post-synaptic TC activity at 10 Hz, and this may have contributed to the additional phases and increase in magnitude and/or duration of existing ECAP phases. Clinical symptoms are suppressed only at high DBS frequencies and low frequencies are ineffective or may lead to exacerbation (Birdno and Grill, 2008), and the extent of post-synaptic synchronization may contribute to this frequency dependence.

We found that TC neurons corresponding to P1 had the lowest activation threshold in five experiments, pre-synaptic inputs corresponding to N1 had a lower threshold in just one experiment, and thresholds were similar in the remaining experiments. Although activation occurs at the axon for both elements (McIntyre and Grill, 1999), the TC neuron initial segment may be hyper-excitable and thereby have lower thresholds than pre-synaptic inputs. Conversely, Baldissera and colleagues applied stimulation to the feline red nucleus and found that the threshold of the preterminal segment of pre-synaptic interpositorubral efferents was only 10% of that for the post-synaptic rubrospinal fibers (Baldissera et al., 1972). Moreover, our model results indicated that pre-synaptic inputs had a lower threshold than TC neurons, with greater activation of the former at 1 V (Fig. 3.4B). Therefore, based on this contradictory evidence, the relative thresholds of pre- and post-synaptic elements in the VPL-VL thalamus remain unclear. The responses in these experiments were recorded at only three stimulation amplitudes, resulting in relatively crude estimates of relative thresholds, which may have contributed to these inconclusive findings.

The consistent effects of stimulation parameters on ECAP characteristics suggest that the ECAP could be used to identify stimulation parameters that generate a sufficient extent of activation of the appropriate types of neural elements. The ECAP signal energy may indicate the extent of neural activation, and if correlated with changes in symptoms, could be used to set the DBS amplitude and pulse width. The signal energy

takes into account changes in either the magnitude or duration of ECAP phases, and may be a more robust measure of neural activation than the ECAP magnitude alone. Similarly, the energy of secondary ECAP phases may enable identification of the critical DBS frequency above which pathological firing patterns are masked and symptoms are suppressed (Kuncel et al., 2007, Birdno and Grill, 2008). The ECAP could also be used to distinguish between activation of pre-synaptic inputs or post-synaptic cells that are associated with clinical benefit or side effects. For example, it is hypothesized that Vim-DBS provides tremor suppression in ET by activating cerebellar axonal inputs (Birdno et al., 2012), whereas paresthesias are caused by stimulation of local neurons within the adjacent ventral caudal (Vc) nucleus of the thalamus (Lenz et al., 1993). Similarly, it is thought that treatment of PD with DBS in the subthalamic nucleus (STN) is effective through activation of pre-synaptic cortico-STN afferents (Gradinaru et al., 2009), whereas stimulation of passing axons in the IC causes side effects (Krack et al., 2002, Tamma et al., 2002). The ECAP could be used to test these hypotheses, and enable selective targeting of elements required for therapy.

3.4.4 Experimental and computational limitations

There were several limitations in this work that should be addressed. First, we did not investigate the relationship between ECAP characteristics and the pathological symptom response to DBS, as required to demonstrate that the ECAP is a viable feedback control signal for closed-loop DBS. Second, use of general anesthetics may

have affected neural activity and the corresponding experimental ECAP response. Ketamine is a NMDA receptor antagonist (Kemp and McKernan, 2002), and may have decreased post-synaptic activation and the corresponding secondary ECAP phases. The mechanisms of action of alpha chloralose remain unclear (Posner and Burns, 2009), and so the resulting effect on the ECAP is uncertain.

We determined the neural origin of ECAPs with pharmacological interventions, but there were several potential limitations in our approach. First, although we found that administration of 5 μL saline control typically had a negligible effect on the ECAP, we delivered up to 20 μL of some pharmacological agents, and therefore we cannot be certain that these larger volumes would not have affected the ECAP due to the mechanical forces of fluid flow. However, this was likely mitigated by the use of a constant injection rate. Second, the volume of a specific pharmacological agent necessary for ECAP modulation varied between experiments, which likely resulted from slight differences in the relative distance between the injection cannula and the DBS electrode. Third, the administration of multiple agents in some experiments may have caused interaction effects on the ECAP characteristics if recovery from one agent was not complete when another agent was delivered.

The computational model corroborated identification of neural elements contributing to the ECAP, but also had several limitations. First, the geometrical representation of the VL thalamus was an approximation (Jimenez Castellanos, 1949)

based on the human Vim thalamus (Birdno et al., 2012) with a reduced dimension along the superior-inferior axis. Using a more accurate morphology of the cat VL thalamus, including the true anatomical shape from a cat brain atlas, accurate fiber trajectories, and correct relative positioning of the DBS electrode, may have changed neural activation and the calculated ECAP response. The use of a simplified prism representation of the nucleus may have contributed to the differences between the experimental and computational ECAPs. Second, while using a population of 500 local neurons generated ECAPs that were consistent across different cell distributions, the responses were not identical. However, there existed a tradeoff between further increasing cell density to reduce this variability and maintaining a shorter computational time by minimizing the number of cells used. Third, we did not account for the ETI, tissue capacitance, or tissue inhomogeneities in our model, which would lead to filtering of both the potentials generated by DBS (Butson and McIntyre, 2005, Yousif et al., 2008a, Grant and Lowery, 2010, Lempka et al., 2010, Tracey and Williams, 2011) and the ECAP signal (Bedard et al., 2004, 2006). Low-pass filtering of the latter would reduce the high frequency fluctuations observed in the computational ECAP and likely produce a closer match between computational and experimental waveforms.

3.5 Appendix

In addition to measuring ECAPs with the monopolar symmetric contact configuration, we also conducted experimental and computational ECAP recordings

with the monopolar asymmetric and bipolar contact configurations. Transmembrane potential recordings of model elements during DBS were also investigated.

3.5.1 Monopolar asymmetric configuration

The experimental ECAPs recorded with the monopolar asymmetric configuration included primary negative (N1') and positive (P1') phases at latencies of 0.23 and 0.5 ms, respectively, followed by a secondary negative phase (N2') at approximately 2 ms (Figs. 3.10A-D, top row). Similarly, the model ECAP had primary N1' and P1' phases, although the smaller magnitude secondary N2' phase observed experimentally was not prominent in the model at 100 Hz (Figs. 3.10A-D, bottom row). Experimental ECAPs exhibited similar waveform shapes for opposite stimulation polarities (Fig. 3.10A), although the positive and negative phases were consistently greater in magnitude with cathodic- and anodic-phase first polarities, respectively. In contrast, the magnitude of primary phases was larger with cathodic-phase first polarity for the computational ECAPs. In addition, the magnitude of the experimental and computational ECAPs increased with DBS amplitude (Fig. 3.10B) and pulse width (Fig. 3.10C). Finally, using a lower DBS frequency in the model led to the generation of a small N2' phase, which was present experimentally but unaffected by frequency (Fig. 3.10D).

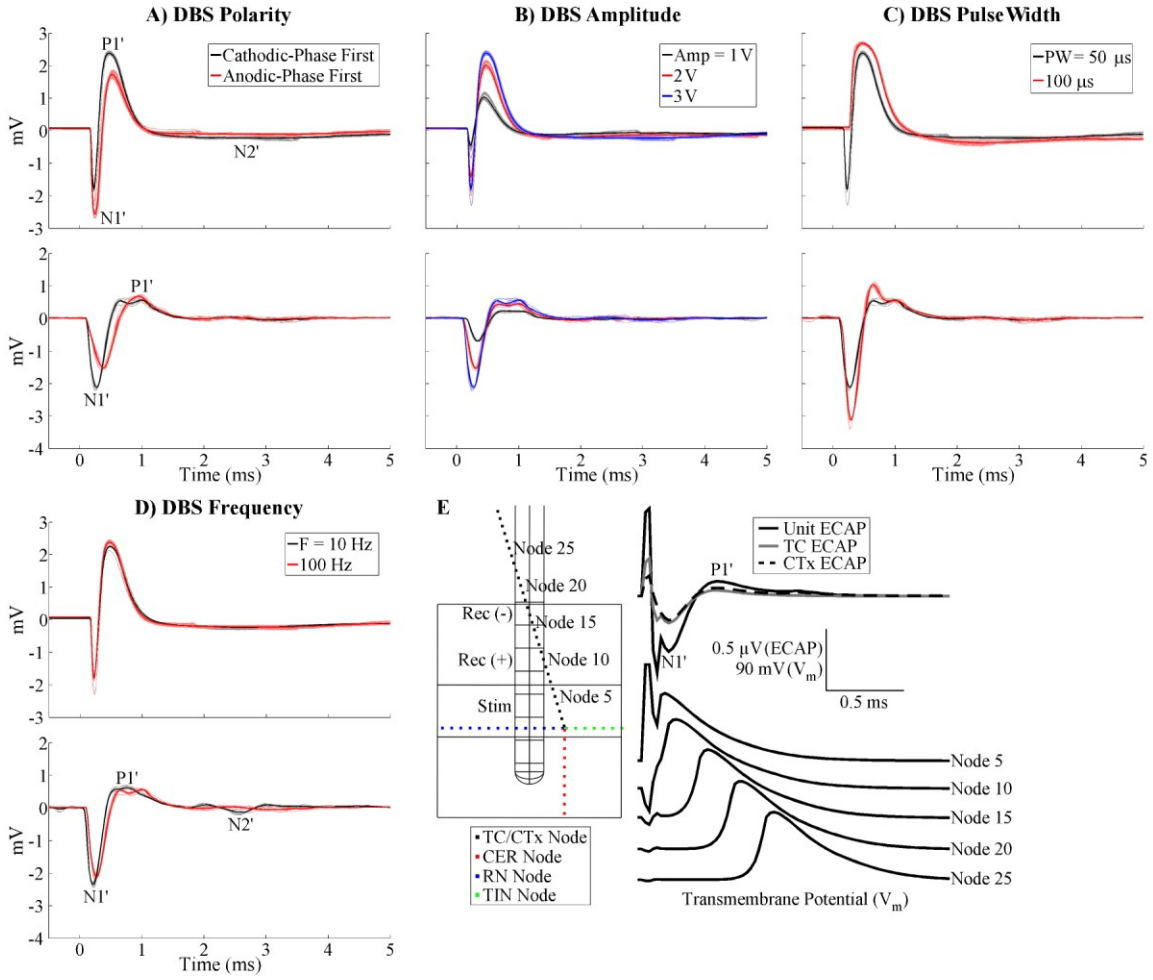

Figure 3.10: ECAPs recorded with the monopolar asymmetric contact configuration. A-D: Comparison of ECAPs recorded experimentally (cat H, top row) and calculated with the computational model (bottom row). Since the same stimulation contact was used as in Fig. 3.4, the percentage neural activation was identical and is therefore omitted here. Data presentation is otherwise similar to Fig. 3.4. The N1' phase is masked in (C) for a pulse width of 100 µs/phase due to amplifier blanking with the DBS-ECAP instrumentation. E: Analysis of the neural origin of the computational ECAP. Left: Diagram of the prism representation of the VL thalamus, implanted DBS electrode (stimulation and recording contacts identified), and axon node locations of the elements from one neural unit (TC and CTx nodes are overlapping). This is viewed from an anterior position perpendicular to the electrode axis. Right: ECAPs recorded from all elements in the neural unit, and selectively from the TC neuron and CTx input (other elements had negligible contribution). The corresponding transmembrane potential is shown at selected nodes in the TC axon during action potential propagation, with nearly identical recordings made in the CTx

axon. The N1' phase was generated by action potential propagation near the positive recording contact, and P1' by subsequent propagation near the negative recording contact.

Using the model, we found that the ECAP recorded with the monopolar asymmetric configuration was generated by action potential propagation in TC neurons and CTx inputs. The contribution of the other neural elements to the ECAP was negligible. The action potential was initiated at a site near the stimulation contact, and local circuit currents generated the negative N1' phase with propagation near the positive recording contact, followed by a positive P1' phase with propagation near the negative recording contact (Fig. 3.10E). The propagation speed and corresponding latency difference between model ECAP primary phases were in agreement with the typical latency difference of 0.2-0.3 ms observed experimentally. The small magnitude N2' phase observed experimentally corresponded in time with post-synaptic activation of model elements (Figs. 3.4, 3.10). However, the lack of DBS frequency effects on N2' suggested another source, and this may have instead been generated by potassium ion efflux during membrane repolarization at the trailing edge of the action potential (Gold et al., 2006).

3.5.2 Bipolar configuration

For the bipolar contact configurations, there were two experimental ECAP waveform variants; the first had primary negative (N1") and positive (P1") phases at approximately 0.2 and 0.5 ms (always less than 0.8 ms across experiments), and a

secondary negative (N2") phase at 1.1 ms (Figs. 3.11A-D, top row). In the second variant, these ECAP phases were inverted (data not shown). Of the 12 experiments in which the bipolar configuration was tested, 4 generated responses of the initial negative phase variant, 7 generated responses with the initial positive phase variant, and 1 generated a large artifact that masked the ECAP. The electrode was generally implanted near the ventral or dorsal border of the VPL-VL thalamus when the initial negative variant was observed, and centrally or near the lateral border of the target nuclei when the initial positive variant was recorded. The model ECAP had primary N1" and P1" phases followed by a secondary N2" phase, which were observed in the initial negative phase variant of the responses seen experimentally (Figs. 3.11A-D, middle row). The effect of DBS parameter adjustment on ECAP characteristics was similar to that observed for the monopolar asymmetric configuration, except that the secondary phase (N2") was modulated by frequency in both the experimental and model conditions, typically being slightly larger at 10 Hz than at 100 Hz.

We attempted to reproduce the apparent dependence of experimental waveform characteristics recorded with the bipolar configuration on the electrode location by implementing in the model a dorsal or ventral shift of the electrode (Fig. 3.11E) or placing the electrode within a population of parallel IC axons (Fig. 3.7B). These alternate electrode positions approximated the experimental electrode locations at the dorsal, ventral, or lateral border of the VL thalamus. Whereas the model indicated that the

original, central location or a dorsal shift generated ECAPs similar to the initial negative phase variant observed experimentally, a ventral shift or lateral position near the population of parallel axons generated responses of the initial positive phase variant. Both the experimental and computational results suggested that the response recorded with the bipolar configuration was particularly sensitive to electrode position.

The temporal pattern of neural activation observed for the monopolar symmetric configuration was very similar for bipolar stimulation (Figs. 3.11A-D, bottom row). The primary phases corresponded to direct neural excitation and secondary phases to post-synaptic activation. Selectively recording the ECAP contribution from pre-synaptic inputs and TC neurons indicated that the former were primarily responsible for all of the phases, N1", P1", and N2" (Fig. 3.11F).

Bipolar stimulation led to a greater extent of activation compared to monopolar stimulation. This was reflected in the larger magnitude ECAPs with bipolar stimulation observed in experiments that used the same recording contacts for both configurations (data not shown), and in the extent of neural activation of model elements between these configurations (Figs. 3.4, 3.11). This result can be explained by the generation of neural activation near both contacts with bipolar stimulation when using symmetric, biphasic pulses.

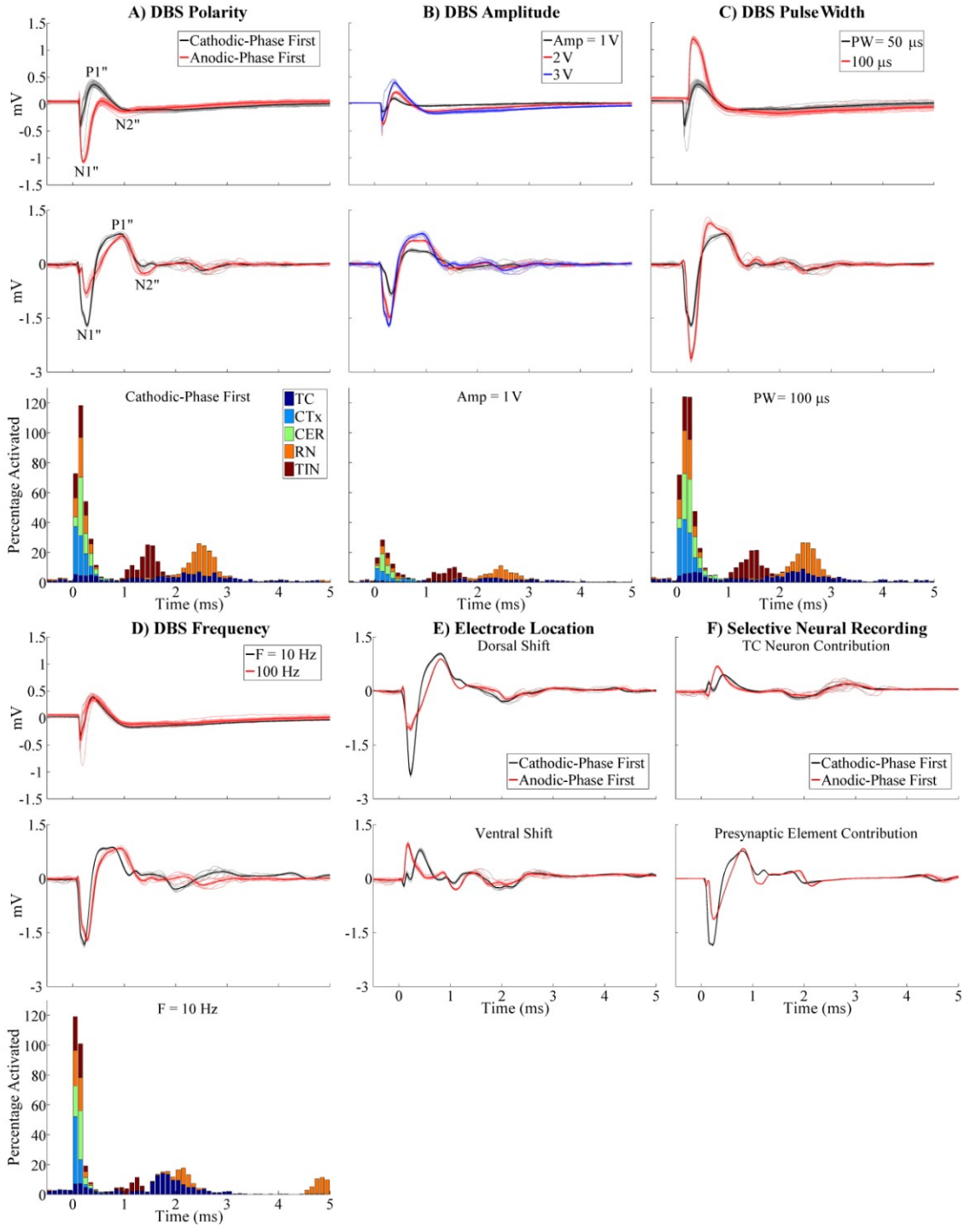

Figure 3.11: ECAPs recorded with the bipolar contact configuration. A-D: Comparison of experimental ECAPs (cat I, top row), computational ECAPs (middle row), and percentage activation of model elements (bottom row). Data presentation is

similar to Fig. 3.4, except that experimental ECAPs for (B) were collected at 10 Hz DBS frequency due to high noise in one response at 100 Hz. The N1" phase is masked in (C) for a pulse width of 100 μs/phase due to amplifier blanking with the DBS-ECAP instrumentation. E: Effect on the model ECAP of a dorsal or ventral shift of the DBS electrode with respect to the VL thalamus. Stimulation parameters were 3 V, 10 Hz, 50 μs/phase, and both cathodic- and anodic-phase first polarities. F: Selective recording of the contribution of TC neurons or pre-synaptic inputs to the model ECAP. The same parameters were used as in (E).

3.5.3 Model transmembrane potential recordings

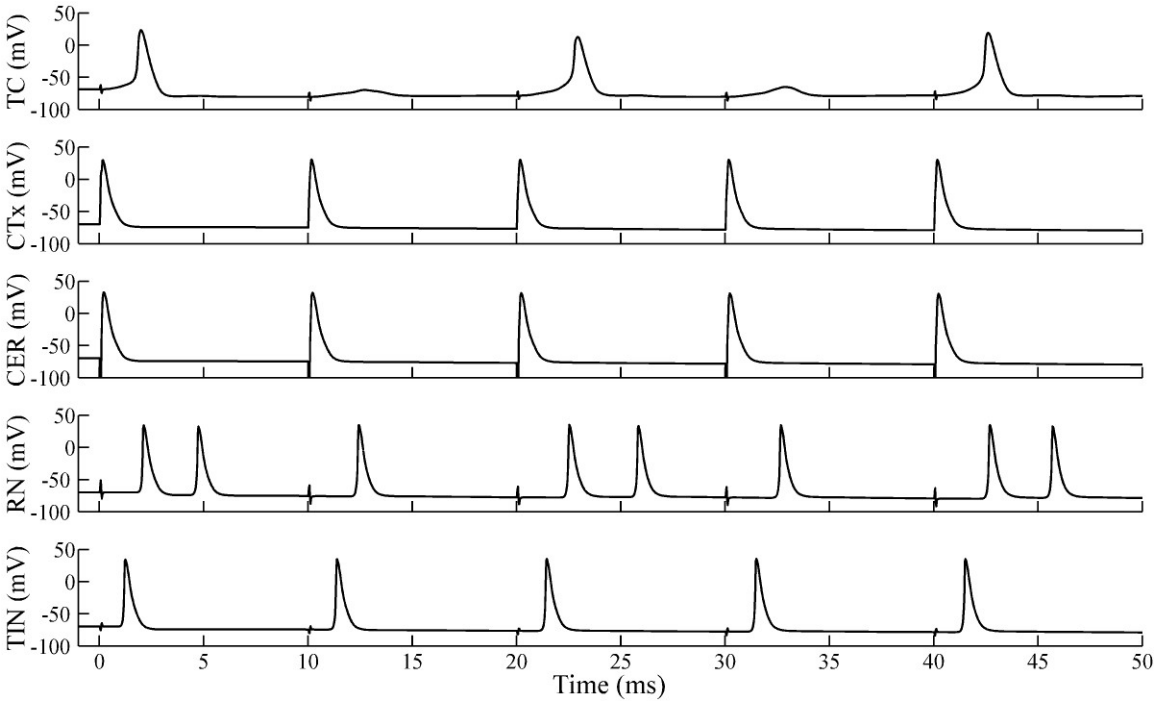

Figure 3.12: Transmembrane potential recordings from model neural elements (TC, CTx, CER, RN, and TIN) with DBS applied at time 0 with 3 V, 100 Hz, 50 μs/phase, and cathodic-phase first polarity.

The effect of synaptic transmission on network activity was investigated through measurement of transmembrane potentials from individual neural elements in the computational model (Fig. 3.12). For the neural unit shown, CTx and CER were activated directly by DBS, based on the short latency of excitation following each pulse

(~0.2 ms). This generated post-synaptic activation of TC at 2-3 ms, RN at ~2.5 ms, and TIN at ~1.5 ms. Finally, the excitatory connection from TC to RN resulted in subsequent post-synaptic excitation of the latter at 4-6 ms. We found that post-synaptic activation of TC was occasionally suppressed due to GABAergic inhibition from RN and TIN, and this depended on the latency of firing of the latter two elements. In another neural unit for which the RN input was removed, we did not observe this suppression of TC post-synaptic excitation (data not shown).

4. Measurement of evoked potentials during thalamic deep brain stimulation

4.1 Introduction

Deep brain stimulation (DBS) is an effective therapy for movement disorders, including essential tremor (ET) and Parkinson's disease (PD) (Benabid et al., 1991, Limousin et al., 1995, Gross and Lozano, 2000). To treat ET and tremor-dominant PD, the DBS electrode is typically implanted in the ventral intermediate (Vim) nucleus of the thalamus, and is connected to an implanted pulse generator (IPG) via a subcutaneous wire. There remains a lack of understanding of the mechanisms of action of DBS, and consequently, tuning of stimulation parameters is an *ad hoc*, empirical process. Parameter adjustment sessions are inconvenient, time-consuming, and costly (Ondo and Bronte-Stewart, 2005), and can result in sub-optimal clinical outcomes (Okun et al., 2005, Moro et al., 2006). Moreover, inappropriate parameter settings can lead to side effects (Limousin et al., 1995, Limousin et al., 1996, Hamani et al., 2005, Pahwa et al., 2006) and deplete the battery more quickly than optimized settings (Moro et al., 2002, Kuncel and Grill, 2004, Volkmann et al., 2006). An automated, rational approach to the selection of DBS parameters could reduce follow-up visits and improve patient outcomes.

Closed-loop DBS systems are one approach to automated selection and optimization of stimulation parameters. Neural activity measured during DBS may provide information related to symptoms, and both single-unit recordings and local field potentials (LFPs) have been proposed as feedback signals. Closed-loop DBS of the

globus pallidus interna (GPi), triggered from single-unit activity measured from the primary motor cortex (M1), generated greater motor symptom reduction in MPTP-treated monkeys than continuous, open loop stimulation (Rosin et al., 2011). However, this approach required implantation of additional hardware, and the long-term stability of microelectrode recordings may not be sufficient for clinical use (Williams et al., 1999). Alternatively, LFPs can be recorded from the DBS electrode, and reflect synchronized oscillatory neural activity (Brown and Williams, 2005). For example, theta oscillations recorded from the basal ganglia or thalamus may be related to tremor in PD and ET (Brown et al., 2001, Brown, 2003, Kane et al., 2009, Pedrosa et al., 2012), and anti-kinetic beta oscillations are elevated in the basal ganglia in PD (Priori et al., 2004, Marceglia et al., 2007, Bronte-Stewart et al., 2009) and are reduced by DBS (Brown et al., 2004, Wingeier et al., 2006, Bronte-Stewart et al., 2009). Proposed LFP-based closed-loop systems would titrate stimulation in response to changes in LFP activity (Burgess et al., 2010, Afshar et al., 2012), or select the most effective stimulation contacts and inform DBS voltage settings (Chen et al., 2006, Miyagi et al., 2009, Yoshida et al., 2010). However, further work is required to demonstrate that LFPs are derived from local sources, rather than volume conducted from other brain regions (Brown and Williams, 2005), and that there is causality between LFP activity and clinical symptoms (Priori et al., 2006, Smirnov et al., 2008, Tass et al., 2010).

In the present work we investigated the evoked compound action potential (ECAP) as a potential feedback control signal. The ECAP is generated by synchronous activation of an ensemble of neural elements near the electrode, and is recorded from two non-stimulating contacts on the DBS electrode implanted for therapy. ECAPs recorded from the DBS electrode during peripheral nerve stimulation were used to determine the electrode position during implantation (Hanajima et al., 2004, Valls-Sole et al., 2008). Further, ECAPs recorded from the cochlear nerve were dependent on stimulation parameters (Miller et al., 1998, Matsuoka et al., 2001, Briaire and Frijns, 2005, Macherey et al., 2008, Miller et al., 2008, van Wieringen et al., 2008, Westen et al., 2011), guided programming of stimulation levels (Miller et al., 2008, Jeon et al., 2010), and were proposed for use in closed-loop cochlear implants (Mc Laughlin et al., 2012). An ECAP-based closed loop DBS system could adjust stimulation settings automatically to generate activation of the appropriate neural elements.

We demonstrated previously the feasibility of recording ECAPs by reducing the stimulus artifact, which can otherwise mask or distort the physiological signal (**Chapter 2**), and ECAPs recorded in acute, preclinical experiments provided insight into the extent and types of neural elements activated during thalamic DBS (**Chapter 3**). However, it was not known whether high-fidelity ECAP signals could be recorded from humans in an acute or chronic state. The objectives of the present work were to determine whether ECAPs could be recorded during clinical DBS; to determine the

source of the ECAP and any artifact; to investigate changes in ECAP characteristics across DBS parameters; and to correlate ECAP characteristics with changes in tremor across DBS parameters.

4.2 Methods

We conducted intraoperative recordings of ECAPs in acute and chronic conditions and investigated correlations between ECAP characteristics and tremor across stimulation parameters. Computational modeling was used to determine the origin of the ECAP signal and stimulus artifact.

4.2.1 Human subjects

The protocol was reviewed and approved by the Institutional Review Boards at Duke University and Emory University, and subjects participated on a volunteer basis following written informed consent. The study was performed on 15 participants, 11 with ET, 3 with tremor-dominant PD, and 1 with Fragile X-associated tremor/ataxia syndrome (FXTAS) (Ferrara et al., 2009). We recruited patients who were either undergoing surgical implantation of the Medtronic 3387 DBS electrode in Vim (acute setting, n=7) or replacement of their battery-depleted IPG for Vim-DBS (chronic setting, n=8). Subjects undergoing IPG replacement surgery were asked to decline general anesthesia, so that they were responsive during the study, and sedation, which can otherwise reduce motor symptoms. Subjects undergoing DBS implantation are not normally given general anesthesia, and sedation was provided only as necessary so as to

minimize the effect on motor symptoms. Further, all subjects were asked to withhold anti-tremor and/or dopaminergic medications overnight prior to the experiment, and subjects that were unable to tolerate withholding medications were excluded from the study. Demographic information for the subjects is shown in Table 4.1. Subject EP13D was enrolled in the study but subsequently declined participation. Some patients reported transient paresthesias during stimulation delivered within the study. One adverse event unrelated to the study occurred: a postoperative reaction to antibiotics administered at the IPG site, which resolved uneventfully.

4.2.2 Intraoperative experimental setup

After implantation of the DBS electrode or removal of the battery-depleted IPG, external hardware for stimulation and recording was connected via a temporary, percutaneous extension cable to the DBS electrode. In subjects undergoing IPG replacement, the connection from the extension cable to the DBS brain lead was made through a Multi-Lead Trialing Cable (355531, Medtronic), and if necessary, a 1x4 Pocket Adapter (64001, Medtronic). For subjects undergoing electrode implantation, the connection to the DBS electrode was made through a Twistlock Screening Cable (3550-03, Medtronic).

ECAPs were recorded differentially from two non-stimulating contacts using three series amplifier stages (A_1, A_2, and A_3) and additional circuit components to reduce the stimulus artifact (Fig. 4.1A), as discussed in detail in **Chapter 2**. The amplifier gains

Table 4.1: Demographic characteristics for each subject. Asterisk (*) indicates that the subject underwent DBS electrode implantation surgery.

Subject	Age/Gender	Diagnosis	Mo. After Implant	Medications Taken Morning of Experiment
EP12A	65/M	ET	34	None
EP12B	73/M	ET	44	None
EP12C	68/M	PD	58	None
EP12D	73/F	ET	77	Fentanyl before surgery
EP12E	76/M	PD	40	None
EP13A	72/M	ET	74	Gabapentin, divalproex before surgery; fentanyl before/during surgery
EP13B*	74/F	ET	0	Primidone before surgery; fentanyl, dexmedetomidine, midazolam during surgery
EP13C*	73/F	ET with mild Parkinsonism	0	Primidone before surgery
EP13E*	64/M	FXTAS	0	Fentanyl during surgery
EP13F	74/M	PD	90	Isoflurane, dexmedetomidine during surgery
EP13G*	62/M	ET	0	Propofol during surgery
EP13H*	66/M	ET	0	Propofol during surgery
EP13I*	70/F	ET	0	Propofol, fentanyl during surgery
EP13J*	61/F	ET	0	Fentanyl before surgery; midazolam, propofol during surgery
EP13K	71/M	ET	176	Gabapentin before surgery

at each stage were set to ensure that amplifier saturation did not occur, and the signal was band-pass filtered at A_2 and A_3 using a low-pass cutoff of 10 kHz and a high-pass cutoff of 0.1 Hz (or 10 Hz, EP12A-D only). DBS was delivered through an isolated

stimulator (bp isolator, FHC) connected in series with two 100 μF capacitors, with stimulation pulses controlled via a high-speed digital-to-analog converter using a custom LabView program (National Instruments), which also controlled digital pulses to operate circuit components and sampled the ECAP at 80 kHz.

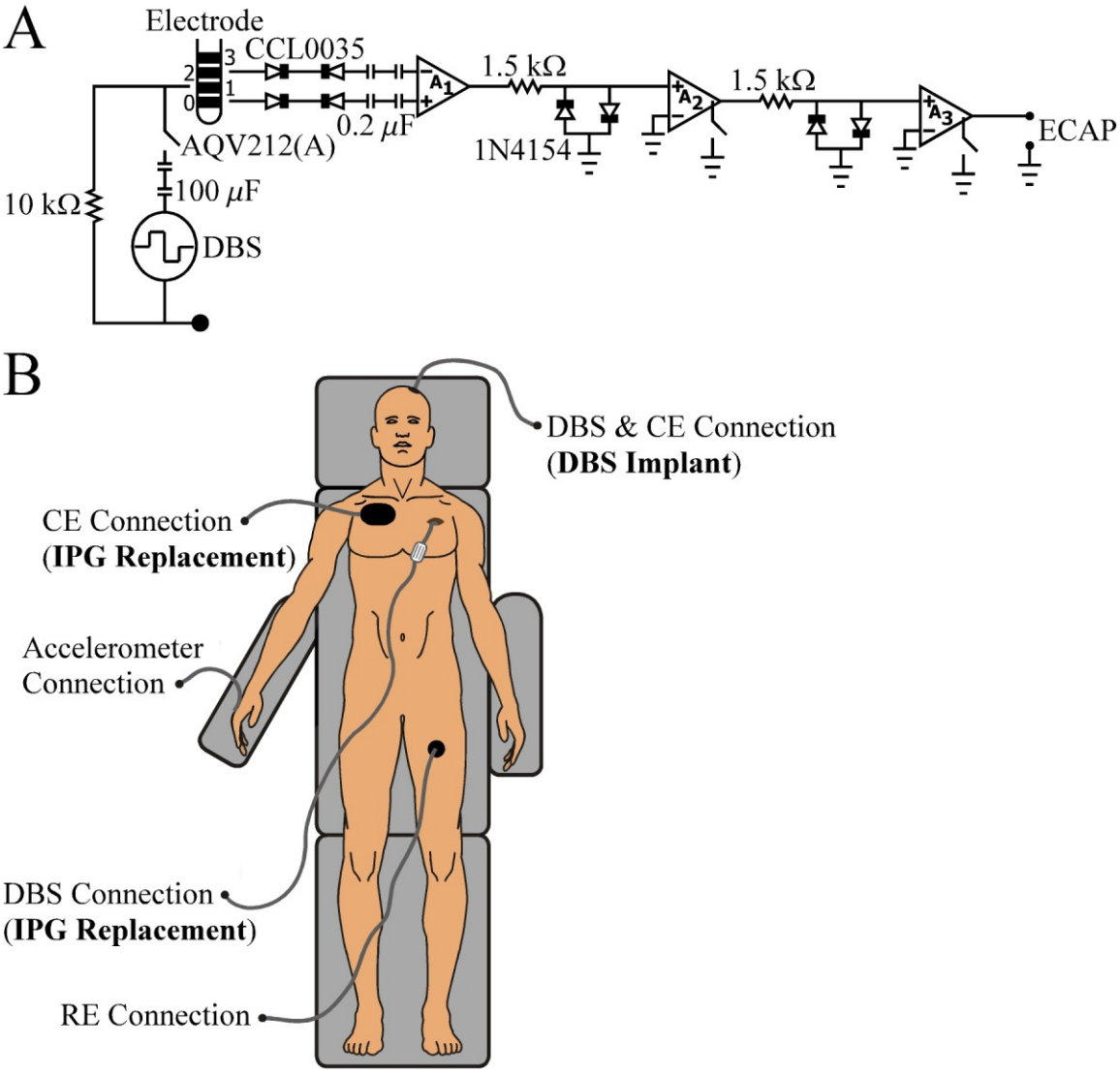

Figure 4.1: Intraoperative recording of ECAPs during DBS. A: Diagram of the recording instrumentation. Stimulation was delivered using a monopolar, AC-coupled configuration between a DBS contact and distant counter electrode. The

PhotoMOS relay (AQV212(A)) opened after each DBS pulse to limit discharge of capacitive charge from the electrode-tissue interface through the parallel 10 kΩ resistor, rather than through the low-impedance stimulator. ECAPs were recorded from the two contacts adjacent to the stimulating contact, and were amplified by a differential SR560 preamplifier stage (A_1) and two subsequent SR560 amplifier stages (A_2 and A_3), which also filtered the signal. To reduce the size of the stimulus artifact, anti-parallel diodes (IN4154) were placed at the inputs to A_2 and A_3, grounding the line if the voltage exceeded ±0.7 V, and the latter two stages were internally blanked during each pulse and the subsequent 60 μs. All amplifiers were AC-coupled at the front-end, either externally (A_1) or internally (A_2 and A_3), and anti-series current limiting diodes (CCL0035) were placed at the inputs to the first amplifier stage. Modified from (Kent and Grill, 2012). B: Diagram of subject positioning and electrode placement for the intraoperative study. For subjects undergoing IPG implantation surgery, the connection to the DBS lead was made through an incision in the chest, and the counter electrode (CE) was typically placed on the chest opposite the surgical site. Alternatively, for subjects undergoing DBS electrode implantation, the connection to the DBS lead was made through the cranial burr hole, and the CE was a retractor at the cranial burr hole or implant cannula. The recording reference electrode (RE) was typically placed on the thigh ipsilateral to stimulation. The accelerometer used for tremor measurement was taped to the hand contralateral to stimulation. Modified from (Swan et al., 2013).

DBS was applied unilaterally with symmetric, biphasic, voltage-regulated pulses. Charge densities were below the manufacturer's recommended limit of 30 μC/cm^2, using a conservative impedance estimate of 500 Ω. We used a monopolar stimulation configuration with symmetrical recording contacts to minimize the size of the artifact (**Chapter 2**). In choosing the hemisphere for stimulation in subjects that had or were receiving bilateral electrode implants, we considered the following: dominant hand, side with greater tremor symptoms with DBS *off*, and side with lower clinical amplitude and pulse width (IPG replacement subjects only). Further, we preferred the side that used a clinical stimulation configuration with contacts 1 or 2 (where contacts are labeled 0-1-2-3

Table 4.2: Clinical stimulation settings and experimental settings for each subject. For stimulation contacts, "C" corresponds to case return for the clinical settings, and a distant counter electrode for experimental settings. Degree symbol (°) indicates that the subject performed a counting task during tremor measurement.

	Clinical Settings				*Experimental Settings*		
Subject	**Voltage (V)**	**Frequency (Hz)**	**Pulse Width (μs)**	**Stim. Contacts**	**Stim. Contacts**	**Rec. Contacts**	**Arm Position During Tremor Measurement**
EP12A°	6.1	185	60	0-/1-/C+	1-/C+	0+/2-	Elbow flexed and unsupported, hand held near face, holding tape roll
EP12B°	4.1	145	90	1-/C+	1-/C+	0+/2-	Elbow extended and unsupported, arm ~30 deg above horizontal
EP12C	4.6	150	60	0-/1+	1-/C+	0+/2-	Elbow flexed 90 deg and unsupported
EP12D°	1.8	180	90	0-/C+	1-/C+	0+/2-	Elbow flexed and unsupported, hand held near face
EP12E	4.6	185	90	1-/2-/C+	2-/C+	1+/3-	Elbow extended and supported, arm parallel to horizontal
EP13A°	2.3	180	60	1-/2-/3+	1-/C+	0+/2-	Elbow extended and unsupported, arm parallel to horizontal
EP13B°	1	180	90	1-/0+	1-/C+	0+/2-	Elbow extended and unsupported, arm ~30 deg above horizontal
EP13C	1	180	90	1-/0+	1-/C+	0+/2-	Elbow flexed and supported, arm ~30 deg above horizontal
EP13E	1	180	90	0-/1+	1-/C+	0+/2-	Elbow extended and unsupported, arm ~45 deg above horizontal
EP13F°	4.6	90	60	0-/1-/3+	1-/C+	0+/2-	Elbow flexed and unsupported, arm perpendicular to horizontal
EP13G	2	180	90	1-/0+	1-/C+	0+/2-	Elbow flexed and unsupported, hand held near face
EP13H	1	180	60	2-/3+	1-/C+	0+/2-	Elbow flexed and unsupported, hand held near face, holding water bottle
EP13I°	1	180	90	1-/2+	1-/C+	0+/2-	Elbow flexed and unsupported, hand held near face, holding cup
EP13J	2	185	90	1-/2+	1-/C+	0+/2-	Elbow extended and unsupported, arm parallel to horizontal
EP13K	4.4	185	90	1+/2-/3-	2-/C+	1+/3-	Elbow extended and unsupported, arm parallel to ground

in the ventral-to-dorsal direction), as it was necessary to use one of these contacts in the monopolar stimulation – symmetrical recording configuration, and we sought to match the clinical configuration as closely as possible (Table 4.2). For subjects undergoing electrode implantation, clinical settings were determined by a neurologist during surgery as the parameters and contacts that maximized tremor reduction without side effects. The recording reference electrode (RedDot M2255, 3M) was placed on the skin, either on the chest opposite the surgical site (EP12A only) or the thigh ipsilateral to stimulation (Fig. 4.1B). For subjects undergoing IPG replacement, the stimulation counter electrode (StimCare Carbon Foam Electrode, Empi) was placed on the thigh (EP12A only) or the chest opposite the surgical site, and in subjects undergoing electrode implantation, the retractor at the cranial burr hole or implant cannula (EP13I and EP13J only) was used as the counter electrode.

We measured tremor with an accelerometer (5 V / 4 g sensitivity, CXL04LP3, Crossbow Technology) taped to the dorsum of the hand contralateral to stimulation. Accelerometer-based tremor measurements correlate well with clinical rating scales of tremor (Elble et al., 2006). Tremor was measured by having the supine subject hold their arm in a position that was pre-determined to maximize tremor, and with the wrist extended such that it was parallel with the forearm. The accelerometer measurement was sampled at 1 kHz.

4.2.3 Stimulation and measurement protocol

We measured ECAPs and tremor in single experimental sessions lasting approximately 45 min, or until the patient was fatigued. In the first phase of the experiment, we determined the maximum tolerable voltage with the experimental contact configuration by slowly increasing the amplitude up to 140% of the clinical voltage (V_{CLIN}). DBS was delivered for 5 s at 130 Hz with the clinical pulse width and cathodic-phase first polarity. In the second phase, we measured ECAPs and tremor across a range of stimulation parameters delivered in a randomized manner with both the subject and the experimenter who was interacting with the subject blinded. Frequencies were 10 Hz and 130 Hz, in which we typically tested only V_{CLIN} for the former and a range of amplitudes for the latter. However, if the subject had low tremor in DBS *off* conditions, a range of amplitudes was instead tested at 10 Hz. Amplitudes were 20%, 60%, 100%, and 140% of V_{CLIN}, but if a higher voltage was not tolerated in the first experimental phase, then we used 40% and/or 80% of V_{CLIN}. Additionally, we tested both cathodic- and anodic-phase first polarities, and pulse width was fixed at the clinical setting. Each trial within the block was 2 min in duration, with DBS *off* for the first minute (*baseline* period) and DBS *on* for the second minute (*stim* period) (Fig. 4.2A). At approximately 30 s into the *baseline* and *stim* periods, we measured the subjects' tremor for 20 s. Further, we recorded ECAPs in the *stim* period, either just when tremor was measured (EP12A-C only) or through the entire period. Depending on patient fatigue,

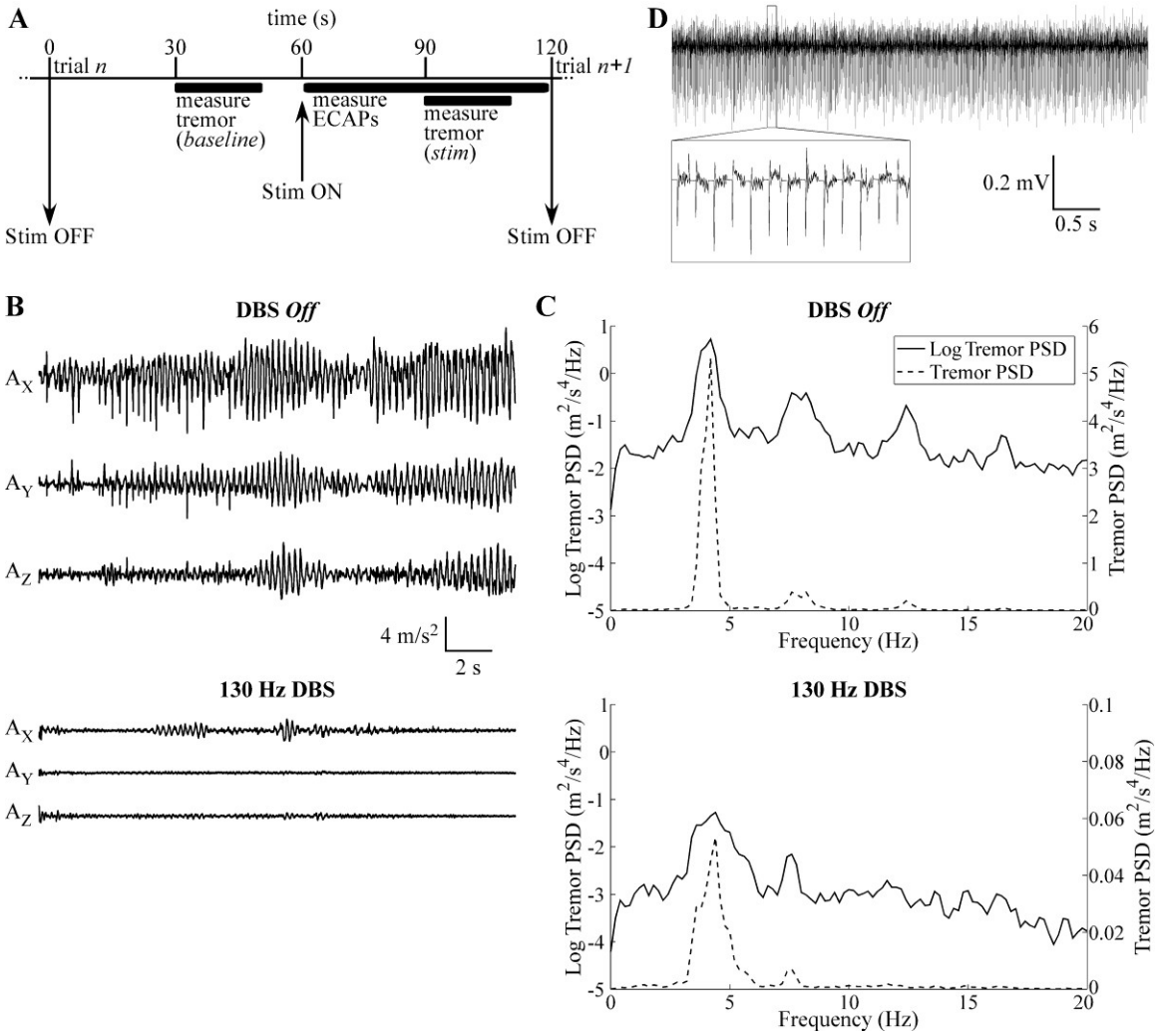

Figure 4.2: Intraoperative measurements of ECAPs and tremor. A: The timeline of each trial, in which ECAPs were measured during DBS (*stim*) and tremor was recorded during *baseline* and *stim* periods. Modified from (Birdno et al., 2012). B: Raw accelerometer measurements made for 20 s along the X-, Y-, and Z- axes for EP12E during 130 Hz DBS at V_{CLIN} with cathodic-phase first polarity, and in the preceding *baseline* period with DBS *off*. C: Power spectral density (PSD) of the tremor data from (B) on both a log scale, for comparison between DBS *off* and DBS *on* conditions, and a linear scale, for comparison of the relative magnitude of different peaks in the signals. D: Raw ECAP recording made from EP12D for 130 Hz DBS at V_{CLIN} with cathodic-phase first polarity.

we conducted a second block with different randomized presentation of stimulation parameters in some experiments. We were unable to complete the first block of the second phase in subjects EP13B, EP13C, and EP13J due to subject fatigue. A poor connection between the hardware and DBS electrode or between the reference electrode and skin in EP13C, EP13E, and EP13H led to low ECAP signal fidelity, and so no further analysis was conducted for these experiments.

4.2.4 Postoperative measurement of impedance

Following completion of the experiment, an IPG (Activa, Medtronic) was implanted (except in some patients undergoing DBS electrode implantation surgery), and post-operative electrode impedance measurements were taken with the Activa device. The Activa impedance measurement used trains of 0.7 or 1.5 V, 210 μs/phase, and 30 Hz, applied between pairs of contacts or between one contact and the IPG case. Impedance was measured at the beginning of the pulse, and since the double-layer capacitance of the electrode-tissue interface (ETI) is shorted at high frequencies (Wei and Grill, 2005), the impedance measurement was dominated by the tissue resistance.

4.2.5 Clinical data analysis

Tremor was analyzed by calculating the power spectral density (PSD) of the acceleration measured along each axis (A_X, A_Y, and A_Z). The acceleration signals were detrended using local linear regression (2 s window size, 1 s step size) (Fig. 4.2B), the PSD was calculated in MATLAB using the *psd* function (Welch's averaged periodogram,

Hanning window, fast Fourier transform (FFT) length of 5,000 samples) with corrected amplitude scaling (Fig. 4.2C), and tremor power was calculated in the X-, Y-, and Z-dimensions by integrating each spectrum over the 2-7 Hz band, to get P_X, P_Y, and P_Z (Kuncel et al., 2007). This band was chosen to exclude steady-state acceleration generated by gravity, and to include the fundamental frequency and first harmonic (Fig. 4.2C). Finally, we summed P_X, P_Y, and P_Z, and change in tremor was quantified for each of *n* trials as:

$$\text{Change in tremor} = \log_{10}\left(\frac{P_{n,stim}}{P_{n,baseline}}\right) \qquad \text{(Equation 4.1)}$$

where $P_{n,stim}$ was tremor power measured during the *stim* period of trial *n* and $P_{n,baseline}$ was that measured during the *baseline* period of trial *n*.

The ECAP was analyzed by calculating signal power in different ECAP phases, as described in **Chapter 3**. First, the raw ECAP signal (Fig. 4.2D) was stimulus-triggered averaged across the first 64 responses. Second, in experiments with a large stimulus artifact tail, we used a polarity averaging technique common in cochlear ECAP recording (Brown and Abbas, 1990), in which responses recorded with opposite polarities (but other stimulation parameters identical) were averaged together. The artifact was expected to be inverted for opposite stimulation polarities and was removed with this technique, whereas the ECAP response was expected to be similar for opposite polarities with symmetric, biphasic DBS pulses and so was relatively unaffected by polarity averaging (**Chapter 3**). Third, any signal offset was calculated as the average of

the final 1 ms of signal and subtracted. Finally, we squared the signal and integrated across distinct ECAP phases. The resulting signal energy measure accounted for both the magnitude and duration of the phases.

Pearson correlation coefficients were calculated for linear regressions between tremor and ECAP signal energy values. One-tailed t-tests were performed to determine whether the slope of the regression was significantly different from zero (α=0.05), and the slope was expected to be negative for 130 Hz DBS and positive for 10 Hz DBS.

4.2.6 Computational model of ECAP recording during thalamic DBS

A computational model of thalamic DBS was used to calculate the ECAP and corresponding neural element activation, and thereby determine the origin of the recorded signal. This three stage model was discussed in detail in **Chapter 3**, and is reviewed briefly here.

The first stage of the model used the finite element method (FEM) to calculate the potentials generated by a three-dimensional representation of the DBS electrode within brain tissue (Fig. 4.3A). A clinical DBS electrode was placed within a prism representation of the Vim thalamus (Birdno et al., 2012), all encompassed within a cylindrical representation of surrounding brain tissue with height and diameter of 190.5 mm. The conductivity of brain tissue was $0.\overline{3}$ S/m (Moffitt and McIntyre, 2005), and that of the DBS contact and insulation were 5×10^{6} S/m and 1×10^{-13} S/m, respectively (Yousif et al., 2008a).

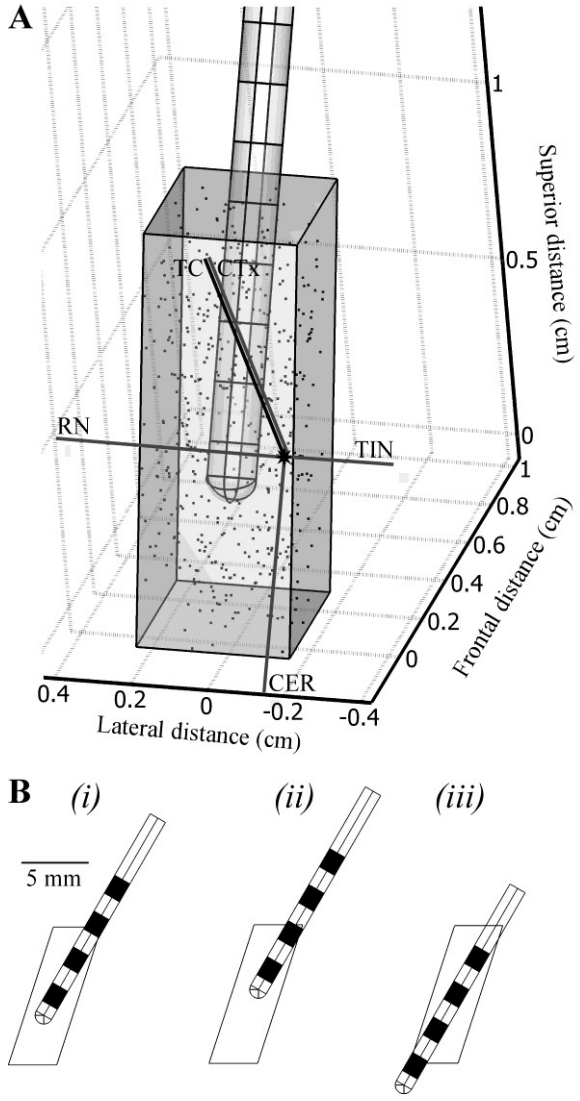

Figure 4.3: Computational model of ECAP recording during thalamic DBS. A: The FEM model included a three-dimensional representation of the DBS electrode within a prism representation of the Vim thalamus, all encompassed within a large volume representing surrounding brain tissue (not shown). The model contained 500 thalamocortical (TC) neurons, with soma locations indicated by the dots, and pre-synaptic inputs from the cortex (CTx), cerebellum (CER), reticular nucleus (RN) and thalamic interneurons (TIN). The anatomical locations of the elements are shown for one neural unit, with the TC neuron and pre-synaptic inputs represented by the black shapes and gray lines, respectively. Modified from (Kent and Grill, 2013). B: FEM geometry of different electrode positions within Vim, including the (i) original position from (Birdno et al., 2012), (ii) a more dorsal position, and (iii) a more ventral position. The geometries are shown from a lateral view.

In the second stage, multi-compartment cable models with appropriate geometrical and ion channel representations of the dendrites, soma, and axon of 500 thalamocortical (TC) neurons were randomly distributed in the thalamic nucleus, along with axonal inputs from the cortex (CTx), cerebellum (CER), reticular nucleus (RN), and thalamic interneurons (TIN) (Birdno et al., 2012). The model included excitatory glutamatergic synaptic connections to TC neurons from CTx and CER, inhibitory GABAergic synapses from RN and TIN, and 1:1 excitatory synapses (one input spike corresponded to one time delayed output spike) from CTx and CER to TIN, and from CTx and TC to RN (Fig. 3.2B). The voltages calculated in the FEM model were interpolated at the neural element compartment locations, scaled to match the desired DBS amplitude, and applied to elements as a stimulation train with a specified frequency, pulse width, and polarity. Transmembrane potentials were measured over time to detect neural activation, and transmembrane currents were measured in all neural compartments within the population to calculate the ECAP signal in the third stage of the model. The simulation time was 1.5 s, with a pre-stimulation period of 0.5 s and a 25 μs time step.

The third stage employed the reciprocity theorem to calculate the differential voltage across the two DBS recording contacts generated by neuronal transmembrane currents over the course of the simulation (Helmholtz, 1853, Moffitt and McIntyre, 2005). The FEM model described in the first stage was solved with a unit current placed at the

boundary of one recording contact, and the resulting potentials were measured at the neural compartment locations. This was repeated for the second recording contact. The resulting scale factors were used to calculate potentials at the recording contacts for a given transmembrane current amplitude. The magnitude of the model-generated ECAP signal was scaled by 364 to account for the cell density of 1,300 cells/mm^3 derived from (Hirai et al., 1989). This signal was then filtered with two cascaded first-order 10 Hz - 10 kHz bandpass filters to replicate experimental filtering, the stimulus artifact was removed using a template subtraction method in which the artifact was calculated using a sub-threshold stimulus (Briaire and Frijns, 2005), and stimulus-triggered averaging was applied 8 times.

Model outcomes included ECAP signals and measurements of neural activation, and were compared across different electrode positions (Fig. 4.3B). The monopolar symmetric configuration was used, with DBS applied at contact 1 using a range of amplitudes, 10 and 130 Hz frequency, 50 μs/phase pulse width, and both cathodic- and anodic-phase first polarities, and differential ECAP recordings were made from contacts 0 and 2. In addition to recording the composite ECAP generated by all neural elements, we selectively measured the ECAP contribution derived from activation of distinct types of elements within the population (i.e., TC, CTx, CER, RN, or TIN). Finally, we analyzed the percentage activation of each type of neural element that fired an action potential in 0.1 ms bins following the stimulus pulse.

4.2.7 Modeling the stimulus artifact

Computational modeling was also conducted to investigate how changes in the properties of the tissue or ETI affected the size of the stimulus artifact. Two models were constructed, one using an electrical circuit equivalent of the recording setup and the second using a FEM model to determine the effect of heterogeneity in tissue conductivity.

The electrical circuit equivalent model was implemented using PSpice (Cadence OrCAD Capture CIS v16.3). This model represented the tissue medium, ETI, DBS voltage source, and components of the recording instrumentation used for ECAP measurement (Fig. 2.2). The development of this model, and validation against artifact waveforms recorded experimentally *in vitro* and *in vivo*, was discussed in detail in **Chapter 2**, and is reviewed briefly here. DBS was delivered using the monopolar symmetric configuration between contact 1 and a distant return electrode, and contacts 0 and 2 served as inputs to an AC-coupled recording amplifier, with input impedance matching that of the amplifier used experimentally. Stimulation parameters were 1 V, 10 and 130 Hz, 50 μs/phase, and cathodic-phase first polarity. A relay was placed between the voltage source and stimulating contact, with operational timing matching that used experimentally, and with an *on* resistance of 0.83 Ω. The ETI was modeled as a parallel double-layer capacitance (C_{DL}) and Faradic resistance (R_F) with values derived from literature (Wei and Grill, 2009). The circuit values used in the initial iteration of the

model are provided in Table 4.3. The PSpice model solved for the differential voltage across the amplifier impedance over time to calculate the stimulus artifact.

Table 4.3: Electrical circuit equivalent model parameters.

Parameter	Value
Interface double-layer capacitance (C_{DL})	1.56 μF
Interface Faradaic resistance (R_F)	1.50 kΩ
Volume resistance between contacts 0 & 1 (R_{V01})	1200.80 Ω
contacts 1 & 2 (R_{V12})	1218.69 Ω
contact 0 & return (R_{V0})	764.70 Ω
contact 1 & return (R_{V1})	773.52 Ω
contact 2 & return (R_{V2})	770.83 Ω
Volume capacitance between contacts & return (C_V)	23.21 nF

The DBS contacts and return were electrically interconnected by impedance representations of neural tissue, including properties of bulk resistivity and permittivity. The PSpice bulk volume resistivity (R_V) values between each contact and the distant return, as well as between contact pairs, were calculated using COMSOL Script v1.2 (COMSOL). A three-dimensional geometrical representation of the clinical DBS electrode was placed within a spherical volume conductor with a radius of 8.75 cm, representing the boundary of the head, and with contact 1 centered in the volume. The conductivity of the brain tissue and DBS electrode matched those used in the thalamic DBS model discussed previously. The resistance values were calculated by applying voltage boundary conditions at the contact(s), measuring the normal current across the contact surface, and using Ohm's law. The mesh density was sufficiently high, as doubling the number of elements changed the calculated resistance values by <2.8%.

The permittivity of the brain tissue was represented by capacitors in parallel with the resistors between each contact and the distant return (Butson and McIntyre, 2005). The capacitance of the volume (C_V) was calculated by considering the geometry of the DBS contact within the volume conductor as two concentric spherical conducting shells, given by Equations 2.1 and 2.2 (Young and Freedman, 2004). The dielectric constant (K) was initially set to 3×10^5.

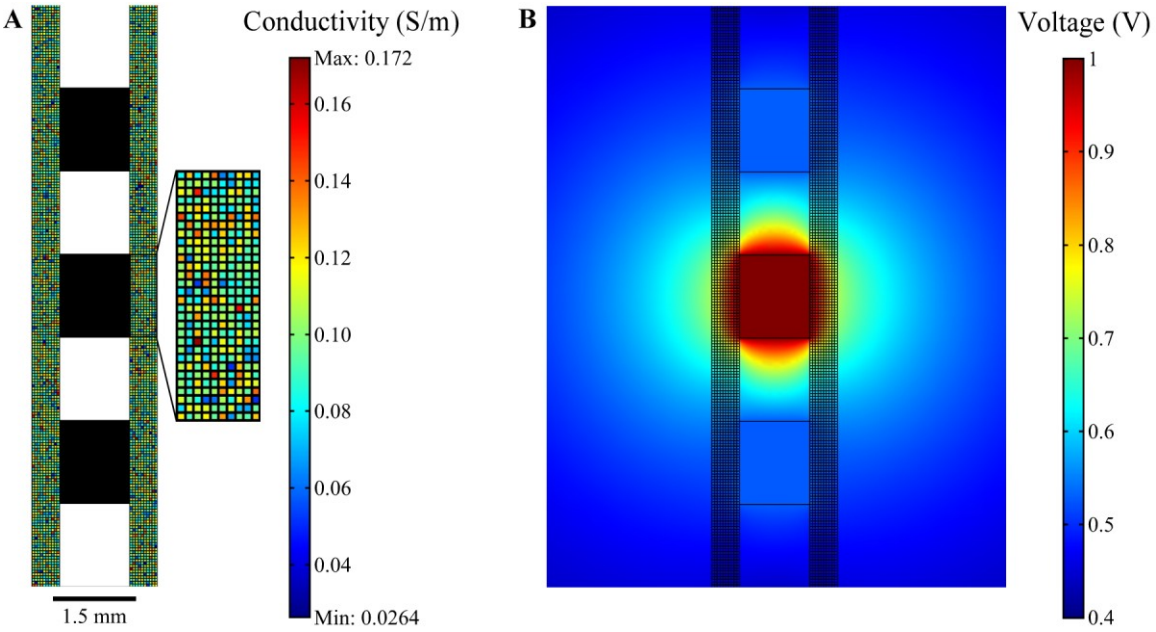

Figure 4.4: Two-dimensional FEM model of the DBS electrode within heterogeneous brain tissue. A: The peri-electrode space was represented using a checkerboard arrangement, with each square having a random conductivity value (refer to color bar legend), and the remaining brain tissue conductivity was fixed. The average conductivity of the peri-electrode space was 0.1±0.02 S/m (mean ± SD) in the figure. The DBS electrode is shown with contacts filled in black. The boundary of the surrounding tissue is not shown. B: FEM voltage solution resulting from a 1 V boundary condition at contact 1 using the conductivity values shown in (A).

A FEM volume conductor model was implemented in COMSOL Script to determine the effect of heterogeneity in tissue conductivity on the artifact (Fig. 4.4). A two-dimensional representation of the clinical DBS electrode was placed within a square volume conductor with 63.5 cm length and with contact 1 centered in the volume. The model included a representation of the peri-electrode space (Yousif et al., 2008b) with thickness of 100-1000 μm (Butson et al., 2006) divided into a checkerboard arrangement (Fishler, 1998), with each square division having 25-100 μm length. The conductivity of each square could be set independently, and random spatial variability was introduced by drawing conductivity values from a normal distribution with mean of $0.05 - 0.\overline{3}$ S/m (Butson et al., 2006) and standard deviation (SD) of 0-0.05 S/m (Fig. 4.4A). For each mean conductivity value, a limit was set on the maximum SD to avoid generating negative conductivity values. Outside of the peri-electrode space, the tissue conductivity was fixed at $0.\overline{3}$ S/m, and the conductive properties of the DBS electrode matched those used in the models described previously. The model was solved by setting a 1 V boundary condition at contact 1 and grounding the outer boundary of the volume conductor (Fig. 4.4B). The differential voltage generated at the boundaries of recording contacts 0 and 2 was calculated as a measure of the artifact magnitude. For each parameter variation, the artifact magnitude was measured across ten replicate trials, each time drawing a new distribution of conductivity values in the peri-electrode space. Sensitivity analysis indicated that the volume conductor was sufficiently large, as doubling the size changed

the calculated artifact magnitude by <7.5%, and the mesh density was sufficient high, as doubling the number of elements changed the magnitude by <0.04%.

4.3 Results

ECAPs were recorded during thalamic DBS and correlated with tremor. 130 Hz DBS was effective in reducing tremor (Figs. 4.2B,C) and 10 Hz DBS exacerbated tremor except in EP12D, EP13A, EP13F, and EP13J. Administration of sedatives or anesthetics in these studies may have limited the expected exacerbation of tremor (Table 4.1). Similarly, no tremor was observed in the DBS *off* condition in several subjects, presumably resulting from a transient microlesion effect in patients undergoing electrode implantation surgery or from administration of sedatives or anesthetics. If tremor was determined to be minimal in the DBS *off* condition at the start of the experiment, the subject was asked to perform a counting task during each tremor measurement (Table 4.2) and/or DBS was delivered predominately with a 10 Hz frequency (EP12B and EP13E) to exacerbate tremor (Table 4.4). Subsequently, computational models were used to investigate the neural origin of the ECAP signal and the source of the stimulus artifact recorded in some experiments.

4.3.1 ECAP measurement and characterization

We studied the effect of stimulation polarity, amplitude, and frequency on the ECAP during intraoperative DBS (Fig. 4.5). The waveform included a primary negative phase (N1), followed by a primary positive phase (P1), secondary negative phase (N2),

and in some cases, a secondary positive phase (P2). The ECAP was similar for opposite polarities with symmetric, biphasic stimulation waveforms, as expected from prior work in **Chapters 2 & 3**. The magnitude of the ECAP phases generally increased with higher DBS amplitudes, particularly the N1 and P1 phases (Fig. 4.5A). Nevertheless, this trend was not always sustained, as exceeding the clinical voltage led to a decrease in N1 for EP12D with anodic-phase first polarity, and a decrease in P1 with both polarities. Reducing DBS frequency from 130 Hz to 10 Hz increased the magnitude of P2 for anodic-phase first polarity, decreased N1, and had an ambiguous effect on P1 (Fig. 4.5B).

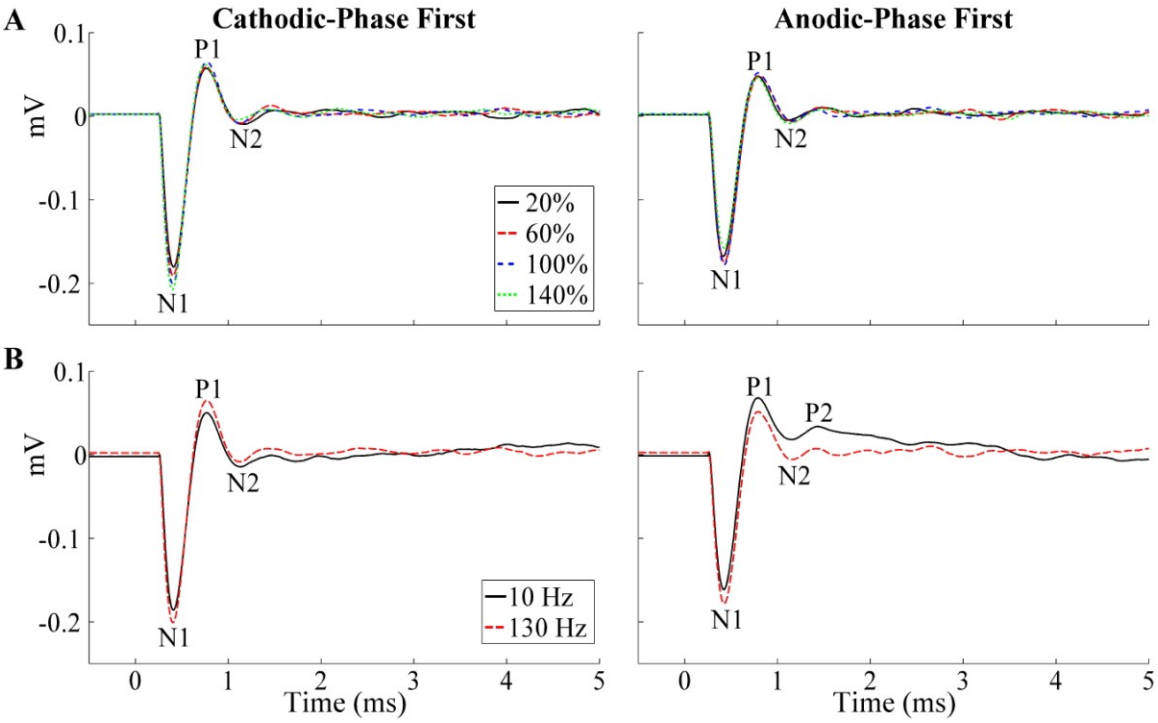

Figure 4.5: Stimulus-triggered average ECAPs recorded during thalamic DBS across stimulation parameters in EP12D. The ECAP phases are labeled. A: Effect on ECAPs of stimulation amplitude, provided as a percentage of V_{CLIN}, and shown for both cathodic- and anodic-phase first polarities. B: Effect on ECAPs of stimulation frequency, shown for both polarities at V_{CLIN}.

Recording ECAPs was technically challenging due to the presence of a stimulus artifact, which had variable amplitude between experiments (Fig. 4.6). The ECAP was recorded without any artifact in EP12D (chronic) as well as EP13B and EP13I (acute), and there was a small residual artifact in EP13G and EP13J (acute). A relatively large artifact tail was observed in all remaining experiments except EP12E, for which amplifier blanking was not used (because of an offset present during the blanking period), and the two artifact phases corresponded to the two phases of the DBS waveform. Therefore, low artifact recordings were obtained in all 4 acute experiments (excluding experiments with poor signal fidelity), but in just 1 of 7 chronic experiments (Table 4.4). Averaging the responses for opposite stimulation polarities cancelled out the stimulus artifact, and revealed an underlying ECAP signal in EP12A and EP12B that otherwise overlapped with the artifact tail. There were negligible ECAP responses even after polarity averaging in EP12C, EP12E, EP13A, EP13K, and EP13F, except at an amplitude 20% of V_{CLIN} for the latter.

When present, the ECAP had a consistent waveform shape, with N1-P1-(N2-P2) phases, where N2 and/or P2 were not always present (Fig. 4.6). Across subjects and DBS parameters, the peak-to-peak ECAP magnitude ranged from 0.17-1.48 mV, and for a fixed DBS voltage (~1 V), was larger in the acute condition (range of 0.40-1.33 mV) than in the chronic condition (range of 0.17-0.35 mV). The latency range for the different ECAP phases were: N1 at 0.21-0.43 ms, P1 at 0.35-0.8 ms, N2 and P2 (when present) at

Table 4.4: ECAP and tremor recording conditions and outcomes across subjects.

Subject	Recording Condition	ECAP Recording Fidelity	Tremor Presence with DBS *Off*, Response to DBS
EP12A	Chronic	ECAP present with large artifact	High, reduced at 130 Hz
EP12B	Chronic	ECAP present with large artifact	Low, exacerbated at 10 Hz
EP12C	Chronic	Large artifact	High, reduced at 130 Hz
EP12D	Chronic	ECAP present	Low, reduced further at 130 Hz
EP12E	Chronic	No amplifier blanking	High, reduced at 130 Hz
EP13A	Chronic	Large artifact	Low, DBS largely ineffective
EP13B	Acute	ECAP present	Low, reduced further at 130 Hz
EP13C	Acute	Poor fidelity due to bad connection	High, reduced at 130 Hz
EP13E	Acute	Poor fidelity due to bad connection	Low, exacerbated at 10 Hz
EP13F	Chronic	Large artifact	High, reduced at 130 Hz
EP13G	Acute	ECAP present with minimal artifact	High, reduced at 130 Hz
EP13H	Acute	Poor fidelity due to bad connection	Low, reduced further at 130 Hz
EP13I	Acute	ECAP present	Low, DBS largely ineffective
EP13J	Acute	ECAP present with minimal artifact	High, reduced at 130 Hz
EP13K	Chronic	Large artifact	High, reduced at 130 Hz

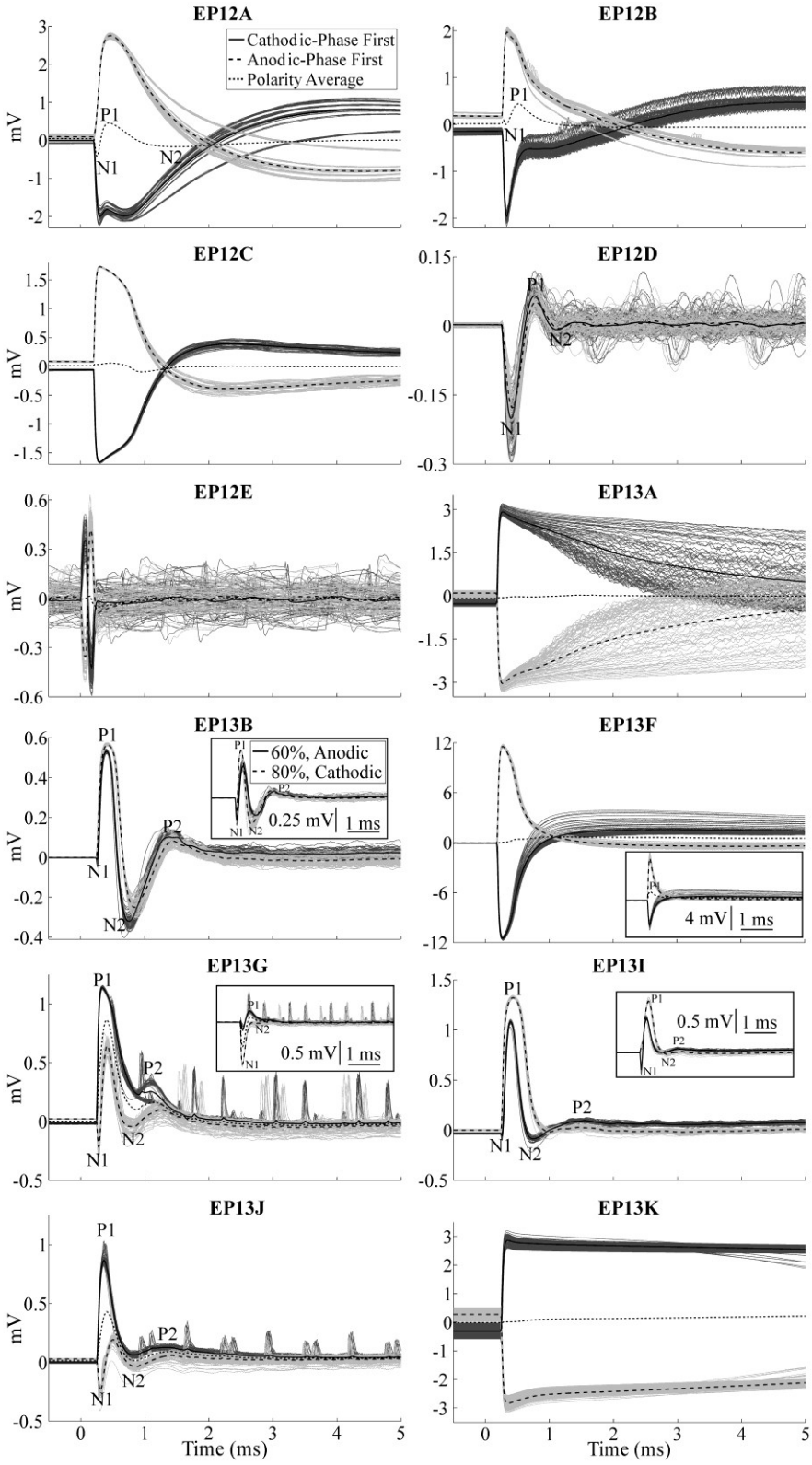
EP12A
Cathodic-Phase First
Anodic-Phase First
Polarity Average
P1
N1
N2
EP12B
EP12C
EP12D
EP12E
EP13A
EP13B
60%, Anodic
80%, Cathodic
0.25 mV
1 ms
EP13F
4 mV
EP13G
0.5 mV
EP13I
EP13J
EP13K
mV
Time (ms)

Figure 4.6: ECAP waveforms recorded during thalamic DBS across subjects who were undergoing either IPG replacement surgery or DBS implantation surgery. Stimulus-triggered average ECAPs are shown in the bold traces, and single responses are shown as the dark and light gray traces for cathodic- and anodic-phase first polarities, respectively. Other DBS parameters were 130 Hz frequency and an amplitude equal to V_{CLIN}, except for EP12C, EP13J, and EP13K for which ECAPs are shown with an amplitude that was 60%, 40%, and 80% of V_{CLIN}, respectively, and was the maximum tested in that experiment. For experiments in which a relatively large artifact was present, the responses for cathodic- and anodic-phase first polarities were averaged. When present, the ECAP phases are labeled. The insets for EP13B, EP13G, and EP13I show ECAP responses for voltages below V_{CLIN}, with cathodic- and anodic-phase first polarities, as well as the polarity average (EP13G only), to demonstrate a more apparent N1 phase. Similarly, the inset for EP13F shows responses for voltages at 20% of V_{CLIN} for cathodic- and anodic-phase first polarities, and the polarity average, to demonstrate the presence of a P1 phase.

0.68-1.98 ms. The N1 phase was not as marked in EP13B, EP13G, EP13I, or EP13J (acute recordings) at the clinical voltage, but was more evident at lower amplitudes (see insets). There were non-monotonic relationships between the signal energy of different ECAP phases and DBS amplitude (Fig. 4.7, rows 1-4). We also found increases in the magnitude of secondary phases as DBS frequency was reduced from 130 Hz to 10 Hz (Fig. 4.7, row 5).

4.3.2 Correlation between tremor and ECAP characteristics

We quantified the relationship between tremor and ECAP characteristics across subjects (Fig. 4.7). With near statistical significance, tremor was negatively correlated with N1 phase energy at 130 Hz for EP12D ($R=0.6$, $P<0.078$) and positively correlated at 10 Hz for EP12B ($R=0.86$, $P<0.068$). Similarly, tremor was negatively correlated with P1 phase energy at 130 Hz for EP12D ($R=0.65$, $P<0.058$), and with secondary phase energy at

130 Hz for EP13G (R=0.87, P<0.067). Finally, the energy of secondary phases was greater at 10 Hz compared to 130 Hz at the clinical voltage for EP12B and EP12D, and this was correlated to increases in tremor with near statistical significance (R=0.69, P<0.061).

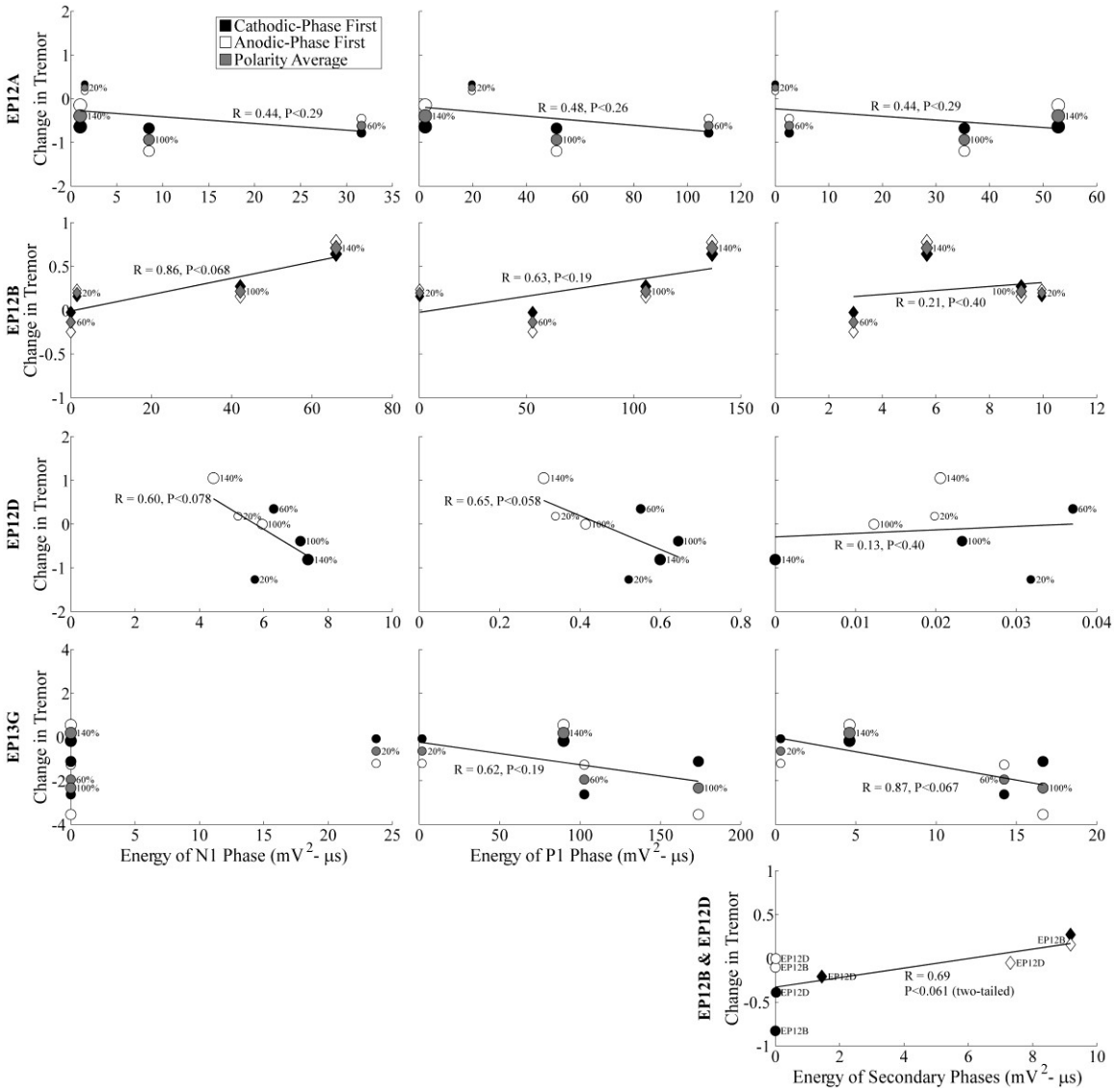

Figure 4.7: Relationship between changes in tremor and ECAP characteristics across stimulation parameters. ECAP characteristics were analyzed by calculating the signal energies of the N1 phase (left column), P1 phase (middle column), and secondary phases (right column). Measurements were made across DBS amplitudes, indicated both by the size of the marker and the adjacent text showing amplitude as a

percentage of V_{CLIN}, and DBS frequencies, including either 130 Hz or 10 Hz shown with circle and diamond markers, respectively. Further, these data are shown for cathodic- and anodic-phase first polarities with black and white fill color, respectively. For experiments requiring polarity averaging of the ECAP signal due to the presence of a stimulus artifact, one value of the ECAP characteristic is given for both stimulation polarities, and the average of the corresponding tremor measurements across polarities is shown with the gray fill color. Change in tremor was defined in Equation 4.1, such that negative values corresponded to reductions in tremor from baseline, and positive values corresponded to tremor exacerbation. Tremor data was not recorded for EP12D at 130 Hz DBS frequency, 60% of V_{CLIN}, and anodic-phase first polarity, and so the data point is not shown. Despite successful ECAP recording, data is not provided for EP13B and EP13J because a full trial block was not completed, and for EP13I because no tremor was evident in the DBS *off* condition. The bottom row shows data collected for both EP12B and EP12D at V_{CLIN} with 10 and 130 Hz DBS frequency and both stimulation polarities. EP12A was not included in this plot since both polarities were not tested at 10 Hz in this subject, and EP13G was not included because of the large relative values for change in tremor. Linear regressions were calculated between tremor and ECAP measures, using the polarity average (gray fills) when applicable.

4.3.3 Neural origin of the ECAP response

A computational model of thalamic DBS was used to determine the neural origin of the clinical ECAP response. Modeling the DBS electrode in its original position within Vim (Birdno et al., 2012) resulted in an initial positive ECAP (P1-N1-P2-N2), rather than the initial negative ECAP (N1-P1-(N2-P2)) observed in clinical recordings (Fig. 4.8A). Shifting the position of the clinical electrode along its axis by 2 mm in a dorsal direction or 6 mm in a ventral position, such that contacts 1 or 0 were at the dorsal or ventral border of the nucleus, respectively, resulted in an ECAP waveform that was more similar to the experimental signal (Figs. 4.3B, 4.8A). The former had a N1-P2-N2 waveform shape (P1 not present), whereas the latter had the P1-N1-P2-N2 waveform, but with a relatively small P1 phase. There was a negligible effect when DBS frequency

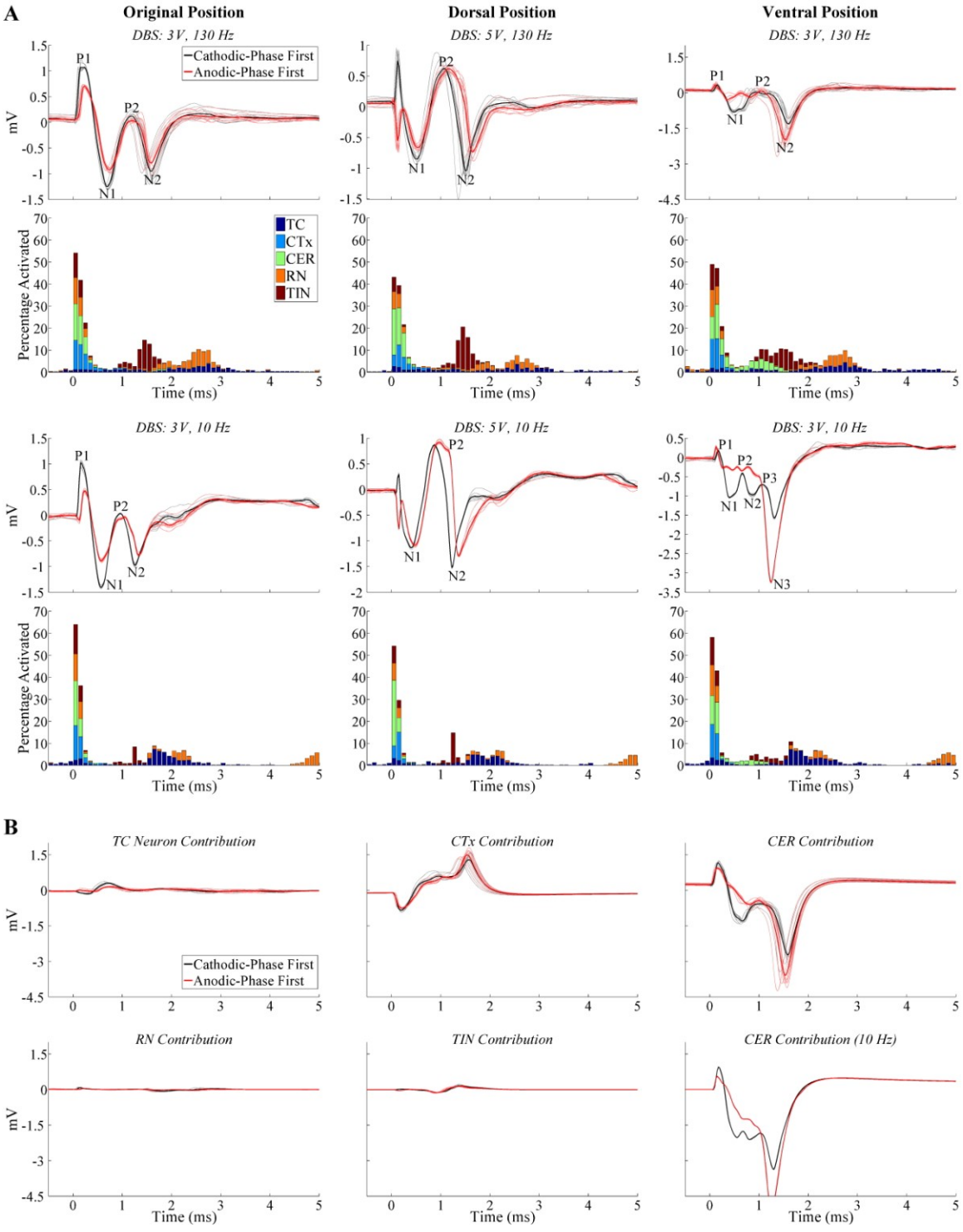

Figure 4.8: ECAP responses calculated with the model of thalamic DBS. A: Model responses for different relative electrode positions within the thalamus (refer

to Fig. 4.3B), including the original position (left column), dorsal position (center column), and ventral position (right column). ECAPs are shown for both cathodic- and anodic-phase first polarities, and the corresponding percentage activation of each neural element type in 0.1 ms bins following DBS pulses is shown for cathodic-phase first polarity. DBS amplitudes for each subplot were varied to generated similar percentage activation, DBS frequencies were 130 or 10 Hz, and pulse width was fixed at 50 μs/phase. The stimulus-triggered ECAP and single responses are shown in the bold and light traces, respectively, and ECAP phases are labeled. A small stimulus artifact remained with the dorsal electrode position following artifact template subtraction, observed as the initial inverted phases for opposite stimulation polarities. B: The contribution of different neural element types to the composite ECAPs recorded with the ventral electrode position at 3 V. The DBS frequency was 130 Hz, unless otherwise designated.

was reduced from 130 Hz to 10 Hz except with the DBS electrode positioned ventrally, for which there was a polarity-dependent effect on secondary phases, as seen experimentally (Fig. 4.5B).

The neural origin of the ECAP signal was determined by analysis of the temporal pattern of neural excitation (Fig. 4.8A) and by measuring the ECAP contribution from activation of distinct types of elements within the population (Fig. 4.8B). For 130 Hz DBS, direct activation of neural elements occurred within ~0.9 ms from the start of the DBS pulse, whereas post-synaptic activation of TC, RN, and TIN occurred within ~0.9-3.3 ms from the start of the pulse. Additionally, with the electrode in the ventral position, CER activation occurred as late as 1.6 ms. This extended CER activation resulted from direct stimulation, since CER received no synaptic input, and occurred in elements located dorsally within the thalamic nucleus. This long latency CER activation, and corresponding ECAP contribution, resulted from the delay for action potential

propagation from the initiation site (near the stimulating contact in ventral Vim) to the proximal node of Ranvier where activation was detected. Reducing DBS frequency from 130 Hz to 10 Hz shifted timing for direct activation to earlier latencies, reduced post-synaptic activation of RN and TIN, and decreased the latency and increased the synchronization of post-synaptic TC cell activation (i.e., less temporal dispersion of activation times). Recording from different neural elements revealed their respective contributions to the ECAP for a ventral electrode position, with direct activation of CER inputs generating the dominant contribution to the P1-N1-P2-N2 waveform (Fig. 4.8B). Contributions from direct excitation of CTx reduced the magnitude of P1, N1, and N2, and shifted P2 to more positive voltages. The contributions to the ECAP of TC and TIN elements were relatively small, and those of RN were negligible. Lastly, the frequency effect observed in the composite ECAP was generated by changes in the contribution from CER inputs at 130 Hz versus 10 Hz DBS. The DBS frequency effect was relatively small for contributions from other types of elements (data not shown).

4.3.4 Origin of the stimulus artifact

The stimulus artifact observed in all experiments except EP12D, EP13B, and EP13I may have resulted from tissue inhomogeneity and corresponding impedance imbalances between the stimulation electrode and each recording contact. Across chronic and acute experiments in which impedance was measured, there was a difference in impedances between the experimental stimulation contact and each

recording contact of 28±10% (mean ± SE, n=7) and 6.1±3.4% (n=3), respectively, calculated by normalizing to the average of the two impedance values. This larger imbalance in chronic experiments would be expected to increase the differential voltage measured between the two recording contacts during each stimulus pulse, resulting in larger artifacts. However, we did not detect any trend across chronic experiments between the percentage impedance imbalance and the artifact magnitude.

Two computational models were implemented to understand better the sources of the stimulus artifact. An electrical circuit equivalent was used to compare the stimulus artifacts with the initial parameter set (Table 4.3) to those after alteration of the ETI or bulk tissue properties (Fig. 4.9). Adding a highly resistive glial encapsulation layer of 0.1 S/m conductivity and 500 μm thickness (Haberler et al., 2000, Moss et al., 2004, Butson et al., 2006) around the electrode (in the FEM model stage) increased R_{V01} and R_{V12} by ~36% and R_{V0}, R_{V1}, and R_{V2} by ~5%, and consequently increased the artifact magnitude and duration (Fig. 4.9A). Introducing impedance imbalances between the stimulation contact and each recording contact by decreasing R_{V01} and increasing R_{V12} by 5 or 10% increased the artifact magnitude by ~9 and 17 times, respectively (Fig. 4.9B). After altering the dielectric constant within the physiological range between 1×10^4 and 1×10^6 (Schwan and Kay, 1957, Foster and Schwan, 1989), for C_V values of 0.77 to 77.36 nF, we found that greater tissue permittivity increased the artifact duration (Fig. 4.9C). Other alterations made to the model, including doubling and halving C_{DL} or R_F, or

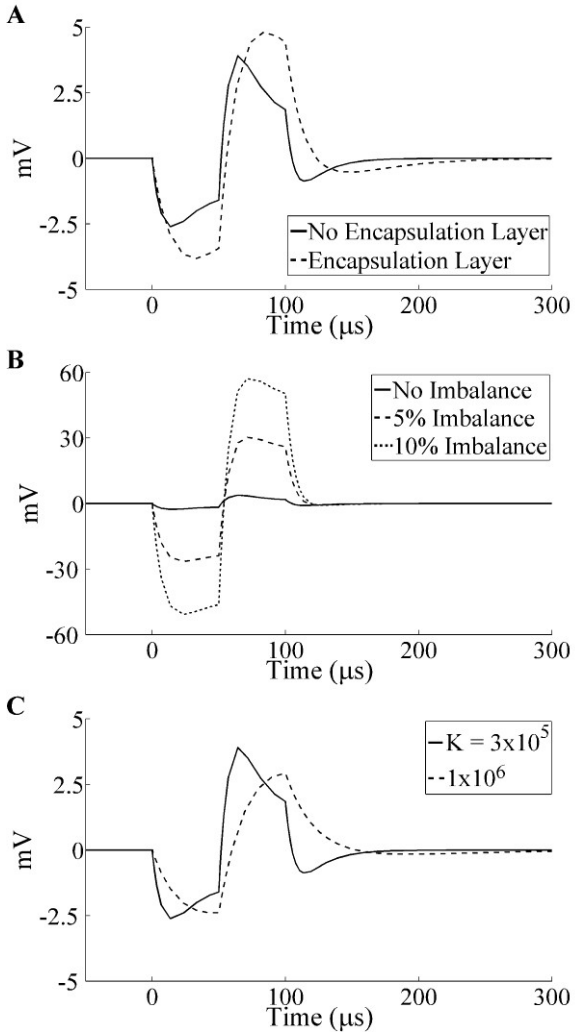

Figure 4.9: Stimulation artifacts calculated with the electrical circuit equivalent model for 130 Hz DBS. An amplifier blanking scheme was not implemented, and so a triphasic artifact waveform was observed. Results were independent of DBS frequency. A: Stimulus artifact waveforms recorded with and without a highly resistive encapsulation layer. B: Artifact waveforms recorded prior to and following unbalancing of volume conductor resistances, by decreasing R_{V01} and increasing R_{V12} by the percentage indicated. C: Artifact waveforms recorded with two different dielectric constants (K).

introducing an imbalance in these values between contacts 0 and 2 by up to 50%, had a negligible effect on the artifact. These results suggest that tissue impedance is the

dominant determinant of stimulus artifact size, particularly the extent of impedance imbalance between recording contacts.

The second FEM model was used to study the effect on the artifact magnitude of changes in the properties of the peri-electrode space, including heterogeneity in the tissue conductivity. In the homogeneous condition, there was a non-monotonic trend between conductivity of the peri-electrode space and the artifact magnitude. The artifact increased as conductivity of the peri-electrode space was reduced from $0.\overline{3}$ to 0.1 S/m, before declining at 0.05 S/m (Fig. 4.10A). An artifact with 0.68 mV magnitude was observed when the conductivity of the peri-electrode space was equal to that of the brain tissue ($0.\overline{3}$ S/m), and was generated by the axial discontinuity arising at the electrode tip and by the presence of the highly conductive but unused contact 3. This was demonstrated both by extending the representation of the insulation downwards, such that the distances between the center of the stimulation contact and the top and bottom of the insulation were equal, and by removing contact 3 from the model, which reduced the artifact magnitude to 0.007 mV.

Heterogeneity of the peri-electrode conductivity generated a range of artifact magnitudes across ten replicate simulations. The maximum artifact was always larger than in the homogenous case with the same mean conductivity, the minimum was always less than the homogenous case, and the median value was close to the homogenous case (Fig. 4.10A). Furthermore, the range of artifact magnitudes generally

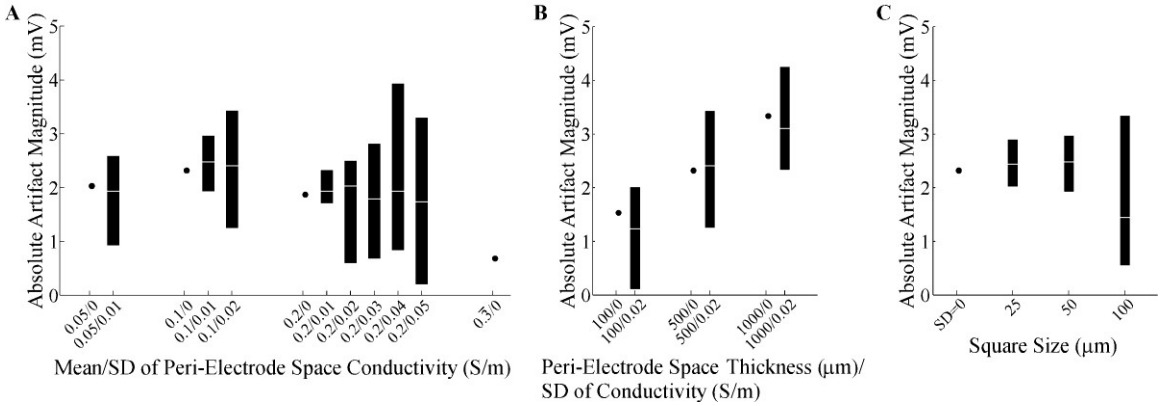

Figure 4.10: Evaluation of stimulation artifacts using the FEM-based model of tissue heterogeneity. A: The artifact magnitude was calculated for different mean and SD conductivity values within the peri-electrode space. The thickness of the peri-electrode space was 500 μm and the square size was 50 μm. The range (black bar) and median values (white line) from 10 repeated trials are provided, except for homogenous conditions (SD=0), in which case a single value is given. B: Artifact magnitude calculated for various peri-electrode space thickness values. The SD of conductivity was also varied for each thickness value, whereas the mean conductivity was fixed at 0.1 S/m and the square size at 50 μm. C: Artifact magnitude calculated for different peri-electrode space square sizes. The thickness of the peri-electrode space was fixed at 500 μm and the conductivity was 0.1±0.02 S/m. For reference, the artifact magnitude for the homogenous condition is also provided (square size had no effect).

increased with greater variability in tissue conductivity. Increasing the thickness of the peri-electrode tissue from 100 to 1000 μm increased the artifact magnitude when the peri-electrode tissue was homogenous, and shifted the range of artifact magnitudes towards higher values when the tissue was heterogeneous (Fig. 4.10B). Finally, increasing the size of the square division from 25 to 100 μm, thereby changing from a fine to a coarse spatial scale, increased the range of artifact magnitude values across trials (Fig. 4.10C). These results show that a glial encapsulation layer can increase the

artifact magnitude, particularly as the thickness of this layer increases, and that heterogeneity in the conductivity can further increase the artifact magnitude.

4.4 Discussion

ECAPs were recorded from implanted electrodes during thalamic DBS in subjects with tremor. There was large subject-to-subject variation in stimulus artifact amplitude, and model-based analysis revealed that the larger artifacts may have been caused by glial encapsulation of the electrode, resulting in imbalances in the tissue impedance between the contacts. High fidelity ECAP recordings obtained from both acute and chronically implanted electrodes revealed that specific phase characteristics of the signal varied systematically with stimulation parameters and were correlated with changes in tremor. Further, results from this study suggest that excitation of cerebellar afferents during DBS is important for reduction of motor symptoms, consistent with prior findings (Coenen et al., 2011, Sandvik et al., 2011, Birdno et al., 2012, Keane et al., 2012). The demonstration of high-fidelity recordings of ECAPs from both acutely and chronically implanted DBS electrodes, as well as the identification of ECAP characteristics correlated with motor symptoms, support the feasibility of an ECAP-based closed-loop DBS system, which could optimize therapy and reduce the clinical burden of parameter selection.

4.4.1 ECAP waveform and the effect of stimulation parameters

The ECAP waveform generally exhibited N1-P1-(N2-P2) phases, although in acute recordings the N1 phase was typically not as evident at the higher stimulation amplitudes. In comparison, ECAP signals recorded in preclinical experiments (**Chapter 3**) were inverted, with primary P1-N1 phases followed by secondary P2-N2 phases. We reproduced the clinical ECAP polarity in the model only with ventral or dorsal positioning of the clinical DBS electrode within the thalamic nucleus (Fig. 4.8A). Clinical electrode implantation for thalamic DBS typically involves placement of contact 0 at the ventral border of Vim, and the model indicated that this location was an important factor in generating the specific ECAP shape observed experimentally.

The ECAP magnitude was larger in the acute stage (EP13B, EP13G, EP13I, and EP13J) than in the chronic stage (EP12A, EP12B, EP12D), with DBS amplitude approximately constant. One possible reason was that the chronic recordings used an external counter electrode, which may have resulted in a voltage drop across the skin that reduced voltages in the brain tissue, ultimately decreasing the number of activated neurons. Second, glial scar formation in the 6 to 8 weeks after chronic electrode implantation leads to neuronal cell loss near the electrode (Henderson et al., 2002, McConnell et al., 2009), which could have reduced the ECAP magnitude, as suggested by prior modeling performed in **Chapter 3**. Third, the glial encapsulation layer could electrically isolate recording contacts from the surrounding neurons and further

diminish the ECAP. On the other hand, LFPs recorded from a DBS electrode at 7 years after DBS implantation were similar to those recorded in the acute condition (Giannicola et al., 2012b), suggesting a smaller effect of glial encapsulation on LFPs.

The ECAP varied systematically with stimulation parameters. Responses were similar for opposite stimulation polarities, as observed in our previous work (**Chapter 3**), and which enabled polarity averaging to remove the stimulus artifact, when necessary. There was a non-monotonic relationship between ECAP magnitude and DBS amplitude (Figs. 4.5, 4.7), as also observed in cochlear nerve recordings (Miller et al., 1998, Matsuoka et al., 2001, Westen et al., 2011). The ECAP magnitude is thought to reflect the spatial extent of neural activation (**Chapter 3**), and the model indicated that the decline in ECAP N1 and N2 magnitude at the highest DBS amplitudes resulted from greater activation of cortical inputs, which increased their corresponding positive ECAP phase contributions and thereby reduced the negative phases through destructive interference. Alternatively, the non-monotonic relationship may have resulted from a hyperpolarizing "anodal surround" region of action potential block close to the electrode at high amplitudes (Ranck, 1975). In contrast, a monotonic relationship between ECAP magnitude and DBS amplitude was observed in preclinical experiments (**Chapter 3**), although the maximum amplitude was limited to 3 V. Decreasing DBS frequency from 130 Hz to 10 Hz increased the magnitude of N2 and/or P2 in EP12B and EP12D, and our previous study suggested that the increased post-synaptic synchronization of TC cells at

low frequencies increased the magnitude of secondary phases (**Chapter 3**). While this increased TC synchronization was still evident with lower DBS frequencies (Fig. 4.8A), the corresponding effect on the ECAP was masked by the much larger contribution from directly excited cerebellar afferents, which were also affected by frequency (Fig. 4.8B).

4.4.2 Relationship between ECAP signatures and clinical effectiveness

Tremor was generally reduced from baseline with 130 Hz DBS and exacerbated at 10 Hz (Birdno and Grill, 2008). For high-frequency DBS, we typically observed a non-monotonic relationship between tremor and stimulation voltage, in which increasing the amplitude initially led to greater reductions in tremor before reversing beyond some optimal voltage (Fig. 4.7). This could have been caused by the activation of more distant, tremor aggravating brain areas at higher voltages (Cooper et al., 2008) or activation of the internal capsule, which might aggravate tremor due to increased stress from the side effects of stimulation (Kuncel et al., 2006).

The relationship between the ECAP signal and tremor provides insights into mechanisms of DBS and reveals a potential feedback signal for automated parameter tuning. Increasing ECAP phase energy was related to reductions in tremor at 130 Hz and exacerbation of tremor at 10 Hz. Since the ECAP signal energy provides a measure of the extent of neural activation (**Chapter 3**), these results suggest that DBS must activate a sufficient volume of tissue for clinical benefit at 130 Hz, or for symptom exacerbation at 10 Hz. The thalamic DBS model revealed that cerebellar afferents were

the dominant contributors to the ECAP response, and since the energy of ECAP phases was correlated with tremor, this suggests that activation of cerebellar inputs is critical to tremor suppression by DBS. This is consistent with the findings that activation of cerebellothalamic afferents suppressed tremor in ET patients by overriding pathological bursting activity, and that electrode contacts in the subthalamic area ventral to Vim may be more effective than contacts within Vim (Coenen et al., 2011, Sandvik et al., 2011, Birdno et al., 2012, Keane et al., 2012). As well, in EP12B and EP12D, increasing secondary phase energy was correlated with reductions in DBS effectiveness across stimulation frequencies, and these changes may have been related to synaptic mechanisms (**Chapter 3**).

The ECAP could provide a feedback control signal for automated adjustment of stimulation parameters in closed-loop DBS systems. For example, DBS amplitude and/or pulse width could be adjusted to attain pre-determined ECAP phase energy threshold values. However, the absolute phase energy values varied by an order of magnitude between subjects, and the relationship between ECAP phase energy and tremor varied across subjects (Fig. 4.7). Therefore, the threshold values used to set DBS parameters may be subject specific, and may need to be specified as a normalized value of some maximum signal energy within subjects. Although not tested in this study, ECAPs could also be used to target a brain region for implantation, given the dependence of ECAP waveform shape on electrode location, and to select the optimal contact(s) for

stimulation, potentially identified as that which attained the target ECAP phase energies using settings that minimized power consumption (Kuncel and Grill, 2004).

4.4.3 Source of the stimulus artifact

The stimulus artifact was highly variable between experiments, and in some cases interfered with the ECAP signal. This variability in stimulus artifact magnitude and ECAP recording fidelity across subjects was consistent with cochlear ECAP measurements (Miller et al., 2008). We initially theorized that larger artifacts resulted from stimulation current traveling past the reference electrode on the chest to the stimulation counter electrode on the leg as used in EP12A, but moving these electrodes in subsequent experiments did not reduce the artifact. Alternatively, the observation that the artifact was minimal in the acute condition, in both clinical and preclinical experiments (**Chapters 2 & 3**), suggested that changes in the cellular milieu around the DBS electrode influenced the stimulus artifact.

The peri-electrode space is filled with cerebrospinal fluid after acute implantation (Yousif et al., 2008b) and is subsequently replaced by a glial scar (Haberler et al., 2000, Henderson et al., 2002) that increases the tissue impedance (Lempka et al., 2009, Newbold et al., 2010). Further, protein and cell adsorption onto the contact surfaces can influence the double-layer capacitance, and thereby the impedance of the ETI (Lempka et al., 2009, Newbold et al., 2010). The electrical circuit equivalent model suggested that the formation of a highly resistive encapsulation layer increased the

magnitude and duration of the artifact, and imbalances of only 5-10% in the resistance between the stimulation contact and each recording contact led to substantial increases in the artifact magnitude. The FEM-based model corroborated these findings, also indicating that increases in the thickness of the encapsulation layer led to larger artifacts. Further, greater heterogeneity within the encapsulation layer increased the range of artifact magnitudes, perhaps reflecting the range of artifact magnitudes observed across subjects. The imbalance in tissue impedance between contacts could result from applying chronic stimulation at just one of the two contacts used for ECAP recording, since this would reduce the impedance in the chronic condition by polarizing the contact surface and causing attached proteins and cells to desorb (Lempka et al., 2010, Newbold et al., 2011, Cheung et al., 2013). Differences in the brain composition and tissue conductivity near each contact could also contribute to the impedance imbalances. Regardless, these results indicate that the cellular milieu near the DBS electrode plays a critical role in determining the size of the stimulus artifact observed in chronic experiments, and thus the fidelity of ECAPs recorded during DBS.

We attempted to document the contribution of impedance imbalances to the stimulus artifact by measuring post-operative impedances of implanted electrodes. In the majority of chronic experiments, one of two ECAP recording contacts had been used for clinical stimulation (Table 4.2), and this generally led to larger impedance imbalances between the experimental stimulation contact and each of the two recording contacts,

compared to acute experiments. However, holding DBS amplitude approximately constant, the artifact size was not related to the impedance imbalance across chronic experiments. This differs from the conclusion made with the two models, and may relate to the temporal evolution of the encapsulation layer, since impedance measurements were taken post-operatively. Specifically, the composition of this layer may have been modulated by discontinuation of chronic, clinical DBS before surgery, and by application of DBS at experimental stimulation contacts during ECAP recording.

4.4.4 Study limitations

There were several limitations in both the experimental and computational aspects of this work. First, the experimental contact configuration often differed from that used clinically and identified by a neurologist as the most effective for therapy. We used the monopolar symmetric contact configuration to minimize the stimulus artifact (**Chapter 2**), and thus only contacts 1 or 2 were available as the stimulation contact. Second, the symmetrical, biphasic DBS waveform, used to minimize the duration of the stimulation artifact, did not match the asymmetrical waveform used clinically in IPGs (Miocinovic et al., 2009). Third, a voltage drop across the skin was likely generated with the use of a skin surface counter electrode in the chronic condition (McGill et al., 1982), which would result in a reduction in the voltage across the brain tissue. Nevertheless, sufficient voltage was still delivered to the thalamus to generate ECAPs, changes in

tremor, and paresthesias. All three of these limitations could reduce the effectiveness of DBS in treating tremor, compared to clinical DBS delivered with an IPG.

Other limitations included the short duration of DBS prior to the assessment of motor symptoms, the short interval between trials, and conducting only a single trial at each DBS setting in most experiments. While tremor reduction following the onset of DBS typically occurs within a few seconds (Beuter and Titcombe, 2003), our trial design may have underestimated the magnitude of changes in tremor after 30 s of stimulation. Nevertheless, similarly short trial lengths have been used previously in testing the effects of parameter settings (Kuncel et al., 2006), and are used routinely for intraoperative testing and post-operative tuning (Moro et al., 2002, O'Suilleabhain et al., 2003). The washout of DBS effects on tremor occurs over seconds to minutes, with 85% of the return in tremor after cessation of DBS occurring within 5 minutes (Beuter and Titcombe, 2003). However, using longer trial lengths, longer intervals between trials, or replicate trials would have resulted in the experiment becoming too long to conduct during an intraoperative procedure, and there are presently no other settings in which to conduct this study.

The correlations between tremor and ECAP signal characteristics were variable and not statistically significant. Testing a larger number of DBS parameter combinations in a given experiment would have increased the number of data points used in the correlation, and thus, the statistical significance. However, we were limited in the

number of trials that could be tested within the intraoperative setting. Similarly, correlations between cochlear ECAP thresholds and perceptional hearing measures were statistically significant but not strong (Miller et al., 2008, Jeon et al., 2010).

There were also limitations in the computational models, which have been discussed previously (**Chapters 2 & 3**). Briefly, in the thalamic DBS model, the position of the DBS electrode and neural fiber trajectories were approximations, and using more accurate representations may have changed neural activation and the model ECAP response. This could potentially explain the smaller positive phase observed in the model compared to the experimental ECAP recordings. Further, this model did not account for the ETI, tissue capacitance, or tissue inhomogeneities, which could filter DBS potentials (Butson and McIntyre, 2005, Yousif et al., 2008a, Grant and Lowery, 2010, Lempka et al., 2010, Tracey and Williams, 2011) and the ECAP signal (Bedard et al., 2004, 2006, Buzsaki et al., 2012). The electrical circuit equivalent model used geometrical approximations to calculate the resistance and capacitance of the medium, and did not account for the capacitive coupling between stimulating and recording leads (McGill et al., 1982, Grumet, 1999), the capacitance of the medium directly between two DBS contacts, or the frequency dependence of tissue permittivity (Bossetti et al., 2008).

5. Analysis of electrode characteristics for neural recording during deep brain stimulation

5.1 Introduction

Deep brain stimulation (DBS) is an effective surgical therapy for the treatment of movement disorders (Benabid et al., 1991, Limousin et al., 1995, Gross and Lozano, 2000, Krauss et al., 2004), and is being investigated for other neurological diseases. However, the mechanisms of action of DBS are still unclear, which limits the optimization of this therapy (Grill and McIntyre, 2001, McIntyre et al., 2004b).

Measuring neural activity using the DBS electrode could contribute to understanding of the therapy and improve outcomes through closed-loop control. Local field potentials (LFPs), representing synchronized neural oscillations, have been recorded from the DBS electrode array (Brown et al., 2004, Wingeier et al., 2006, Bronte-Stewart et al., 2009), and may serve as a feedback control signal for automatic adjustment of stimulation to optimize therapy (Priori et al., 2012, Stanslaski et al., 2012). The evoked compound action potential (ECAP) can also be recorded from the DBS electrode. The ECAP is generated by activation of an ensemble of neurons adjacent to the electrode and provides insight into the type and spatial extent of neural element excitation during DBS (**Chapters 3 & 4**). The aim of the current work was to conduct a systematic assessment of the influence of the electrode on ECAP and LFP recording, including the physical presence of the recording contacts, the dimensions of the

electrode, and the presence of edema or glial encapsulation in acute and chronic recording conditions, respectively.

We first determined the effect of the large, highly conductive electrode contacts on the recorded signals, as well as changes in the electrode diameter, contact length, and contact spacing. Prior analyses of electromyogram (EMG) recording (van Dijk et al. 2009) and cortical pyramdical cell recording (Moffitt and McIntyre 2005) suggested modest effects of the presence of the electrode on the recorded signal. Reductions in the recording contact surface area generally increased signal amplitude, as demonstrated by LFP recordings with a microelectrode versus a DBS electrode (Lempka and McIntyre, 2013), single-unit recordings made with microelectrodes (Moffitt and McIntyre, 2005, Lempka et al., 2011), electroneurogram (ENG) recordings with needle electrodes (Schoonhoven and De Weerd, 1984), and motor unit EMG recordings with surface electrodes (Dimitrova et al., 1999). Further, smaller contacts should be more spatially sensitive, with neuronal contributions extending several millimeters with measurement from a DBS electrode (Lempka and McIntyre, 2013) and only ~100 μm from a microelectrode (Henze et al., 2000, Moffitt and McIntyre, 2005). Smaller contact spacings reduce the distance from recording contacts to the activated neural population, but can also reduce contributions from more distant neurons, and therefore may decrease the maximum signal amplitude (Lempka and McIntyre, 2013). Previous studies have investigated modified DBS electrode design for targeted stimulation or improved energy

efficiency, including segmentation of electrodes (Wei and Grill, 2005, Buhlmann et al., 2011, Keane et al., 2012), adjustment of the contact diameter-to-length ratio (Butson and McIntyre, 2006), and high perimeter contact shapes (Grill and Wei, 2009), but we are unaware of analogous DBS electrode design analysis for improving neural recording fidelity.

Subsequently, we quantified the effects of changes in the peri-electrode space between acute and chronic recording conditions on the recorded signals. Several studies have documented the reduction in voltages within the brain during stimulation following acute edema or chronic glial encapsulation (Yousif et al., 2008a, Lempka et al., 2010). Further, acute edema reduced the amplitude of simulated single-unit recordings by 24% while glial encapsulation increased the signal amplitude by 17%, contrary to the notion that encapsulation leads to electrical isolation of the recording contacts (except when the resistivity of the peri-electrode space is sufficiently high) (Moffitt and McIntyre, 2005). Further, the impedance of the peri-electrode space was correlated with the amplitude of the low frequency LFPs (2-7 Hz, including theta band), but not the beta band LFPs (Yousif et al., 2008b, Rosa et al., 2010, Lempka and McIntyre, 2013). In prior work, we studied how changes in the conductivity of the peri-electrode space can influence the stimulus artifact in ECAP recordings (**Chapter 4**), but not the ECAP itself.

5.2 Methods

A computational model was used to calculate ECAPs and LFPs recorded with a DBS electrode from a population of model thalamic neurons, as well as evoked responses generated by single neural elements. The model is reviewed in detail in **Chapter 4**, and is described here only briefly. The three stage model included: (1) a finite element method (FEM) volume conductor model of the DBS electrode implanted within the ventral intermediate (Vim) nucleus of the thalamus, (2) multi-compartment cable models of thalamocortical neurons and their pre-synaptic inputs, which provided the electrical sources for the ECAP or LFP, and (3) application of the reciprocity theorem to calculate potentials generated by neuronal transmembrane currents at the DBS recording contacts. ECAPs and LFPs were calculated for different electrode representations, various electrode geometries, and following inclusion of a peri-electrode space to represent acute and chronic recording conditions. The monopolar symmetric contact configuration (monopolar stimulation contact between two symmetrical, bipolar recording contacts) was used to match previous studies (**Chapters 2-4**). The model was also modified to explore the spatial selectivity of single-units, measured with monopolar or bipolar recording contacts, under various recording conditions and with different electrode geometries.

5.2.1 FEM volume conductor model

The first stage used a FEM model developed in COMSOL Script v.1.2 (COMSOL) to calculate potentials generated by DBS (Fig. 5.1). The volume conductor included geometrical representations of the DBS electrode within a prism-shaped Vim, and both were surrounded by adjacent brain tissue represented as a cylinder parallel to the DBS electrode and centered at the electrode tip (Birdno et al., 2012). The conductivities of the electrode contacts, electrode insulation, and brain tissue were 5×10^{6}, 1×10^{-13}, and $0.\overline{3}$ S/m, respectively (Moffitt and McIntyre, 2005, Yousif et al., 2008a). In a subsequent version of this model, a 500 μm thick peri-electrode space was introduced around the DBS electrode to represent edema (1.7 S/m) or a glial encapsulation layer (0.1 S/m) (Butson et al., 2006, Yousif et al., 2008a). The DBS electrode was shifted from its original location (Birdno et al., 2012) by 6 mm along its axis in a ventral direction, which more accurately represented clinical electrode placement as well as the experimental ECAP shape recorded in humans during Vim-DBS (**Chapter 4**). The dimensions of the electrode initially matched that of the Medtronic 3387 clinical electrode, with 1.27 mm diameter, 1.5 mm contact length, and 1.5 mm contact spacing, and were subsequently varied with diameters ranging from 0.5 to 1.5 mm, recording contact lengths of 1 to 2 mm, and contact spacings of 0.1 to 2 mm. For the different contact lengths and spacings, the electrode tip location was shifted to maintain the same location for the stimulating contact, which preserved neural activation across geometries. To calculate potentials

generated by monopolar DBS, a 1 V boundary condition was imposed at contact 1, the outer boundary of the surrounding cylindrical tissue was grounded, and the model was meshed and solved.

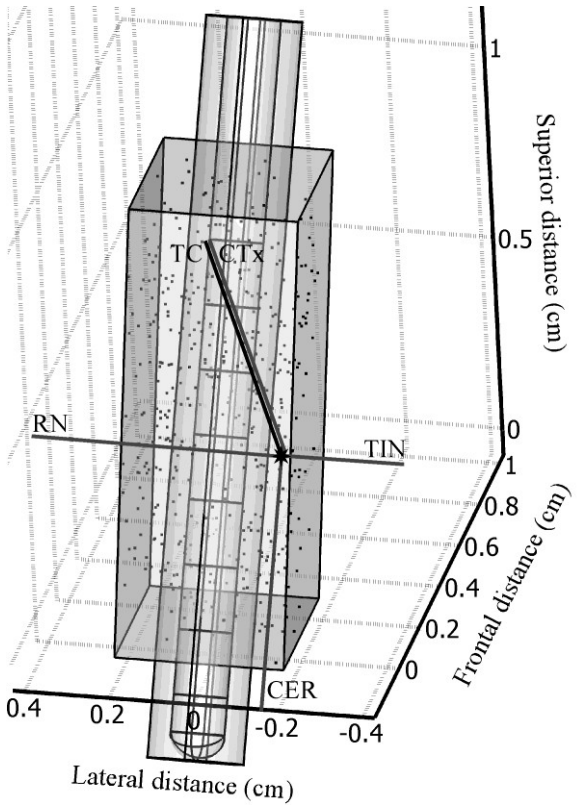

Figure 5.1: Computational model used to determine the effects of the electrode and peri-electrode tissue properties on recorded neural signals. The FEM geometry of a Medtronic 3387 DBS electrode is shown, surrounded by a peri-electrode space domain, and implanted in a prism representation of the Vim thalamus. The locations of 500 thalamocortical (TC) somata within the Vim are indicated by the dots, and the axon positioning is shown for one neuronal unit, which includes a TC neuron and pre-synaptic inputs from the cortex (CTx), cerebellum (CER), reticular nucleus (RN), and thalamic interneurons (TIN).

5.2.2 Multi-compartment cable models

The potentials from the FEM model were coupled to validated multi-compartment cable models of neurons implemented in NEURON v7.1 (Hines and Carnevale, 2001). The neuron models had appropriate geometrical and ion channel representations of thalamocortical (TC) neurons, including the soma, initial segment, and dendritic tree (McIntyre et al., 2004a) and their pre-synaptic inputs from the cortex (CTx), cerebellum (CER), reticular nucleus (RN), and thalamic interneurons (TIN) (Birdno et al., 2012). Interconnections between neural elements included excitatory glutamatergic synapses from CTx and CER to TC, inhibitory GABAergic synapses from RN and TIN to TC, and excitatory 1:1 synapses from TC and CTx to RN, and from CTx and CER to TIN, implemented with virtual terminating axons (Fig. 3.2B) (Birdno et al., 2012). A single neural unit, defined as one TC cell and its pre-synaptic axonal inputs from CTx, CER, RN, and TIN, was repeated 500 times, with TC soma locations randomly distributed within Vim (Fig. 5.1). Any neural elements that intersected the DBS electrode or peri-electrode space (when present) were removed. The potentials at the FEM mesh nodes were interpolated at the compartment locations of all model elements, and extracellular stimulation was delivered to the cable models by scaling the potentials by the specified DBS amplitude. The stimulation waveform was symmetric and biphasic, delivered in a 1 s train with 100 Hz frequency, 50 μs/phase pulse duration, and cathodic-phase first polarity, with a pre-stimulation period of 0.5 s and simulation time step of 25

μs. The resulting transmembrane currents were measured from each model compartment as a function of time and served as the electrical sources for ECAP calculation. Additionally, transmembrane potentials were measured at the initial segment of the TC neuron and at the proximal node of Ranvier of each pre-synaptic input for detection of neural activation. LFPs were calculated in a similar manner but without delivery of DBS. The intrinsic patterns of activity present in the original model, including harmaline bursting of CER inputs and 20 Hz Poisson spiking of CTx inputs (Birdno et al., 2012), was introduced in the LFP model, but not the ECAP model.

5.2.3 Calculation of ECAPs and LFPs using the reciprocity theorem

The reciprocity theorem was used to calculate the potentials generated by neuronal transmembrane currents (Helmholtz, 1853, Moffitt and McIntyre, 2005). This approach first required calculation of the reciprocal FEM solution, in which a unit current source was placed at the boundary of each recording contact (0 and 2) in turn, and the resulting potentials were calculated at each compartmental location. This was interpreted as the voltage impressed on each contact for a unit current at a given compartmental location, and was adjusted by multiplicative scaling according to the actual magnitude and sign of the respective transmembrane current. The process was repeated for the currents at all compartments, and the differential voltage across the two contacts was summed at each time step to calculate the ECAP or LFP.

5.2.4 ECAP and LFP data processing

The model-calculated ECAPs and LFPs were post-processed in MATLAB. The signal magnitude was scaled by 364 to account for the true cell density in the human Vim (65 cells/mm^2 in 50 μm sections (Hirai et al., 1989)). The stimulus artifact in the ECAP signal was removed by template subtraction (Briaire and Frijns, 2005), in which the artifact template was calculated using a subthreshold stimulation pulse (0.01 V), scaled to match the artifact generated in the trial of interest, and subtracted. Further, the ECAP was band-pass filtered from 10 Hz - 10 kHz with two cascaded first-order Butterworth filters and stimulus-triggered averaged over eight responses to replicate the processing performed experimentally (**Chapters 3 & 4**). The LFP was filtered from 2-100 Hz with a first-order Butterworth filter (Pedrosa et al., 2012).

ECAP signals were compared across model iterations using calculations of signal energy and RMS error (RMS_E). ECAP signal energy was calculated by squaring the signal and integrating over individual ECAP phases. RMS_E was calculated using the equation below (van Dijk et al., 2009):

$$RMS_E = 100\% \times \sqrt{\frac{\sum_i (signal_A(i) - signal_B(i))^2}{\sum_i signal_A^2(i)}} \qquad \text{(Equation 5.1)}$$

The magnitude of LFP signals was calculated as the standard deviation over a 2.5 s duration waveform and compared across model iterations.

5.2.5 Single-unit recordings

The thalamic population model was modified to enable calculation of evoked responses generated by a single local cell (TC neuron) or passing axon (60 node, 2 μm diameter MRG model (McIntyre et al., 2002)) positioned near a single monopolar recording contact 0 or two bipolar contacts (0+/2-). The axons of both elements were parallel to the electrode, and the lateral distance to the electrode boundary varied from 0.125 to 10 mm. The TC soma was centered lengthwise on contact 0 for both monopolar and bipolar recordings. Similarly, the center node of the passing axon was centered on contact 0 for monopolar recording or contact 1 for bipolar recording. The elements were activated by applying a suprathreshold depolarizing intracellular stimulation pulse with 100 nA amplitude and 50 μs duration at the TC soma or most ventral node of the passing axon. ECAPs were calculated as before, by coupling the multi-compartment cable models and reciprocal FEM approach. The stimulus artifact was removed using the template subtraction method, with the template calculated using a hyperpolarizing intracellular stimulation pulse of equal magnitude. Finally, signal energy was calculated by squaring the signal and integrating over the first 5 ms.

5.3 Results

Computer simulation was used to calculate how the ECAP and LFP generated by a population of model thalamic neurons, or the evoked response measured from single

neural elements, were affected by the presence of the electrode, the geometry of the electrode, and changes in the composition of the peri-electrode space.

5.3.1 ECAP and LFP signal waveforms

The ECAP waveform recorded from the population model was similar to that from clinical recordings (**Chapter 4**), with a small, initial positive (P1) phase, followed by a large negative (N1) phase, secondary positive (P2) phase, and large, secondary negative (N2) phase (Fig. 5.2A). Cerebellar afferents generated the dominant contribution to all phases of the model ECAP, although contributions from cortical inputs reduced the magnitude of P1, N1, and N2 through destructive interference and shifted P2 to more positive voltages. The remaining elements had negligible contributions.

The LFP signal recorded with DBS *off* oscillated at a fundamental frequency of 7.2 Hz, in the high theta band (Figs. 5.2B,C). This was similar to recordings made in humans with ET (Kane et al., 2009, Pedrosa et al., 2012).

5.3.2 Effect of the presence of the DBS electrode

We analyzed how ECAPs and LFPs were altered by the presence of the electrode (Medtronic 3387 dimensions) by changing the conductivity of the recording contacts to that of the insulating shaft in the reciprocal FEM solution (*insulating contact* model). Compared to the *original* model, in which the recording contacts were highly conductive, the *insulating contact* model resulted in a similar ECAP waveform

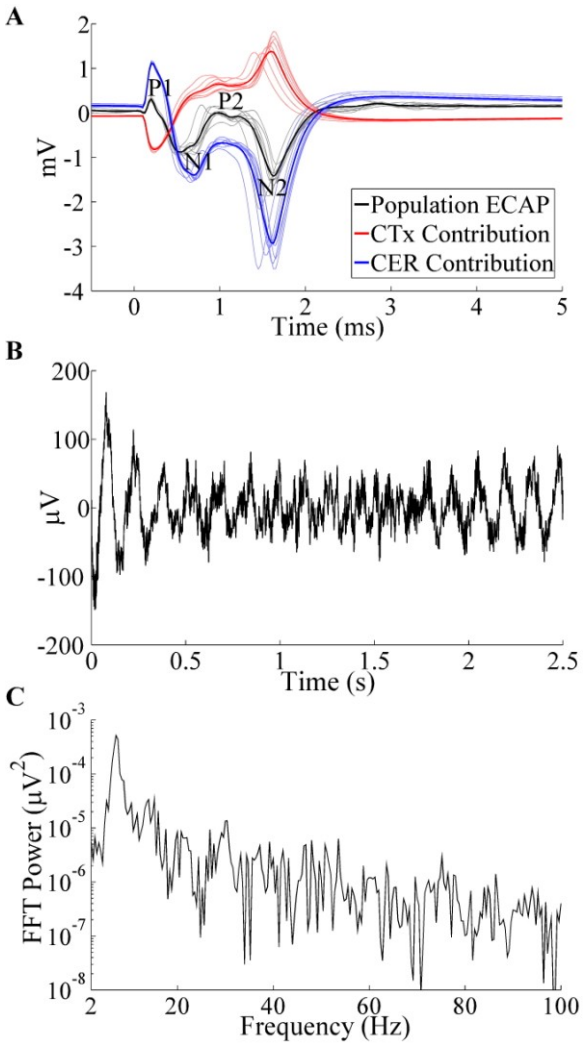

Figure 5.2: ECAP and LFP signals recorded with the Medtronic 3387 electrode. A: Composite ECAP response, and individual contributions from activation of CTx and CER inputs, with 3 V DBS. The average ECAP and single responses are shown in the bold and light traces, respectively, and phases of the ECAP are labeled. B: LFP signal arising from intrinsic network activity. The LFP magnitude (standard deviation) was 37.04 μV. C: FFT power spectrum of LFP signal from (B), with peak frequency at 7.2 Hz.

(RMS_E=6.9%) with a 3.7% and 13.1% reduction in N1 and N2 phase energy, respectively, indicating that the presence of the recording contacts had a negligible effect on the ECAP (Fig. 5.3A). Similarly, the LFP magnitude was reduced by only 5.1% when the

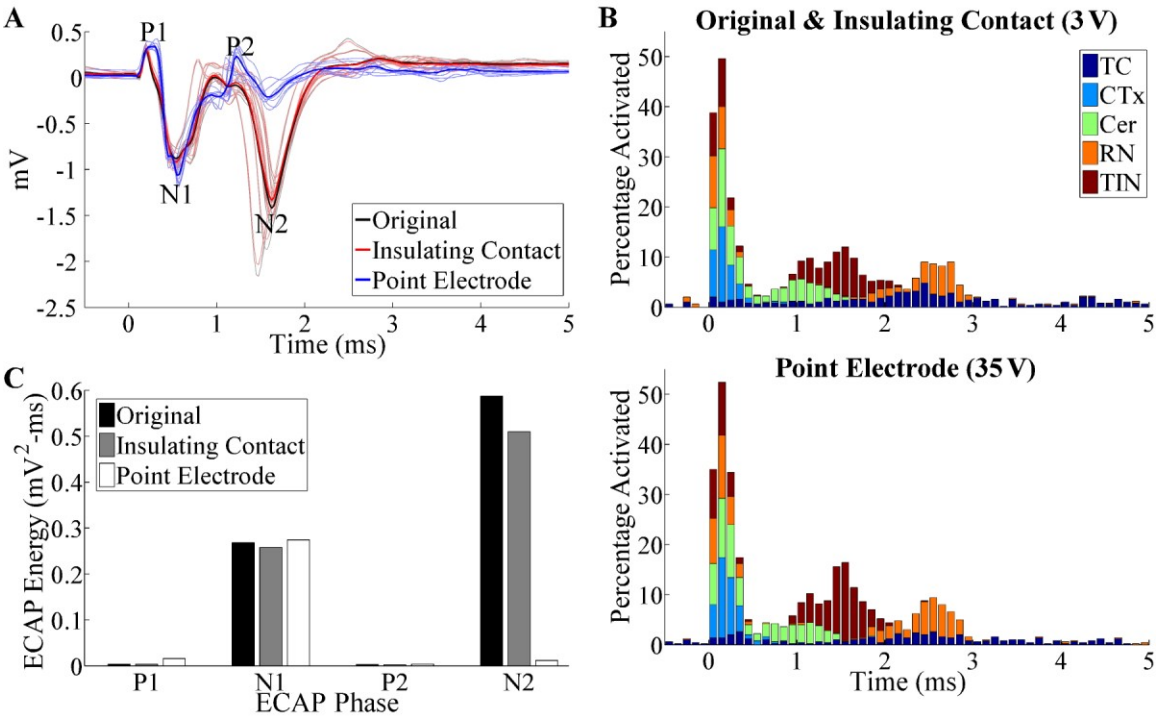

Figure 5.3: A: ECAP responses for different electrode representations in the reciprocal FEM model. The DBS amplitude was 3 V for the *original* and *insulating contact* models, and 35 V for the *point electrode* model. B: Neural activation for the conditions tested in (A), shown as a percentage of each type of element (TC, CTx, CER, RN, and TIN) that fired an action potential in a given 0.1 ms bin following DBS pulses. C: Signal energy of each phase from the ECAP responses in (A).

highly conductive recording contacts were absent (*insulating contact*), as compared to the *original* model. In the *point electrode* model, the DBS electrode was replaced by zero area point electrodes at the center of the original locations of the stimulating and recording contacts. The DBS amplitude was increased from 3 V to 35 V to maintain similar neural activation, with a difference of 1.1% in total neural activation within the first 0.2 ms of the DBS pulse (Fig. 5.3B). There was a large difference between the ECAPs from the *original* and *point electrode* models (RMS_E=74.1%), with the latter have increased ECAP

phases energies in P1 (340.4%) and P2 (14.9%), but with the N2 phase reduced by 98.0% (Fig. 5.3A,C).

5.3.3 Effect of electrode geometry

The signals generated by a single TC local cell and a single passing axon during action potential propagation past the two bipolar recording contacts are shown in Fig. 5.4A. A residual stimulus artifact was measured from the passing axon, observed as the initial positive deflection, and was not included in the calculation of signal energy. The maximum peak-to-peak signal amplitudes measured with bipolar recording contacts from the local cell and passing axon with a Medtronic 3387 electrode were 0.21 μV and 0.32 μV, respectively, and decreased as the electrode to element lateral distance increased (Figs. 5.4B-D). ECAP energy was negligible (≥2 orders of magnitude smaller than the greatest ECAP energy observed) at electrode to element distances beyond ~1 mm. Additionally, the ECAP energy recorded from elements stimulated with a sub-threshold pulse (~40 nA) was 2-3 orders of magnitude smaller than that from excited neural elements for a given electrode to element distance.

For both the local cell and the passing axon, signal energy increased with smaller electrode diameters (Fig. 5.4B) or shorter contact lengths (Fig. 5.4C). Further, smaller contacts were more spatially sensitive, producing steeper reductions in signal energy as the electrode to element distance increased, whereas there was less relative decline in signal energy over distance with the larger contacts. Compared to the original design,

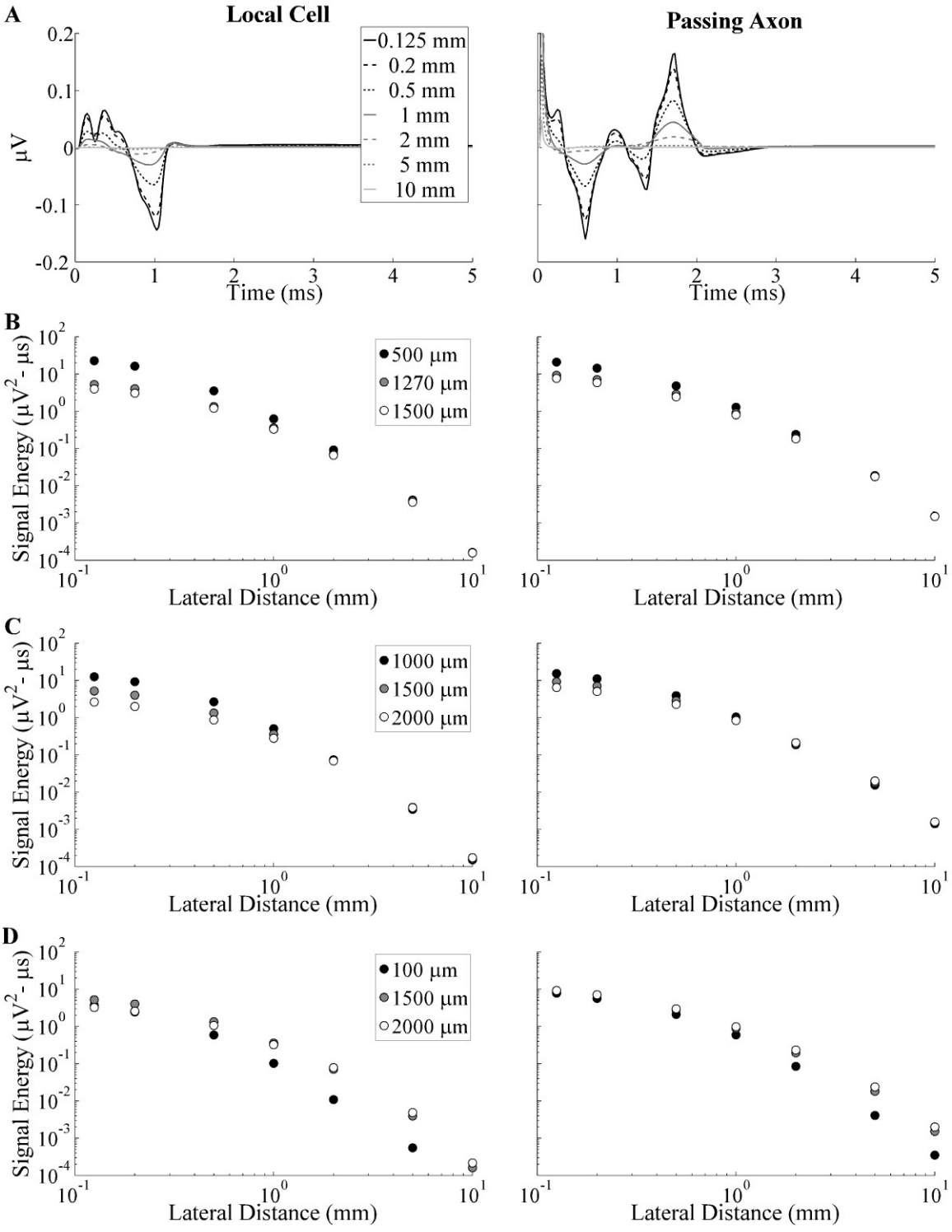

Figure 5.4: Single-unit responses measured from a local cell or passing axon with bipolar recording contacts across electrode designs. A: The evoked response at

various lateral distances between the neural element and electrode using the dimensions of the Medtronic 3387 electrode. B-D: Signal energy versus lateral distance across electrode diameters (B), contact lengths (C), and contact spacings (D).

using the smallest contact diameter (500 μm) increased recording selectivity for the local cell over the passing axon (ECAP energy ratio of 1.09 at a cell distance of 0.125 mm), whereas the largest diameter (1500 μm) was more selective for the passing axon (ratio of 0.52). Similar trends between electrode geometry and signal energy were observed using a monopolar recording configuration (data not shown). Contact-to-contact distances smaller than that of the Medtronic 3387 electrode reduced the energy of the recorded response, whereas larger spacings had an ambiguous effect dependent on element type (Fig. 5.4D). Smaller contact spacings also reduced contributions from more distant neurons, based on the faster reduction in signal energy at longer cell distances.

The effects of contact diameter and length on the ECAP were phase-dependent, as expected from the neural element specific effects observed in the single-unit analysis. Reducing the diameter from 1270 μm (Medtronic 3387) to 500 μm increased N1 and P2 phase energy by 32.1% and 109.9%, respectively, and decreased N2 phase energy by 71.2%, whereas increasing the diameter to 1500 μm increased the energy of the N1 phase (158.2%) and reduced only the N2 phase (-69.8%) (Figs. 5.5A, 5.6A). The larger diameter electrode also distorted the typical ECAP waveform (Fig. 5.5A), greatly reducing the P1 and P2 peaks to below 0 mV. DBS amplitude was adjusted to maintain similar activation across the diameters tested, and there was only a difference of 8.1% in total neural

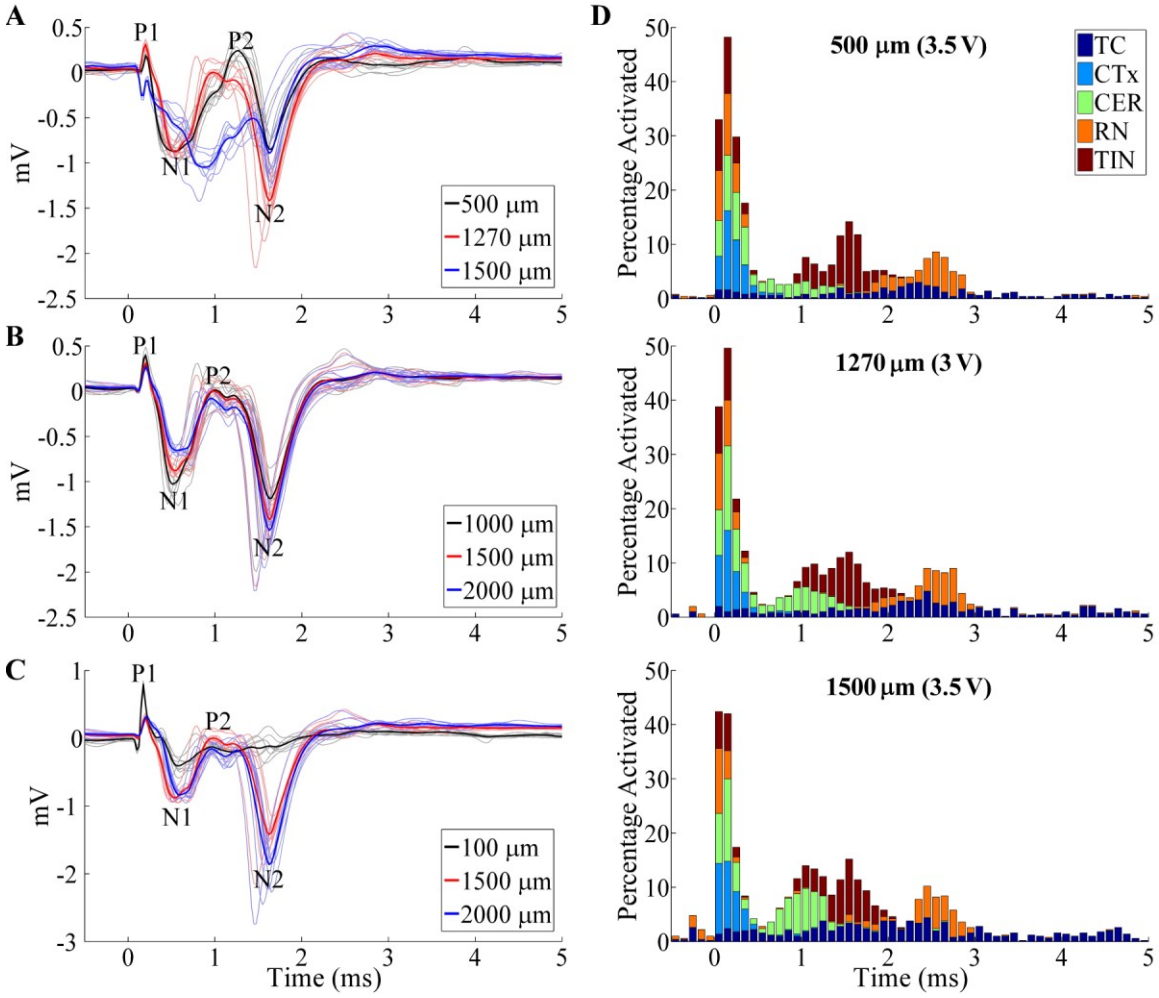

Figure 5.5: ECAP responses across electrode geometries, including electrode diameters (A), recording contact lengths (B), and contact spacings (C). The initial negative and positive peaks of the ECAP with a 100 µm contact spacing in (C) corresponded to a residual stimulus artifact. DBS amplitude was 3 V for all electrode designs except with diameters of 500 or 1500 µm, for which DBS amplitude was increased to 3.5 V. D: Neural activation for the three electrode diameters tested. Data presentation is similar to Fig. 5.3B.

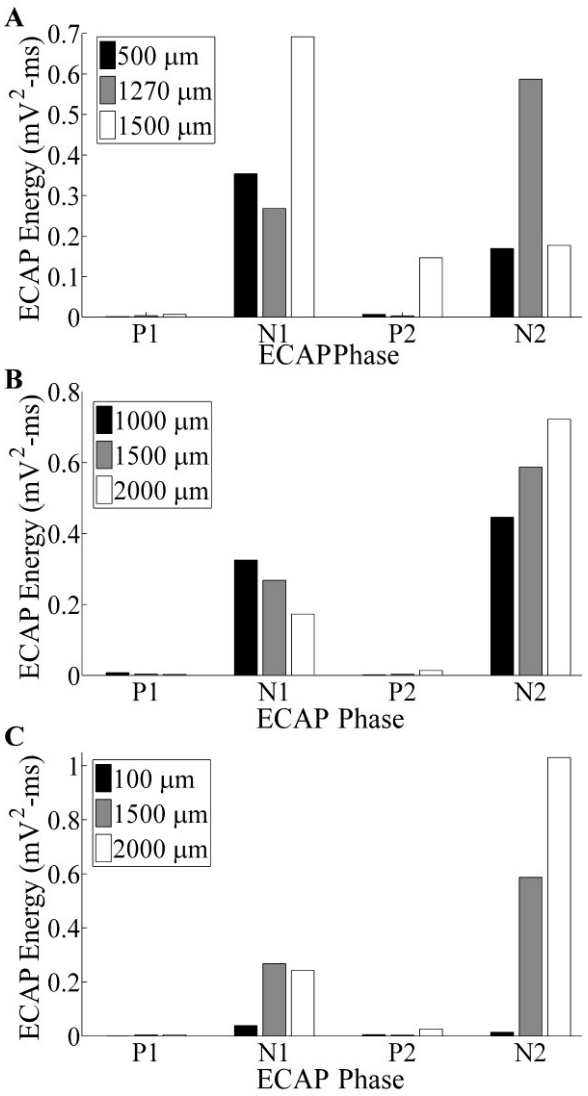

Figure 5.6: Signal energy of each phase from the ECAP responses in Fig. 5.5 across different electrode geometries, including electrode diameters (A), recording contact lengths (B), and contact spacings (C).

activation within the first 0.2 ms of the DBS pulse (Fig. 5.5D). Nevertheless, differences in neural activation across contact diameters remained, and this may have contributed to ECAP distortion. Reducing the contact length from 1500 μm to 1000 μm increased N1 energy by 21.3% but decreased N2 energy by 24.0%, whereas increasing the contact

length to 2000 μm decreased N1 (-35.4%) and increased N2 (23.0%) phase energies (Figs. 5.5B, 5.6B). Lastly, a shorter inter-contact spacing of 100 μm (originally 1500 μm) reduced the overall ECAP, particularly the N1 (-85.8%) and N2 (-97.6%) phases, whereas increasing the spacing to 2000 μm increased N2 energy by 75.5% (Figs. 5.5C, 5.6C).

Local field potentials were also recorded with different geometries. The LFP amplitude was relatively stable across the geometries tested (≤10% change compared to the Medtronic 3387 design), except for a large increase (24%) when the diameter was reduced to 500 μm and decrease (-34%) when the contact spacing was reduced to 100 μm.

5.3.4 Effect of recording conditions

We investigated the effect of acute edema or chronic glial encapsulation on the recorded signal by introducing a 500 μm thick peri-electrode space with the appropriate conductivity. Edema or glial encapsulation decreased or increased signal energy, respectively, in bipolar recordings from a single local cell or passing axon, particularly when the element was located within the peri-electrode space (Fig. 5.7A). Similar trends were observed with measurement from single neural elements with a monopolar recording configuration (data not shown). We attempted to maintain a similar extent of neural activation in the ECAP model across conditions, with or without representation of the peri-electrode space, and there was only a difference of 7.9% in total neural activation within the first 0.2 ms (Figs. 5.7B,C). Despite these adjustments, removing

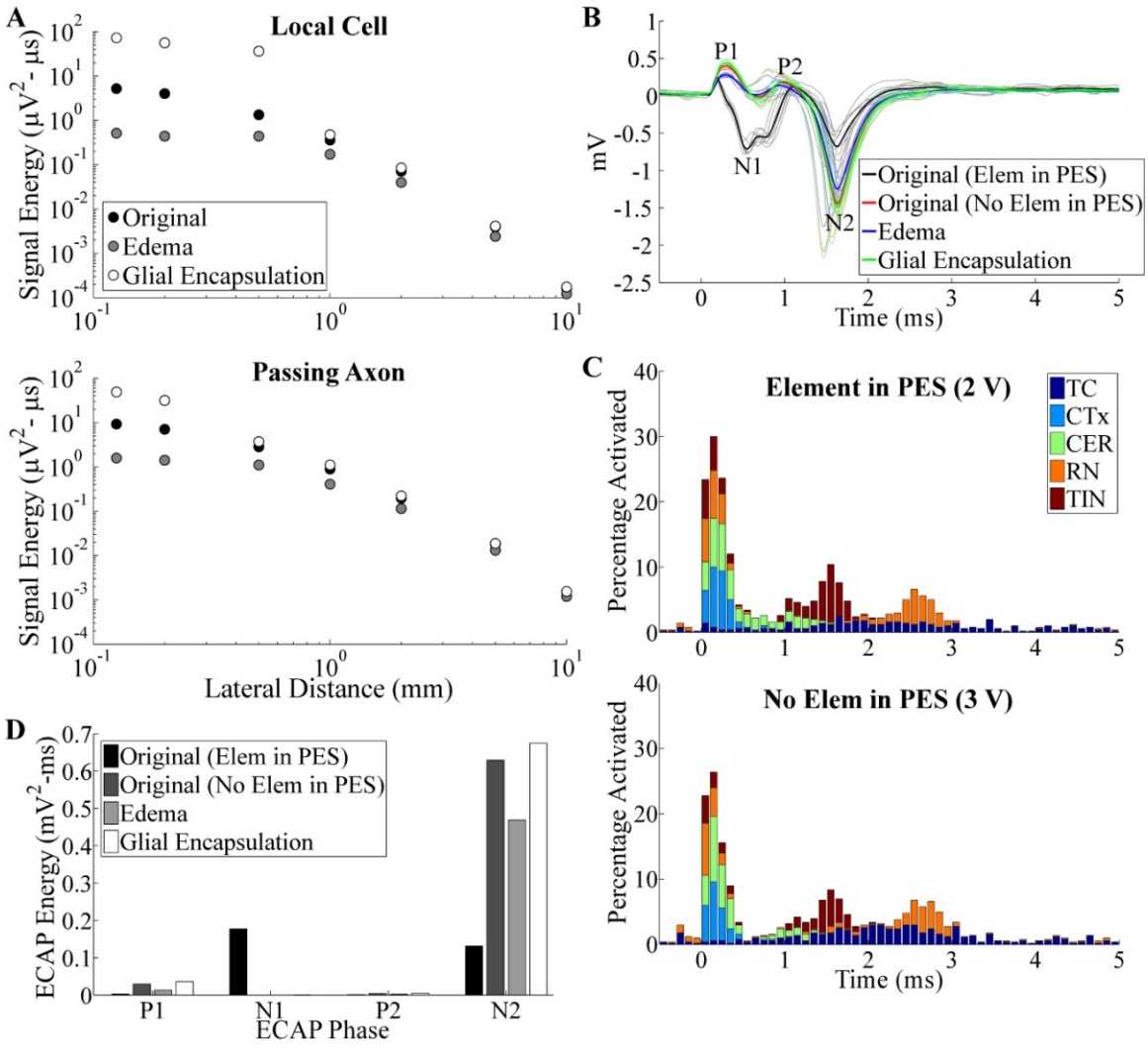

Figure 5.7: Neural responses recorded in the original, acute edema, and chronic glial encapsulation models. A: Signal energy of single-unit responses versus lateral distance of the local cell or passing axon, measured with bipolar recording contacts. B: ECAP responses for the original model with and without elements in the peri-electrode space (PES), and for the edema and glial encapsulation models, with no elements in the PES. DBS amplitude was 2 V with neurons in the PES, and 3 V otherwise. C: Neural activation for the conditions tested in (B). Data presentation is similar to Fig. 5.3B. D: Signal energy of each phase from the ECAP responses in (B).

neural elements from the peri-electrode space alone had a large effect on the ECAP, with increases in phase energy of P1 (845.5%) and N2 (380.2%), and a reduction in that of N1 (-99.9%), due to changes in electrode to element distances. Subsequent changes to the peri-electrode space conductivity to represent edema caused decreases in the energy of all phases (-25.4-87.6%), whereas glial encapsulation increased the energy of all phases (7.3-130.9%).

The composition of the peri-electrode space also had a substantial impact on the LFP. Removing neural elements from the peri-electrode space alone reduced the LFP magnitude by 31.4%, and acute edema led to further reductions, with a magnitude 43.3% smaller than that under the original conditions. Conversely, glial encapsulation generated only a 27.8% reduction in LFP magnitude, or a 5.2% increase over the condition where neural elements were removed from the peri-electrode space, but the conductivity was that of the surrounding grey matter.

5.4 Discussion

We conducted a systematic investigation of how the presence and geometry of the DBS electrode, as well the changing conditions between acute and chronic electrode placements, affected recorded evoked (single-unit and ECAP) and intrinsic (LFP) neural signals. The highly conductive contacts had a negligible effect on the ECAP (RMS_E=6.9%) and LFP (5.1% magnitude change), in agreement with prior work (van Dijk et al., 2009). Van Dijk and colleagues suggested that this result occurred only if the impedance of the

electrode-tissue interface (ETI) was high relative to the effective tissue impedance, although we did not include the ETI in our model. The differences in ECAPs recorded with the DBS electrode versus a point electrode indicated that spatial averaging across the larger contact surface decreased the signal magnitude in a phase-dependent manner (RMS_E=77.9%). This differed from a previous study, which found small differences in single-unit recordings made with a microelectrode compared to those made with a point source representation (Moffitt and McIntyre, 2005), but this likely resulted from the already small surface area of the microelectrode (400 μm^2) compared to the DBS macroelectrode (5.98 mm^2).

Smaller contact diameters and lengths increased signal energy in single-unit recordings. This increase in signal strength for smaller contact surfaces confirmed previous findings (Schoonhoven and De Weerd, 1984, Dimitrova et al., 1999, Moffitt and McIntyre, 2005, Lempka et al., 2011, Lempka and McIntyre, 2013), and can be explained by considering how recording the full potential generated by a nearby neuron requires that the contact area be small compared to the "steepest portion" of the corresponding extracellular field (Humphrey and Schmidt, 1990); otherwise, potentials are reduced by averaging. Similar trends were observed between ECAP energy and electrode diameter or contact length, although with variable effects on different phases of the ECAP. Changing electrode diameter also impacts the size of the stimulation contact, which can alter neural activation and distort the typical ECAP waveform, and we attempted to

mitigate this effect by adjusting DBS amplitude accordingly. In addition, we confirmed that smaller recording contacts are more sensitive to signals from nearby neurons, whereas larger contacts have more uniform volumes of recording sensitivity. This could be used to tune the size of the recorded volume to encompass only the neuronal population that is critical to therapeutic effectiveness. Finally, we demonstrated that electrodes with diameters smaller than the Medtronic 3387 electrode had increased recording selectivity for local cells over passing axons, whereas the opposite was true with larger electrode dimensions. Selective recording from cerebellothalamic passing axons may be desired, given that their activation during DBS appears critical to effective therapy (Coenen et al., 2011, Sandvik et al., 2011, Birdno et al., 2012, Keane et al., 2012), as observed in **Chapter 4**.

Reducing contact spacing from 1500 μm to 100 μm decreased the ECAP energy, particularly the N1 and N2 phases, whereas increasing contact spacing to 2000 μm increased the N2 phase. Similarly, shorter contact-to-contact distances reduced substantially the LFP signal magnitude. We initially expected that moving the recording contacts closer to the stimulating contact would increase ECAP signal strength by reducing the distance between activated neurons and recording contacts. However, this was more than offset by the reduced contribution from distant neurons associated with shorter distances between bipolar recording contacts (Lempka and McIntyre, 2013). Monopolar recording will maximize contributions from distant neurons, but even still, it

is unlikely that the ECAP would include contributions from all activated neurons. Single-unit recordings indicated that neural elements contribute to the ECAP up to lateral distances of ~1 mm, whereas the average radius of neural activation could extend to ~2.8 mm during clinical DBS, assuming a spherical volume of activation of 91 mm^3 about a monopolar stimulating contact (Frankemolle et al., 2010).

These results inform electrode design for improved ECAP recording. Reducing the recording contact length and electrode diameter, as well as increasing contact spacing, can increase the signal magnitude, and the two former changes can also increase spatial sensitivity. We envision a novel electrode design that, compared to the Medtronic 3387 electrode, has a smaller recording contact length (1000 μm) and diameter (500 μm), as well as greater contact spacing (2000 μm). After adjusting stimulation voltage to maintain equal neural activation between the Medtronic 3387 electrode and this design (5.4% difference in the percentage of total neural activation in the first 0.2 ms), the ECAPs recorded with the new electrode exhibited greater energy of phases P1 (198.8%), N1 (119.3%), and P2 (2170.7%), although N2 was reduced (-63.7%) (Fig. 5.8). Moreover, the greater spacing between stimulating and recording contacts in the novel electrode reduced the artifact magnitude by 23% compared to the Medtronic 3387 electrode, calculated using the tissue heterogeneity model methodology (Fig. 4.4), but with homogenous conductivity in the peri-electrode space ($0.\overline{3}$ S/m). Two potential shortcomings of this design are the increase in stimulation voltage requirements, due to

the smaller stimulating contact diameter, and increased selectivity for local cells, such as thalamocortical neurons, relative to passing axons, such as cerebellothalamic afferents, even though the latter may mediate the therapeutic effectiveness of Vim-DBS. Additionally, if contacts on the new electrode are to be used for stimulation, there are changes in the risks for tissue damage and electrode corrosion.

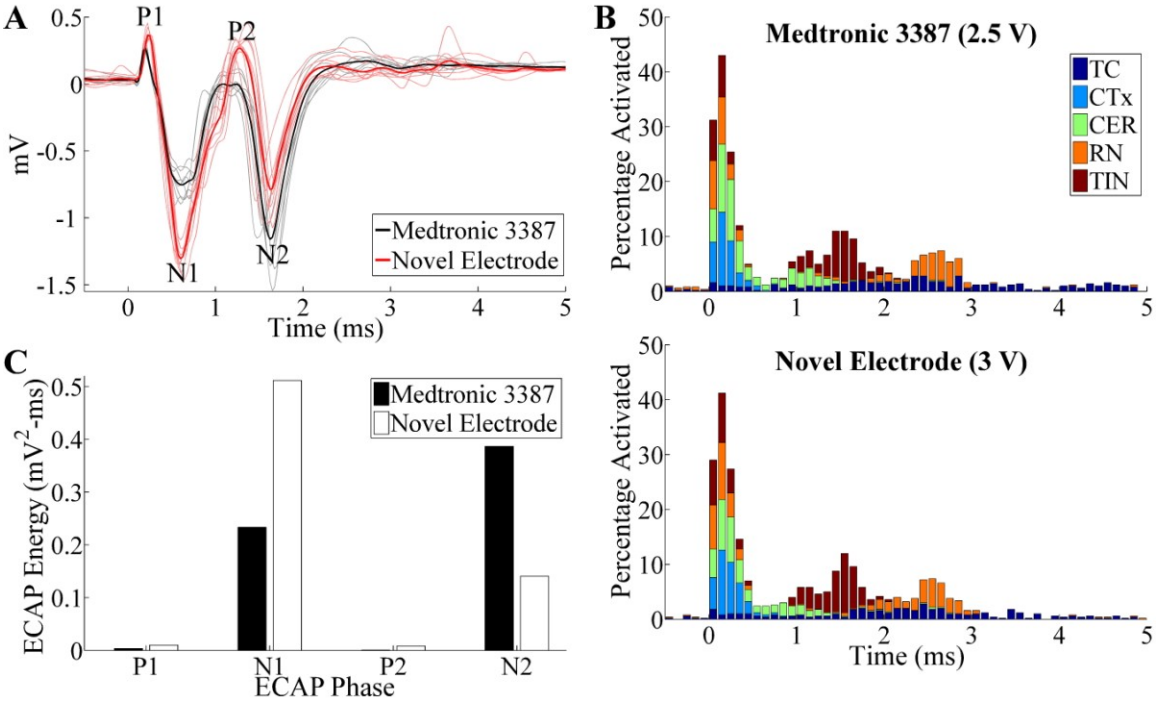

Figure 5.8: A: ECAPs recorded with the original, Medtronic 3387 electrode and the novel electrode with smaller recording contact area and larger contact spacings. DBS amplitude was 2.5 V for the original electrode and 3 V for the novel electrode. B: Neural activation for the electrodes tested in (A). Data presentation is similar to Fig. 5.3B. C: Signal energy of each phase from the ECAP responses in (A).

The ECAP was affected by changes in the composition of the peri-electrode space intended to represent recording with acute or chronic placement of the electrode. Neuronal cell loss in the peri-electrode space alone had a substantial impact on ECAP

and LFP recordings, even with adjustments in stimulation amplitude to maintain similar levels of neural activation for the former. Further, acute edema decreased the signal energy in single-unit recordings, ECAPs, and LFPs, while chronic glial encapsulation had the opposite effect. Similarly, Moffitt and McIntyre found that reductions in current density with glial encapsulation were counteracted by increases in resistivity and resulted in a net increase in electric potentials, per Ohm's law, while the opposite was true for edema (Moffitt and McIntyre, 2005). It is also important to consider how glial encapsulation of the electrode can increase the magnitude of the stimulus artifact, particularly with impedance imbalances between contacts. The stimulus artifact can overlap with and distort the ECAP (**Chapter 4**), and thereby negate potential increases in ECAP amplitude under chronic recording conditions.

The computational model used in this work provided insight into how properties of the electrode and peri-electrode space affect recorded neural activity, but there were several limitations. First, geometrical approximations were made for the location of the DBS electrode and for the neural fiber trajectories, which could have affected neural activation during DBS and the resulting ECAP signal. Second, the model did not include representations of the ETI, tissue capacitance, or tissue inhomogeneity, which could have influenced both neural activation during DBS (Butson and McIntyre, 2005, Yousif et al., 2008a, Grant and Lowery, 2010, Lempka et al., 2010, Tracey and Williams, 2011) as well as the recorded activity. In a modeling study of beta band LFP

recordings made from a DBS electrode, the capacitance of the ETI and bulk brain tissue had no significant effect on the signal, although these effects are expected to be frequency-dependent (Lempka and McIntyre, 2013). Specifically, tissue capacitance and tissue inhomogeneities generate a low-pass filtering effect (Bedard et al., 2004, 2006, Buzsaki et al., 2012) that could impact the higher frequency components of the ECAP signal. Conversely, the ETI acts as a high-pass filter (Wise and Angell, 1975, Butson and McIntyre, 2005), which can affect theta LFP recordings (Yousif et al., 2008b, Rosa et al., 2010), but should not substantially alter the ECAP. The electrode impedance is related to the surface area of the contacts (Butson et al., 2006), meaning that the effects of the ETI on the LFP may vary across electrode designs. Third, we did not consider the impact on signal fidelity of thermal noise (or other noise sources), which would increase with the higher ETI impedance expected for a smaller contact surface area (Dimitrova et al., 1999, Lempka et al., 2011). Consequently, both the signal and noise amplitudes may increase with the use of smaller electrode diameters or contact lengths, leading to a potentially ambiguous effect on the signal-to-noise ratio.

6. Conclusions

Deep brain stimulation (DBS) is an FDA-approved, surgical therapy for movement disorders, including essential tremor (ET) and Parkinson's disease (PD), but the mechanisms of action remain unclear. The clinical efficacy of DBS depends on identifying appropriate stimulation parameters, but programming sessions are time consuming, costly, and can result in sub-optimal outcomes. Closed-loop systems could provide automatic parameter adjustment to optimize treatment using a neural feedback control signal, such as local field potentials (LFPs) or single-unit recordings.

We hypothesized that the evoked compound action potential (ECAP) could serve as a closed-loop feedback signal by providing insight into the element type and extent of neural activation in the vicinity of the DBS electrode during stimulation. This was based on analogous ECAP recordings from the cochlear nerve that are used to assist programming of cochlear implants. The purpose of this dissertation was to determine the suitability of the ECAP as a feedback control signal by recording and characterizing the signal, using experimental and computational methods. The work includes the first ECAP recordings made from the same DBS lead used for stimulation in preclinical and clinical studies. We demonstrated that ECAPs: 1) could be measured in the presence of a stimulus artifact using our novel recording hardware, 2) provided insight into neural activation across a range of stimulation parameters, 3) had characteristics that were

correlated to clinical tremor, and 4) were affected by the recording conditions and the DBS electrode design.

6.1 Summary of results

6.1.1 Instrumentation to record ECAPs during DBS

The first aim was to develop recording instrumentation that could record ECAPs with high fidelity in the presence of a stimulus artifact (**Chapter 2**). The relatively large artifact can saturate recording amplifiers and mask or distort short latency ECAPs. Previous techniques to remove the artifact include post-processing (i.e., template subtraction) and filtering, but these were inadequate for a closed-loop application, where "real time" recording is required. We developed DBS-ECAP instrumentation, which combined commercial amplifiers and additional circuit components to reduce the artifact. These components included anti-parallel diodes at amplifier inputs to clip selectively the artifact, internal amplifier blanking during delivery of each stimulus pulse, and a relay disconnecting the stimulating electrodes following each pulse to limit capacitive discharge from the electrode-tissue interface (ETI). ECAPs were recorded from non-stimulating contacts on the DBS electrode, eliminating the need for additional electrodes and ensuring that recording contacts were near the activated neural elements, using a differential configuration that reduced common-mode noise.

We validated the capability of this instrumentation to reduce the artifact and enable high fidelity recordings through *in vitro* and *in vivo* experiments. *In vitro* testing

performed in a saline tank demonstrated that reduction of the artifact magnitude with DBS-ECAP instrumentation enabled an increase in gain by a factor of 1,000-5,000 times without saturation, compared to a conventional biopotential amplifier. The recording fidelity of mock ECAPs (mECAPs), which were delivered by a pair of microelectrodes near the DBS electrode, was increased by the higher gains and reduced temporal overlap with the artifact. Sub-millivolt mECAPs with short latencies of only 0.5 ms could be recorded with low distortion using clinically-relevant DBS parameters and short, symmetric, biphasic pulses. However, longer, asymmetric pulses, such as those used in implanted pulse generators (IPGs), precluded recording ECAPs with low distortion except at latencies of ≥1 ms. The artifact was smaller when recording contacts were symmetrical about a monopolar stimulation contact (*monopolar symmetric*), thereby balancing the potentials generated by stimulation, in comparison to configurations using *bipolar* stimulation or monopolar stimulation with asymmetrical recording contacts (*monopolar asymmetric*). Physiological ECAPs were also recorded *in vivo* from an anesthetized cat, implanted with a mini DBS electrode in the ventrolateral (VL) nucleus of the thalamus, without contamination by the artifact. Based on these findings, we used the DBS-ECAP instrumentation for all subsequent experimental work in this dissertation.

As well, we developed an electrical circuit equivalent model (PSpice), which represented the properties of the electrode and medium, stimulation output, and

components of the DBS-ECAP instrumentation, to study the sources of any residual stimulus artifact. First, the turn-off delay of the stimulator relay allowed some capacitive discharging before the electrodes were completely disconnected, and using a relay with a more rapid *off* time could have further reduced the corresponding third phase of the artifact. Second, the larger artifact observed *in vivo*, particularly in post-mortem recordings, compared to *in vitro*, was presumably generated by tissue inhomogeneities between contacts, and by discharging of the tissue capacitance after each pulse.

6.1.2 Investigating the neural origin of ECAPs

For the second aim, we characterized the ECAP *in vivo* across stimulation parameters and determined the neural elements contributing to this signal (**Chapter 3**). ECAPs recorded during acute DBS in the VL thalamus of anesthetized cats were consistent across experiments, and depended on the stimulation and recording contact configuration. For the monopolar symmetric configuration, we observed primary positive (P1) and negative (N1) phases, followed by secondary positive (P2) and negative (P2) phases, with the latency of secondary phases dependent on electrode location. Responses were similar for cathodic- and anodic-phase first polarities, as expected with the use of symmetric, biphasic pulses, ECAP signal energy increased with larger DBS amplitudes ($P<0.0001$) and pulse widths ($P<0.002$), and the signal energy of secondary ECAP phases was larger at 10 Hz than 100 Hz DBS ($P<0.002$). While the ECAP waveform shape differed for alternative contact configurations, the effect of stimulation

parameters was similar to the monopolar symmetric case. The monopolar asymmetric configuration generated a N1'-P1'-N2' waveform, corresponding to action potential propagation past each of the two recording contacts, and the waveform recorded with the bipolar configuration was highly dependent on electrode location.

We investigated the neural origin of the ECAP using pharmacological interventions and a validated computational model of thalamic DBS. The model was extended to enable calculation, using the reciprocity theorem, of the ECAP response generated by neuronal transmembrane currents. The experimental and computational ECAPs were similar in shape for different contact configurations, and were correlated across stimulation parameters for the monopolar symmetric configuration ($R=0.80$-0.95, $P<0.002$). The model indicated that direct activation of thalamocortical (TC) cells produced P1 and direct activation of pre-synaptic inputs produced N1. Moreover, post-synaptic activation of TC cells and inputs from the reticular nucleus and thalamic interneurons generated the secondary phases. This was confirmed by the reduction of secondary phases following microinjection of glutamate receptor antagonists CNQX/APV, and by the increased secondary phase latency with administration of muscimol, a $GABA_A$ receptor agonist, which hyperpolarized TC neurons. The model also demonstrated that increases in ECAP signal energy with DBS amplitude and pulse width resulted from greater neural activation, and the effect of frequency on secondary phases likely resulted from increased synchronization of post-synaptic TC activation at

10 Hz compared to 100 Hz DBS. Therefore, ECAPs provide information about the spatiotemporal activation pattern (based on the timing and polarity of ECAP phases), the spatial extent of activation (ECAP magnitude), and types of elements activated (pre- or post-synaptic cells).

The computational model could have been improved in several ways to generate ECAP waveforms that were even more similar to experimental recordings. The cat VL thalamus was represented using a geometrical approximation based on the human ventral intermediate (Vim) nucleus of the thalamus (Birdno et al., 2012). Model accuracy may have increased by instead using the true anatomical shape of the cat VL thalamus (Jimenez Castellanos, 1949), as well as accurate fiber trajectories and correct electrode positioning. Second, inclusion of thalamocortical-corticothalamic reciprocal synaptic connections (Hersch and White, 1981, Briggs and Usrey, 2007, Mina et al., 2013) may have led to more accurate representation of secondary ECAP phases. A final improvement would have been incorporation of the ETI, tissue capacitance, and tissue inhomogeneities, which may have filtered the ECAP signal.

6.1.3 Relationship between ECAP characteristics and tremor during thalamic DBS

For the third aim, we determined the feasibility of recording ECAPs in human subjects, investigated the neural origin of this ECAP and the sources of any stimulus artifact, and correlated ECAP characteristics with motor symptoms (**Chapter 4**). Experiments were conducted intraoperatively, with external stimulating and recording

hardware connected to the subject's implanted DBS brain lead unilaterally. We recorded ECAPs and measured tremor using an accelerometer across DBS amplitudes, pulse widths, and polarities. This was performed on patients with ET, tremor-dominant PD, or fragile-X associated tremor/ataxia syndrome (FXTAS), who were undergoing surgery for initial electrode implantation (acute) or replacement of their IPG (chronic).

There was large subject-to-subject variation in stimulus artifact amplitude, especially among the chronically implanted electrodes. This artifact variability was consistent with cochlear ECAP measurement (Miller et al., 2008), and was explored using the electrical circuit equivalent model from **Chapter 2** and a finite element method (FEM) volume conductor model that represented the heterogeneous conductivity in the peri-electrode space. Both models revealed that the larger stimulus artifacts may have been caused by chronic glial encapsulation of the electrode, resulting in imbalances in tissue impedance between contacts. While the impedance imbalance was greater in chronic experiments compared to acute experiments, a relationship for the former between the extent of impedance imbalance and the magnitude of the stimulus artifact was not observed. The difference in recording fidelity between acute and chronic conditions demonstrates the importance of measuring neural activity at both time points within a study, rather than the acute setting alone, by utilizing the IPG replacement surgery for intraoperative clinical recordings (Birdno et al., 2008).

Despite the presence of the stimulus artifact, we obtained high fidelity ECAP recordings from both acutely- and chronically-implanted electrodes. In recordings containing a stimulus artifact, polarity averaging was performed to remove residual artifact. When present, ECAPs displayed a consistent waveform with N1-P1-(N2-P2) phases (N2 and P2 not always observed). Further, specific ECAP phase characteristics varied systematically with stimulation parameters, including non-monotonic relationships between ECAP energy and DBS amplitude, and increases in secondary phase energy with reductions in frequency from 130 to 10 Hz. With variation in DBS amplitude and polarity, increases in the energy of ECAP phases were correlated with reductions in tremor at 130 Hz or exacerbation of tremor at 10 Hz across subjects with near statistical significance ($R=0.6\text{-}0.87$, $P<0.078$). Moreover, the energy of secondary phases was positively correlated with tremor across DBS frequencies ($R=0.69$, $P<0.061$). The statistical power of these relationships could have been increased by testing a greater number of parameters in a given experiment, performing replicate trials to reduce variability, or measuring ECAPs when DBS was applied at other, less therapeutically effective contacts. However, the intraoperative setting and patient fatigue limited the number of parameters that could be tested. ECAPs can be recorded in the clinical setting, and their relationship with tremor suggests that they may provide a feedback control signal for automated DBS parameter adjustment.

The computational model of thalamic DBS was used to explore the neural origin of clinical ECAPs. Shifting the electrode from its original position (Birdno et al., 2012) along its axis in the ventral direction resulted in a similar waveform to that recorded experimentally, and aligned with targeted clinical electrode placement of contact 0 at the ventral border of Vim. The positional dependence could be useful in targeting the Vim during implantation or in selecting the optimal contact(s) for stimulation. The model also indicated that activation of cerebellothalamic fibers dominated the clinically measured ECAP, and given the experimental relationship between ECAP energy and tremor, this suggested that excitation of these fibers is critical in DBS therapy, a conclusion supported by other studies (Hamel et al., 2007, Herzog et al., 2007, Sandvik et al., 2011, Birdno et al., 2012, Keane et al., 2012). The model also helped to explain the non-monotonic relationship between ECAP energy and DBS amplitude, in which contributions from additional activation of corticothalamic inputs at higher amplitudes destructively interfered with the composite ECAP and reduced the apparent signal magnitude.

There are several changes to the clinical protocol that may have improved the quality of ECAP recordings. First, the stimulation counter electrode used in IPG replacement surgeries was placed externally, and the resulting voltage drop across the skin could have reduced voltages in the brain tissue, and therefore, decreased the extent of neural activation. Using an internally-placed counter electrode, such as a retractor at

the incision site, would have mitigated this voltage drop effect. Second, the impedance imbalances between contacts in subjects undergoing IPG replacement surgery may have been generated by chronic stimulation at only one of the two recording contacts, since stimulation at a contact causes attached proteins and cells to desorb from the surface (Lempka et al., 2010). One solution is to select the contact configuration appropriately, with the expectation that chronic DBS will reduce the impedance at the clinical stimulating contacts, and which may require use of the monopolar asymmetric configurations (or alternatives). Another solution is to apply low amplitude DBS temporarily at all contacts used for stimulation or recording immediately prior to the ECAP recording protocol. This would disrupt the encapsulation layer and thereby reduce the overall impedance as well as any imbalances between contacts, and it would take approximately 30 minutes for the effect to reach steady state (Lempka et al., 2010). A third solution is to perform impedance balancing at the inputs to the differential amplifier in the DBS-ECAP instrumentation. Placing an adjustable load, such as a potentiometer, at the front-end of this amplifier stage could minimize differences in impedance between the stimulation contact and each recording input, and thereby reduce the stimulus artifact.

6.1.4 Influence on the neural signal of recording conditions and electrode design

The fourth aim was to understand better the factors that influence ECAP recording, including the physical presence and dimensions of the electrode, as well as

changes in the peri-electrode space composition in the transition from acute to chronic recording stages (**Chapter 5**). The computational model from **Chapter 4** was used to calculate the evoked response from an activated single elements (local cell or passing axon), as well as ECAP responses and LFP activity from the thalamic neuronal population, across different conditions. The population ECAP and LFP signals were unaffected by the presence of the highly conductive recording contacts. Acute edema or glial encapsulation in the peri-electrode space decreased or increased, respectively, the magnitude of the single-unit response, ECAP signal, and LFP signal response, after accounting for neuronal cell loss in the peri-electrode space. On the other hand, we saw previously that glial encapsulation can generate impedance imbalances and increase the stimulus artifact magnitude, which may negate increases in recording fidelity associated with a larger ECAP.

Reducing the recording contact surface area by reducing diameter or length increased the magnitude of the single-unit response, had variable effects on the different phases of the ECAP, and in most cases had a small effect on the LFP. Smaller contacts increased spatial selectivity for nearby neurons by averaging biopotentials over a smaller area, and smaller diameter recording contacts increased selectivity for local cells over passing axons, whereas the opposite was true with larger diameters. This indicated that larger diameter electrodes would preferentially record from pre-synaptic inputs such as cerebellothalamic fibers over TC neurons, and was confirmed when comparing

the neural contributions to the ECAPs from preclinical and clinical studies in **Chapters 3 & 4**. Shorter spacing between contacts reduced ECAP energy and LFP magnitude due to smaller contributions from more distant neurons (Lempka and McIntyre, 2013), whereas increasing contact spacing had variable effects on the ECAP phases and a small effect on the LFP. An improved electrode for high fidelity ECAP recording would therefore use a smaller diameter and recording contact length, and longer contact spacing, which we found would increase ECAP signal energy. This study informed recording conditions that improved ECAP recording fidelity, and was the first to investigate alternative DBS electrode designs for improved neural recording.

6.2 Clinical relevance of findings

The work performed in this dissertation supported the use of the ECAP as a feedback control signal for automated parameter adjustment, and provided insight into the mechanisms of action of DBS. The clinical study performed in **Chapter 4** identified ECAP signatures of clinical effectiveness, including a correlation between greater phase energy and reductions in tremor at 130 Hz, which could be used to adjust DBS amplitude or pulse width. Further, secondary phase energy was increased at lower frequencies, and was correlated with exacerbation of tremor. This relationship could be used to identify the critical DBS frequency that masked pathological firing patterns (Kuncel et al., 2007). The relationship between ECAP phase energy and tremor differed between subjects, and the absolute phase energy varied by an order of magnitude,

suggesting that the threshold ECAP energy value used for parameter selection needs to be subject specific and normalized to some maximum energy value.

Automated selection of stimulation parameters and contacts in clinical programming sessions could increase the therapeutic benefit of DBS, reduce side effects, and improve battery life. Moreover, periodic parameter adjustments in closed-loop DBS systems would maintain optimal settings as the disease progressed or the response to DBS changed over time, and proof-of-concept was demonstrated in a computational model-based implementation of this system (**Appendix A**).

The results from the clinical study also improved our understanding of DBS by indicating the type and extent of activation required for therapy. Cerebellothalamic afferent inputs were the dominant contributor to clinical ECAPs, and given the correlation between ECAP phase energy and tremor, this suggests that activation of these elements is critical. This was in agreement with prior work showing that effective DBS for ET masked pathological bursting activity from the cerebellum to the thalamus (Birdno et al., 2012, Keane et al., 2012), and that targeting these fibers during DBS implantation may be more effective than implantation in the Vim proper (Hamel et al., 2007, Herzog et al., 2007, Sandvik et al., 2011). Given the apparent role of cerebellothalamic afferent activation in tremor reduction, novel electrodes or stimulation waveforms targeting those neural elements are expected to maximize therapeutic outcomes. ECAP measurement also provided insight into whether effective DBS

required activation of a specific volume of tissue within the targeted Vim nucleus, irrespective of location, or a particular region within the Vim nucleus. Given the correlation between ECAP signal energy and tremor, and noting that the former provides a measure of the extent of neural activation, we concluded that DBS must activate a sufficient volume of tissue for clinical benefit. If it was necessary to activate a particular brain region, then increases in ECAP signal energy would not necessarily be related to motor symptoms. However, using high DBS amplitudes (i.e., above the clinical voltage) that extend activation outside of Vim and into brain regions that aggravate tremor, such as the internal capsule, can reduce the effectiveness of tremor, as we saw with the non-monotonic relationships between tremor and DBS amplitude.

6.3 Future directions

The findings from this dissertation suggest several future research directions to pursue, exploring further the electrode location dependency of ECAP characteristics, including exploring ECAP recording from other brain targets, clinically validating an ECAP-based closed-loop DBS system, and testing *in vivo* the effect on ECAP recording fidelity of different electrode dimensions.

The focus of this dissertation was on ECAP recording during thalamic DBS, but other brain targets are commonly targeted for treatment of movement disorders, including the subthalamic nucleus (STN) for PD. The preclinical, clinical, and computational modeling studies presented in **Chapters 3 & 4** could be extended to

ECAP recording during STN-DBS. The experimental setups would be very similar, except that clinical assessment of motor symptoms would use an alternating finger tapping task (Brocker et al., 2013), which is significantly correlated with UPDRS scores in PD, particularly the bradykinesia subscore (Taylor Tavares et al., 2005). Additionally, because there is a longer latency before onset or washout of the effects of STN-DBS, compared to thalamic DBS, trial lengths should be extended from 2 min to 8 min, with DBS *off* for the first 4 min and *on* for the next 4 min (Beuter and Titcombe, 2003, Temperli et al., 2003). During STN-DBS, one would expect ECAP contributions from local STN neurons and pre-synaptic inputs from the GPe and cortex, measured at the ventral recording contact, and contributions from projecting axons from the GPi to the thalamus, measured at the dorsal recording contact (Miocinovic et al., 2006). Activation of fibers in the adjacent internal capsule (IC) could also contribute to the measured ECAP signal. A computational model of ECAP recording during STN-DBS could determine the neural origin of the signal. We propose using the Miocinovic model (Miocinovic et al., 2006), modified with explicit representation of pre-synaptic inputs into the STN. This work may help to validate the hypotheses that effective STN-DBS requires activation of pre-synaptic cortico-STN afferents (Gradinaru et al., 2009), and that side effects are generated by stimulation of the IC (Krack et al., 2002, Tamma et al., 2002). It would also be useful in investigating the feasibility of using ECAPs for automated parameter adjustment in closed-loop STN-DBS.

Another extension of this work is to investigate further the electrode location dependent character of the ECAP within preclinical *in vivo* experiments. We observed previously that ECAP characteristics varied with electrode location in both the preclinical *in vivo* study (**Chapter 3**), and the clinical thalamic DBS computational model (**Chapter 4**). For the former, the electrode was fixed in one location for the duration of each experiment, and ECAPs were compared across animals in conjunction with histological identification of electrode locations. However, to confirm this electrode location dependency, ECAPs should be measured within a given cat experiment at several locations as the electrode is advanced in a dorsal-to-ventral trajectory.

An additional potential extension of this work is implementation of a real-time, ECAP-based closed-loop DBS system, using the intraoperative clinical setting discussed in **Chapter 4**. This system would provide automated modulation of DBS parameters, including amplitude, pulse width, and/or frequency, using a closed-loop controller (i.e., proportional-integral-derivative or fuzzy logic (Lin et al., 2012, Gorzelic et al., 2013)) to obtain a target ECAP energy value that maximized therapy. An initial assessment of correlations between ECAP signal energy and motor symptom responses would need to be conducted in each subject to identify this target ECAP value. For safety, the closed-loop system should have specified maximum values for DBS parameters, with current density limited below 30 $\mu C/cm^2$, in the event that the controller becomes unstable. Motor symptom assessment would be conducted periodically to quantify DBS

effectiveness, and any side effects noted on a 1-10 scale. Finally, measures of DBS effectiveness, side effects, and power usage should be compared between the steady-state closed-loop parameters and open-loop parameters selected previously by a neurologist.

We assessed the effect of variation in electrode designs on ECAP recording fidelity using a computational model in **Chapter 5**, and in future work these outcomes could be validated through an *in vivo* study. DBS electrodes of various diameters, contact lengths, and contact spacings would first need to be fabricated. Using the preclinical experimental setup described in **Chapters 2 & 3**, ECAPs would then be recorded from each electrode design in-turn, and compared against that recorded with the original design. The same implantation trajectory should be used between each tested electrode, with the stereotactic location of the stimulating contact(s) remaining constant, to generate equal neural activation between the tested designs.

6.4 Concluding remarks

Closed-loop DBS systems could reduce the clinical burden of parameter selection and optimize therapeutic outcomes. We hypothesized that the ECAP could provide insight into neural activation during DBS and therefore serve as a suitable feedback control signal for a closed-loop system. We measured ECAPs in preclinical and clinical studies using instrumentation that reduced the stimulus artifact to improve recording fidelity, and with a computational model that provided insight into the neural origin of

the signal. These represent the first ECAP measurements made during DBS from the same brain lead used for stimulation. We provided experimental and computational evidence that the ECAP provides insight into the type and extent of neural activation following each DBS pulse, varies systemically with stimulation parameters, and is correlated with tremor. Moreover, the character of the ECAP and stimulus artifact is affected by changes in the composition of the peri-electrode space, and the former varies with dimensions of the DBS electrode. Our results support previous findings that suggested effective DBS requires activation of cerebellothalamic fibers, and demonstrate the feasibility of the ECAP as a potential feedback signal in closed-loop DBS systems.

Appendix A: Closed-loop deep brain stimulation based on evoked compound action potentials: a simulation analysis

A.1 Introduction

Deep brain stimulation (DBS) is a FDA-approved therapy for treatment of Parkinson's disease, essential tremor, and other movement disorders. DBS systems currently operate in an open-loop manner, in which invariant stimulation is delivered continuously, and a physician periodically closes the loop by adjusting stimulation parameters based on the symptom response and side effects profile. However, this methodology requires significant clinical effort (Ondo and Bronte-Stewart, 2005) and may not result in optimal settings (Okun et al., 2005, Moro et al., 2006). Alternatively, closed-loop DBS systems have been proposed to adjust DBS settings automatically based on a recorded neuronal feedback signal.

Several closed-loop brain stimulation systems have been tested experimentally or in simulations. DBS in the globus pallidus interna (GPi), with timing controlled by single-unit activity in the motor cortex, ameliorated Parkinsonian symptoms in MPTP-treated monkeys better than continuous, open-loop, 130 Hz DBS (Rosin et al., 2011). Recordings of local field potentials (LFPs) from the hippocampus (HC) in sheep were used to detect seizures during HC-DBS and temporarily discontinue stimulation (Stanslaski et al., 2012). Similarly, seizures were automatically detected in clinical electrocorticogram (ECoG) recordings and triggered high-frequency stimulation, either

locally in the cortex or remotely in the anterior thalamus, which reduced the mean seizure rate (Kossoff et al., 2004, Fountas et al., 2005, Osorio et al., 2005). A modeling study of thalamic DBS demonstrated that an adaptive minimum variance controller of stimulation amplitude could more closely restore the recorded LFP spectrum to a tremor-free reference spectrum than open-loop DBS (Santaniello et al., 2011). Additionally, thalamic fidelity was improved in the Rubin-Terman (RT) network model of the basal ganglia (Rubin and Terman, 2004) with subthalamic nucleus (STN) DBS proportional to the filtered and time-delayed STN-LFP signal (Guo and Rubin, 2011). Finally, a proportional-integral-derivative (PID) closed-loop controller was successfully implemented in the RT model, with the amplitude or frequency of GPi-DBS driven by estimates of thalamic reliability or synaptic conductances between GPi and thalamus (Gorzelic et al., 2013). PID controllers have also be used to regulate muscle force or joint angle via stimulation with intramuscular or nerve cuff electrodes in animal models (Crago et al., 1980, Lin et al., 2012) and in human upper (Crago et al., 1991, Lemay and Crago, 1997) and lower (Chizeck et al., 1985, Abbas and Chizeck, 1991) extremities.

The objective of this work was to determine the feasibility of closed-loop DBS using the evoked compound action potential (ECAP) as the feedback control signal. In prior studies, we showed that ECAPs can be recorded during DBS in preclinical and clinical studies, are modulated systematically by stimulation parameters, and are correlated to clinical motor symptoms (**Chapters 2-4**). The correlation between ECAP

characteristics and motor symptoms served as the basis for a PID controller or its variants, including P and PD controllers, for adjustment of DBS amplitude or hybrid amplitude/pulse width modulation (Tyler and Durand, 1997, Lin et al., 2012). We evaluated in simulation the ability of this system to identify parameters that minimized burst-driver band power in thalamocortical neurons, a proxy for clinical effectiveness (Birdno et al., 2012), and to adjust stimulation parameters in response to disturbances.

A.2 Methods

We implemented in simulation an ECAP-based closed-loop DBS system (Fig. A.1) consisting of a P, PD, or PID controller coupled to a DBS parameter modulator. Stimulation was delivered to the plant, which was a validated biophysically-based population model of thalamic DBS and generated the ECAP responses that were subsequently analyzed by the controller.

The details of the thalamic DBS model have been described in detail in **Chapter 3**, and are reviewed briefly. A finite element method (FEM) volume conductor model was used to calculate the voltages generated by a three-dimensional geometrical representation of a NuMed mini DBS electrode within the cat ventrolateral (VL) nucleus of the thalamus, all encompassed in a cylindrical brain tissue volume. The FEM model output was coupled to validated biophysical cable models, which included anatomical

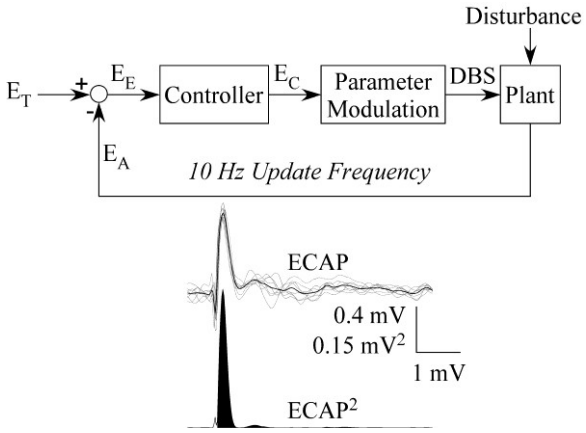

Figure A.1: Implementation of a closed-loop DBS system in simulation. The ECAP signal energy error (E_E) was defined as the difference between the target (E_T) and actual (E_A) signal energies. To obtain the latter, ECAPs were measured from a thalamic DBS model ("plant"), the stimulus-triggered average (black trace, *below*) was calculated from single ECAP responses (gray traces), the averaged signal was squared, and integration was performed over the duration of the signal (black fill), excluding the residual stimulus artifact. E_E served as the input to the controller, and the controller output (E_C) was used by the DBS parameter modulator to adjust amplitude and/or pulse width.

and electrical representations of thalamocortical (TC) neurons, pre-synaptic inputs from the cortex (CTx), cerebellum (CER), reticular nucleus (RN) and thalamic interneurons (TIN), and their synaptic connections. A neural unit was defined as a single TC neuron and its corresponding pre-synaptic inputs from the four brain areas, and 500 of these units were randomly distributed with TC soma locations confined within the VL thalamus. Neural elements that intersected with the electrode or the surrounding 150 μm thick peri-electrode space were removed. The GABAergic synaptic conductances from RN and TIN to TC neurons were varied to generate 50% bursting, 30% regular spiking, and 20% random spiking TC neurons (Birdno et al., 2012). Additionally, two models were used, designated as *healthy* and *tremor* conditions, and were differentiated

by intrinsic network activity. Specifically, a 20 Hz Poisson train of spikes was introduced to CTX inputs in both *healthy* and *tremor* conditions, whereas a 5.8 Hz harmaline burst input was introduced to 50% of CER afferents in the *tremor* condition only. Finally, the somatic noise injection present in the original model was removed (Birdno et al., 2012).

Following an initialization period of 500 ms, symmetric, biphasic, cathodic-phase first, voltage-controlled stimulation was applied from DBS contact 1. We recorded the transmembrane potential (V_M) of all TC somata, and calculated the mean fraction of V_M power in the burst-driver band (5.8±1 Hz, 0.4 Hz resolution) after removing any DC offset. Additionally, the transmembrane currents were measured in the compartments of all neural elements to calculate the differential ECAP voltage across DBS recording contacts 0 and 2 using the reciprocity theorem (Helmholtz, 1853, Moffitt and McIntyre, 2005). Subsequent ECAP post-processing steps included stimulus artifact template subtraction, in which the template was calculated with a subthreshold voltage in the absence of intrinsic network activity with linear detrending, two cascaded filtering stages with a 10 Hz - 10 kHz band-pass, and stimulus-triggered averaging over 8 responses to replicate post-processing performed experimentally (**Chapter 3**). Finally, ECAP signal energy was calculated by squaring the signal and integrating over its duration, excluding residual stimulus artifact (Fig. A.1). The simulation time step was 25 μs.

The ECAP signal energy error ($E_E = E_T - E_A$) was the difference between the user-specified target signal energy (E_T) and the actual signal energy generated in the thalamic DBS model (E_A) and served as the feedback control signal (Fig. A.1). The target energy was selected by quantifying the relationship between ECAP signal energy and the fraction of somatic V_M power in the burst-driver band. The latter is strongly correlated with tremor across DBS conditions (R^2=0.81) (Birdno et al., 2012) and was used as a proxy for clinical effectiveness. Both ECAP signal energy and burst-driver band power were calculated in 2.5 s trials across DBS amplitudes, pulse widths, and frequencies in the *tremor* condition, and burst-driver band power was also calculated with DBS *off* in the *healthy* and *tremor* conditions. The target ECAP signal energy was selected such that the burst-driver band power was reduced from the elevated level in the *tremor* condition without stimulation to the level in the *healthy* condition.

DBS parameters were updated over multiple iterations at a 10 Hz frequency using a P, PD, or PID controller. The initial DBS parameter set was 1 V amplitude and 60 μs pulse width. After each 100 ms iteration, the actual ECAP signal energy and corresponding energy error were measured, and the controller output at the at the n^{th} iteration ($E_C(n)$) was calculated as:

$$E_C(n) = K_P E_E(n) + K_I T \sum_{i=n-2}^{n} E_E(i) + K_D \frac{E_E(n) - E_E(n-1)}{T} \qquad \text{(Equation A.1)}$$

where K_P, K_I, and K_D were the proportional, integral, and derivative gains, and T was the sampling period of 100 ms. The gains were determined with the Ziegler-Nichols (Z-N)

tuning methodology (Ziegler and Nichols, 1942) in a separate simulation trial. For Z-N tuning, K_D and K_I were set to zero and K_P was adjusted to the minimum value (K_U) that generated oscillations in the controller output with constant amplitude and period (P_U). Using DBS amplitude modulation alone, oscillations were generated with a period of P_U=200 ms (two controller iterations) using K_U=38. The P and PID controller gains were then tuned with Z-N values, and the PD controller gains tuned using Z-N values for the PID controller and the integral term removed:

P controller: $K_P = 0.5K_U$; $K_I = 0$; $K_D = 0$ (Equation A.2)

PD controller: $K_P = 0.6K_U$; $K_I = 0$; $K_D = (K_P \times P_U)/8$ (Equation A.3)

PID controller: $K_P = 0.6K_U$; $K_I = 2K_P/P_U$; $K_D = (K_P \times P_U)/8$ (Equation A.4)

The DBS parameter modulator used the controller output to adjust the stimulation amplitude exclusively, or both amplitude and pulse width in tandem. For the former, DBS amplitude was adjusted in direct proportion to $E_C(n)$, rounded to the nearest 0.1 V (Volkmann et al., 2006), and pulse width was fixed at 60 μs to minimize charge (Kuncel and Grill, 2004). For hybrid amplitude and pulse width modulation, we compared the power requirements (power ~ voltage^2 × pulse width (Kuncel and Grill, 2004)) for an adjustment of amplitude, again proportional to $E_C(n)$, or for an adjustment of pulse width by 30 μs, increasing for $E_C(n) > 0$ and decreasing for $E_C(n) < 0$, with a lower bound of 60 μs. Whichever adjustment, amplitude or pulse width, minimized power was implemented for that controller iteration, although we forced adjustment of

amplitude in the first controller iteration due to the low starting voltage value. The closed-loop controller ran until E_A reached steady state and E_E approached zero, after which a disturbance was introduced. In one implementation, the percentage of TC neurons with bursting behavior was increased from 50% to 100%, as a way to model progression of the disease state. For a second disturbance, a glial encapsulation layer was introduced in the FEM model by reducing the conductivity of the peri-electrode space from that of brain tissue ($0.\overline{3}$ S/m) to 0.1 S/m (Butson et al., 2006), representing a transition to a chronic implantation condition (Yousif et al., 2008a, Lempka et al., 2010).

A.3 Results

An ECAP-based closed-loop DBS system was implemented in simulation to automatically identify DBS parameters that minimized TC soma burst-driver band power, a proxy for clinical effectiveness.

The fraction of power in the burst-driver band was calculated from the TC soma transmembrane potential, and averaged across the thalamic population. The target ECAP energy was selected from the relationship between burst-driver band power and ECAP signal energy across stimulation parameters (Fig. A.2A). With stimulation *off*, the mean burst-driver band power was 0.0106 for the *healthy* condition and 0.0347 for the *tremor* condition. Increasing the amplitude or pulse width of 130 Hz DBS reduced burst-driver band power, and 5.5 V DBS restored this to the *healthy* level. Conversely, 10 Hz

DBS led to relatively small reductions in burst-driver band power, and did not restore the *healthy* level for the parameters tested.

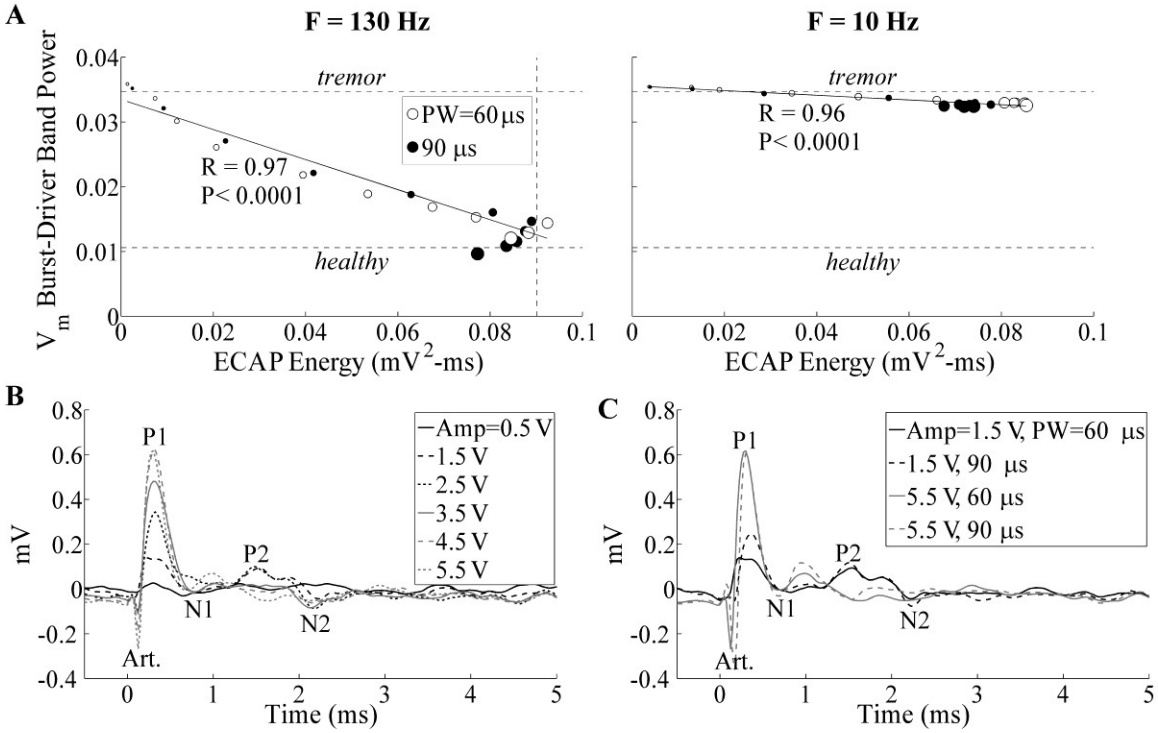

Figure A.2: Mean fraction of TC somatic V_M power in the burst-driver band and ECAP responses across stimulation parameters and model conditions. A: Relationship between burst-driver band power and ECAP signal energy at 130 Hz and 10 Hz DBS, with stimulation amplitudes of 0.5-5.5 V (proportional to data point size) and pulse widths of 60 µs (open circles) and 90 µs (filled circles). The burst-driver band power is shown for the healthy and tremor conditions with DBS *off* (horizontal dashed lines), and the target ECAP signal energy for 130 Hz DBS is indicated (vertical dashed line). Linear regressions were calculated between burst-driver band power and ECAP signal energy, with only the data points constituting the negative linear trend used for 130 Hz DBS. B: Stimulus-triggered average ECAPs for a range of DBS amplitudes, with 130 Hz DBS frequency and 60 µs pulse width. C: Stimulus-triggered average ECAPs for different combinations of pulse widths and amplitudes, with 130 Hz DBS frequency. The artifact ("Art") and ECAP phases are labeled in (B) and (C).

Changes in ECAP signal energy were non-monotonic with increasing DBS amplitude; ECAP energy initially increased before declining above 3-4.5 V, depending

on the pulse width and frequency (Figs. A.2A,B). Moreover, longer DBS pulse widths led to increases in ECAP energy only at low stimulation amplitudes (≤4 V), whereas the opposite was true at high stimulation amplitudes (Figs. A.2A,C). Importantly, the relationship between burst-driver band power and ECAP signal energy across DBS parameters was non-monotonic at 130 Hz, with a negative, linear relationship up to ~4 V ($R=0.97$, $P<0.0001$), before reversing at higher amplitudes (Fig. A.2A). This relationship suggested a target ECAP energy of 0.09 mV^2-ms, which corresponded to the approximate reversal point of ECAP energy with increasing DBS amplitude, as well as a burst-driver band value of 0.0145, or a 83.8% decline from the *tremor* to the *healthy* conditions. On the other hand, there was a relatively flat, linear, monotonic relationship between burst-driver band power and ECAP signal energy at 10 Hz DBS ($R=0.96$, $P<0.0001$), consistent with the ineffectiveness of low frequency DBS for tremor.

The relationship between burst-driver power and ECAP energy was also explored across DBS frequencies (Fig. A.3). Reductions in burst-driver power were significantly correlated ($\alpha=0.05$) with increasing P1 phase energy ($R=0.67$, $P<0.04$), and nearly significantly correlated with decreasing N1 phase energy ($R=0.61$, $P<0.06$) generated by higher DBS frequencies. Conversely, we did not identify linear correlations between the burst-driver band and either the energy of the entire ECAP signal or the secondary phases.

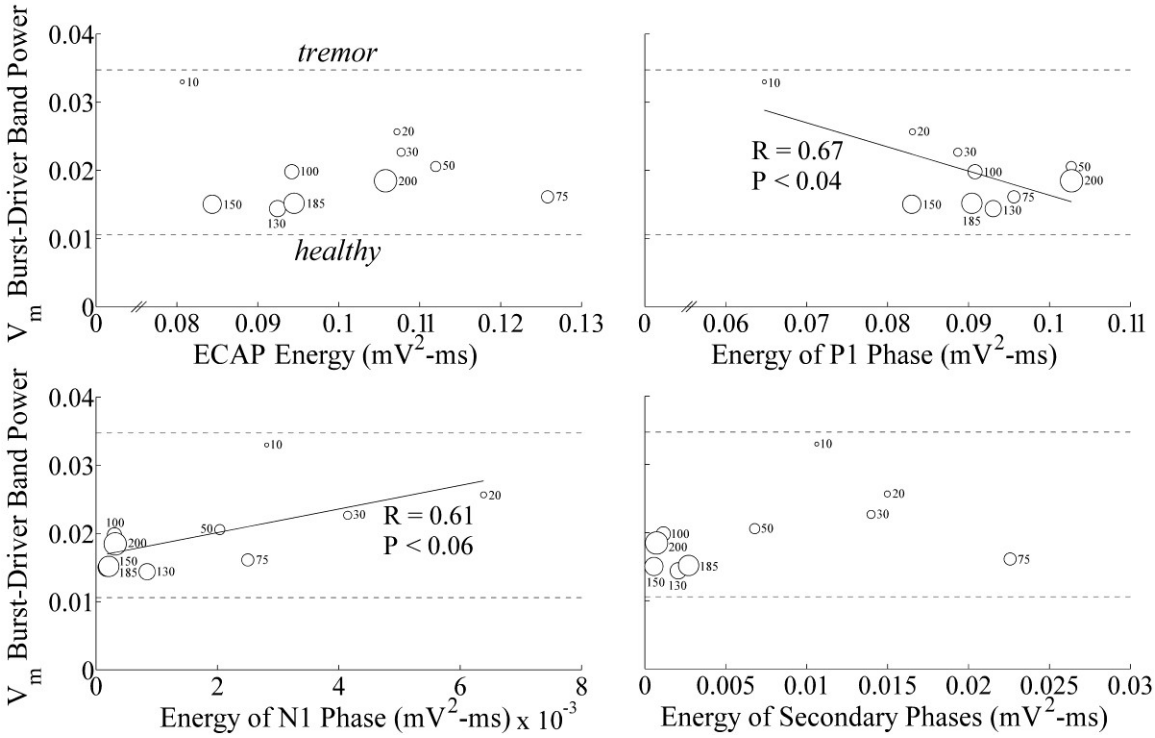

Figure A.3: Relationship between burst-driver band power and ECAP signal energy for stimulation frequencies of 10-200 Hz (proportional to data point size and labeled). The four sub-plots show ECAP energy over the entire signal, and for P1, N1, and secondary phases. DBS amplitude was fixed at 4.5 V and pulse width was fixed at 60 μs. Data presentation is otherwise similar to Fig. A.2A.

The closed-loop DBS system was first implemented with a P controller with DBS amplitude modulation, and a disturbance was introduced after the system reached steady state (Fig. A.4). Prior to the disturbance, the system increased the stimulation amplitude automatically from the starting value of 1 V to a steady state value of 4.73±0.09 V (mean ± SD of iterations 6-30). The rise time to reach 90% of the target ECAP energy was 500 ms, equivalent to five controller iterations. ECAP energy eventually

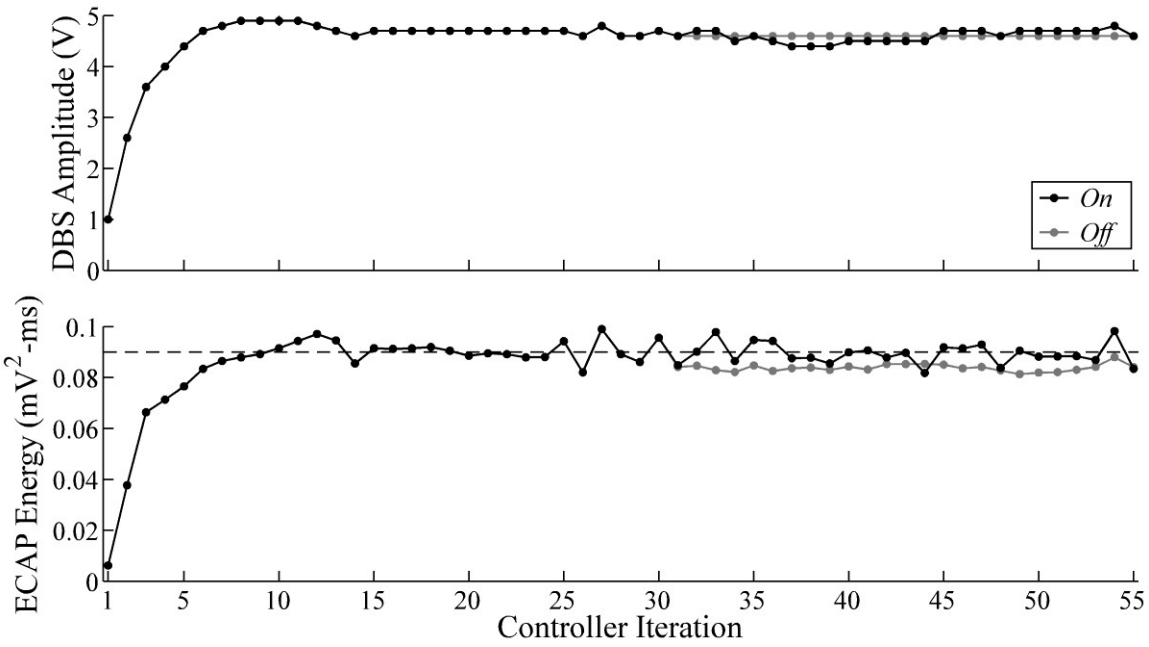

Figure A.4: DBS amplitude modulation by a proportional (P) closed-loop controller (top) and corresponding ECAP signal energy relative to the target value, indicated by the horizontal dashed line (bottom). A disturbance increasing the number of TC model neurons exhibiting bursting was introduced at iteration number 31, and the response to this disturbance was compared with closed-loop DBS modulation turned *on* or *off*.

reached the target value at the tenth iteration (1 s real-time), which was followed by a small overshoot and then steady state after the 15th iteration. Near the 25th iteration, there was a small, intrinsic perturbation of ECAP energy away from steady state, and the system made corresponding adjustments of DBS amplitude. The average absolute error was 0.0032±0.0025 mV^2-ms over iterations 6-30. The number of TC neurons exhibiting burst activity was increased at iteration 31, and the closed-loop controller subsequently reduced DBS amplitude to 4.60±0.12 V, maintaining ECAP energy error at 0.0033±0.0026

mV^2-ms. If closed-loop control was suspended, the average absolute error increased to 0.0061±0.0014 mV^2-ms after the disturbance.

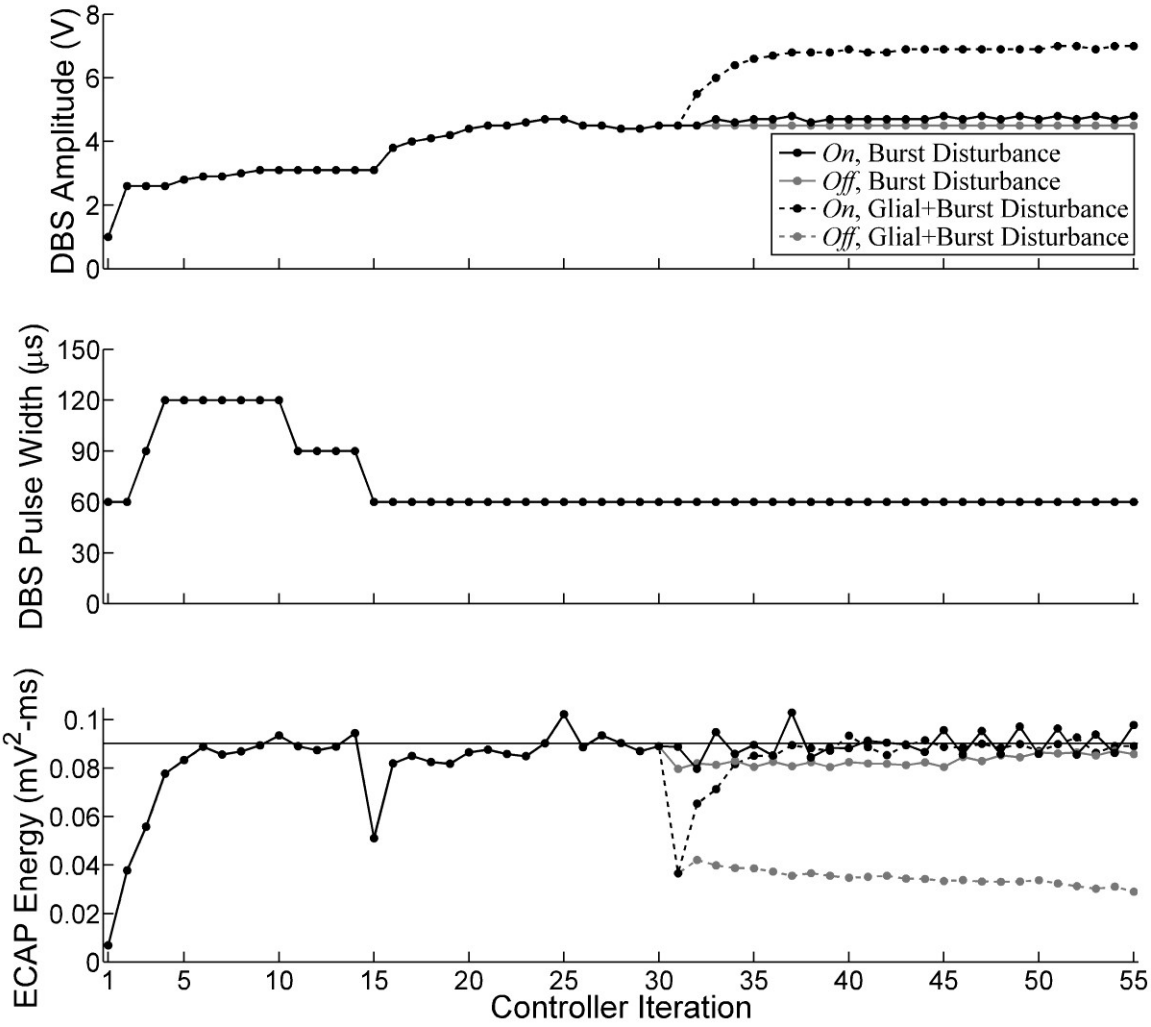

Figure A.5: Hybrid adjustment of DBS amplitude (top) and pulse width (middle) by a P controller, and corresponding ECAP signal energy value (bottom). Data presentation is similar to Fig. A.4, except that a glial encapsulation disturbance was introduced, in addition to the disturbance affecting the number of TC model neurons exhibiting bursting, at iteration number 31. Pulse width data are overlapping for the different conditions tested, and amplitude data are overlapping for the two closed-loop *off* conditions.

A P controller for hybrid modulation of DBS amplitude and pulse width generated similar results (Fig. A.5). Initial adjustments included rapid increase of the pulse width from 60 μs to 120 μs, with relatively small changes in DBS amplitude compared to that observed with amplitude modulation alone. The rise time was 500 ms, and the target ECAP value was reached by 900 ms, with minimal overshoot. This was followed by a reduction in pulse width back to 60 μs and a corresponding increase in DBS amplitude to 4.31±0.41 V (iterations 15-30) to restore ECAP energy to the target value. The average absolute error was 0.0050±0.0076 mV^2-ms over iterations 6-30. After increasing the number of bursting TC neurons, the controller increased DBS amplitude to 4.70±0.08 V, maintaining the ECAP energy error at 0.0044±0.0030 mV^2-ms, and if the controller was suspended the error increased to 0.0068±0.0022 mV^2-ms. Following addition of a glial encapsulation layer in the FEM model, the controller maintained a low ECAP energy error of 0.0058±0.0114 mV^2-ms by increasing the amplitude to 6.67±0.56 V, while suspending the controller led to an increase in error to 0.0551±0.0031 mV^2-ms.

Alternative implementations of the closed-loop system used a PD or PID controller for DBS parameter adjustment. With exclusive amplitude modulation, the PD controller reached the target ECAP energy value with a rise time of 600 ms and minimal overshoot, by increasing DBS amplitude to 4.63±0.13 V (Fig. A.6). The actual ECAP energy oscillated about the target value, never reaching steady state, with an average

ECAP energy error of 0.0045±0.0025 mV^2-ms, which was 40.6% higher than that for the P controller with amplitude modulation. Following the introduction of both model disturbances, the PD controller maintained a low ECAP energy of 0.0054±0.0110 mV^2-ms by increasing amplitude to 6.70±0.52 V.

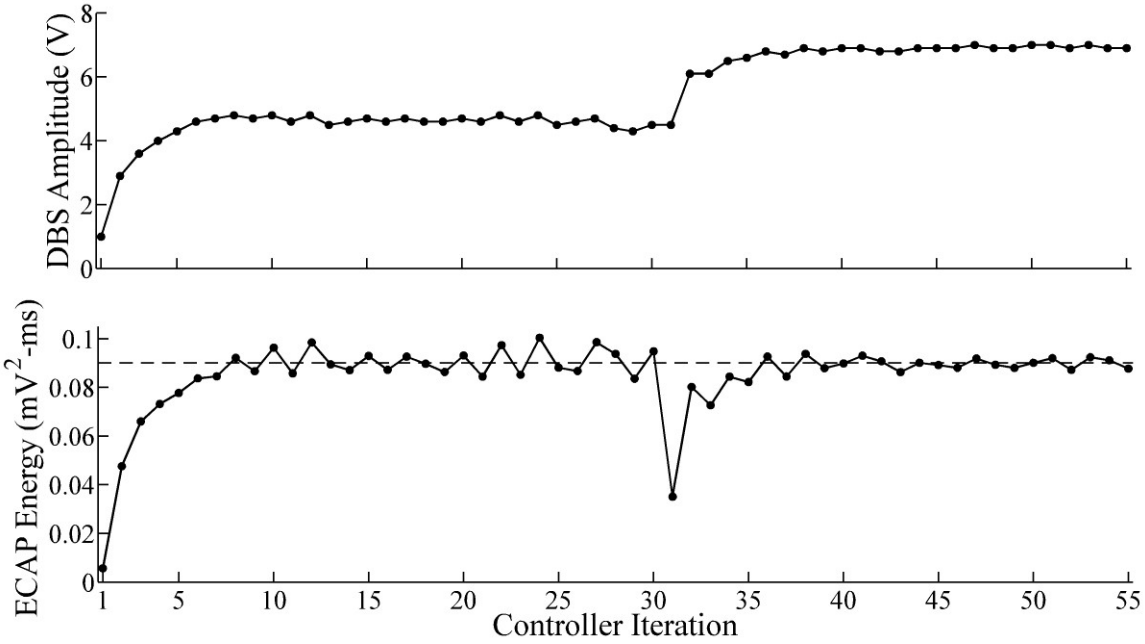

Figure A.6: DBS amplitude modulation by a PD controller. Data presentation is similar to Fig. A.4. The glial encapsulation and TC bursting disturbances were both introduced at iteration number 31.

Using a PID controller with DBS amplitude modulation, the system identified an amplitude (4.8 V) that generated ECAPs with energy near the target value by just the second iteration (Fig. A.7A). However, a subsequent overshoot of the controller output produced an excessive DBS amplitude of 6.2 V at the third iteration. As a consequence of the non-monotonic relationship between DBS amplitude and ECAP signal energy, the overshoot of the former resulted in a *reduction* of the latter away from the target value.

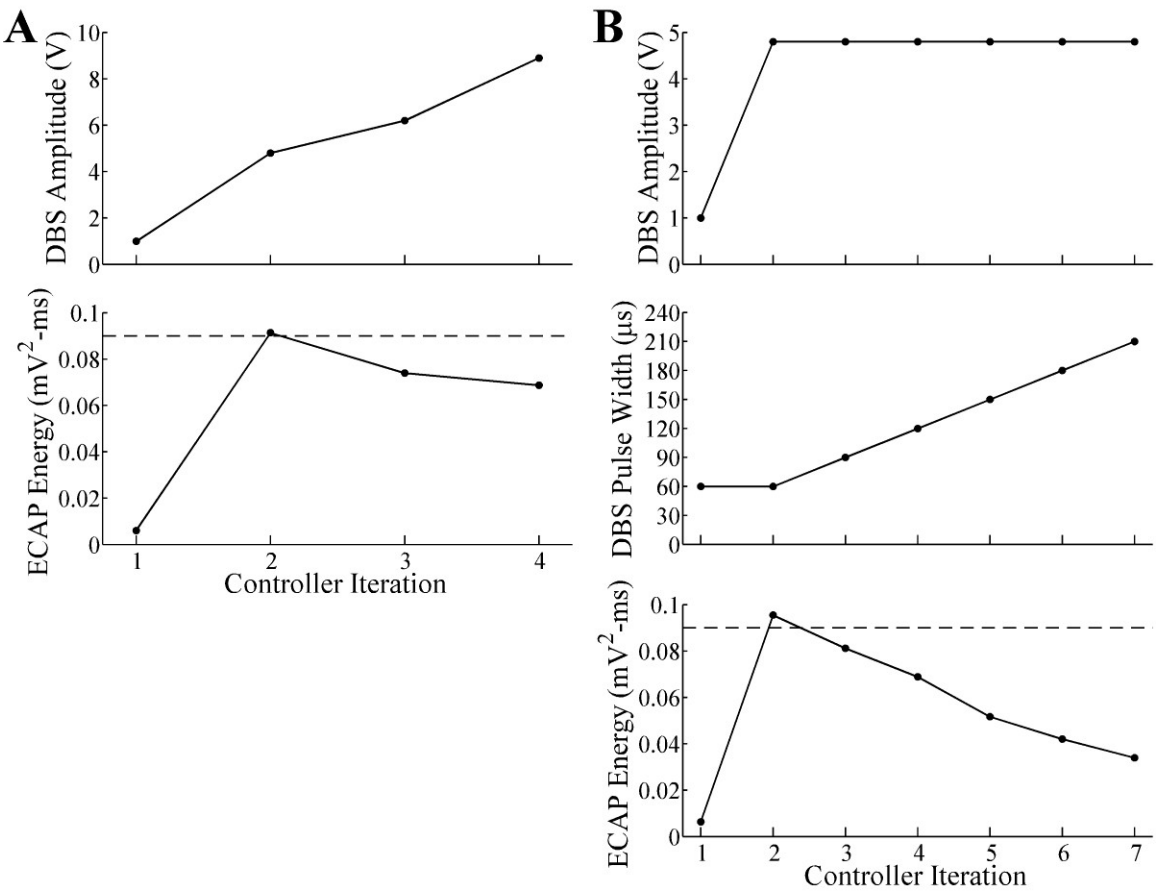

Figure A.7: DBS parameter adjustment and corresponding ECAP signal energy with a PID controller, with exclusive amplitude adjustment (A), or hybrid adjustment of amplitude and pulse width (B). Data presentation is similar to Fig. A.4.

The system unsuccessfully tried to compensate by increasing DBS amplitude still further, and the trial was terminated due to system instability. An analogous situation arose for hybrid amplitude and pulse width modulation, in which overshoot of the PID controller output produced an incremental increase in pulse width at the third iteration, despite ECAP energy already exceeding the target value at the second iteration (Fig. A.7B). The longer pulse width reduced ECAP signal energy, since DBS amplitude was

high (4.8 V), and the controller unsuccessfully tried to compensate by increasing pulse width still further, after which the trial was terminated due to system instability.

A.4 Discussion

We implemented an ECAP-based closed-loop DBS system in simulation and demonstrated that a P or PD controller adjusted DBS parameters appropriately before and after introduction of disturbances. Conversely, the PID controller was unstable as a result of the non-monotonic relationship between DBS parameters and ECAP characteristics. Nevertheless, the results of this study suggest that ECAPs could be clinically useful in closed-loop DBS systems.

A.4.1 Relationship between ECAP signal energy and burst-driver band power across stimulation parameters

The relationship between ECAP signal energy and burst-driver band power, which was used a proxy for clinical effectiveness, was dependent on the stimulation frequency. This relationship was non-monotonic at 130 Hz, and was used to establish a target energy that corresponded to an 83.8% reduction in burst-driver band power from the *tremor* condition to the *healthy* condition. In contrast, the relationship between burst-driver band power and ECAP signal energy at 10 Hz was relatively flat. Since ECAP energy was not a good indicator of clinical effectiveness at low DBS frequencies, we fixed DBS frequency at 130 Hz and used ECAP energy to adjust only DBS amplitude and/or pulse width. However, we could foresee the use of another ECAP characteristic, such as N1 phase energy (Fig. A.3), to identify the critical DBS frequency for symptom

reduction (Kuncel et al., 2007). In previous experimental work (**Chapter 4**), we identified a negative linear correlation between tremor and ECAP signal energy at 130 Hz that was nearly significant (R=0.6-0.87, P<0.078), and a similar, statistically significant relationship was found in this work with amplitudes below ~4 V (R=0.97, P<0.0001). In the experimental study, we also found a positive, linear correlation at 10 Hz (R=0.86, P<0.068), which differed from the relatively flat but statistically significant relationship identified in this work (R=0.96, P<0.0001). The differing results found from this simulation and prior clinical results suggest that the burst-driver band power may not be perfectly aligned with clinical effectiveness across the stimulation conditions tested.

We examined further the origin of the non-monotonic relationships between ECAP signal energy and DBS amplitude or pulse width. The percentage of neural elements activated directly by stimulation increased with higher DBS amplitudes and longer pulse widths (data not shown), as expected from the strength-distance and strength-duration relationships (Kuncel and Grill, 2004). Since the ECAP reflects the extent of neural activation (**Chapter 3**), it would be expected that ECAP signal energy would increase with these DBS parameters. However, we also found that post-synaptic activation of neural elements decreased above 3-3.5 V, depending on the pulse width, which contributed to a reduction in secondary phase signal energy (**Chapter 3**), such as that of the P2 phase (Fig. A.2B). In addition, destructive interference of ECAP contributions from different types of neural elements reduced the size of composite

ECAP phases at higher DBS amplitudes and longer pulse widths (**Chapter 4**). For example, there was a larger negative phase contribution from CER inputs at longer pulse widths that reduced the P1 phase (Fig. A.2C). These effects resulted in the non-monotonic relationships between ECAP signal energy and DBS parameters. This finding was confirmed by similar non-monotonic relationships found in clinical studies between the signal energy of ECAP phases and DBS amplitude (**Chapter 4**), although this was not observed in preclinical studies (**Chapter 3**), presumably because DBS amplitude was limited to ≤3 V.

A.4.2 Closed-loop control of DBS

We implemented PID-based controllers for automatic modulation of DBS amplitude and/or pulse width to reach and maintain ECAP energy at the target value, even in the presence of disturbances. This work successfully demonstrated the suitability of P and PD controllers in closed-loop DBS systems. These controller adjusted the amplitude and/or pulse width from the initial setting to reach the target ECAP energy in ≤1 s real-time, and maintained a relatively low average ECAP energy error before and after introduction of disturbances affecting TC bursting, representing progression of the disease state, and/or impacting DBS-generated potentials via glial encapsulation, representing the transition to the chronic implantation stage. For the latter, the controllers increased DBS amplitude by 45-55% to compensate for electrical insulation of the stimulating contact by the encapsulation layer. Conversely, for open-

loop DBS, ECAP energy error was increased by 36-91% after the increase in TC bursting and by ~1000% after glial encapsulation. With hybrid amplitude and pulse width modulation, the system ultimately selected the lowest pulse width available (60 μs) to maximize power efficiency, and so the final parameter set was similar to that observed with amplitude modulation alone. The PD controller approached the target ECAP energy, but never obtained true steady state before presentation of disturbances, with an ECAP energy error 40.6% higher than that of the P controller. This may have resulted from non-optimized PD controller gains, which were not defined for Z-N tuning.

A PID-based controller was selected for this work because it is simple, intuitive, and easy to tune. However, the main disadvantage of a PID controller is that it is linear, which can result in instabilities when implemented in a non-linear system, as observed in this work. Alternative closed-loop controllers that have been tested in neural prostheses include an adaptive minimum variance controller (Santaniello et al., 2011) and a fuzzy logic controller (Lin et al., 2012), which could offer improved performance in our application. Nevertheless, the PID-based closed-loop system implemented in this work demonstrated proof-of-principle for the ECAP as a feedback signal.

A.4.3 Study limitations

There were several limitations of this work that should be addressed. First, the computational model used a representation of the mini DBS electrode within the cat VL thalamus, rather than a clinical DBS electrode in the human Vim thalamus, which would

more accurately reflect clinical implementation of closed-loop DBS (**Chapter 4**). However, the former was selected because the neural origin of the ECAP was better understood through a prior study using pharmacological interventions and computational modeling (**Chapter 3**). Second, the selected target ECAP energy did not correspond to a full reduction in the burst-driver band power to the *healthy* condition, which would represent optimal therapy, due to the non-monotonic relationship between these two variables. On the other hand, the linear, monotonic correlations observed in clinical experiments between ECAP signal energy and motor symptoms suggests that target ECAP energy values selected in the clinic could correspond to an optimal therapeutic response (**Chapter 4**). Third, we did not perform additional tuning of PID controller gains, beyond using the Z-N methodology, which could have reduced the overshoot of the PID controller output (i.e., increasing derivative gain or decreasing integral gain). Fourth, the closed-loop controllers did not account for non-monotonicity between ECAP signal energy and DBS amplitude or pulse width.

The closed-loop controller proposed in this work did not account for the possible generation of side effects with increasing DBS amplitude and pulse width. As these parameters are increased to obtain the target ECAP signal energy, stimulation current could leak into adjacent brain areas, such as the ventral caudal (Vc) nucleus of the thalamus, and generate paresthesias. In subsequent versions of the controller, ECAP energy could be measured from distinct phases that correspond to activation of neural

elements that generate therapeutic effects (i.e. cerebellothalamic afferents) or side effects (i.e. local cells in the Vc thalamus), for more precise DBS parameter tuning. Moreover, clinical implementation of a closed-loop DBS controller would require that the physician set maximum limits on DBS parameter values to maintain patient safety.

Appendix B: Comparison of local field potential and tremor spectrograms

B.1 Introduction

Abnormal network oscillations present in movement disorders are reflected in local field potentials (LFPs) recorded from the ventral intermediate (Vim) nucleus of thalamus in persons with essential tremor (ET) or Parkinson's disease (PD). Previous studies have noted intra-thalamic LFP coherence, measured from two recording microelectrodes, and LFP-tremor coherence, with tremor measured by EMG or an accelerometer, at the tremor frequency (4-8 Hz) and its first harmonic in ET and PD (Kane et al., 2009, Pedrosa et al., 2012). This suggested that elevated LFP theta band (4-7 Hz) power was related to tremulous activity, although coherence between theta LFP and tremor was not always observed across subjects (Marsden et al., 2000, Pedrosa et al., 2012). Alternatively, coherence was reported in all subjects with ET and PD between EMG-measured tremor signals and 8-27 Hz LFPs, which encompassed alpha (8-12 Hz) and beta (13-35 Hz) bands (Marsden et al., 2000). Holdefer and colleagues confirmed the presence of beta band LFPs in Vim in PD and ET (Holdefer et al., 2010). Beta oscillations in the basal ganglia appear to reflect an anti-kinetic state and may be a signature of PD (Bronte-Stewart et al., 2009), and these oscillations could be propagated to the thalamus through functional brain loops (Holdefer et al., 2010). Using linear and non-linear causality methods, Tass, et. al. demonstrated bidirectional coupling between both theta band and broadband (>2 Hz) LFPs recorded from the thalamus and resting tremor in PD

(Tass et al., 2010). The authors suggested that theta band oscillations, and possibly beta band oscillations, play an efferent role in generating tremor, with a delay for signal propagation of 1-2 tremor cycles.

The aim of this work was to compare theta and beta band LFPs recorded from the DBS brain lead in subjects with ET or PD with the onset and amplitude of tremor. These signals were recorded during the intraoperative clinical study described in **Chapter 4**. We investigated whether an increase in theta band power or suppression of beta band power preceded the onset of tremor (Wang et al., 2007). These measurements were made with each subject holding his or her arm in one of three specified positions, which was intended to evoke tremor with different amplitudes and durations. We then studied frequency-time spectrograms of LFP and tremor signals for temporal association analysis.

B.2 Methods

We compared clinical recordings of LFP and tremor signals using frequency-time spectrograms. These signals were recorded intraoperatively using the identical experimental setup discussed in **Chapter 4**. Specifically, this protocol was performed in subjects EP12B (ET diagnosis), EP12C (PD), EP13A (ET), EP13F (PD), and EP13G (ET), and EP13I (ET). Three trials of 1 min length were conducted with DBS *off*, and at 30 s into each trial the subject held his or her arm in one of three specified positions for 20 s, and tremor was measured with an accelerometer. For all positions, the arm was held

straight out with the elbow fully extended, and either (1) parallel to the ground, (2) at a 45° angle, or (3) perpendicular to the ground. LFPs were recorded differentially from DBS contacts using the DBS-ECAP instrumentation and sampled at 80 kHz. Signals were recorded either just when tremor was measured (EP12B and EP12C only) or through the entire 60 s trial period. Multitaper spectrograms were constructed from the tremor signals, after summing across the three accelerometer axes and detrending with local linear regression (2 s window size, 1 s step size), and from LFP signals (down-sampled to 10 kHz), using the Chronux analysis toolbox (www.chronux.org) in MATLAB (*mtspecgramc* function: 1 s sliding window, 0.2 s step size, 2 Hz bandwidth).

B.3 Results

Frequency-time spectrograms of LFP and tremor were constructed across clinical experiments (Fig. B.1). Large tremor power was observed at the fundamental frequency and its harmonics for short periods in EP12C (Fig. B.1A), and throughout the entire trial in the remaining experiments, including EP13G (Fig. B.1B). The amplitude and duration of tremor were similar between different arm positions within a given experiment, with the exception of relatively little tremor present in EP13A only when the arm was parallel to the ground. In EP12C, we observed short periods of theta and beta LFPs, with close temporal association to periods of large tremor (Fig. B.1A). Further, the amplitude of tremor matched the relative amount of LFP power. Although theta band LFP activity was not observed in the remaining experiments, we did observe beta band LFPs in

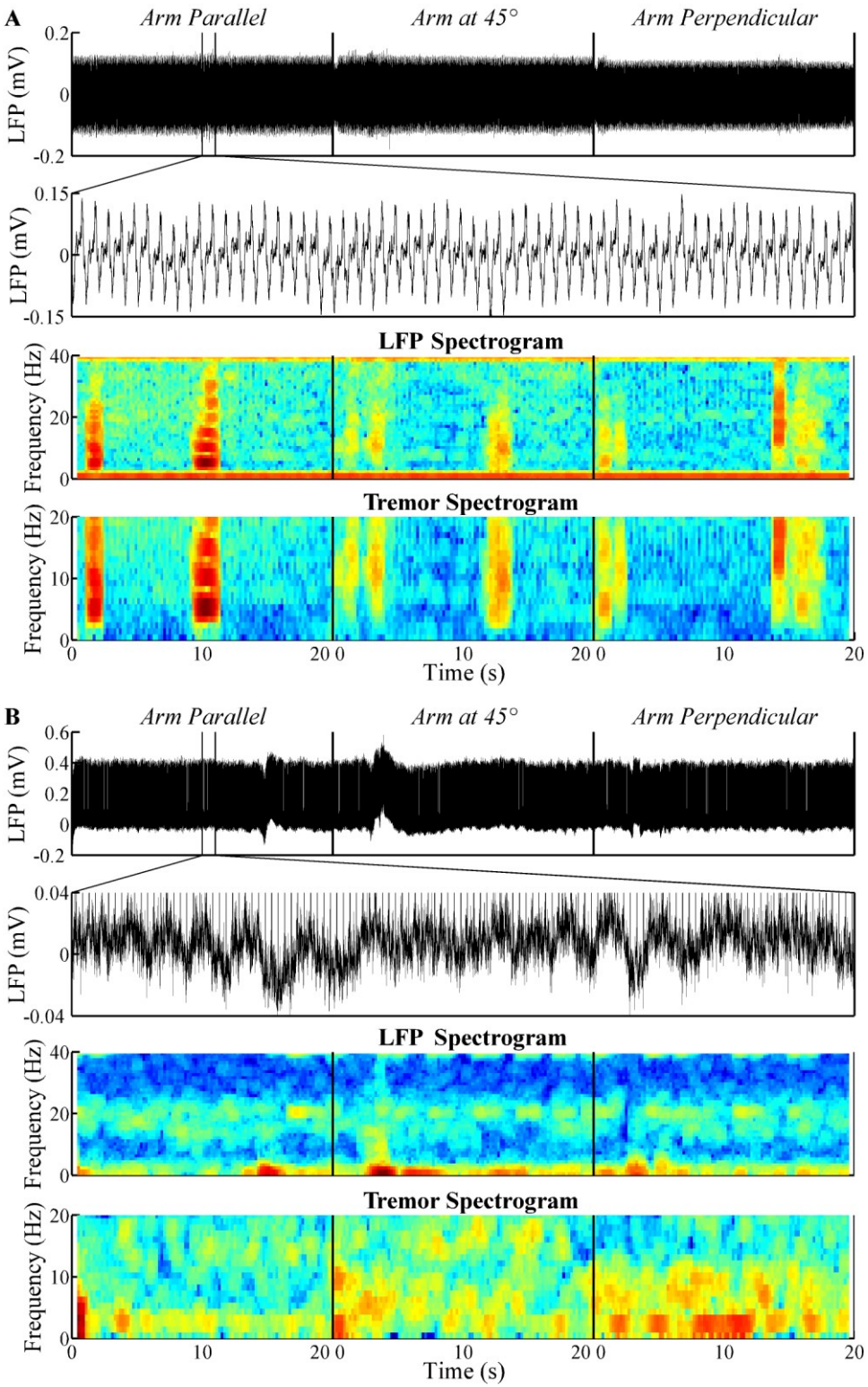
A
Arm Parallel
Arm at 45°
Arm Perpendicular
LFP (mV)
0.2
0
-0.2
0.15
-0.15
LFP Spectrogram
Frequency (Hz)
40
20
Tremor Spectrogram
10
0 10 20 0 10 20 0 10 20
Time (s)
B
0.6
0.4
0.04
-0.04

Figure B.1: Raw LFP signals (entire signal and 1 s zoomed view), LFP spectrograms, and tremor spectrograms from subjects (A) EP12C and (B) EP13G. Subjects held their arm for 20 s in the position indicated, and tremor and LFP signals were measured. There was a rest period of 40 s between each trial (thick black vertical lines in each plot), and the measurements made from the three distinct trials were merged into the one continuous recording shown. Hotter colors in the spectrograms correspond to greater power.

EP13G (Fig. B.1B) and EP13F. However, there was no obvious association between beta activity and changes in tremor over time. Finally, theta and beta band activity was not observed in LFPs recorded from subjects EP12B, EP13A, or EP13I.

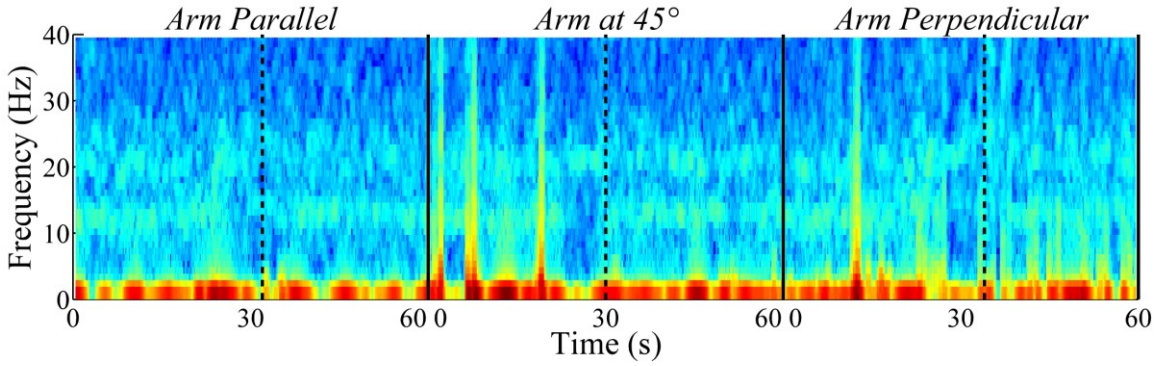

Figure B.2: LFP spectrogram from subject EP13F, including recordings made during rest, movement, and posture. During each 60 s trial, the subject moved his arm from a rest position to one of the three designated arm positions at the ~30 s mark, and held it in that posture for 20 s. The dashed vertical line marks the start of tremor recording, after the subject had already moved to the designated arm position, and the solid vertical line marks the end of a trial.

Spectrogram analysis was also conducted on the entire LFP signal, which included periods of rest, movement to the designated arm position, and posture during tremor measurement. We observed a reduction in the low beta band (~13 Hz) during movement to the designated arm position, preceding the tremor measurement, in subject EP12F (Fig. B.2). However, no differences were detected between the rest and

tremor periods. Moreover, we did not observe beta reductions during movement in the other three subjects for which LFPs were recorded during the entire trial period.

B.4 Discussion

We investigated relationships between LFP activity and the onset and amplitude of tremor. High LFP power was observed in the theta and/or beta band in two subjects with PD, and in the beta band in one subject with ET, whereas no LFP activity was recorded in three other subjects, two with ET and the other with PD. In one subject, beta band activity was reduced during movement from rest to the designated arm position, similar to observations in the basal ganglia (Cassidy et al., 2002, Levy et al., 2002, Priori et al., 2002, Kuhn et al., 2004, Williams et al., 2005). We found a tight temporal association between increased theta and beta power and the onset of tremor, and between the relative magnitude of LFP and tremor power, in only one subject, EP12C (Kane et al., 2009, Holdefer et al., 2010, Pedrosa et al., 2012). The inconsistent association between LFP and tremor power across recordings was in agreement with prior work (Marsden et al., 2000, Pedrosa et al., 2012). Further, it is difficult to rule out the possibility that the LFP activity recorded in EP12C was a motion artifact, given the presence of LFP peaks at the tremor frequency and its harmonics. Nevertheless, our experimental setup was designed to reduce motion artifact in LFP recordings by using a large separation distance between the arm used for tremor measurement and the location of the recording reference electrode, which was placed on the contralateral

thigh. Therefore, the relationship between LFP activity and tremor was not reproducible within the relatively small patient population that we tested, and additional experiments may help to elucidate any association between these signals.

There were several limitations to this work that should be addressed in future work. First, we did not generate tremor with sufficiently different amplitudes or durations using the three arm positions tested (except in EP13A), which would have been valuable in comparing the relative power of LFP and tremor activity. Using additional arm orientations, such as holding the hand near the face, or asking the subject to perform an action, may have led to greater differences in tremor. Second, coherence analysis could be used to quantify the relationship between LFP and tremor, as performed previously (Marsden et al., 2000, Kane et al., 2009, Pedrosa et al., 2012). However, temporal information is lost with a traditional coherence calculation, and time-dependent coherence analysis (Wang et al., 2007) may be more useful for this application.

Appendix C: Investigating a harmaline tremor model in anesthetized cats

C.1 Introduction

Our previous preclinical studies of evoked compound action potential (ECAP) recording during deep brain stimulation (DBS) lacked a behavioral measure of the motor symptom response to stimulation (**Chapters 2 & 3**). However, identifying signatures of therapeutic effectiveness requires quantifying changes in tremor across thalamic DBS parameters, and correlating these changes with ECAP characteristics. The objective of these experiments was to record simultaneously changes in ECAPs and tremor in a cat model of essential tremor (ET). However, we were not able to generate consistent tremor despite repeated experiments across a range of conditions.

Harmaline-induced tremor is a widely accepted preclinical model of tremor (Martin et al., 2005) that shares many features with ET in humans (Wilms et al., 1999). Specifically, harmaline administration in cats elicits a "fine generalized tremor" at 8-12 Hz, along with periodic muscle contractions of 1-10 s duration, and is generated by rhythmic activation in the olivo-cerebellar system (de Montigny and Lamarre, 1973), consistent with the etiology of ET in humans (Deuschl and Elble, 2000). A partial lesion of the lateral cerebellar nuclei or superior cerebellar peduncle can lower the tremor frequency on the lesioned side to that of ET (6-7 Hz) (Lamarre, 1995). Single-unit recordings after harmaline administration showed a rhythmic firing of inferior olive neurons (8-12 Hz discharge), which induced a corresponding rhythmic response in

climbing fibers and Purkinje cells, and resulted in a bursting firing pattern in the fastigial nucleus, reticular formation, and vestibular nuclei (de Montigny and Lamarre, 1973, Batini et al., 1979, Weiss, 1982). Harmaline may act on GABA receptor-controlled gap junctions, enhancing electronic coupling of cells in the inferior olive, and facilitating the pacemaker behavior of these neurons (Llinas et al., 1974, Lamarre, 1995). The rhythmic activity of the cerebellum is transmitted to downstream spinal motor neurons via the reticulospinal and vestibulospinal pathways (Lamarre, 1995), and both the motor neurons and muscle tremor activity were shown to be phase-locked to cerebellar activity (de Montigny and Lamarre, 1973, Weiss, 1982). Tremor is typically generated 3-10 min after harmaline is administered, with the effect lasting for 30 min to 2 hr, and is elicited both during rest and during movement (Wilms et al., 1999).

The objective of this work was to generate harmaline tremor in anesthetized cats. In prior studies, cats were usually decerebrated (Villablanca and Riobo, 1970, de Montigny and Lamarre, 1973, Weiss, 1982) or awake (Villablanca and Riobo, 1970, Batini et al., 1981a) when harmaline was administered. Further, after tremor commenced, Flaxedil was used to induce paralysis and eliminate proprioceptive feedback (Villablanca and Riobo, 1970, de Montigny and Lamarre, 1973, Batini et al., 1979, Batini et al., 1981a, Batini et al., 1981b, Weiss, 1982). Pentobarbital anesthesia was used during harmaline treatment in one study (Batini et al., 1979), but large doses of barbiturates can block the resulting tremor (Lamarre, 1995). It was necessary to have the animals

anesthetized in our acute ECAP recording study, which was performed under non-sterile, non-survival conditions. Additionally, decerebration could have affected the ECAP response by destroying thalamocortical-corticothalamic connections. We tested whether harmaline could generate tremor in cats anesthetized with alpha chloralose or pentobarbital.

C.2 Methods

All animal use and experimental protocols were reviewed and approved by the Duke University Institutional Animal Care and Use Committee. We administered harmaline in seven anesthetized cats and monitored the animals for any manifestations of tremor. Cats were either lying prone or were elevated with limbs hanging free. The animals were initially anesthetized with ketamine HCl (35 mg/kg i.m.), and four cats were maintained with alpha chloralose (65 mg/kg i.v. supplemented at 15 mg/kg as needed), whereas the remaining three cats were maintained with pentobarbital (10 mg/kg i.v. supplemented at 2-5 mg/kg as needed). There was a latency of at least 12 hours from when ketamine was administered to harmaline delivery. Harmaline (Sigma-Aldrich, 51330) or harmaline HCl (Sigma-Aldrich, H1392) were given intravenously at 2-20 mg/kg, with progressive dosing of 2 or 5 mg/kg increments in some experiments (Villablanca and Riobo, 1970, de Montigny and Lamarre, 1973, Batini et al., 1979, Batini et al., 1981a, Batini et al., 1981b, Fagni et al., 1982). We waited at least 10 min after each

dose of harmaline for a tremor response. A summary of the anesthesia and harmaline dosages, as well as the body positioning of the animals, is provided in Table C.1.

Table C.1: Summary of anesthesia and harmaline dosages, as well as body position, across cat experiments. The tremor response following harmaline administration is also provided.

Cat	Anesthesia Dosage	Harmaline Dosage	Body Position	Tremor Response
A	α-chloralose	5 mg/kg harmaline	Prone	None
B	α-chloralose	10 mg/kg harmaline	Prone	None
C	Pentobarbital (2 mg/kg suppl.)	20 mg/kg harmaline (5 mg/kg increments)	Elevated	Tremor in forelimbs & hind limbs and periodic muscle contractions elicited immediately after administration of 20 mg/kg harmaline
D	α-chloralose	20 mg/kg harmaline	Elevated	None
E	Pentobarbital (2 mg/kg suppl.)	20 mg/kg harmaline HCl (5 mg/kg increments) 20 mg/kg harmaline (5 mg/kg increments)	Elevated	Slight tremor with 15 mg/kg harmaline HCl after 5 min
F	Pentobarbital (5 mg/kg suppl.)	10 mg/kg harmaline (5 mg/kg increments)	Elevated	None; cat died at 1 min after administration of 10 mg/kg harmaline
G	α-chloralose	10 mg/kg harmaline (2 mg/kg increments)	Prone	Slight tremor with 8 mg/kg harmaline after 15 min

C.3 Results

Tremor induction in cats by harmaline administration was inconsistent between experiments (Table C.1). A pronounced tremor was generated only in one of the seven cats tested (cat C), in which we administered pentobarbital anesthesia and a large dose of harmaline (20 mg/kg). This tremor was observed in the cat's free-hanging forelimbs and hind limbs for over 15 min, as were periodic muscle contractions of ~10 s duration each (de Montigny and Lamarre, 1973). In addition, we observed a slight tremor for approximately 5 min in two other animals (cats E and G), one anesthetized with pentobarbital and the other with alpha chloralose, after administration of 8-15 mg/kg harmaline or harmaline HCl. In the remaining experiments, no tremor response was observed. However, cat F died almost immediately after a moderate dose of harmaline (10 mg/kg) was delivered.

C.4 Discussion

We investigated the induction of tremor by harmaline in anesthetized cats by testing different anesthesia regimens, harmaline formulations and dosages, and body positions. We generated a pronounced tremor only in cat C, anesthetized with pentobarbital, using a large dose of harmaline, consistent with literature (Batini et al., 1979). However, this was not replicated in other animals, either with pentobarbital or alpha chloralose anesthesia, except for a slight tremor in two other experiments with either harmaline or harmaline HCl. While the body of cat C was elevated so that the

limbs were hanging free, it is unclear if this was critical for observation of tremor. Personal communications with Dr. Jaime Villablanca, who had performed similar work (Villablanca and Riobo, 1970), suggested that harmaline tremor can only be generated in awake or decerebrated cats. The reason for the death of cat F after harmaline administration remains unclear.

There are several other alternative models of tremor in the cat that may be useful for our application, although these were developed in unanesthetized animals. First, MPTP was shown to generate "tremulousness or shaking of head and extremities" in cats (Schneider et al., 1986), and is a good model of Parkinson's disease in primates (Wilms et al., 1999). Second, cholinergic drugs, such as carbachol, generated fine head tremor and coarse limb tremor with a frequency of 21 Hz (Connor et al., 1966). Third, a lesion in the ventromedial tegmentum elicited a 4-8 Hz tremor (Kaelber, 1963). Successful identification of a tremor model for use in anesthetized cats would provide a behavioral measure of the motor symptom response to DBS, which could be correlated to characteristics of recorded ECAPs (or local field potentials) to enable identification of signatures of therapeutic effectiveness.

References

Abbas JJ, Chizeck HJ (1991) Feedback control of coronal plane hip angle in paraplegic subjects using functional neuromuscular stimulation. IEEE Trans Biomed Eng 38:687-698.

Afshar P, Khambhati A, Stanslaski S, Carlson D, Jensen R, Linde D, Dani S, Lazarewicz M, Cong P, Giftakis J, Stypulkowski P, Denison T (2012) A translational platform for prototyping closed-loop neuromodulation systems. Front Neural Circuits 6:117.

Airaksinen K, Makela JP, Taulu S, Ahonen A, Nurminen J, Schnitzler A, Pekkonen E (2011) Effects of DBS on auditory and somatosensory processing in Parkinson's disease. Hum Brain Mapp 32:1091-1099.

Alonso-Frech F, Zamarbide I, Alegre M, Rodriguez-Oroz MC, Guridi J, Manrique M, Valencia M, Artieda J, Obeso JA (2006) Slow oscillatory activity and levodopa-induced dyskinesias in Parkinson's disease. Brain 129:1748-1757.

Alvarez I, de la Torre A, Sainz M, Roldan C, Schoesser H, Spitzer P (2007) Generalized alternating stimulation: a novel method to reduce stimulus artifact in electrically evoked compound action potentials. J Neurosci Methods 165:95-103.

Amirnovin R, Williams ZM, Cosgrove GR, Eskandar EN (2004) Visually guided movements suppress subthalamic oscillations in Parkinson's disease patients. J Neurosci 24:11302-11306.

Anderson ME, Postupna N, Ruffo M (2003) Effects of high-frequency stimulation in the internal globus pallidus on the activity of thalamic neurons in the awake monkey. J Neurophysiol 89:1150-1160.

Anderson TR, Hu B, Iremonger K, Kiss ZH (2006) Selective attenuation of afferent synaptic transmission as a mechanism of thalamic deep brain stimulation-induced tremor arrest. J Neurosci 26:841-850.

Ando N, Izawa Y, Shinoda Y (1995) Relative contributions of thalamic reticular nucleus neurons and intrinsic interneurons to inhibition of thalamic neurons projecting to the motor cortex. J Neurophysiol 73:2470-2485.

Ashby P, Kim YJ, Kumar R, Lang AE, Lozano AM (1999) Neurophysiological effects of stimulation through electrodes in the human subthalamic nucleus. Brain 122:1919-1931.

Babb TL, Mariani E, Strain GM, Lieb JP, Soper HV, Crandall PH (1978) A sample and hold amplifier system for stimulus artifact suppression. Electroencephalogr Clin Neurophysiol 44:528-531.

Bahmer A, Peter O, Baumann U (2010) Recording and analysis of electrically evoked compound action potentials (ECAPs) with MED-EL cochlear implants and different artifact reduction strategies in Matlab. J Neurosci Methods 191:66-74.

Baldissera F, Lundberg A, Udo M (1972) Stimulation of pre- and postsynaptic elements in the red nucleus. Exp Brain Res 15:151-167.

Balser JR, Nuss HB, Romashko DN, Marban E, Tomaselli GF (1996) Functional consequences of lidocaine binding to slow-inactivated sodium channels. J Gen Physiol 107:643-658.

Bar-Gad I, Elias S, Vaadia E, Bergman H (2004) Complex locking rather than complete cessation of neuronal activity in the globus pallidus of a 1-methyl-4-phenyl-1,2,3,6-tetrahydropyridine-treated primate in response to pallidal microstimulation. J Neurosci 24:7410-7419.

Basu I, Tuninetti D, Graupe D, Slavin KV (2011) Adaptive control of deep brain stimulator for essential tremor: entropy-based tremor prediction using surface-EMG. Conf Proc IEEE Eng Med Biol Soc 2011:7711-7714.

Batini C, Bernard JF, Buisseret-Delmas C, Conrath-Verrier M, Horcholle-Bossavit G (1981a) Harmaline-induced tremor. II. Unit activity correlation in the interposito-rubral and oculomotor systems of cat. Exp Brain Res 42:383-391.

Batini C, Buisseret-Delmas C, Conrath-Verrier M (1979) Olivo-cerebellar activity during harmaline-induced tremor.A 2-[14C]deoxyglucose study. Neurosci Lett 12:241-246.

Batini C, Buisseret-Delmas C, Conrath-Verrier M (1981b) Harmaline-induced tremor. I. Regional metabolic activity as revealed by [14C]2-deoxyglucose in cat. Exp Brain Res 42:371-382.

Bechtereva NP, Bondartchuk AN, Smirnov VM, Meliutcheva LA, Shandurina AN (1975) Method of electrostimulation of the deep brain structures in treatment of some chronic diseases. Confin Neurol 37:136-140.

Bedard C, Kroger H, Destexhe A (2004) Modeling extracellular field potentials and the frequency-filtering properties of extracellular space. Biophys J 86:1829-1842.

Bedard C, Kroger H, Destexhe A (2006) Model of low-pass filtering of local field potentials in brain tissue. Phys Rev E Stat Nonlin Soft Matter Phys 73:051911.

Benabid AL, Pollak P, Gervason C, Hoffmann D, Gao DM, Hommel M, Perret JE, de Rougemont J (1991) Long-term suppression of tremor by chronic stimulation of the ventral intermediate thalamic nucleus. Lancet 337:403-406.

Benabid AL, Pollak P, Gross C, Hoffmann D, Benazzouz A, Gao DM, Laurent A, Gentil M, Perret J (1994) Acute and long-term effects of subthalamic nucleus stimulation in Parkinson's disease. Stereotact Funct Neurosurg 62:76-84.

Benabid AL, Pollak P, Louveau A, Henry S, de Rougemont J (1987) Combined (thalamotomy and stimulation) stereotactic surgery of the VIM thalamic nucleus for bilateral Parkinson disease. Appl Neurophysiol 50:344-346.

Bergman H, Feingold A, Nini A, Raz A, Slovin H, Abeles M, Vaadia E (1998) Physiological aspects of information processing in the basal ganglia of normal and parkinsonian primates. Trends Neurosci 21:32-38.

Bergman H, Wichmann T, Karmon B, DeLong MR (1994) The primate subthalamic nucleus. II. Neuronal activity in the MPTP model of parkinsonism. J Neurophysiol 72:507-520.

Berkley KJ (1983) Spatial relationships between the terminations of somatic sensory motor pathways in the rostral brainstem of cats and monkeys. II. Cerebellar projections compared with those of the ascending somatic sensory pathways in lateral diencephalon. J Comp Neurol 220:229-251.

Berman AL, Jones EG (1982) The Thalamus and Basal Telencephalon of the Cat. Madison: The University of Wisconsin Press.

Beurrier C, Bioulac B, Audin J, Hammond C (2001) High-frequency stimulation produces a transient blockade of voltage-gated currents in subthalamic neurons. J Neurophysiol 85:1351-1356.

Beuter A, Titcombe MS (2003) Modulation of tremor amplitude during deep brain stimulation at different frequencies. Brain Cogn 53:190-192.

Bevan MD, Magill PJ, Terman D, Bolam JP, Wilson CJ (2002) Move to the rhythm: oscillations in the subthalamic nucleus-external globus pallidus network. Trends Neurosci 25:525-531.

Bikson M, Lian J, Hahn PJ, Stacey WC, Sciortino C, Durand DM (2001) Suppression of epileptiform activity by high frequency sinusoidal fields in rat hippocampal slices. J Physiol 531:181-191.

Birdno MJ, Cooper SE, Rezai AR, Grill WM (2007) Pulse-to-pulse changes in the frequency of deep brain stimulation affect tremor and modeled neuronal activity. J Neurophysiol 98:1675-1684.

Birdno MJ, Grill WM (2008) Mechanisms of deep brain stimulation in movement disorders as revealed by changes in stimulus frequency. Neurotherapeutics 5:14-25.

Birdno MJ, Kuncel AM, Dorval AD, Turner DA, Grill WM (2008) Tremor varies as a function of the temporal regularity of deep brain stimulation. Neuroreport 19:599-602.

Birdno MJ, Kuncel AM, Dorval AD, Turner DA, Gross RE, Grill WM (2012) Stimulus features underlying reduced tremor suppression with temporally patterned deep brain stimulation. J Neurophysiol 107:364-383.

Blomstedt P, Hariz GM, Hariz MI, Koskinen LO (2007) Thalamic deep brain stimulation in the treatment of essential tremor: a long-term follow-up. Br J Neurosurg 21:504-509.

Blum RA, Ross JD, Brown EA, DeWeerth SP (2007) An integrated system for simultaneous, multichannel neuronal stimulation and recording. IEEE Trans Circ Syst 54:2608-2618.

Boehnke SE, Rasmusson DD (2001) Time course and effective spread of lidocaine and tetrodotoxin delivered via microdialysis: an electrophysiological study in cerebral cortex. J Neurosci Methods 105:133-141.

Boex C, de Balthasar C, Kos MI, Pelizzone M (2003) Electrical field interactions in different cochlear implant systems. J Acoust Soc Am 114:2049-2057.

Boivie J (1971) The termination of the spinothalamic tract in the cat. An experimental study with silver impregnation methods. Exp Brain Res 112:331-353.

Bond M, Mealing S, Anderson R, Elston J, Weiner G, Taylor RS, Hoyle M, Liu Z, Price A, Stein K (2009) The effectiveness and cost-effectiveness of cochlear implants for severe to profound deafness in children and adults: a systematic review and economic model. Health Technol Assess 13:1-330.

Bossetti CA, Birdno MJ, Grill WM (2008) Analysis of the quasi-static approximation for calculating potentials generated by neural stimulation. J Neural Eng 5:44-53.

Briaire JJ, Frijns JH (2005) Unraveling the electrically evoked compound action potential. Hear Res 205:143-156.

Briggs F, Usrey WM (2007) A fast, reciprocal pathway between the lateral geniculate nucleus and visual cortex in the macaque monkey. J Neurosci 27:5431-5436.

Brocker DT, Swan BD, Turner DA, Gross RE, Tatter SB, Koop MM, Bronte-Stewart H, Grill WM (2013) Improved efficacy of temporally non-regular deep brain stimulation in Parkinson's disease. Exp Neurol 239:60-67.

Bronstein JM, Tagliati M, Alterman RL, Lozano AM, Volkmann J, Stefani A, Horak FB, Okun MS, Foote KD, Krack P, Pahwa R, Henderson JM, Hariz MI, Bakay RA, Rezai A, Marks WJ, Jr., Moro E, Vitek JL, Weaver FM, Gross RE, DeLong MR (2011) Deep brain stimulation for Parkinson disease: an expert consensus and review of key issues. Arch Neurol 68:165.

Bronte-Stewart H, Barberini C, Koop MM, Hill BC, Henderson JM, Wingeier B (2009) The STN beta-band profile in Parkinson's disease is stationary and shows prolonged attenuation after deep brain stimulation. Exp Neurol 215:20-28.

Brown CJ, Abbas PJ (1990) Electrically evoked whole-nerve action potentials: parametric data from the cat. J Acoust Soc Am 88:2205-2210.

Brown P (2003) Oscillatory nature of human basal ganglia activity: relationship to the pathophysiology of Parkinson's disease. Mov Disord 18:357-363.

Brown P, Marsden CD (1998) What do the basal ganglia do? Lancet 351:1801-1804.

Brown P, Mazzone P, Oliviero A, Altibrandi MG, Pilato F, Tonali PA, Di Lazzaro V (2004) Effects of stimulation of the subthalamic area on oscillatory pallidal activity in Parkinson's disease. Exp Neurol 188:480-490.

Brown P, Oliviero A, Mazzone P, Insola A, Tonali P, Di Lazzaro V (2001) Dopamine dependency of oscillations between subthalamic nucleus and pallidum in Parkinson's disease. J Neurosci 21:1033-1038.

Brown P, Williams D (2005) Basal ganglia local field potential activity: character and functional significance in the human. Clin Neurophysiol 116:2510-2519.

Buhlmann J, Hofmann L, Tass PA, Hauptmann C (2011) Modeling of a segmented electrode for desynchronizing deep brain stimulation. Front Neuroeng 4:15.

Burgess JG, Warwick K, Ruiz V, Gasson MN, Aziz TZ, Brittain JS, Stein J (2010) Identifying tremor-related characteristics of basal ganglia nuclei during movement in the Parkinsonian patient. Parkinsonism Relat Disord 16:671-675.

Butler AB, Hodos W (2005) Comparative Vertebrate Neuroanatomy: Evolution and Adaptation. Hoboken: John Wiley & Sons, Inc.

Butson CR, Maks CB, McIntyre CC (2006) Sources and effects of electrode impedance during deep brain stimulation. Clin Neurophysiol 117:447-454.

Butson CR, McIntyre CC (2005) Tissue and electrode capacitance reduce neural activation volumes during deep brain stimulation. Clin Neurophysiol 116:2490-2500.

Butson CR, McIntyre CC (2006) Role of electrode design on the volume of tissue activated during deep brain stimulation. J Neural Eng 3:1-8.

Buzsaki G, Anastassiou CA, Koch C (2012) The origin of extracellular fields and currents--EEG, ECoG, LFP and spikes. Nat Rev Neurosci 13:407-420.

Cassidy M, Mazzone P, Oliviero A, Insola A, Tonali P, Di Lazzaro V, Brown P (2002) Movement-related changes in synchronization in the human basal ganglia. Brain 125:1235-1246.

Chaturvedi A, Butson CR, Lempka SF, Cooper SE, McIntyre CC (2010) Patient-specific models of deep brain stimulation: influence of field model complexity on neural activation predictions. Brain Stimul 3:65-67.

Chen CC, Pogosyan A, Zrinzo LU, Tisch S, Limousin P, Ashkan K, Yousry T, Hariz MI, Brown P (2006) Intra-operative recordings of local field potentials can help localize the subthalamic nucleus in Parkinson's disease surgery. Exp Neurol 198:214-221.

Cheung T, Nuno M, Hoffman M, Katz M, Kilbane C, Alterman R, Tagliati M (2013) Longitudinal Impedance Variability in Patients with Chronically Implanted DBS Devices. Brain Stimul.

Chizeck HJ, Lalonde R, Chang CW, Rosenthal JA, Marsolais EB (1985) Performance of a closed-loop controller for electrically-stimulated standing in paralyzed patients. Proc 8th Annual RESNA Meet.

Chou KL (2007) Indications for subthalamic nucleus deep brain stimulation. In: Deep brain stimulation for Parkinson's disease (Baltuch, G. H. and Stern, M. B., eds) New York: Informa Healthcare USA, Inc.

Coenen VA, Madler B, Schiffbauer H, Urbach H, Allert N (2011) Individual fiber anatomy of the subthalamic region revealed with diffusion tensor imaging: a concept to identify the deep brain stimulation target for tremor suppression. Neurosurgery 68:1069-1075; discussion 1075-1066.

Cohen CJ, Bean BP, Colatsky TJ, Tsien RW (1981) Tetrodotoxin block of sodium channels in rabbit Purkinje fibers. Interactions between toxin binding and channel gating. J Gen Physiol 78:383-411.

Connor JD, Rossi GV, Baker WW (1966) Characteristics of tremor in cats following injections of carbachol into the caudate nucleus. Exp Neurol 14:371-382.

Cooper IS, Upton AR, Amin I (1980) Reversibility of chronic neurologic deficits. Some effects of electrical stimulation of the thalamus and internal capsule in man. Appl Neurophysiol 43:244-258.

Cooper IS, Upton AR, Amin I (1982) Chronic cerebellar stimulation (CCS) and deep brain stimulation (DBS) in involuntary movement disorders. Appl Neurophysiol 45:209-217.

Cooper SE, Kuncel AM, Wolgamuth BR, Rezai AR, Grill WM (2008) A model predicting optimal parameters for deep brain stimulation in essential tremor. J Clin Neurophysiol 25:265-273.

Courtney KR (1975) Mechanism of frequency-dependent inhibition of sodium currents in frog myelinated nerve by the lidocaine derivative GEA. J Pharmacol Exp Ther 195:225-236.

Crago PE, Mortimer JT, Peckham PH (1980) Closed-loop control of force during electrical stimulation of muscle. IEEE Trans Biomed Eng 27:306-312.

Crago PE, Nakai RJ, Chizeck HJ (1991) Feedback regulation of hand grasp opening and contact force during stimulation of paralyzed muscle. IEEE Trans Biomed Eng 38:17-28.

Craig AD, Burton H (1985) The distribution and topographical organization in the thalamus of anterogradely-transported horseradish peroxidase after spinal injections in cat and raccoon. Exp Brain Res 58:227-254.

Creutzfeldt OD, Watanabe S, Lux HD (1966) Relations between EEG phenomena and potentials of single cortical cells. I. Evoked responses after thalamic and erpicortical stimulation. Electroencephalogr Clin Neurophysiol 20:1-18.

Danish SF, Moyer JT, Finkel LH, Baltuch GH, Jaggi JL, Priori A, Foffani G (2007) High-frequency oscillations (>200 Hz) in the human non-parkinsonian subthalamic nucleus. Brain Res Bull 74:84-90.

de Montigny C, Lamarre Y (1973) Rhythmic activity induced by harmaline in the olivo-cerebello-bulbar system of the cat. Brain Res 53:81-95.

Degos B, Deniau JM, Thierry AM, Glowinski J, Pezard L, Maurice N (2005) Neuroleptic-induced catalepsy: electrophysiological mechanisms of functional recovery induced by high-frequency stimulation of the subthalamic nucleus. J Neurosci 25:7687-7696.

Delgado JM, Hamlin H, Chapman WP (1952) Technique of intracranial electrode implacement for recording and stimulation and its possible therapeutic value in psychotic patients. Confin Neurol 12:315-319.

Detsch O, Kochs E, Siemers M, Bromm B, Vahle-Hinz C (2002) Differential effects of isoflurane on excitatory and inhibitory synaptic inputs to thalamic neurones in vivo. Br J Anaesth 89:294-300.

Deuschl G, Elble RJ (2000) The pathophysiology of essential tremor. Neurology 54:S14-20.

Deuschl G, Herzog J, Kleiner-Fisman G, Kubu C, Lozano AM, Lyons KE, Rodriguez-Oroz MC, Tamma F, Troster AI, Vitek JL, Volkmann J, Voon V (2006) Deep brain stimulation: postoperative issues. Mov Disord 21 Suppl 14:S219-237.

Deuschl G, Raethjen J, Lindemann M, Krack P (2001) The pathophysiology of tremor. Muscle Nerve 24:716-735.

Devergnas A, Wichmann T (2011) Cortical potentials evoked by deep brain stimulation in the subthalamic area. Front Syst Neurosci 5:30.

Dimitrova NA, Dimitrov GV, Chikhman VN (1999) Effect of electrode dimensions on motor unit potentials. Med Eng Phys 21:479-485.

Dorval AD, Kuncel AM, Birdno MJ, Turner DA, Grill WM (2010) Deep brain stimulation alleviates parkinsonian bradykinesia by regularizing pallidal activity. J Neurophysiol 104:911-921.

Dorval AD, Russo GS, Hashimoto T, Xu W, Grill WM, Vitek JL (2008) Deep brain stimulation reduces neuronal entropy in the MPTP-primate model of Parkinson's disease. J Neurophysiol 100:2807-2818.

Dostrovsky JO, Levy R, Wu JP, Hutchison WD, Tasker RR, Lozano AM (2000) Microstimulation-induced inhibition of neuronal firing in human globus pallidus. J Neurophysiol 84:570-574.

Dostrovsky JO, Lozano AM (2002) Mechanisms of deep brain stimulation. Mov Disord 17 Suppl 3:S63-68.

Elble RJ, Pullman SL, Matsumoto JY, Raethjen J, Deuschl G, Tintner R (2006) Tremor amplitude is logarithmically related to 4- and 5-point tremor rating scales. Brain 129:2660-2666.

Eusebio A, Cagnan H, Brown P (2012) Does suppression of oscillatory synchronisation mediate some of the therapeutic effects of DBS in patients with Parkinson's disease? Front Integr Neurosci 6:47.

Fagni L, Weiss M, Pellet J, Hugon M (1982) The possible mechanisms of the high pressure-induced motor disturbances in the cat. Electroencephalogr Clin Neurophysiol 53:590-601.

Ferrara JM, Adam OR, Ondo WG (2009) Treatment of fragile-X-associated tremor/ataxia syndrome with deep brain stimulation. Mov Disord 24:149-151.

Fishler MG (1998) Syncytial heterogeneity as a mechanism underlying cardiac far-field stimulation during defibrillation-level shocks. J Cardiovasc Electrophysiol 9:384-394.

Foffani G, Ardolino G, Egidi M, Caputo E, Bossi B, Priori A (2006) Subthalamic oscillatory activities at beta or higher frequency do not change after high-frequency DBS in Parkinson's disease. Brain Res Bull 69:123-130.

Foffani G, Ardolino G, Meda B, Egidi M, Rampini P, Caputo E, Baselli G, Priori A (2005) Altered subthalamo-pallidal synchronisation in parkinsonian dyskinesias. J Neurol Neurosurg Psychiatry 76:426-428.

Foffani G, Priori A, Egidi M, Rampini P, Tamma F, Caputo E, Moxon KA, Cerutti S, Barbieri S (2003) 300-Hz subthalamic oscillations in Parkinson's disease. Brain 126:2153-2163.

Fogelson N, Kuhn AA, Silberstein P, Limousin PD, Hariz M, Trottenberg T, Kupsch A, Brown P (2005) Frequency dependent effects of subthalamic nucleus stimulation in Parkinson's disease. Neurosci Lett 382:5-9.

Foster KR, Schwan HP (1989) Dielectric properties of tissues and biological materials: a critical review. Crit Rev Biomed Eng 17:25-104.

Fountas KN, Smith JR, Murro AM, Politsky J, Park YD, Jenkins PD (2005) Implantation of a closed-loop stimulation in the management of medically refractory focal epilepsy: a technical note. Stereotact Funct Neurosurg 83:153-158.

Frankemolle AM, Wu J, Noecker AM, Voelcker-Rehage C, Ho JC, Vitek JL, McIntyre CC, Alberts JL (2010) Reversing cognitive-motor impairments in Parkinson's disease patients using a computational modelling approach to deep brain stimulation programming. Brain 133:746-761.

Frost JD, Jr. (1968) EEG-intracellular potential relationships in isolated cerebral cortex. Electroencephalogr Clin Neurophysiol 24:434-443.

Garcia L, Audin J, D'Alessandro G, Bioulac B, Hammond C (2003) Dual effect of high-frequency stimulation on subthalamic neuron activity. J Neurosci 23:8743-8751.

Garcia L, D'Alessandro G, Fernagut PO, Bioulac B, Hammond C (2005) Impact of high-frequency stimulation parameters on the pattern of discharge of subthalamic neurons. J Neurophysiol 94:3662-3669.

Gatev P, Darbin O, Wichmann T (2006) Oscillations in the basal ganglia under normal conditions and in movement disorders. Mov Disord 21:1566-1577.

Geddes LA, Baker LE (1967) The specific resistance of biological material--a compendium of data for the biomedical engineer and physiologist. Med Biol Eng 5:271-293.

Giannicola G, Marceglia S, Rossi L, Mrakic-Sposta S, Rampini P, Tamma F, Cogiamanian F, Barbieri S, Priori A (2010) The effects of levodopa and ongoing deep brain stimulation on subthalamic beta oscillations in Parkinson's disease. Exp Neurol 226:120-127.

Giannicola G, Rosa M, Marceglia S, Scelzo E, Rossi L, Servello D, Menghetti C, Pacchetti C, Zangaglia R, Locatelli M, Caputo E, Cogiamanian F, Ardolino G, Barbieri S, Priori A (2012a) The Effects of Levodopa and Deep Brain Stimulation on Subthalamic Local Field Low-Frequency Oscillations in Parkinson's Disease. Neurosignals 21:89-98.

Giannicola G, Rosa M, Servello D, Menghetti C, Carrabba G, Pacchetti C, Zangaglia R, Cogiamanian F, Scelzo E, Marceglia S, Rossi L, Priori A (2012b) Subthalamic local field potentials after seven-year deep brain stimulation in Parkinson's disease. Exp Neurol 237:312-317.

Gildenberg PL (2005) Evolution of neuromodulation. Stereotact Funct Neurosurg 83:71-79.

Gold C, Henze DA, Koch C, Buzsaki G (2006) On the origin of the extracellular action potential waveform: A modeling study. J Neurophysiol 95:3113-3128.

Gorzelic P, Schiff SJ, Sinha A (2013) Model-based rational feedback controller design for closed-loop deep brain stimulation of Parkinson's disease. J Neural Eng 10:1-16.

Gradinaru V, Mogri M, Thompson KR, Henderson JM, Deisseroth K (2009) Optical deconstruction of parkinsonian neural circuitry. Science 324:354-359.

Grant PF, Lowery MM (2010) Effect of dispersive conductivity and permittivity in volume conductor models of deep brain stimulation. IEEE Trans Biomed Eng 57:2386-2393.

Graupe D, Basu I, Tuninetti D, Vannemreddy P, Slavin KV (2010) Adaptively controlling deep brain stimulation in essential tremor patient via surface electromyography. Neurol Res 32:899-904.

Griffith RW, Humphrey DR (2006) Long-term gliosis around chronically implanted platinum electrodes in the Rhesus macaque motor cortex. Neurosci Lett 406:81-86.

Grill WM, McIntyre CC (2001) Extracellular excitation of central neurons: implications for the mechanisms of deep brain stimulation. Thalamus Relat Syst 1:269 –277.

Grill WM, Snyder AN, Miocinovic S (2004) Deep brain stimulation creates an informational lesion of the stimulated nucleus. Neuroreport 15:1137-1140.

Grill WM, Wei XF (2009) High efficiency electrodes for deep brain stimulation. Conf Proc IEEE Eng Med Biol Soc 2009:3298-3301.

Gross RE, Lozano AM (2000) Advances in neurostimulation for movement disorders. Neurol Res 22:247-258.

Grumet AE (1999) Electric stimulation parameters for an epi-retinal prosthesis. vol. PhD thesis: Massachusetts Institute of Technology.

Grumet AE, Wyatt JL, Jr., Rizzo JF, 3rd (2000) Multi-electrode stimulation and recording in the isolated retina. J Neurosci Methods 101:31-42.

Guo Y, Rubin JE (2011) Multi-site stimulation of subthalamic nucleus diminishes thalamocortical relay errors in a biophysical network model. Neural Netw 24:602-616.

Haberler C, Alesch F, Mazal PR, Pilz P, Jellinger K, Pinter MM, Hainfellner JA, Budka H (2000) No tissue damage by chronic deep brain stimulation in Parkinson's disease. Ann Neurol 48:372-376.

Hall RD (1990) Estimation of surviving spiral ganglion cells in the deaf rat using the electrically evoked auditory brainstem response. Hear Res 49:155-168.

Hamani C, Richter E, Schwalb JM, Lozano AM (2005) Bilateral subthalamic nucleus stimulation for Parkinson's disease: a systematic review of the clinical literature. Neurosurgery 56:1313-1321; discussion 1321-1314.

Hamel W, Herzog J, Kopper F, Pinsker M, Weinert D, Muller D, Krack P, Deuschl G, Mehdorn HM (2007) Deep brain stimulation in the subthalamic area is more effective than nucleus ventralis intermedius stimulation for bilateral intention tremor. Acta Neurochir (Wien) 149:749-758; discussion 758.

Hammond C, Bergman H, Brown P (2007) Pathological synchronization in Parkinson's disease: networks, models and treatments. Trends Neurosci 30:357-364.

Hanajima R, Dostrovsky JO, Lozano AM, Hutchison WD, Davis KD, Chen R, Ashby P (2004) Somatosensory evoked potentials (SEPs) recorded from deep brain stimulation (DBS) electrodes in the thalamus and subthalamic nucleus (STN). Clin Neurophysiol 115:424-434.

Hariz MI, Blomstedt P, Zrinzo L (2010) Deep brain stimulation between 1947 and 1987: the untold story. Neurosurg Focus 29:E1.

Hariz MI, Krack P, Alesch F, Augustinsson LE, Bosch A, Ekberg R, Johansson F, Johnels B, Meyerson BA, N'Guyen JP, Pinter M, Pollak P, von Raison F, Rehncrona S, Speelman JD, Sydow O, Benabid AL (2008) Multicentre European study of thalamic stimulation for parkinsonian tremor: a 6 year follow-up. J Neurol Neurosurg Psychiatry 79:694-699.

Hashimoto T, Elder CM, Okun MS, Patrick SK, Vitek JL (2003) Stimulation of the subthalamic nucleus changes the firing pattern of pallidal neurons. J Neurosci 23:1916-1923.

Hashimoto T, Elder CM, Vitek JL (2002) A template subtraction method for stimulus artifact removal in high-frequency deep brain stimulation. J Neurosci Methods 113:181-186.

Helmholtz HLF (1853) Ueber einige gesetze der vertheilung elektrischer strome in korperlichen leitern mit anwendung auf die thierisch-electrischen versuche. Ann Physik Chemie 89:354-377.

Henderson JM, Pell M, O'Sullivan DJ, McCusker EA, Fung VS, Hedges P, Halliday GM (2002) Postmortem analysis of bilateral subthalamic electrode implants in Parkinson's disease. Mov Disord 17:133-137.

Henze DA, Borhegyi Z, Csicsvari J, Mamiya A, Harris KD, Buzsaki G (2000) Intracellular features predicted by extracellular recordings in the hippocampus in vivo. J Neurophysiol 84:390-400.

Hersch SM, White EL (1981) Thalamocortical synapses with corticothalamic projection neurons in mouse SmI cortex: electron microscopic demonstration of a monosynaptic feedback loop. Neurosci Lett 24:207-210.

Hershey T, Revilla FJ, Wernle AR, McGee-Minnich L, Antenor JV, Videen TO, Dowling JL, Mink JW, Perlmutter JS (2003) Cortical and subcortical blood flow effects of subthalamic nucleus stimulation in PD. Neurology 61:816-821.

Herzog J, Hamel W, Wenzelburger R, Potter M, Pinsker MO, Bartussek J, Morsnowski A, Steigerwald F, Deuschl G, Volkmann J (2007) Kinematic analysis of thalamic versus subthalamic neurostimulation in postural and intention tremor. Brain 130:1608-1625.

Hines ML, Carnevale NT (2001) NEURON: a tool for neuroscientists. Neuroscientist 7:123-135.

Hirai T, Jones EG (1988) Segregation of lemniscal inputs and motor cortex outputs in cat ventral thalamic nuclei: application of a novel technique. Exp Brain Res 71:329-344.

Hirai T, Ohye C, Nagaseki Y, Matsumura M (1989) Cytometric analysis of the thalamic ventralis intermedius nucleus in humans. J Neurophysiol 61:478-487.

Hodaie M, Wennberg RA, Dostrovsky JO, Lozano AM (2002) Chronic anterior thalamus stimulation for intractable epilepsy. Epilepsia 43:603-608.

Holdefer RN, Cohen BA, Greene KA (2010) Intraoperative local field recording for deep brain stimulation in Parkinson's disease and essential tremor. Mov Disord 25:2067-2075.

Holt GR, Koch C (1999) Electrical interactions via the extracellular potential near cell bodies. J Comput Neurosci 6:169-184.

Hosobuchi Y, Adams JE, Rutkin B (1973) Chronic thalamic stimulation for the control of facial anesthesia dolorosa. Arch Neurol 29:158-161.

Hua SE, Lenz FA, Zirh TA, Reich SG, Dougherty PM (1998) Thalamic neuronal activity correlated with essential tremor. J Neurol Neurosurg Psychiatry 64:273-276.

Hughes ML, Brown CJ, Abbas PJ, Wolaver AA, Gervais JP (2000) Comparison of EAP thresholds with MAP levels in the nucleus 24 cochlear implant: data from children. Ear Hear 21:164-174.

Humphrey DR, Schmidt EM (1990) Extracellular single-unit recording methods. In: Neurophysiological Techniques, II: Applications to Neural Systems (Boulton, A. A. et al., eds), pp 1-64 Clifton, NJ: Humana Press.

Humphrey DR, Schmidt EM (1991) Neurophysiological Techniques : Applications to Neural Systems. In: Neuromethods, vol. 15 (Boulton, A. A. et al., eds) New York: Humana Press.

Jech R, Urgosik D, Tintera J, Nebuzelsky A, Krasensky J, Liscak R, Roth J, Ruzicka E (2001) Functional magnetic resonance imaging during deep brain stimulation: a pilot study in four patients with Parkinson's disease. Mov Disord 16:1126-1132.

Jeon EK, Brown CJ, Etler CP, O'Brien S, Chiou LK, Abbas PJ (2010) Comparison of electrically evoked compound action potential thresholds and loudness estimates for the stimuli used to program the Advanced Bionics cochlear implant. J Am Acad Audiol 21:16-27.

Jimbo Y, Kasai N, Torimitsu K, Tateno T, Robinson HP (2003) A system for MEA-based multisite stimulation. IEEE Trans Biomed Eng 50:241-248.

Jimenez Castellanos J (1949) Thalamus of the cat in Horsley-Clarke coordinates. J Comp Neurol 91:307-330, illust.

Johnson MD, Miocinovic S, McIntyre CC, Vitek JL (2008) Mechanisms and targets of deep brain stimulation in movement disorders. Neurotherapeutics 5:294-308.

Joksovic PM, Weiergraber M, Lee W, Struck H, Schneider T, Todorovic SM (2009) Isoflurane-sensitive presynaptic R-type calcium channels contribute to inhibitory synaptic transmission in the rat thalamus. J Neurosci 29:1434-1445.

Jones EG, Burton H (1974) Cytoarchitecture and somatic sensory connectivity of thalamic nuclei other than the ventrobasal complex in the cat. J Comp Neurol 154:395-432.

Kaelber WW (1963) Tremor at Rest from Tegmental Lesions in the Cat. J Neuropathol Exp Neurol 22:695-701.

Kajikawa Y, Schroeder CE (2011) How local is the local field potential? Neuron 72:847-858.

Kane A, Hutchison WD, Hodaie M, Lozano AM, Dostrovsky JO (2009) Enhanced synchronization of thalamic theta band local field potentials in patients with essential tremor. Exp Neurol 217:171-176.

Katzner S, Nauhaus I, Benucci A, Bonin V, Ringach DL, Carandini M (2009) Local origin of field potentials in visual cortex. Neuron 61:35-41.

Keane M, Deyo S, Abosch A, Bajwa JA, Johnson MD (2012) Improved spatial targeting with directionally segmented deep brain stimulation leads for treating essential tremor. J Neural Eng 9:1-10.

Kemp JA, McKernan RM (2002) NMDA receptor pathways as drug targets. Nat Neurosci 5 Suppl:1039-1042.

Kent AR, Grill WM (2011) Instrumentation to record evoked potentials for closed-loop control of deep brain stimulation. Conf Proc IEEE Eng Med Biol Soc 6777-6780.

Kent AR, Grill WM (2012) Recording evoked potentials during deep brain stimulation: development and validation of instrumentation to suppress the stimulus artefact. J Neural Eng 9:1-17.

Kent AR, Grill WM (2013) Neural origin of evoked potentials during thalamic deep brain stimulation. J Neurophysiol.

Khodorov BL, Shishkova L, Peganov E, Revenko S (1976) Inhibition of sodium currents in frog ranvier node treated with local anesthetics. Role of slow sodium inactivation. Biochim Biophys Acta 433:409-435.

Kitagawa M, Murata J, Uesugi H, Kikuchi S, Saito H, Tashiro K, Sawamura Y (2005) Two-year follow-up of chronic stimulation of the posterior subthalamic white matter for tremor-dominant Parkinson's disease. Neurosurgery 56:281-289; discussion 281-289.

Kossoff EH, Ritzl EK, Politsky JM, Murro AM, Smith JR, Duckrow RB, Spencer DD, Bergey GK (2004) Effect of an external responsive neurostimulator on seizures and electrographic discharges during subdural electrode monitoring. Epilepsia 45:1560-1567.

Krack P, Batir A, Van Blercom N, Chabardes S, Fraix V, Ardouin C, Koudsie A, Limousin PD, Benazzouz A, LeBas JF, Benabid AL, Pollak P (2003) Five-year follow-up of bilateral stimulation of the subthalamic nucleus in advanced Parkinson's disease. N Engl J Med 349:1925-1934.

Krack P, Fraix V, Mendes A, Benabid AL, Pollak P (2002) Postoperative management of subthalamic nucleus stimulation for Parkinson's disease. Mov Disord 17 Suppl 3:S188-197.

Krauss JK, Yianni J, Loher TJ, Aziz TZ (2004) Deep brain stimulation for dystonia. J Clin Neurophysiol 21:18-30.

Kreiman G, Hung CP, Kraskov A, Quiroga RQ, Poggio T, DiCarlo JJ (2006) Object selectivity of local field potentials and spikes in the macaque inferior temporal cortex. Neuron 49:433-445.

Kuhn AA, Kupsch A, Schneider GH, Brown P (2006) Reduction in subthalamic 8-35 Hz oscillatory activity correlates with clinical improvement in Parkinson's disease. Eur J Neurosci 23:1956-1960.

Kuhn AA, Trottenberg T, Kivi A, Kupsch A, Schneider GH, Brown P (2005) The relationship between local field potential and neuronal discharge in the subthalamic nucleus of patients with Parkinson's disease. Exp Neurol 194:212-220.

Kuhn AA, Tsui A, Aziz T, Ray N, Brucke C, Kupsch A, Schneider GH, Brown P (2009) Pathological synchronisation in the subthalamic nucleus of patients with Parkinson's disease relates to both bradykinesia and rigidity. Exp Neurol 215:380-387.

Kuhn AA, Williams D, Kupsch A, Limousin P, Hariz M, Schneider GH, Yarrow K, Brown P (2004) Event-related beta desynchronization in human subthalamic nucleus correlates with motor performance. Brain 127:735-746.

Kultas-Ilinsky K, Fogarty JD, Hughes B, Ilinsky IA (1988) Distribution and binding parameters of GABA and benzodiazepine receptors in the cat motor thalamus and adjacent nuclear groups. Brain Res 459:1-16.

Kumar K, Toth C, Nath RK (1997) Deep brain stimulation for intractable pain: a 15-year experience. Neurosurgery 40:736-746; discussion 746-737.

Kuncel AM, Cooper SE, Wolgamuth BR, Clyde MA, Snyder SA, Montgomery EB, Jr., Rezai AR, Grill WM (2006) Clinical response to varying the stimulus parameters in deep brain stimulation for essential tremor. Mov Disord 21:1920-1928.

Kuncel AM, Cooper SE, Wolgamuth BR, Grill WM (2007) Amplitude- and frequency-dependent changes in neuronal regularity parallel changes in tremor With thalamic deep brain stimulation. IEEE Trans Neural Syst Rehabil Eng 15:190-197.

Kuncel AM, Grill WM (2004) Selection of stimulus parameters for deep brain stimulation. Clin Neurophysiol 115:2431-2441.

Lamarre Y (1995) Central mechanisms of experimental tremor and their clinical relevance. In: Handbook of Tremor Disorders (Findley, L. J. and Koller, W. C., eds) New York City: Dekker.

Lee JY, Jeon BS, Paek SH, Lim YH, Kim MR, Kim C (2010) Reprogramming guided by the fused images of MRI and CT in subthalamic nucleus stimulation in Parkinson disease. Clin Neurol Neurosurg 112:47-53.

Lee KH, Blaha CD, Garris PA, Mohseni P, Horne AE, Bennet KE, Agnesi F, Bledsoe JM, Lester DB, Kimble C, Min HK, Kim YB, Cho ZH (2009) Evolution of Deep Brain Stimulation: Human Electrometer and Smart Devices Supporting the Next Generation of Therapy. Neuromodulation 12:85-103.

Lemay MA, Crago PE (1997) Closed-loop wrist stabilization in C4 and C5 tetraplegia. IEEE Trans Rehabil Eng 5:244-252.

Lempka SF, Johnson MD, Miocinovic S, Vitek JL, McIntyre CC (2010) Current-controlled deep brain stimulation reduces in vivo voltage fluctuations observed during voltage-controlled stimulation. Clin Neurophysiol 121:2128-2133.

Lempka SF, Johnson MD, Moffitt MA, Otto KJ, Kipke DR, McIntyre CC (2011) Theoretical analysis of intracortical microelectrode recordings. J Neural Eng 8:1-15.

Lempka SF, McIntyre CC (2013) Theoretical analysis of the local field potential in deep brain stimulation applications. PLoS One 8:e59839.

Lempka SF, Miocinovic S, Johnson MD, Vitek JL, McIntyre CC (2009) In vivo impedance spectroscopy of deep brain stimulation electrodes. J Neural Eng 6:1-11.

Lenz FA, Seike M, Richardson RT, Lin YC, Baker FH, Khoja I, Jaeger CJ, Gracely RH (1993) Thermal and pain sensations evoked by microstimulation in the area of human ventrocaudal nucleus. J Neurophysiol 70:200-212.

Lenz FA, Tasker RR, Kwan HC, Schnider S, Kwong R, Murayama Y, Dostrovsky JO, Murphy JT (1988) Single unit analysis of the human ventral thalamic nuclear group: correlation of thalamic "tremor cells" with the 3-6 Hz component of parkinsonian tremor. J Neurosci 8:754-764.

Levy R, Ashby P, Hutchison WD, Lang AE, Lozano AM, Dostrovsky JO (2002) Dependence of subthalamic nucleus oscillations on movement and dopamine in Parkinson's disease. Brain 125:1196-1209.

Levy R, Lang AE, Dostrovsky JO, Pahapill P, Romas J, Saint-Cyr J, Hutchison WD, Lozano AM (2001) Lidocaine and muscimol microinjections in subthalamic nucleus reverse Parkinsonian symptoms. Brain 124:2105-2118.

Limousin P, Pollak P, Benazzouz A, Hoffmann D, Le Bas JF, Broussolle E, Perret JE, Benabid AL (1995) Effect of parkinsonian signs and symptoms of bilateral subthalamic nucleus stimulation. Lancet 345:91-95.

Limousin P, Pollak P, Hoffmann D, Benazzouz A, Perret JE, Benabid AL (1996) Abnormal involuntary movements induced by subthalamic nucleus stimulation in parkinsonian patients. Mov Disord 11:231-235.

Lin CC, Liu WC, Chan CC, Ju MS (2012) Fuzzy control with amplitude/pulse-width modulation of nerve electrical stimulation for muscle force control. J Neural Eng 9:1-12.

Linden H, Tetzlaff T, Potjans TC, Pettersen KH, Grun S, Diesmann M, Einevoll GT (2011) Modeling the spatial reach of the LFP. Neuron 72:859-872.

Liu J, Newsome WT (2006) Local field potential in cortical area MT: stimulus tuning and behavioral correlations. J Neurosci 26:7779-7790.

Liu X, Griffin IC, Parkin SG, Miall RC, Rowe JG, Gregory RP, Scott RB, Aziz TZ, Stein JF (2002) Involvement of the medial pallidum in focal myoclonic dystonia: A clinical and neurophysiological case study. Mov Disord 17:346-353.

Llinas R, Baker R, Soleto C (1974) Electronic coupling between neurons in cat inferior olive. J Neurophysiol 37:560-571.

Llinas RR, Ribary U, Jeanmonod D, Kronberg E, Mitra PP (1999) Thalamocortical dysrhythmia: A neurological and neuropsychiatric syndrome characterized by magnetoencephalography. Proc Natl Acad Sci U S A 96:15222-15227.

Long SK, Smith DA, Siarey RJ, Evans RH (1990) Effect of 6-cyano-2,3-dihydroxy-7-nitro-quinoxaline (CNQX) on dorsal root-, NMDA-, kainate- and quisqualate-mediated depolarization of rat motoneurones in vitro. Br J Pharmacol 100:850-854.

Lopez-Azcarate J, Tainta M, Rodriguez-Oroz MC, Valencia M, Gonzalez R, Guridi J, Iriarte J, Obeso JA, Artieda J, Alegre M (2010) Coupling between beta and high-frequency activity in the human subthalamic nucleus may be a pathophysiological mechanism in Parkinson's disease. J Neurosci 30:6667-6677.

Lyons KE, Pahwa R (2004) Deep brain stimulation and essential tremor. J Clin Neurophysiol 21:2-5.

Macherey O, Carlyon RP, van Wieringen A, Deeks JM, Wouters J (2008) Higher sensitivity of human auditory nerve fibers to positive electrical currents. J Assoc Res Otolaryngol 9:241-251.

Magnin M, Morel A, Jeanmonod D (2000) Single-unit analysis of the pallidum, thalamus and subthalamic nucleus in parkinsonian patients. Neuroscience 96:549-564.

Mallart A (1968) Thalamic projection of muscle nerve afferents in the cat. J Physiol 194:337-353.

Marceglia S, Mrakic-Sposta S, Foffani G, Cogiamanian F, Caputo E, Egidi M, Barbieri S, Priori A (2006) Gender-related differences in the human subthalamic area: a local field potential study. Eur J Neurosci 24:3213-3222.

Marceglia S, Rossi L, Foffani G, Bianchi A, Cerutti S, Priori A (2007) Basal ganglia local field potentials: applications in the development of new deep brain stimulation devices for movement disorders. Expert Rev Med Devices 4:605-614.

Marsden JF, Ashby P, Limousin-Dowsey P, Rothwell JC, Brown P (2000) Coherence between cerebellar thalamus, cortex and muscle in man: cerebellar thalamus interactions. Brain 123 (Pt 7):1459-1470.

Marsden JF, Limousin-Dowsey P, Ashby P, Pollak P, Brown P (2001) Subthalamic nucleus, sensorimotor cortex and muscle interrelationships in Parkinson's disease. Brain 124:378-388.

Martin FC, Thu Le A, Handforth A (2005) Harmaline-induced tremor as a potential preclinical screening method for essential tremor medications. Mov Disord 20:298-305.

Matsuoka AJ, Rubinstein JT, Abbas PJ, Miller CA (2001) The effects of interpulse interval on stochastic properties of electrical stimulation: models and measurements. IEEE Trans Biomed Eng 48:416-424.

Mayberg HS, Lozano AM, Voon V, McNeely HE, Seminowicz D, Hamani C, Schwalb JM, Kennedy SH (2005) Deep brain stimulation for treatment-resistant depression. Neuron 45:651-660.

Mazars GJ (1975) Intermittent stimulation of nucleus ventralis posterolateralis for intractable pain. Surg Neurol 4:93-95.

Mazzone P, Lozano A, Stanzione P, Galati S, Scarnati E, Peppe A, Stefani A (2005) Implantation of human pedunculopontine nucleus: a safe and clinically relevant target in Parkinson's disease. Neuroreport 16:1877-1881.

Mc Laughlin M, Lu T, Dimitrijevic A, Zeng FG (2012) Towards a closed-loop cochlear implant system: application of embedded monitoring of peripheral and central neural activity. IEEE Trans Neural Syst Rehabil Eng 20:443-454.

McConnell GC, Rees HD, Levey AI, Gutekunst CA, Gross RE, Bellamkonda RV (2009) Implanted neural electrodes cause chronic, local inflammation that is correlated with local neurodegeneration. J Neural Eng 6:1-12.

McConnell GC, So RQ, Hilliard JD, Lopomo P, Grill WM (2012) Effective deep brain stimulation suppresses low-frequency network oscillations in the basal ganglia by regularizing neural firing patterns. J Neurosci 32:15657-15668.

McGill KC, Cummins KL, Dorfman LJ, Berlizot BB, Leutkemeyer K, Nishimura DG, Widrow B (1982) On the nature and elimination of stimulus artifact in nerve signals evoked and recorded using surface electrodes. IEEE Trans Biomed Eng 29:129-137.

McIntyre CC, Grill WM (1999) Excitation of central nervous system neurons by nonuniform electric fields. Biophys J 76:878-888.

McIntyre CC, Grill WM (2000) Selective microstimulation of central nervous system neurons. Ann Biomed Eng 28:219-233.

McIntyre CC, Grill WM, Sherman DL, Thakor NV (2004a) Cellular effects of deep brain stimulation: model-based analysis of activation and inhibition. J Neurophysiol 91:1457-1469.

McIntyre CC, Richardson AG, Grill WM (2002) Modeling the excitability of mammalian nerve fibers: influence of afterpotentials on the recovery cycle. J Neurophysiol 87:995-1006.

McIntyre CC, Savasta M, Kerkerian-Le Goff L, Vitek JL (2004b) Uncovering the mechanism(s) of action of deep brain stimulation: activation, inhibition, or both. Clin Neurophysiol 115:1239-1248.

Meissner W, Leblois A, Hansel D, Bioulac B, Gross CE, Benazzouz A, Boraud T (2005) Subthalamic high frequency stimulation resets subthalamic firing and reduces abnormal oscillations. Brain 128:2372-2382.

Merrill DR, Bikson M, Jefferys JG (2005) Electrical stimulation of excitable tissue: design of efficacious and safe protocols. J Neurosci Methods 141:171-198.

Middlebrooks JC, Bierer JA, Snyder RL (2005) Cochlear implants: the view from the brain. Curr Opin Neurobiol 15:488-493.

Miller CA, Abbas PJ, Brown CJ (2000) An improved method of reducing stimulus artifact in the electrically evoked whole-nerve potential. Ear Hear 21:280-290.

Miller CA, Abbas PJ, Robinson BK (2001a) Response properties of the refractory auditory nerve fiber. J Assoc Res Otolaryngol 2:216-232.

Miller CA, Abbas PJ, Robinson BK, Rubinstein JT, Matsuoka AJ (1999) Electrically evoked single-fiber action potentials from cat: responses to monopolar, monophasic stimulation. Hear Res 130:197-218.

Miller CA, Abbas PJ, Rubinstein JT, Robinson BK, Matsuoka AJ, Woodworth G (1998) Electrically evoked compound action potentials of guinea pig and cat: responses to monopolar, monophasic stimulation. Hear Res 119:142-154.

Miller CA, Brown CJ, Abbas PJ, Chi SL (2008) The clinical application of potentials evoked from the peripheral auditory system. Hear Res 242:184-197.

Miller CA, Robinson BK, Rubinstein JT, Abbas PJ, Runge-Samuelson CL (2001b) Auditory nerve responses to monophasic and biphasic electric stimuli. Hear Res 151:79-94.

Mina F, Benquet P, Pasnicu A, Biraben A, Wendling F (2013) Modulation of epileptic activity by deep brain stimulation: a model-based study of frequency-dependent effects. Front Comput Neurosci 7:94.

Miocinovic S, Lempka SF, Russo GS, Maks CB, Butson CR, Sakaie KE, Vitek JL, McIntyre CC (2009) Experimental and theoretical characterization of the voltage distribution generated by deep brain stimulation. Exp Neurol 216:166-176.

Miocinovic S, Parent M, Butson CR, Hahn PJ, Russo GS, Vitek JL, McIntyre CC (2006) Computational analysis of subthalamic nucleus and lenticular fasciculus activation during therapeutic deep brain stimulation. J Neurophysiol 96:1569-1580.

Mitzdorf U (1985) Current source-density method and application in cat cerebral cortex: investigation of evoked potentials and EEG phenomena. Physiol Rev 65:37-100.

Miyagi Y, Okamoto T, Morioka T, Tobimatsu S, Nakanishi Y, Aihara K, Hashiguchi K, Murakami N, Yoshida F, Samura K, Nagata S, Sasaki T (2009) Spectral analysis of field potential recordings by deep brain stimulation electrode for localization of subthalamic nucleus in patients with Parkinson's disease. Stereotact Funct Neurosurg 87:211-218.

Moffitt MA, McIntyre CC (2005) Model-based analysis of cortical recording with silicon microelectrodes. Clin Neurophysiol 116:2240-2250.

Moro E, Esselink RJ, Xie J, Hommel M, Benabid AL, Pollak P (2002) The impact on Parkinson's disease of electrical parameter settings in STN stimulation. Neurology 59:706-713.

Moro E, Poon YY, Lozano AM, Saint-Cyr JA, Lang AE (2006) Subthalamic nucleus stimulation: improvements in outcome with reprogramming. Arch Neurol 63:1266-1272.

Moss J, Ryder T, Aziz TZ, Graeber MB, Bain PG (2004) Electron microscopy of tissue adherent to explanted electrodes in dystonia and Parkinson's disease. Brain 127:2755-2763.

Newbold C, Richardson R, Millard R, Huang C, Milojevic D, Shepherd R, Cowan R (2010) Changes in biphasic electrode impedance with protein adsorption and cell growth. J Neural Eng 7:1-11.

Newbold C, Richardson R, Millard R, Seligman P, Cowan R, Shepherd R (2011) Electrical stimulation causes rapid changes in electrode impedance of cell-covered electrodes. J Neural Eng 8:1-13.

Nielsen MS, Bjarkam CR, Sorensen JC, Bojsen-Moller M, Sunde NA, Ostergaard K (2007) Chronic subthalamic high-frequency deep brain stimulation in Parkinson's disease--a histopathological study. Eur J Neurol 14:132-138.

Nini A, Feingold A, Slovin H, Bergman H (1995) Neurons in the globus pallidus do not show correlated activity in the normal monkey, but phase-locked oscillations appear in the MPTP model of parkinsonism. J Neurophysiol 74:1800-1805.

Noudoost B, Moore T (2011) A reliable microinjectrode system for use in behaving monkeys. J Neurosci Methods 194:218-223.

Nuttin BJ, Gabriels L, van Kuyck K, Cosyns P (2003) Electrical stimulation of the anterior limbs of the internal capsules in patients with severe obsessive-compulsive disorder: anecdotal reports. Neurosurg Clin N Am 14:267-274.

O'Suilleabhain PE, Frawley W, Giller C, Dewey RB, Jr. (2003) Tremor response to polarity, voltage, pulsewidth and frequency of thalamic stimulation. Neurology 60:786-790.

Okun MS, Tagliati M, Pourfar M, Fernandez HH, Rodriguez RL, Alterman RL, Foote KD (2005) Management of referred deep brain stimulation failures: a retrospective analysis from 2 movement disorders centers. Arch Neurol 62:1250-1255.

Ondo WG, Bronte-Stewart H (2005) The North American survey of placement and adjustment strategies for deep brain stimulation. Stereotact Funct Neurosurg 83:142-147.

Osorio I, Frei MG, Sunderam S, Giftakis J, Bhavaraju NC, Schaffner SF, Wilkinson SB (2005) Automated seizure abatement in humans using electrical stimulation. Ann Neurol 57:258-268.

Owen SL, Green AL, Stein JF, Aziz TZ (2006) Deep brain stimulation for the alleviation of post-stroke neuropathic pain. Pain 120:202-206.

Pahwa R, Lyons KE, Wilkinson SB, Simpson RK, Jr., Ondo WG, Tarsy D, Norregaard T, Hubble JP, Smith DA, Hauser RA, Jankovic J (2006) Long-term evaluation of deep brain stimulation of the thalamus. J Neurosurg 104:506-512.

Pedrosa DJ, Reck C, Florin E, Pauls KA, Maarouf M, Wojtecki L, Dafsari HS, Sturm V, Schnitzler A, Fink GR, Timmermann L (2012) Essential tremor and tremor in Parkinson's disease are associated with distinct 'tremor clusters' in the ventral thalamus. Exp Neurol 237:435-443.

Perozzo P, Rizzone M, Bergamasco B, Castelli L, Lanotte M, Tavella A, Torre E, Lopiano L (2001) Deep brain stimulation of subthalamic nucleus: behavioural modifications and familiar relations. Neurol Sci 22:81-82.

Pesenti A, Priori A, Locatelli M, Egidi M, Rampini P, Tamma F, Caputo E, Chiesa V, Barbieri S (2003) Subthalamic somatosensory evoked potentials in Parkinson's disease. Mov Disord 18:1341-1345.

Phillips MD, Baker KB, Lowe MJ, Tkach JA, Cooper SE, Kopell BH, Rezai AR (2006) Parkinson disease: pattern of functional MR imaging activation during deep

brain stimulation of subthalamic nucleus--initial experience. Radiology 239:209-216.

Pierantozzi M, Mazzone P, Bassi A, Rossini PM, Peppe A, Altibrandi MG, Stefani A, Bernardi G, Stanzione P (1999) The effect of deep brain stimulation on the frontal N30 component of somatosensory evoked potentials in advanced Parkinson's disease patients. Clin Neurophysiol 110:1700-1707.

Plaha P, Ben-Shlomo Y, Patel NK, Gill SS (2006) Stimulation of the caudal zona incerta is superior to stimulation of the subthalamic nucleus in improving contralateral parkinsonism. Brain 129:1732-1747.

Plonsey R (1965) Dependence of scalar potential measurements on electrode geometry. The Review of Scientific Intruments 36:1034-1036.

Plonsey R, Barr RC (2007) Bioelectricity: A quantitative approach New York: Springer Science+Business Media.

Pogosyan A, Yoshida F, Chen CC, Martinez-Torres I, Foltynie T, Limousin P, Zrinzo L, Hariz MI, Brown P (2010) Parkinsonian impairment correlates with spatially extensive subthalamic oscillatory synchronization. Neuroscience 171:245-257.

Pollak P, Benabid AL, Gross C, Gao DM, Laurent A, Benazzouz A, Hoffmann D, Gentil M, Perret J (1993) [Effects of the stimulation of the subthalamic nucleus in Parkinson disease]. Rev Neurol (Paris) 149:175-176.

Pollak P, Benabid AL, Krack P, Limousin P, Benazzouz A (1998) Deep brain stimulation. Baltimore: Williams & Wilkins.

Posner LP, Burns P (2009) Injectable Anesthetic Agents. In: Veterinary Pharmacologicy & Therapeutics (Riviere, J. E. and Papich, M. G., eds), pp 265-300 Ames: Wiley-Blackwell.

Priori A, Ardolino G, Marceglia S, Mrakic-Sposta S, Locatelli M, Tamma F, Rossi L, Foffani G (2006) Low-frequency subthalamic oscillations increase after deep brain stimulation in Parkinson's disease. Brain Res Bull 71:149-154.

Priori A, Foffani G, Pesenti A, Bianchi A, Chiesa V, Baselli G, Caputo E, Tamma F, Rampini P, Egidi M, Locatelli M, Barbieri S, Scarlato G (2002) Movement-related modulation of neural activity in human basal ganglia and its L-DOPA dependency: recordings from deep brain stimulation electrodes in patients with Parkinson's disease. Neurol Sci 23 Suppl 2:S101-102.

Priori A, Foffani G, Pesenti A, Tamma F, Bianchi AM, Pellegrini M, Locatelli M, Moxon KA, Villani RM (2004) Rhythm-specific pharmacological modulation of subthalamic activity in Parkinson's disease. Exp Neurol 189:369-379.

Priori A, Foffani G, Rossi L, Marceglia S (2012) Adaptive deep brain stimulation (aDBS) controlled by local field potential oscillations. Exp Neurol.

Ramsden RT (2002) Cochlear implants and brain stem implants. Br Med Bull 63:183-193.

Ranck JB, Jr. (1963) Specific impedance of rabbit cerebral cortex. Exp Neurol 7:144-152.

Ranck JB, Jr. (1975) Which elements are excited in electrical stimulation of mammalian central nervous system: a review. Brain Res 98:417-440.

Rathnasingham R, Kipke DR, Bledsoe SC, Jr., McLaren JD (2004) Characterization of implantable microfabricated fluid delivery devices. IEEE Trans Biomed Eng 51:138-145.

Rauschecker JP, Shannon RV (2002) Sending sound to the brain. Science 295:1025-1029.

Ray NJ, Jenkinson N, Wang S, Holland P, Brittain JS, Joint C, Stein JF, Aziz T (2008) Local field potential beta activity in the subthalamic nucleus of patients with Parkinson's disease is associated with improvements in bradykinesia after dopamine and deep brain stimulation. Exp Neurol 213:108-113.

Rodriguez-Oroz MC, Lopez-Azcarate J, Garcia-Garcia D, Alegre M, Toledo J, Valencia M, Guridi J, Artieda J, Obeso JA (2011) Involvement of the subthalamic nucleus in impulse control disorders associated with Parkinson's disease. Brain 134:36-49.

Rohatgi P, Langhals NB, Kipke DR, Patil PG (2009) In vivo performance of a microelectrode neural probe with integrated drug delivery. Neurosurg Focus 27:E8.

Romito LM, Albanese A (2010) Dopaminergic therapy and subthalamic stimulation in Parkinson's disease: a review of 5-year reports. J Neurol 257:S298-304.

Rosa M, Giannicola G, Marceglia S, Fumagalli M, Barbieri S, Priori A (2012) Neurophysiology of deep brain stimulation. Int Rev Neurobiol 107:23-55.

Rosa M, Giannicola G, Servello D, Marceglia S, Pacchetti C, Porta M, Sassi M, Scelzo E, Barbieri S, Priori A (2011) Subthalamic local field beta oscillations during

ongoing deep brain stimulation in Parkinson's disease in hyperacute and chronic phases. Neurosignals 19:151-162.

Rosa M, Marceglia S, Servello D, Foffani G, Rossi L, Sassi M, Mrakic-Sposta S, Zangaglia R, Pacchetti C, Porta M, Priori A (2010) Time dependent subthalamic local field potential changes after DBS surgery in Parkinson's disease. Exp Neurol 222:184-190.

Rosin B, Slovik M, Mitelman R, Rivlin-Etzion M, Haber SN, Israel Z, Vaadia E, Bergman H (2011) Closed-loop deep brain stimulation is superior in ameliorating parkinsonism. Neuron 72:370-384.

Rossi L, Foffani G, Marceglia S, Bracchi F, Barbieri S, Priori A (2007) An electronic device for artefact suppression in human local field potential recordings during deep brain stimulation. J Neural Eng 4:96-106.

Rossi L, Marceglia S, Foffani G, Cogiamanian F, Tamma F, Rampini P, Barbieri S, Bracchi F, Priori A (2008) Subthalamic local field potential oscillations during ongoing deep brain stimulation in Parkinson's disease. Brain Res Bull 76:512-521.

Rouse AG, Stanslaski SR, Cong P, Jensen RM, Afshar P, Ullestad D, Gupta R, Molnar GF, Moran DW, Denison TJ (2011) A chronic generalized bi-directional brain-machine interface. J Neural Eng 8:1-19.

Rubin JE, Terman D (2004) High frequency stimulation of the subthalamic nucleus eliminates pathological thalamic rhythmicity in a computational model. J Comput Neurosci 16:211-235.

Rubinstein JT (2004) An introduction to the biophysics of the electrically evoked compound action potential. Int J Audiol 43 Suppl 1:S3-9.

Sandvik U, Lars-Owe K, Anders L, Patric B (2011) Thalamic and Subthalamic Deep Brain Stimulation for Essential Tremor: Where Is the Optimal Target? Neurosurgery 70:840-846.

Santaniello S, Fiengo G, Glielmo L, Grill WM (2011) Closed-loop control of deep brain stimulation: a simulation study. IEEE Trans Neural Syst Rehabil Eng 19:15-24.

Sato F, Nakamura Y, Shinoda Y (1996) Three-dimensional analysis of cerebellar terminals and their postsynaptic components in the ventral lateral nucleus of the cat thalamus. J Comp Neurol 371:537-551.

Schmid G, Neubauer G, Illievich UM, Alesch F (2003) Dielectric properties of porcine brain tissue in the transition from life to death at frequencies from 800 to 1900 MHz. Bioelectromagnetics 24:413-422.

Schneider JS, Yuwiler A, Markham CH (1986) Production of a Parkinson-like syndrome in the cat with N-methyl-4-phenyl-1,2,3,6-tetrahydropyridine (MPTP): behavior, histology, and biochemistry. Exp Neurol 91:293-307.

Schoonhoven R, De Weerd JP (1984) On the optimal choice of a recording electrode in electroneurography. Electroencephalogr Clin Neurophysiol 58:308-316.

Schwan HP, Kay CF (1957) The conductivity of living tissues. Ann N Y Acad Sci 65:1007-1013.

Sherman SM (2004) Interneurons and triadic circuitry of the thalamus. Trends Neurosci 27:670-675.

Shukla P, Basu I, Graupe D, Tuninetti D, Slavin KV (2012) A neural network-based design of an on-off adaptive control for Deep Brain Stimulation in movement disorders. Conf Proc IEEE Eng Med Biol Soc 2012:4140-4143.

Silberstein P, Kuhn AA, Kupsch A, Trottenberg T, Krauss JK, Wohrle JC, Mazzone P, Insola A, Di Lazzaro V, Oliviero A, Aziz T, Brown P (2003) Patterning of globus pallidus local field potentials differs between Parkinson's disease and dystonia. Brain 126:2597-2608.

Silberstein P, Oliviero A, Di Lazzaro V, Insola A, Mazzone P, Brown P (2005a) Oscillatory pallidal local field potential activity inversely correlates with limb dyskinesias in Parkinson's disease. Exp Neurol 194:523-529.

Silberstein P, Pogosyan A, Kuhn AA, Hotton G, Tisch S, Kupsch A, Dowsey-Limousin P, Hariz MI, Brown P (2005b) Cortico-cortical coupling in Parkinson's disease and its modulation by therapy. Brain 128:1277-1291.

Smirnov DA, Barnikol UB, Barnikol TT, Bezruchko BP, Hauptmann C, Buhrle C, Maarouf M, Sturm V, Freund HJ, Tass PA (2008) The generation of parkinsonian tremor as revealed by directional coupling analysis. Europhys Lett 83:1-6.

Snider RS, Niemer WT (1961) A Stereotaxic Atlas of the Cat Brain. Chicago: The University of Chicago Press.

Stanslaski S, Afshar P, Cong P, Giftakis J, Stypulkowski P, Carlson D, Linde D, Ullestad D, Avestruz AT, Denison T (2012) Design and validation of a fully implantable, chronic, closed-loop neuromodulation device with concurrent sensing and stimulation. IEEE Trans Neural Syst Rehabil Eng 20:410-421.

Stanslaski S, Cong P, Carlson D, Santa W, Jensen R, Molnar G, Marks WJ, Jr., Shafquat A, Denison T (2009) An implantable bi-directional brain-machine interface system for chronic neuroprosthesis research. Conf Proc IEEE Eng Med Biol Soc 2009:5494-5497.

Steriade M, Jones EG, McCormick DA (1997) Thalamus. Oxford: Elsevier Science Ltd.

Strichartz GR (1973) The inhibition of sodium currents in myelinated nerve by quaternary derivatives of lidocaine. J Gen Physiol 62:37-57.

Stypulkowski PH, Giftakis JE, Billstrom TM (2011) Development of a large animal model for investigation of deep brain stimulation for epilepsy. Stereotact Funct Neurosurg 89:111-122.

Sun DA, Yu H, Spooner J, Tatsas AD, Davis T, Abel TW, Kao C, Konrad PE (2008) Postmortem analysis following 71 months of deep brain stimulation of the subthalamic nucleus for Parkinson disease. J Neurosurg 109:325-329.

Surowiec A, Stuchly SS, Swarup A (1986) Postmortem changes of the dielectric properties of bovine brain tissues at low radiofrequencies. Bioelectromagnetics 7:31-43.

Swan BD, Grill WM, Turner DA (2013) Investigation of deep brain stimulation mechanisms during implantable pulse generator replacement surgery. Submitted for publication.

Tamma F, Caputo E, Chiesa V, Egidi M, Locatelli M, Rampini P, Cinnante C, Pesenti A, Priori A (2002) Anatomo-clinical correlation of intraoperative stimulation-induced side-effects during HF-DBS of the subthalamic nucleus. Neurol Sci 23 Suppl 2:S109-110.

Tang JK, Moro E, Lozano AM, Lang AE, Hutchison WD, Mahant N, Dostrovsky JO (2005) Firing rates of pallidal neurons are similar in Huntington's and Parkinson's disease patients. Exp Brain Res 166:230-236.

Tass P, Smirnov D, Karavaev A, Barnikol U, Barnikol T, Adamchic I, Hauptmann C, Pawelcyzk N, Maarouf M, Sturm V, Freund HJ, Bezruchko B (2010) The causal

relationship between subcortical local field potential oscillations and Parkinsonian resting tremor. J Neural Eng 7:1-16.

Taylor Tavares AL, Jefferis GS, Koop M, Hill BC, Hastie T, Heit G, Bronte-Stewart HM (2005) Quantitative measurements of alternating finger tapping in Parkinson's disease correlate with UPDRS motor disability and reveal the improvement in fine motor control from medication and deep brain stimulation. Mov Disord 20:1286-1298.

Temperli P, Ghika J, Villemure JG, Burkhard PR, Bogousslavsky J, Vingerhoets FJ (2003) How do parkinsonian signs return after discontinuation of subthalamic DBS? Neurology 60:78-81.

Terman D, Rubin JE, Yew AC, Wilson CJ (2002) Activity patterns in a model for the subthalamopallidal network of the basal ganglia. J Neurosci 22:2963-2976.

Timmermann L, Wojtecki L, Gross J, Lehrke R, Voges J, Maarouf M, Treuer H, Sturm V, Schnitzler A (2004) Ten-Hertz stimulation of subthalamic nucleus deteriorates motor symptoms in Parkinson's disease. Mov Disord 19:1328-1333.

Tracey B, Williams M (2011) Computationally efficient bioelectric field modeling and effects of frequency-dependent tissue capacitance. J Neural Eng 8:1-7.

Tyler DJ, Durand DM (1997) Combined modulation of pulse width and pulse amplitude to enhance functional selectivity of neural stimulation. Conf Proc IEEE Eng Med Biol Soc 1997:1109-1110.

Uhlhaas PJ, Singer W (2006) Neural synchrony in brain disorders: relevance for cognitive dysfunctions and pathophysiology. Neuron 52:155-168.

Ulbricht W, Wagner HH (1975) The influence of pH on equilibrium effects of tetrodotoxin on myelinated nerve fibres of Rana esculenta. J Physiol 252:159-184.

Upton AR, Cooper IS, Springman M, Amin I (1985) Suppression of seizures and psychosis of limbic system origin by chronic stimulation of anterior nucleus of the thalamus. Int J Neurol 19-20:223-230.

Urbano F, Leznik E, Llinás R (2002) Cortical activation patterns evoked by afferent axons stimuli at different frequencies: an in vitro voltage-sensitive dye imaging study. Thalamus & Related Systems 1:371-378.

Ushe M, Mink JW, Revilla FJ, Wernle A, Schneider Gibson P, McGee-Minnich L, Hong M, Rich KM, Lyons KE, Pahwa R, Perlmutter JS (2004) Effect of stimulation frequency on tremor suppression in essential tremor. Mov Disord 19:1163-1168.

Valls-Sole J, Compta Y, Costa J, Valldeoriola F, Rumia J (2008) Human central nervous system circuits examined through the electrodes implanted for deep brain stimulation. Clin Neurophysiol 119:1219-1231.

van den Honert C, Mortimer JT (1979) The response of the myelinated nerve fiber to short duration biphasic stimulating currents. Ann Biomed Eng 7:117-125.

van Dijk JP, Lowery MM, Lapatki BG, Stegeman DF (2009) Evidence of potential averaging over the finite surface of a bioelectric surface electrode. Ann Biomed Eng 37:1141-1151.

van Wieringen A, Macherey O, Carlyon RP, Deeks JM, Wouters J (2008) Alternative pulse shapes in electrical hearing. Hear Res 242:154-163.

Villablanca J, Riobo F (1970) Electroencephalographic and behavioral effects of harmaline in intact cats and in cats with chronic mesencephalic transection. Psychopharmacologia 17:302-313.

Vitek JL, Chockkan V, Zhang JY, Kaneoke Y, Evatt M, DeLong MR, Triche S, Mewes K, Hashimoto T, Bakay RA (1999) Neuronal activity in the basal ganglia in patients with generalized dystonia and hemiballismus. Ann Neurol 46:22-35.

Volkmann J, Herzog J, Kopper F, Deuschl G (2002) Introduction to the programming of deep brain stimulators. Mov Disord 17 Suppl 3:S181-187.

Volkmann J, Moro E, Pahwa R (2006) Basic algorithms for the programming of deep brain stimulation in Parkinson's disease. Mov Disord 21 Suppl 14:S284-289.

Wagenaar DA, Potter SM (2002) Real-time multi-channel stimulus artifact suppression by local curve fitting. J Neurosci Methods 120:113-120.

Wang LY, Kaczmarek LK (1998) High-frequency firing helps replenish the readily releasable pool of synaptic vesicles. Nature 394:384-388.

Wang P, Anderko A (2001) Computation of dielectric constants of solvent mixtures and electrolyte solutions. Fluid Phase Equilib 186:103-122.

Wang Q, Millard DC, Zheng HJ, Stanley GB (2012) Voltage-sensitive dye imaging reveals improved topographic activation of cortex in response to manipulation of thalamic microstimulation parameters. J Neural Eng 9:1-14.

Wang S, Chen Y, Ding M, Feng J, Stein JF, Aziz TZ, Liu X (2007) Revealing the dynamic causal interdependence between neural and muscular signals in Parkinsonian tremor. Jour Frank Institute 344:180-195.

Weaver FM, Follett KA, Stern M, Luo P, Harris CL, Hur K, Marks WJ, Jr., Rothlind J, Sagher O, Moy C, Pahwa R, Burchiel K, Hogarth P, Lai EC, Duda JE, Holloway K, Samii A, Horn S, Bronstein JM, Stoner G, Starr PA, Simpson R, Baltuch G, De Salles A, Huang GD, Reda DJ (2012) Randomized trial of deep brain stimulation for Parkinson disease: thirty-six-month outcomes. Neurology 79:55-65.

Wei XF, Grill WM (2005) Current density distributions, field distributions and impedance analysis of segmented deep brain stimulation electrodes. J Neural Eng 2:139-147.

Wei XF, Grill WM (2009) Impedance characteristics of deep brain stimulation electrodes in vitro and in vivo. J Neural Eng 6:1-9.

Weinberger M, Hutchison WD, Dostrovsky JO (2009) Pathological subthalamic nucleus oscillations in PD: can they be the cause of bradykinesia and akinesia? Exp Neurol 219:58-61.

Weinberger M, Mahant N, Hutchison WD, Lozano AM, Moro E, Hodaie M, Lang AE, Dostrovsky JO (2006) Beta oscillatory activity in the subthalamic nucleus and its relation to dopaminergic response in Parkinson's disease. J Neurophysiol 96:3248-3256.

Weiss M (1982) Rhythmic activity of spinal interneurons in harmaline-treated cats. A model for olivo-cerebellar influence at the spinal level. J Neurol Sci 54:341-348.

Welter ML, Houeto JL, Bonnet AM, Bejjani PB, Mesnage V, Dormont D, Navarro S, Cornu P, Agid Y, Pidoux B (2004) Effects of high-frequency stimulation on subthalamic neuronal activity in parkinsonian patients. Arch Neurol 61:89-96.

Wennberg RA, Lozano AM (2003) Intracranial volume conduction of cortical spikes and sleep potentials recorded with deep brain stimulating electrodes. Clin Neurophysiol 114:1403-1418.

Wesseling JF, Lo DC (2002) Limit on the role of activity in controlling the release-ready supply of synaptic vesicles. J Neurosci 22:9708-9720.

Westen AA, Dekker DM, Briaire JJ, Frijns JH (2011) Stimulus level effects on neural excitation and eCAP amplitude. Hear Res 280:166-176.

Wichmann T, Bergman H, Starr PA, Subramanian T, Watts RL, DeLong MR (1999) Comparison of MPTP-induced changes in spontaneous neuronal discharge in the internal pallidal segment and in the substantia nigra pars reticulata in primates. Exp Brain Res 125:397-409.

Wilke M, Logothetis NK, Leopold DA (2006) Local field potential reflects perceptual suppression in monkey visual cortex. Proc Natl Acad Sci U S A 103:17507-17512.

Williams D, Kuhn A, Kupsch A, Tijssen M, van Bruggen G, Speelman H, Hotton G, Loukas C, Brown P (2005) The relationship between oscillatory activity and motor reaction time in the parkinsonian subthalamic nucleus. Eur J Neurosci 21:249-258.

Williams D, Tijssen M, Van Bruggen G, Bosch A, Insola A, Di Lazzaro V, Mazzone P, Oliviero A, Quartarone A, Speelman H, Brown P (2002) Dopamine-dependent changes in the functional connectivity between basal ganglia and cerebral cortex in humans. Brain 125:1558-1569.

Williams JC, Rennaker RL, Kipke DR (1999) Long-term neural recording characteristics of wire microelectrode arrays implanted in cerebral cortex. Brain Res Brain Res Protoc 4:303-313.

Wilms H, Sievers J, Deuschl G (1999) Animal models of tremor. Mov Disord 14:557-571.

Windels F, Bruet N, Poupard A, Feuerstein C, Bertrand A, Savasta M (2003) Influence of the frequency parameter on extracellular glutamate and gamma-aminobutyric acid in substantia nigra and globus pallidus during electrical stimulation of subthalamic nucleus in rats. J Neurosci Res 72:259-267.

Winestone JS, Zaidel A, Bergman H, Israel Z (2012) The use of macroelectrodes in recording cellular spiking activity. J Neurosci Methods 206:34-39.

Wingeier B, Tcheng T, Koop MM, Hill BC, Heit G, Bronte-Stewart HM (2006) Intra-operative STN DBS attenuates the prominent beta rhythm in the STN in Parkinson's disease. Exp Neurol 197:244-251.

Wise KD, Angell JB (1975) A low-capacitance multielectrode probe for use in extracellular neurophysiology. IEEE Trans Biomed Eng 22:212-219.

Witjas T, Kaphan E, Regis J, Jouve E, Cherif AA, Peragut JC, Azulay JP (2007) Effects of chronic subthalamic stimulation on nonmotor fluctuations in Parkinson's disease. Mov Disord 22:1729-1734.

Wu XS, Sun JY, Evers AS, Crowder M, Wu LG (2004) Isoflurane inhibits transmitter release and the presynaptic action potential. Anesthesiology 100:663-670.

Xing D, Yeh CI, Shapley RM (2009) Spatial spread of the local field potential and its laminar variation in visual cortex. J Neurosci 29:11540-11549.

Xu W, Russo GS, Hashimoto T, Zhang J, Vitek JL (2008) Subthalamic nucleus stimulation modulates thalamic neuronal activity. J Neurosci 28:11916-11924.

Ying SW, Werner DF, Homanics GE, Harrison NL, Goldstein PA (2009) Isoflurane modulates excitability in the mouse thalamus via GABA-dependent and GABA-independent mechanisms. Neuropharmacology 56:438-447.

Yoshida F, Martinez-Torres I, Pogosyan A, Holl E, Petersen E, Chen CC, Foltynie T, Limousin P, Zrinzo LU, Hariz MI, Brown P (2010) Value of subthalamic nucleus local field potentials recordings in predicting stimulation parameters for deep brain stimulation in Parkinson's disease. J Neurol Neurosurg Psychiatry 81:885-889.

Young HD, Freedman RA (2004) University Physics. San Francisco: Pearson Education.

Yousif N, Bayford R, Liu X (2008a) The influence of reactivity of the electrode-brain interface on the crossing electric current in therapeutic deep brain stimulation. Neuroscience 156:597-606.

Yousif N, Bayford R, Wang S, Liu X (2008b) Quantifying the effects of the electrode-brain interface on the crossing electric currents in deep brain recording and stimulation. Neuroscience 152:683-691.

Yousif N, Pavese N, Naushahi MJ, Nandi D, Bain PG (2012) Reversing the polarity of bipolar stimulation in deep brain stimulation for essential tremor: A theoretical explanation for a useful clinical intervention. Neurocase.

Yu H, Neimat JS (2008) The treatment of movement disorders by deep brain stimulation. Neurotherapeutics 5:26-36.

Zeng FG (2004) Trends in cochlear implants. Trends Amplif 8:1-34.

Zhao YB, Sun BM, Li DY, Wang QS (2004) Effects of bilateral subthalamic nucleus stimulation on resting-state cerebral glucose metabolism in advanced Parkinson's disease. Chin Med J (Engl) 117:1304-1308.

Ziegler JG, Nichols NB (1942) Optimum settings for automatic controllers. Trans ASME 64:759-768.

Zrinzo L, Zrinzo LV, Hariz M (2007) The peripeduncular nucleus: a novel target for deep brain stimulation? Neuroreport 18:1301-1302.

Zucker RS, Regehr WG (2002) Short-term synaptic plasticity. Annu Rev Physiol 64:355-405.

Biography

Alexander Rafael Kent was born in Albany, NY on June 18, 1985. He attended the University of Pennsylvania from 2003 to 2007, and earned a BS from the Department of Bioengineering. In August 2007, he matriculated at Duke University as a graduate student in the Department of Biomedical Engineering. He performed a one semester lab rotation with Dr. Lori Setton before joining the lab of Dr. Warren Grill in January 2008. He was the recipient of several awards while at Duke, including the Medtronic Foundation Fellowship, Duke University Department of Biomedical Engineering Robert Plonsey Fellowship, and National Institutes of Health Kirschstein Predoctoral Fellowship. In addition, he was awarded the North American Finalist in the Student Paper Competition at the 2011 IEEE-EMBS conference, and his 2012 publication in the *Journal of Neural Engineering* was selected by the journal as a "Highlight of 2012." His graduate research with Dr. Warren Grill focused on two areas: 1) measuring and characterizing evoked neural activity during deep brain stimulation, and 2) designing a nerve cuff and stimulation methods for selective stimulation of the pudendal nerve to restore bladder function. In August 2013 he completed his PhD.

Publications

Kent AR, Grill WM (2011) Instrumentation to record evoked potentials for closed-loop control of deep brain stimulation. Conf Proc IEEE Eng Med Biol Soc 2011:6777-6780.

Kent AR, Grill WM (2012) Recording evoked potentials during deep brain stimulation: development and validation of instrumentation to suppress the stimulus artefact. J Neural Eng 9:1-17.

Kent AR, Grill WM (2013) Neural origin of evoked potentials during deep brain stimulation. J Neurophysiol. *In Press*.

Kent AR, Grill WM (2013) Model-based analysis and design of nerve cuff electrodes for restoring bladder function by selective stimulation of the pudendal nerve. J Neural Eng 10:1-15.